

ISBN 978-82-326-4666-1 (printed version)  
ISBN 978-82-326-4667-8 (electronic version)  
ISSN 1503-8181

Doctoral theses at NTNU, 2020:159

Fredrik Mentzoni

# Hydrodynamic Loads on Complex Structures in the Wave Zone

**NTNU**  
Norwegian University of  
Science and Technology  
Faculty of Engineering  
Department of Marine Technology

Doctoral theses at NTNU, 2020:159

Fredrik Mentzoni

# Hydrodynamic Loads on Complex Structures in the Wave Zone

Thesis for the degree of Philosophiae Doctor

Trondheim, May 2020

Norwegian University of Science and Technology  
Faculty of Engineering  
Department of Marine Technology



Norwegian University of  
Science and Technology



**NTNU**

Norwegian University of Science and Technology

Thesis for the degree of Philosophiae Doctor

Faculty of Engineering

Department of Marine Technology

© Fredrik Mentzoni

ISBN 978-82-326-4666-1 (printed version)

ISBN 978-82-326-4667-8 (electronic version)

ISSN 1503-8181

Doctoral theses at NTNU, 2020:159



Printed by Skipnes Kommunikasjon as

# Abstract

The hydrodynamic loads on simplified structures relevant for deployment of sub-sea modules are studied in a two-dimensional setting. Experimental investigations and numerical simulations are performed. In the experiments, models are fixed in incident waves or forced to oscillate. Numerical simulations are conducted for models fixed in incident waves, oscillating flow and orbital flow. The simulations are performed using implemented potential flow and viscous flow (Navier–Stokes) solvers. Good agreement between the experimental and numerical results is, in general, found.

The main focus is on perforated platelike structures. The hydrodynamic added mass and damping coefficients are obtained in experiments and simulations of forced oscillations. The importance of the damping force is discussed; the hydrodynamic force of ideal perforated plates is dominated by damping if the perforation ratio,  $\tau$ , is larger than 10 %. In general, the coefficients increase with increasing Keulegan–Carpenter (KC) number and decreasing perforation ratio. An exception is if the perforation ratio is equal to or smaller than 20 %, in which case the damping of perforated plates can be larger than that of a corresponding solid plate for small KC numbers. The largest KC number where this is observed is  $KC = 1.25$  ( $\tau = 5$  %). The coefficients depend on the structural details of the plate, but are relatively insensitive to the number of perforations or holes. However, for very small KC numbers, i.e.,  $KC \rightarrow 0$ , the number of holes, not the perforation ratio, is the important parameter for the added mass coefficient of the structure.

The importance of flow-separation from the plate-ends of perforated plates is highlighted. Comparisons are made between numerical simulations where the flow is allowed to separate everywhere on the plates, and simulations using a hybrid numerical scheme where the flow is allowed to separate through the perforations of the plate only, not at the plate-ends. The importance of the global plate-end flow separation increases considerably with increasing KC number and decreasing perforation ratio, however, it is important even for KC numbers smaller than  $KC = 0.5$ .

The characteristics of the force on perforated structures fixed in incident waves depend on the distance from the mean free-surface to the structure. Nonlinear free-surface effects are important if the structure can go in and out of water, in particular a large slamming peak occurs, due to water entry of the structure into the incident wave. Contrary, if the model is fully submerged, the force charac-

teristics share strong similarities with the force characteristics of forced orbital or oscillating flows in infinite fluid domains. The normalized force amplitude of fully submerged perforated plates in incident waves increases, in general, with increasing KC number, increasing wavelength and increasing distance to the mean free-surface. The force on fully submerged models in incident waves is similar to the force on models in oscillating flow for small KC numbers, but considerably smaller for large KC numbers.

The hydrodynamic loads of single and parallel perforated plates in orbital flow are similar to that of oscillating flow for small KC numbers, and smaller than in oscillating flow for large KC numbers. Contrary to the near symmetric plate-end vortices which are found in oscillating flow, the plate-end flow separation is asymmetric in orbital flow. This reduces the force in orbital compared to oscillating flow, and is a likely reason why the force is smaller on fully submerged perforated plates in incident waves than in oscillating flow.

In oscillating flow, the hydrodynamic loads on a structure consisting of two perforated plates with five relatively large bodies in between, are completely dominated by the loads on the perforated plates. For two parallel perforated plates in oscillating flow, interaction effects reduce the total force on the configuration compared to superposition of two single plates. The force is reduced on both plates, in particular the instantaneously downstream plate. The added mass of parallel perforated plates is similar to superposition of two corresponding single plates, however, the damping is considerably reduced.

Based on present results, simple expressions for the force on perforated plates are presented. The expressions are inspired by the hydrodynamic load model for solid plates, analytically derived by Graham. The present method yields the added mass and damping coefficients of ideal perforated plates in oscillating flow as functions of the perforation ratio and the KC number.

# Acknowledgements

This work was financed by the Research Council of Norway, NFR project 237929 CRI MOVE. I am thankful for the opportunity to be part of the MOVE project.

Professor Trygve Kristiansen has been my supervisor throughout this project. It is safe to say that I won the lottery within the lottery. Trygve has been the best supervisor I could ever dream of. I am forever thankful for your excellent guidance, suggestions and enthusiasm for my work.

I would also like to thank Professor Odd Magnus Faltinsen, who has been co-supervisor of my project, Professor Bernard Molin and Professor Marilena Greco for their interest in my work; thank you for your advice and the helpful discussions.

The office would never had been the same without my colleague and friend Senthuran Ravinthrakumar. Thanks for the many interesting discussions these years, for the moments of joy and laughter, and for the endless hours of debugging and frustration.

Also, I would like to thank my colleagues in MOVE and at the Department of Marine Technology, in particular Mia Abrahamsen-Prsic and Frøydis Solaas, for the cooperation these years.

For valuable help during the final process of writing the thesis, I would like to thank Professor Ivar Farup for providing a neat template and excellent support, and my little sister Sofie for proofreading.

Finally, there is this girl at home. And I am not referring to my bike. Ina, you shelter my soul. You are my fire when I am cold. Thank you for always believing in me.



# Contents

<b>Abstract</b> . . . . .	<b>iii</b>
<b>Acknowledgements</b> . . . . .	<b>v</b>
<b>Contents</b> . . . . .	<b>vii</b>
<b>Nomenclature</b> . . . . .	<b>ix</b>
<b>1 Introduction</b> . . . . .	<b>1</b>
1.1 Main findings . . . . .	1
1.2 Background . . . . .	2
1.3 Scope; simplifications of complex problems . . . . .	3
1.4 Previous and related work . . . . .	6
1.5 Present contribution and structure of thesis . . . . .	12
<b>2 Governing equations and dimensionless quantities</b> . . . . .	<b>15</b>
2.1 Viscous flows and the Navier–Stokes equation . . . . .	15
2.2 Potential flows . . . . .	16
2.3 Hydrodynamic coefficients and parameters . . . . .	17
<b>3 Experimental investigations</b> . . . . .	<b>23</b>
3.1 Facilities . . . . .	23
3.2 Experimental setup . . . . .	24
3.3 Error sources and experimental uncertainty . . . . .	35
3.4 List of experimentally tested configurations . . . . .	38
<b>4 Potential flow solver</b> . . . . .	<b>41</b>
4.1 Implementation . . . . .	41
4.2 Verification . . . . .	44
<b>5 Viscous flow solver</b> . . . . .	<b>47</b>
5.1 Governing equations . . . . .	47
5.2 Discretization . . . . .	50
5.3 Boundary conditions . . . . .	53
5.4 Validation and verification . . . . .	59
5.5 Modeling perforated structures . . . . .	67
<b>6 Perforated structures in oscillating flow</b> . . . . .	<b>75</b>
6.1 Ideal perforated plates . . . . .	75
6.2 Perforated structures consisting of cylinders . . . . .	82
6.3 Comparing different perforated plates . . . . .	93
6.4 On the importance of plate-end flow separation . . . . .	100

<b>7</b>	<b>Perforated structures in waves</b>	<b>107</b>
7.1	Partly submerged—water entry and exit	113
7.2	Fully submerged	127
7.3	Comparing incident waves and forced oscillations	132
7.4	Numerical simulations of incident waves	139
<b>8</b>	<b>A semi-analytical method for forces on perforated plates</b>	<b>143</b>
8.1	Graham's plate in oscillating flow	143
8.2	Numerical study on the perforation effect	150
8.3	Comparison with Molin's method	156
8.4	Semi-analytical method inspired by Graham	159
8.5	Comparison with 3D experiments	163
<b>9</b>	<b>Interaction effects</b>	<b>169</b>
9.1	Simplified subsea structure	169
9.2	Parallel ideal perforated plates	174
9.3	Hydrodynamic interaction of perforated plates and channel walls	192
9.4	Simplified mudmats	196
	<b>Conclusion</b>	<b>209</b>
	<b>Bibliography</b>	<b>211</b>
<b>A</b>	<b>Experimental time-series and spectra</b>	<b>217</b>

# Nomenclature

Frequently used abbreviations and symbols are presented in the following. If a symbol is not listed, its use is limited to a small part of the text, e.g. a section, in which a description is provided.

## Abbreviations

BEM	Boundary element method
CFD	Computational fluid dynamics
CFL	Courant–Friedrichs–Lewy condition
DNS	Direct numerical simulation
MOVE	Marine Operations in Virtual Environments
wp	Wave probe

## Dimensionless numbers and force coefficients

KC	Keulegan–Carpenter number
$KC_{\text{por}}$	Porous Keulegan–Carpenter number
Re	Reynolds number
$\frac{A}{A_0}$	Added mass coefficient, $C_A$ , $C_a$
$\frac{B}{\omega A_0}$	Damping coefficient, $C_B$ , $C_b$
$C_D$	Quadratic damping coefficient (drag)
$C_M$	Inertia coefficient, $\frac{A+\rho V}{A_0}$
$C_S$	Slamming coefficient



**Greek letters**

$\alpha$	Drag correction coefficient
$\beta$	Reynolds number divided by the KC number
$\Delta$	Grid cell size
$\Delta t$	Time-step
$\delta t$	Duration of impact
$\delta z_{\max}$	Maximum deflection
$\zeta$	Wave elevation
$\zeta_a$	Wave amplitude
$\eta, \eta_a$	Vertical motion and vertical motion amplitude
$\dot{\eta}$	Vertical velocity
$\ddot{\eta}$	Vertical acceleration
$\lambda$	Wavelength
$\mu$	Discharge coefficient
$\nu$	Kinematic viscosity
$\rho$	Fluid density
$\tau$	Perforation ratio
$\Phi$	Velocity potential
$\omega$	Oscillation/wave frequency

**Roman letters**

$A$	Added mass
$A_0$	Reference added mass
$a_0, a_1, b_1$	Constants in analytical method by Graham
$B$	Damping
$B_w$	Wave-radiation damping
$D$	Characteristic length (width/diameter)
$d$	Small characteristic length (width/diameter)

$\overline{d_r}$	Mean relative difference
$d_g$	Gap distance between side-by-side plates
$F, F_a$	Force and force amplitude (vertical, hydrodynamic)
$g$	Gravity of Earth, $9.81 \text{ ms}^{-2}$
$h$	Water depth
$h_f$	Length of wave flap
$K$	Resistance coefficient
$k$	Wave number
$L$	Length or lateral distance
$l$	Domain size
$l_h$	Length of hole/opening
$n_h$	Number of holes/openings
$n_p$	Number of plates or plate elements
$n_s$	Number of sources
$p$	Pressure
$T$	Oscillation/wave period
$t$	Time or plate thickness
$u, w$	Horizontal and vertical velocity components
$V$	Volume
$x, y, z$	Cartesian coordinates
$z_w$	Wetted vertical coordinate
$z_m$	Vertical position of model



# Chapter 1

## Introduction

In this thesis, I study the hydrodynamic loads on perforated and solid structures in forced motions and fixed in incident waves in a two-dimensional setting. The hydrodynamic loads are functions of the Keulegan–Carpenter (KC) number. In harmonically oscillating flow, the KC number describes the relation between the amplitude of motion,  $\eta_a$ , and the characteristic length,  $D$ ,

$$KC = 2\pi \frac{\eta_a}{D}. \quad (1.1)$$

Perforated plates are emphasized. The characteristic length of perforated plates is the plate width. The perforation ratio,  $\tau$ , is the ratio between the open area and the total area of the structure,

$$\tau = \frac{\text{Open area}}{\text{Total area}} = 1 - \frac{\text{Solid area}}{\text{Total area}}. \quad (1.2)$$

Hence,  $0 \leq \tau < 1$ , or alternatively,  $0 \leq \tau < 100\%$ . Further details on relevant parameters and dimensionless quantities are given in Chapter 2.

### 1.1 Main findings

The main findings, along with references to the relevant sections of the thesis, are presented in the following.

- The hydrodynamic force on perforated plates in oscillating flow is, in general, dominated by damping. In numerical simulations of ideal perforated plates, the damping force dominates if  $\tau \geq 0.1$ . Sections 6.3.2 and 8.2.
- The force coefficients of perforated plates in oscillating flow depend on the structural details of the plates, but are relatively insensitive to how many openings/holes the plate has. However, for very small KC numbers, the number of holes is the important parameter, not the perforation ratio. Sections 4.1.2, 5.5.2 and 6.3.

- Consistent with previous studies, the added mass and damping coefficients of perforated plates increase with increasing  $KC$  and decreasing  $\tau$ . An exception is for small  $\tau$  and limited  $KC$  numbers, in which case the damping coefficient can be larger than that of a corresponding solid plate. Nonetheless, the hydrodynamic force amplitude increases monotonically with increasing  $KC$  and decreasing  $\tau$ . Sections 6.1, 6.2 and 8.2.
- Plate-end flow separation is important for the hydrodynamic loads of perforated plates even for relatively small  $KC$  numbers. The importance increases, in general, with increasing  $KC$  and decreasing  $\tau$ . Section 6.4.
- Nonlinear free-surface effects are important for the loads on perforated structures in incident waves if the structure can go in and out of water, in particular due to slamming when the wave hits the structure. Section 7.1.
- The normalized force on perforated structures fully submerged in incident waves increases, in general, with increasing  $KC$ , increasing wavelength and increasing distance to the free-surface. Section 7.2.
- The normalized force amplitude on single perforated plates fully submerged in incident waves, and single and parallel perforated plates in orbital flow, is similar to that in oscillating flow for small  $KC$  numbers, but reduced compared to that in oscillating flow for large  $KC$  numbers. Contrary to oscillating flow, which yields near symmetric plate-end vortices, the flow is asymmetric in orbital flow. This reduces the force. Sections 7.3 and 9.2.
- In oscillating flow, the hydrodynamic loads on a structure consisting of two parallel perforated plates with five cylinders between the plates are dominated completely by the force on the perforated plates. Section 9.1.
- Compared to superposition of two corresponding single plates, the hydrodynamic loads on parallel perforated plates in oscillating flow are reduced. This is mainly due to reduction in the force on the downstream plate. Superposition principles can be applicable for estimating the added mass, but will considerably overestimate the damping. Section 9.2.
- The hydrodynamic load model for solid plates by Graham is compared with experiments and simulations. Good agreement is found for  $KC < 5$ . The model is tuned to yield appropriate estimates of the forces on perforated plates. Relations are provided for the added mass and damping as functions of  $KC$  and  $\tau$ . Sections 8.1 and 8.4.

## 1.2 Background

The development of subsea fields rely on marine operations for lifting and lowering of structures that are installed on the seabed. Typically, the operations are performed by lifting the structure with a crane on a vessel, and lowering it off the side of the vessel. Moonpool operations, where the structure is lowered through an opening in the ship, is an alternative approach.

There is an increasing demand for all-year operability of marine operations for subsea fields. Rystad Energy, an energy research and business intelligence com-

pany, predicted in March 2019 “the subsea market to increase significantly in the years to come” [1]. Increased activity increases the need for installation of new structures, but also modifications and maintenance of existing ones.

In order to achieve all-year operability, there is a need for accurate estimates of the forces that the structures will feel during the operation, important for the crane hook load. The hydrodynamic loads that act on the structure as it enters water and is lowered through the wave zone and placed on the seabed, are of particular interest. If there is a lack of accurate load estimates, a conservative approach must be taken in order to ensure safe operational conditions. However, since the hydrodynamic loads will depend on the environmental conditions, being conservative can reduce the operational weather window. Furthermore, increasing load estimate accuracy, and reducing conservatism, may be cost-saving by reduced vessel or crane size requirements for performing the operation.

Subsea structures, or subsea modules, can be, from a geometrical point of view, quite large and complex. These structures tend to consist of various equipment, pipes and protection that are densely packed in modules. The size of the structures depend on their function, and range from a few meters up to a few tens of meters. Larger subsea structures can consist of a large template frame where smaller modules are installed in different stations. The Åsgard subsea gas compression by Equinor is one such example [2].

### 1.3 Scope; simplifications of complex problems

The present project is part of Marine Operations in Virtual Environments (MOVE), which is a Center for Research-based Innovation (CRI), located in Norway. The purpose of MOVE is to “support the entire marine operations value chain by developing knowledge, methods and computer tools for safe and efficient analysis of both the equipment and the installation process” [3]. One of the projects within MOVE is related to on-board decision support, which, among other subjects, focuses on the hydrodynamic loads of subsea structures during lifting operations. The present thesis is part of this sub-project, and the scope follows from the sub-project’s objectives and goals.

The focus of the thesis is on hydrodynamic forces on complex structures in the wave zone. The ultimate goal is to be able to determine the exact force on a subsea structure during all phases of a lifting operation. In order to do so, the complexity of the structure and the complexity of its surrounding environment—irregular waves and flow, nonlinear forces, interaction between the model, crane and ship motions, and so forth—must be taken into account. This is neither feasible nor efficient, and simplifications are needed. By making rational simplifications, more generic results, which can be useful in more than one particular situation, can be obtained. Further, rational simplifications can be useful to determine the relative importance of different forces, and to better understand the dominating effects in the complex real world. Therefore, the goal of this research is to decrease the knowledge gap that exist for the hydrodynamic loads on complex structures in the

wave zone, by applying smart simplifications to both 1) the complexity of complex structures, and 2) the complexity of the wave zone environment.

Complex subsea structures include several members and structure types of interest. The thesis includes studies of relevant structure types, as well as studies of the interaction between typical members of subsea structures. A considerable part of the work has been dedicated to studying perforated platelike structures. Perforated plates are relevant for several marine applications, in particular for complex subsea structures. Ventilated or perforated platelike structures of subsea modules include, among others, protection structures, hatch covers and mudmats.

The complexity of the environment is related to the different phases of a subsea lift operation, which can be expressed in terms of five stages:

0. The structure is lifted from the ship deck and positioning over the side of the vessel. The lowering of the structure is started, but the structure is dry.
1. The initial water entry occurs, and the structure can go in and out of water, but is yet to be fully submerged.
2. The structure is fully submerged, but still close to the free-surface.
3. The structure is lowered further and far from the free-surface, but still far from the seabed.
4. Final lowering. The distance to the seabed becomes important for the hydrodynamic loads.

Illustrations of Stages 1–3 are presented in Fig. 1.1. Note that the present definition of lifting stages may vary slightly from that of others, e.g. [4, 5].

Contrary to Stages 1–4, Stage 0 is a dry stage without hydrodynamic loads on the structure, and thus the reason I denote this is as Stage 0. Stage 0 is not part of the scope of this project.

Stage 1 starts with the initial water entry of the structure. Large pressure peaks and considerable slamming forces can occur in this phase. Consequently, higher-order effects can be important for the forces on the structure. Depending on the wave conditions, the structure can go in and out of water in Stage 1. This can be particularly challenging since slamming and added buoyancy when the structure gets wet releases tension in the lifting wire, whereas the loss of buoyancy during water exit increases the tension.

In Stage 2, the structure is fully wet, and the challenges of water entry and exit are no longer an issue. Nevertheless, the structure is still close to the free-surface, and the orbital and oscillating motion of the incident waves can be important for the forces on the structure. Moreover, the oscillating motion of the ship and crane will contribute to the forces in Stage 2. Additionally, drag forces due to current and lowering of the module can be of influence.

The forces on the structure in Stage 3 can be similar to those of Stage 2, but there is no interaction with the free-surface. The motions of the fluid-structure interaction is less orbital than in Stage 2, since the dynamics of the waves die out exponentially with depth. If the lowering velocity is relatively small, the fluid-structure interaction in Stage 3 is similar to that of forced oscillations in an infinite

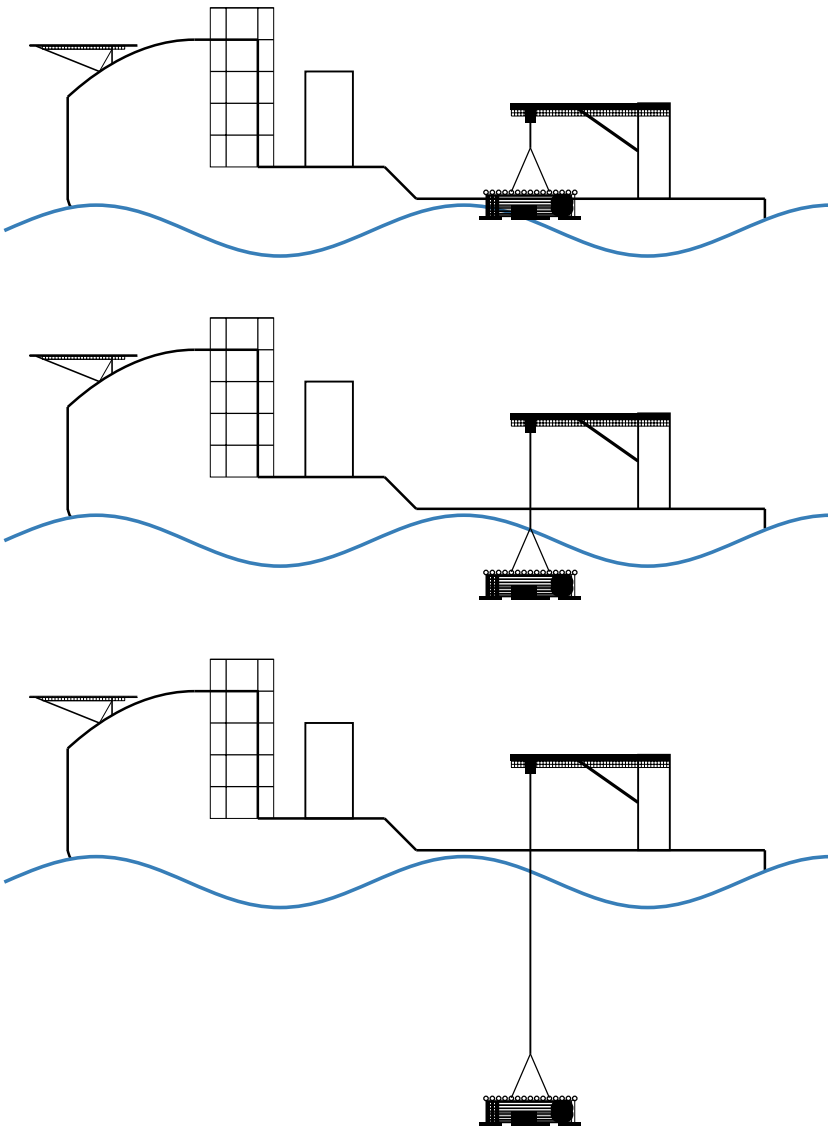


**Figure 1.1:** Stages 1 (top), 2 (middle) and 3 (bottom) of a subsea lift operation.



fluid domain, where the structure oscillates due to the ship and crane motions.

The operation enters Stage 4 when the presence of the seabed starts to influence the loads on the structure. Stage 3 is hence a transition stage where there is interaction with neither the free-surface nor the seabed. Contrary, in Stage 4, the hydrodynamic forces are expected to increase with decreasing distance to the seabed [4, 6–8]. Stage 4 ends when the structure is placed and installed on the seabed.

The studies in this thesis are relevant for Stages 1–4 of a subsea lift operation, however, there is an emphasis on experiments and simulations using forced oscillations. There are three main reasons for this: 1) Oscillating (or orbital) flow conditions are useful for studying various hydrodynamic effects, and investigate the sensitivity of changing different parameters, in a (relatively) controlled environment. 2) The results from studies of oscillating flow are relevant for all stages. 3) Hydrodynamic coefficients obtained in oscillating flow conditions in infinite fluid domains are used by project engineers for planing and analysis of a subsea lift operation [4, 5, 9, 10]. The values of the coefficients influence the result of the analysis, e.g. the limiting sea state and the required vessel and crane capacity. Therefore, proper estimates of the hydrodynamic coefficients is of interest. The coefficients can be obtained from dedicated experiments or numerical simulations. A less costly option is to apply values from recommended practices or experience from previous work. However, such an approach may increase the uncertainty and reduce the likelihood of safe all-year operability. Consequently, experimental and numerical investigations of force coefficients in oscillating flow, for structures relevant for subsea modules, are highlighted. Providing knowledge and recommendations to project engineers, on how hydrodynamic coefficients for subsea structures should be estimated, is emphasized as a specific objective within the relevant MOVE sub-project. Comparisons of oscillating flow conditions are made with models in orbital flow and incident waves, including both fully submerged conditions, and wave conditions where the structure goes in and out of water. The studies are two-dimensional, but comparisons with three-dimensional investigations and three-dimensional effects are discussed. Confidence in results is achieved by using a combination of analytical, experimental and numerical methods.

## **1.4 Previous and related work**

### **1.4.1 Model tests by Øritsland at Marintek**

During the 1980s, experiments with scaled imitations of subsea modules of different complexity were performed at Marintek in Norway. These studies were lead by Ola Øritsland. The results were presented in Marintek reports [11–14]. Øritsland and colleagues considered several relevant flow conditions including steady flows, oscillating flows and waves. However, most of their testing was devoted to decay tests for the evaluation of added mass and damping coefficients [13]. The tested

models were simplifications of complex subsea structures, and included among others, a framework structure with many openings, a plate, spheres and boxes. Tests were performed on individual models as well as combinations of structure parts. Some of their findings and observations are highlighted in the following.

- Interaction effects between members of a simplified subsea structure are important for the force coefficients. If the interaction effects are not taken into account, the added mass and damping coefficients can be considerably overpredicted.
- No considerable changes in natural periods were observed in the decay tests, hence the KC number dependence of the added mass coefficients could not be obtained.
- Both linear and quadratic damping is relevant for these structures. Øritsland argued that for KC numbers relevant for lifting operations of subsea modules, constant values for the linear and quadratic damping coefficients could be used. For these KC numbers, the quadratic damping term was found to be approximately 2-3 times larger than the corresponding quadratic damping in steady flow.
- The complexity of the forces in waves was highlighted. A coefficient-based approach, taking into account the influence of submergence on the hydrodynamic coefficients, was recommended as the most realistic alternative.

#### 1.4.2 Molin's force model for perforated structures

Bernard Molin and colleagues have performed an extensive amount of work on the hydrodynamics of perforated structures, cf. e.g. [15–19]. In his 2011 review paper, he presents a summary of their results from more than 20 years of work [19]. Complex subsea structures consist of several member types, of which perforated structures are important for the forces that these structures experience during lifting operations. Therefore, the work by Molin on perforated structures is highly relevant within the present project. In addition to performing experimental investigations, Molin developed a semi-analytical method for estimating the hydrodynamic coefficients of perforated structures. A summary of this force model is presented in the following.

The method by Molin assumes a quadratic pressure-drop condition for the flow through the openings of a perforated structure, combined with the assumption of potential flow conditions in the fluid domain, such that all vorticity is constrained to a thin strip coinciding with the plate. A notable finding of the method is that both the added mass and damping coefficients are functions of the amplitude of motion. Further, both coefficients go to zero when the amplitude goes to zero. Contrary, solid structures have nonzero added mass in the limit of zero amplitude. For the case of a perforated plate with zero thickness, the added mass will go to zero when the number of openings goes to infinite, independently on the perforation ratio. Such a plate is, in the present text, denoted an *ideal* perforated plate. Contrary, a perforated plate with finite thickness and finite number of openings is

denoted a *real* perforated plate.

The hydrodynamic added mass and damping coefficients are obtained from Fourier-series by eigenfunction expansion of the velocity potential [19]. The resulting hydrodynamic added mass and damping coefficients are found to be functions only of the so-called porous KC number,

$$KC_{\text{por}} = \frac{\eta_a (1 - \tau)}{D \mu \tau^2}. \quad (1.3)$$

Hence, the force coefficients are functions of the amplitude of motion,  $\eta_a$ , the width of the plate,  $D$ , the perforation ratio,  $\tau$ , and the discharge coefficient,  $\mu$ , only.

The discharge coefficient is a function of the local geometry of the plate openings, and may be estimated based on model tests. According to Molin et al. [17–19], the discharge coefficient is usually  $0.3 < \mu < 1.0$ . A sensitivity study performed by An and Faltinsen [20], showed that the value of the discharge coefficient is of importance, especially for the added mass coefficient. In his 2011 review [19], Molin presents various models for estimating the resistance coefficient,  $K$ , where the relation between the resistance coefficient and the discharge coefficient is

$$\mu = \frac{1 - \tau}{K \tau^2}. \quad (1.4)$$

Hence, the discharge coefficients may be estimated based on the resistance coefficient. Values for the resistance coefficient are provided by e.g. Blevins [21].

### 1.4.3 Sandvik's drag correction

In 2006, Sandvik et al. [9] proposed a drag correction to Molin's method, in order to account for the flow separation at the ends of perforated plates. The semi-analytical method by Molin including the drag correction term represents the state-of-the-art for force coefficient calculation of perforated plates. Sandvik et al. used the method to estimate the hydrodynamic coefficients of subsea roof structures. They found improved predictions of the hydrodynamic coefficients, compared with experimental results, when adding the drag correction term.

The drag correction method adds a drag force to the perforated plate, which in two-dimensional flow is written

$$F = \frac{1}{2} \rho C_D D \overline{w_r} |\overline{w_r}|, \quad (1.5)$$

with a drag coefficient,

$$C_D = \alpha KC^{-\frac{1}{3}}. \quad (1.6)$$

The relative velocity in the drag force term,  $\overline{w_r}$ , is the plate velocity minus the relative fluid velocity through the plate, averaged over the plate [19]. Consequently, with the drag force term added, the added mass and damping coefficients become functions of KC in addition to  $KC_{\text{por}}$ .

The drag correction coefficient,  $\alpha$ , is inspired by the analytical results for solid plates by Graham [22]. Graham's theoretical analysis yields  $\alpha = 11.8$ . However, for a perforated plate, the flow separation at the plate ends will be weaker than for a solid plate [18, 20]. Consequently,  $\alpha$  should be less than the value for a solid plate, and remains an unknown that, intuitively, depends on both the geometry of the plate and the perforation ratio. Sandvik et al. [9] used  $\alpha = 2$ , but other studies have found better predictions using considerably higher values, e.g.  $\alpha = 6$  and  $\alpha = 9$  [18, 20]. Hence, both  $\mu$  and  $\alpha$  are unknowns that must be determined prior to calculation.

#### 1.4.4 DNVGL-RP-N103

A recommended practice (RP) for modeling and analysis of marine operations is issued by DNV GL, the DNVGL-RP-N103 [4]. The RP provides “simplified formulations for establishing design loads to be used for planning and execution of marine operations” [4]. Methods and guidelines for estimating loads and hydrodynamic coefficients when lifting objects through the wave zone are highlighted in the RP.

Of particular interest are relations provided by DNV GL for estimating the effect of perforation on a structure's hydrodynamic coefficients. Two relations for estimating the added mass of perforated structures are included in the RP. Based on results from potential flow calculations of the added mass of perforated plates with circular holes, DNV GL provides the following relation for the added mass in the low-KC limit [4, Section 3.3.4],

$$\frac{A}{A_0} = \exp\left(\frac{-\tau}{0.28}\right). \quad (1.7)$$

Note that contrary to the result by Molin (zero added mass for  $KC \rightarrow 0$ ), the expression by DNV GL suggests that *real* (cf. Section 1.4.2) perforated plates have a considerable added mass in the low-KC limit, e.g.  $\tau = 0.3 \rightarrow \frac{A}{A_0} = 0.343$ . The fact that  $\frac{A}{A_0} \not\rightarrow 0$  is consistent with potential flow solutions of a structure consisting of several cylindrical members with finite diameter (i.e., a *real* plate), but the actual limiting value will depend largely on the diameter of the members.

The second relation for the added mass of perforated structures is “based upon a limited number of model test data and includes hence a safety margin” [4, Section 4.6.4],

$$\frac{A}{A_0} = \begin{cases} 1; & \tau \leq 0.05, \\ 0.7 + 0.3 \cos\left(\pi \left(\frac{\tau - 0.05}{0.34}\right)\right); & 0.05 < \tau < 0.34, \\ \exp\left(\frac{0.1 - \tau}{0.28}\right); & 0.34 \leq \tau \leq 0.50. \end{cases} \quad (1.8)$$

As for the low-KC relation in (1.7), the second relation in (1.8) is a function of perforation ratio only.

#### 1.4.5 Other relevant studies

There exist several previous studies of relevance for the present topic. Some of these are briefly summarized in the following.

Already mentioned Sandvik and colleagues performed experimental investigations of five perforated structures, in addition to the development of the previously described force model [9]. Models of three roof structures and two simpler hatches were tested and hydrodynamic coefficients were obtained. The structures had perforation ratios in a range from  $\tau = 0.15$  to  $\tau = 0.47$ . The added mass coefficients of the structures were found dependent on the amplitude of oscillation, but independent of the oscillation period. If the added mass coefficients for the different perforation ratios were plotted against a porous KC number, the spread between the different perforation ratios was reduced. The linearized damping was presented for the three roof models; an almost linearly increasing damping coefficient was found for increasing KC number.

Tao and Dray [23] performed experiments for  $0.2 \leq KC \leq 1.2$  of four solid and perforated disks of diameter 400 mm. The perforated disks had circular holes of diameter 4.4 mm and perforation ratios  $\tau = 0.05$ ,  $\tau = 0.1$  and  $\tau = 0.2$ . The hydrodynamic coefficients increased with KC for all perforation ratios. In general, the coefficients increased with decreasing perforation ratio. An exception was for very small KC numbers where the damping could be larger for the perforated disks than for the corresponding solid disk. For  $KC = 0.2$  and frequency 0.1 Hz ( $T = 10$  s), the disk with perforation ratio  $\tau = 0.2$  yielded approximately 30 % larger damping than the solid disk [23].

Sarkar and Gudmedstad [5] evaluated the use of DNVGL-RP-N103 [4], cf. Section 1.4.4, for lifting analysis of subsea structures. They concluded that the RP by DNV GL provides an “excellent basis” for analysis of subsea lifting operations [5]. However, they recommended more model testing in order to better understand the amplitude dependence of the hydrodynamic coefficients of complex subsea structures. Challenges with estimating the effect of perforation were highlighted. The expressions provided by DNV GL, Eqs. (1.7) and (1.8), could be conservative, in particular for structures with flat surfaces. Moreover, it was pointed out that the added mass of perforated structures depend on the amplitude of motion.

An and Faltinsen studied perforated plates analytically, experimentally and numerically [20, 24]. Their experimental studies consisted of three-dimensional model tests of two rectangular perforated plates with perforation ratios  $\tau = 0.08$  and  $\tau = 0.16$ . Circular holes were used to make the plates perforated. In their experimental study, the two perforated plates, both with cross-sectional areas of 520 mm  $\times$  365 mm, were forced to oscillate at two different submergences, for different periods of motions and a range of amplitudes corresponding to Keulegan–Carpenter numbers of  $0.17 \leq KC \leq 1.7$  with KC based on the smallest of the two plate sides ( $D = 365$  mm). They found strong KC number dependence for both the added mass and damping coefficients.

An and Faltinsen developed a semi-analytical method, similar to that of Molin

[19], by assuming anti-symmetric vortices distributed along the plate. The resulting hydrodynamic coefficients corresponded to those found using the method by Molin. Compared with their experimental investigations, improved agreement was found in the hydrodynamic coefficients of the semi-analytical method when adding a drag force—similar to that suggested by Sandvik et al. [9]—to account for flow separation at the plate-ends in an empirical manner.

Li et al. [25] performed an experimental study of heave plates for spar platforms. The plates were flat square sections of  $400\text{ mm} \times 400\text{ mm}$ . Four of the tested plates were perforated, with perforation ratios of  $\tau = 0.01$ ,  $\tau = 0.05$  (two different hole sizes) and  $\tau = 0.10$ . The plates were forced to oscillate harmonically in heave for Keulegan–Carpenter numbers ranging from  $0.2 \leq KC \leq 1.2$ . Only minor differences were found in both hydrodynamic coefficients between the two hole sizes tested. The added mass coefficients increased with increasing  $KC$  and decreasing  $\tau$ . A quadratic damping model was used. The quadratic damping coefficient decreased, in general, with decreasing perforation ratio and increasing  $KC$ . Note, however, the small perforation ratios considered and that the largest  $KC$  number is 1.2. The differences in the quadratic damping coefficients between the three different perforation ratios were negligible for  $KC > 1.0$ , and were similar to those of a solid plate. This is consistent with analysis by Molin [16], which found that the damping from perforated disks can be larger than the damping from solid disks, but only for  $KC < 1$ .

In addition to testing single solid and perforated disks, configurations consisting of three plates in parallel were investigated by Li et al. [25]. The tests included three times a solid disk and three times a disk with perforated ratio  $\tau = 0.05$ . Different gap distances between the plates were tested. The relative spacing of the plates was varied from 0.5 to 1.5 times the width of the plates. When the plates were placed relatively far from each other, the hydrodynamic coefficients were similar to three times that of a single plate, whereas when the plates were placed closer to each other, interaction effects between the plates reduced the hydrodynamic coefficients. The quadratic damping coefficient was in general more sensitive to the relative spacing than the added mass coefficient. For relative spacing larger than one plate width, the added mass of the three perforated plates in parallel was similar to superposition of three single plates.

Tian et al. [26] performed an experimental investigation of oscillating flat circular disks. Unlike many previous studies, their experiments included high  $KC$  numbers, with a total range  $0.15 \leq KC \leq 3.15$  when normalizing with the disk diameter. Seven perforated disks were investigated, with perforation ratios  $\tau = 0.05$ ,  $\tau = 0.10$  (five different hole sizes), and  $\tau = 0.20$ . Amplitude dependence was found to be important for both the added mass and damping coefficients, for all perforation ratios, generally with increasing coefficients for increasing amplitude. A significant decrease in the added mass coefficients was found when increasing the perforation ratio; for the whole range of considered  $KC$  numbers, the added mass coefficient of the most perforated disk ( $\tau = 0.20$ ) was approximately half that of the solid disk. The damping coefficients were less sensitive

to the perforation ratio, however, a slight reduction was in general found when increasing the perforation ratio. The sensitivity to hole size was found to be small, and the coefficients were almost identical for the five different versions of the  $\tau = 0.10$  disk, throughout the whole range of KC numbers tested.

In addition to single disk configurations, Tian et al. [26] studied configurations with solid disks in parallel with varying gap distances. Five gap distances were tested for two parallel disks, with a ratio of the distance between the two disks to the disk diameter ranging from 0.075 to 0.755. Four gap distances (from 0.075 to 0.3975 times the disk diameter) were tested for three parallel disks. The obtained hydrodynamic coefficients increased, in general, with increasing gap distance between the disks. However, none of the parallel configurations had larger coefficients than superposition of the single plate results. Furthermore, it was found that when the gap distance was very small, the coefficients of two parallel disks could be smaller than those of one disk. According to Tian et al. [26], this is because the hydrodynamics of two parallel plates with a very small gap is similar to that of a single thick plate, which for large KC numbers can have hydrodynamic coefficients smaller than that of thin plates. The study by Tian et al. included both perforated and solid disks, however, the multiple disk configurations consisted of solid disks only.

The mentioned previous studies on perforated plates and disks highlight the following two observations: 1) For a given perforation ratio, increasing the KC number increases, in general, the hydrodynamic coefficients. 2) For a given KC number, increasing the perforation ratio decreases, in general, the hydrodynamic coefficients. An exception to 2) is the damping for small KC numbers which is found to be larger for dense perforated plates than for corresponding solid plates. Additionally, the studies of multiple parallel plates agree that plate interactions decrease the hydrodynamic coefficients relative to superposition of single plates. Furthermore, several studies have highlighted the importance of flow separation at the plate-ends [9, 18–20, 25], in particular when the perforation ratio is small and/or the KC number is large.

## 1.5 Present contribution and structure of thesis

Despite the considerable amount of valuable and useful studies related to hydrodynamic loads of complex subsea structures, knowledge gaps still exist. A typical industrial approach is to estimate the loads based on hydrodynamic coefficients for the various members of the structure. The structures are in general very complex, but some main member types are perforated and solid protection structures like hatch covers and mudmats, suction anchors and various cylindrical elements like pumps and other equipment. There is still a need for better understanding of the hydrodynamic forces on these types of structures, and the applicability of their hydrodynamic coefficients. Moreover, superposition principles are typically applied, but interaction effects are suspected to be of importance.

The present thesis aims at closing some of the knowledge gaps within hydrody-

namics of complex subsea structures. Due to the shapes of subsea structures, and the fact that the structures are lowered to the seabed from a crane on a ship, the vertical hydrodynamic forces are likely to be most important. Perforated protection structures can be of particular importance since they can have large surface areas normal to the direction of flow. Therefore, the vertical hydrodynamic forces on perforated platelike structures are studied in detail. The present study starts by considering the forces on these structures subjected to oscillating flow. The influence of various parameters on the forces is investigated. Previous studies have suggested that plate-end flow separation can be important for the forces on these structures; in the present study, a detailed analysis of this effect is presented. Further, perforated structures are studied in waves, and the hydrodynamic forces are compared with those of pure vertical oscillations. The applicability of simplified force estimates, relevant for industrial use, is discussed. Finally, the complexity of the structures is increased by joining more sub-structures together; interaction effects are investigated, and the validity of superposition principles is discussed.

The thesis is organized in nine main chapters. Chapters 1 and 2 serve as introduction; I present the background and motivation for the project, literature review and the mathematical formulation in terms of governing equations and dimensionless quantities. Chapters 3, 4 and 5 cover the methods used—the experimental setup (Chapter 3) and the presently implemented potential flow solver (Chapter 4) and viscous flow solver (Chapter 5). The results are then presented and discussed in Chapters 6, 7, 8 and 9. Finally, concluding remarks are given.

The results are divided into four chapters based on the topics covered. Each of the four result chapters contains both presentation and discussion of results. In Chapter 6, I present experimental and numerical results of perforated plates in forced oscillations. In Chapter 7, results for perforated plates in incident waves are presented and discussed. A simplified method for calculating the hydrodynamic coefficients of perforated structures is presented in Chapter 8. Lastly, in Chapter 9, aspects related to interaction effects are presented and discussed.





## Chapter 2

# Governing equations and dimensionless quantities

In the following, I will give a brief introduction to relevant governing equations and dimensionless quantities. I start by presenting the governing equations for viscous flows, which the viscous flow solver implemented in this project is trying to solve. Potential flows are treated in a separate section with a presentation of the governing equations for the present potential flow solver. Potential and viscous methods can be combined, as is done in modeling of the free surface, in simulations of incident waves, within the framework of the numerical viscous flow solver. Lastly, a presentation of the relevant hydrodynamic coefficients and dimensionless parameters is given.

### 2.1 Viscous flows and the Navier–Stokes equation

Humans have been fascinated by viscous flows for many hundreds of years. An early, systematic approach was taken by Leonardo da Vinci (1452–1519). One of his sketches, which I find of particular interest within the present work, is presented in Fig. 2.1 [27].

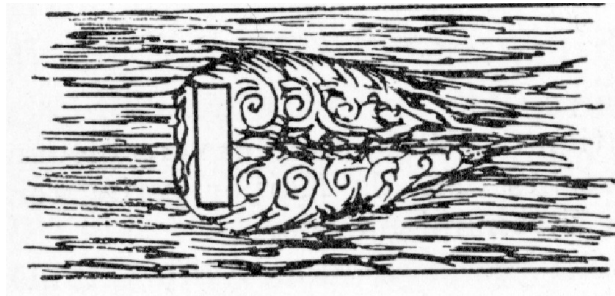


**Figure 2.1:** Sketch by Leonardo da Vinci [27].

In the years from 1821 to 1845, Navier, Cauchy, Poisson, Saint-Venant and Stokes, developed, independently, relations for the momentum of fluid flows that included frictional resistance based on Euler's inviscid equation derived in 1755 [28, 29]. Navier was the first to introduce the element of viscosity, and Stokes was the first to use the concept of viscosity in terms of a coefficient [29]. Today, we refer to this equation as the Navier–Stokes equation.

The Navier–Stokes equation is the governing equation for the momentum of viscous flows. Together with the continuity equation, it is the cornerstone of the present viscous flow solver. For incompressible and isothermal flows of a homogeneous Newtonian fluid with negligible bulk viscosity, the equations can be written

$$\frac{\partial u_i}{\partial x_i} = 0, \quad (2.1)$$

$$\frac{\partial u_i}{\partial t} + u_j \frac{\partial u_i}{\partial x_j} = -\frac{1}{\rho} \frac{\partial p}{\partial x_i} + \nu \frac{\partial^2 u_i}{\partial x_j^2}. \quad (2.2)$$

Here  $u_i$  represents the velocity component in the  $x_i$  direction,  $\rho$  is the fluid density,  $p$  the pressure and  $\nu$  the kinematic viscosity. Summation convention is used when multiple indices are used. Standard index notation is used. In two dimensions, I use  $x = x_1$  as the horizontal coordinate, and  $z = x_2$  as the vertical coordinate. Corresponding velocity components are denoted  $u = u_1$  and  $w = u_2$ .

I use the term *Navier–Stokes equation(s)* to refer to the momentum equation, a single vector equation or, in terms of the components, that is, the spatial coordinates, plural equations. Some authors include the continuity equation (and, if relevant, the energy equation(s) [30]) in addition to the momentum equation(s) when referring to the Navier–Stokes equations. However, the referred works by Navier and Stokes are based on Euler's momentum equation, and do not affect the continuity equation. Consistent with several authors, working in a broad range of subdisciplines within fluid dynamics, e.g. [29, 31–33], I therefore refer to Eq. (2.1) as the continuity equation, and to Eq. (2.2) as the Navier–Stokes or momentum equation. Regardless of linguistic preferences, the most important thing to remember is that a continuity equation, or statement of the conservation of mass—in addition to a momentum equation—is necessary for solving viscous flow problems.

## 2.2 Potential flows

If we assume zero vorticity, the velocity field can be described as the gradient of a scalar, the velocity potential,  $\Phi$ . Hence, such flows are referred to as potential flows. In the case of a homogeneous incompressible fluid, from the continuity equation, Eq. (2.1), the velocity potential satisfies Laplace's equation,

$$\nabla^2 \Phi = 0. \quad (2.3)$$

When the vorticity is zero, the Navier–Stokes equation may be greatly simplified. The viscosity term is zero and the nonlinear convection term can be rewritten. After integration, one obtains the Bernoulli equation for the pressure from the Navier–Stokes equation,

$$p + \rho g z + \rho \frac{\partial \Phi}{\partial t} + \frac{1}{2} \rho |\nabla \Phi|^2 = c(t) \quad (2.4)$$

Here  $g = 9.81 \text{ ms}^{-2}$  and  $p_a$  is the integration constant that satisfies atmospheric pressure,  $c(t) = p_a$ , in calm water at the mean free-surface,  $z = 0$ .

### 2.2.1 Linearized free-surface conditions

Boundary conditions for a free surface with mean position  $z = 0$  and wave elevation  $z = \zeta(x, y, t)$ , can be obtained from the substantial derivatives of the wave elevation (kinematic condition) and pressure (dynamic condition). First, the velocity potential and wave elevation are expressed as power series of the wave nonlinearities. Then, the equations are Taylor expanded from  $z = 0$  to the actual wave elevation,  $z = \zeta$ . The linearized equations follows by considering linear terms only,

$$-\frac{\partial \zeta}{\partial t} + \frac{\partial \Phi}{\partial z} = 0; \quad z = 0, \quad (2.5)$$

$$-\rho \frac{\partial \Phi}{\partial t} - \rho g \zeta = 0; \quad z = 0. \quad (2.6)$$

A combined equation can be obtained by time differentiation of the dynamic condition. If the velocity potential is assumed to vary harmonically in time, with frequency  $\omega$ , the combined equation can be written

$$\Phi - \frac{g}{\omega^2} \frac{\partial \Phi}{\partial z} = 0; \quad z = 0. \quad (2.7)$$

The linearized kinematic and dynamic boundary conditions, Eqs. (2.5) and (2.6), are used when simulating incident waves in the present numerical viscous flow solver. The combined linearized equation with assumed harmonically time-varying velocity potential, Eq. (2.7), is used as an assumption for the water entry module of the present potential flow solver.

## 2.3 Hydrodynamic coefficients and parameters

### 2.3.1 Added mass and damping

In 1950, Morison and colleagues presented a semi-empirical relation for the in-line force on a body in oscillating flow, i.e., the Morison equation [34]. The equation consists of two terms, one term proportional to the acceleration and one term proportional to the velocity squared. Based on this decomposition, the force on

a body in oscillating flow can be calculated from its added mass and quadratic damping coefficients.

Presently, a similar approach is used to present the forces on bodies in oscillating flow, however, the quadratic damping force is linearized. This has several favorable consequences, in particular that the limiting value of the damping coefficient is limited as the amplitude goes to zero. The limiting value is typically very small, although due to friction drag, the limit is not exact zero [8, 35]. Contrary, the alternative, i.e., using a quadratic damping model, has the unfavorable feature that the quadratic damping coefficient goes to infinity as the amplitude goes to zero. This is due to the friction drag force being linearly proportional to the velocity, cf. discussion by Thiagarajan and Troesch [35]. Furthermore, the tools used for design and analysis of marine operations typically require a linear model for the forces.

Consider a body forced to oscillate harmonically in otherwise calm water. Using the decomposition, the hydrodynamic force is written in terms of an added mass term and a damping term,

$$F = A\ddot{\eta} + B\dot{\eta} \quad (2.8)$$

with  $F$  being the hydrodynamic force,  $A$  the added mass coefficient,  $\ddot{\eta}$  the harmonically oscillating acceleration,  $B$  the damping coefficient and  $\dot{\eta}$  the harmonically oscillating velocity. If, however, the body is fixed and experiences an oscillating flow, there is an additional term arising from the unsteady pressure field of the fluid, the Froude–Krylov force,  $F_{FK}$ ,

$$F = A\ddot{\eta} + B\dot{\eta} + F_{FK} = (A + \rho V)\ddot{\eta} + B\dot{\eta} \quad (2.9)$$

with  $\rho$  being the fluid density and  $V$  the volume of the body. If the Froude–Krylov force is subtracted, an experimental investigation of a harmonically oscillating body in otherwise calm water can be compared with numerical simulations of the fixed body in an ambient oscillating flow.

Equation (2.8) can be written nondimensional by assuming a harmonically oscillating flow with velocity  $\dot{\eta} = \omega\eta_a \sin \omega t$ , and a reference added mass,  $A_0$ ,

$$\frac{F}{\omega^2\eta_a A_0} = \frac{A}{A_0} \cos \omega t + \frac{B}{\omega A_0} \sin \omega t. \quad (2.10)$$

The reference added mass is chosen to be the analytical added mass of a solid flat plate (or circular cylinder) of equal width,  $D$ , as the body. In two-dimensional flow, this is

$$A_0 = \rho \frac{\pi}{4} D^2 L, \quad (2.11)$$

with  $L$  being the length in the lateral direction, that is, into the plane. Note that by using this reference,  $\frac{A}{A_0}$  coincides with the added mass coefficient typically denoted  $C_A$  or  $C_a$  in the literature, or, if including the Froude–Krylov contribution,  $\frac{A+\rho V}{A_0} = C_M$  or  $C_m$ . Likewise, the damping coefficient,  $\frac{B}{\omega A_0}$ , is commonly referred to as  $C_B$  or  $C_b$ .

The nondimensional force, Eq. (2.10), can be rewritten as

$$\frac{F}{\omega^2 \eta_a A_0} = \sqrt{\left(\frac{A}{A_0}\right)^2 + \left(\frac{B}{\omega A_0}\right)^2} \sin(\omega t + \theta). \quad (2.12)$$

Here  $\theta$  is the phase difference between the velocity and the nondimensional force. The amplitude of the nondimensional force,  $F_a$ , is of particular interest,

$$\frac{F_a}{\omega^2 \eta_a A_0} = \sqrt{\left(\frac{A}{A_0}\right)^2 + \left(\frac{B}{\omega A_0}\right)^2}. \quad (2.13)$$

I would like to stress that since the amplitude of the nondimensional force is a function of the squared nondimensional added mass and damping coefficients, the ratio between the two,

$$\frac{\frac{B}{\omega A_0}}{\frac{A}{A_0}} = \frac{B}{\omega A}, \quad (2.14)$$

is a parameter that requires attention. A ratio equal to 1 means that both force components are equally important. If the ratio is larger than 1, the force is dominated by damping. If the ratio is smaller than 1, the force is dominated by added mass. Note the importance of squaring of terms in Eq. (2.13). Consider for instance that the force is dominated by damping, i.e., a ratio that is larger than one. Due to squaring of terms, damping alone can be a considerable part of the force, even for relatively small ratios larger than one,

$$\frac{\sqrt{\left(\frac{B}{\omega A_0}\right)^2}}{\sqrt{\left(\frac{A}{A_0}\right)^2 + \left(\frac{B}{\omega A_0}\right)^2}} = \frac{\frac{B}{\omega A}}{\sqrt{1 + \left(\frac{B}{\omega A}\right)^2}}. \quad (2.15)$$

Take as an example a ratio of 2, which is a typical value for a perforated plate with 20 % perforation ratio. Since the coefficients are squared, damping alone corresponds to 89 % of the force amplitude,

$$\frac{B}{\omega A} = 2 \rightarrow \frac{\frac{B}{\omega A}}{\sqrt{1 + \left(\frac{B}{\omega A}\right)^2}} = \frac{2}{\sqrt{1 + 2^2}} = 89 \%.$$

Correspondingly, added mass alone can be a considerable part of the force amplitude if the ratio is less than one.

In order to obtain added mass and damping coefficients from an experiment or a numerical simulation where the force and motion are known, several techniques can be applied. However, not all are equally appropriate, see for example the discussion by Chakrabarti [36, pp. 189-194]. Furthermore, different test settings, e.g. forced oscillations versus decay tests, can yield considerable differences in the hydrodynamic coefficients [37]. In the present studies, hydrodynamic coefficients

are obtained from forced oscillation experiments and numerical simulations of oscillating and orbital flow conditions. The added mass and damping coefficients are obtained by Fourier averaging,

$$A \int_{mT} \ddot{\eta} \ddot{\eta} dt + 0 = \int_{mT} F \ddot{\eta} dt, \quad (2.16)$$

$$0 + B \int_{mT} \dot{\eta} \dot{\eta} dt = \int_{mT} F \dot{\eta} dt. \quad (2.17)$$

Here  $m$  indicates a selected oscillation period and  $T$  is the oscillation period.

### 2.3.2 Keulegan–Carpenter and Reynolds numbers

In 1958, Keulegan and Carpenter [38] reported that the force coefficients of various bodies in oscillating flow were functions of a dimensionless quantity

$$\frac{WT}{D}. \quad (2.18)$$

Here  $W$  is the amplitude of the velocity,  $T$  the oscillation period and  $D$  the characteristic dimension (width) of the body. Thereafter, the quantity has been referred to as the Keulegan–Carpenter (KC) number. If the motions are oscillating harmonically, the KC number can be written

$$KC = \frac{WT}{D} = 2\pi \frac{\eta_a}{D}. \quad (2.19)$$

Note the use of  $W$  as the velocity amplitude. I use  $W$  instead of the more commonly used  $U$  since the models are forced to oscillate vertically in the present forced oscillation experiments and in the presently implemented numerical viscous flow solver. In the numerical viscous flow solver, the vertical coordinate is  $z$  and the vertical velocity component is  $w$ , hence the prescribed vertical velocity component has amplitude  $W$ .

In regular waves of amplitude  $\zeta_a$  and wave number  $k = \frac{2\pi}{\lambda}$ , if a model is placed at a vertical position  $z_m$  and the water depth is  $h$ , the KC number can be estimated, using linear wave theory [6], as

$$KC = 2\pi \frac{\zeta_a}{D} \frac{\sinh k(z_m + h)}{\sinh kh}. \quad (2.20)$$

The concept of viscosity introduced by Stokes led the way to another important dimensionless quantity in fluid flows. In 1883, Osborne Reynolds conducted one of the most famous experiments within the field of fluid mechanics. He found that the ratio of inertia forces to viscous forces was important for the behavior of fluid flows. Later, in 1908, Sommerfeld referred to the quantity simply as the Reynolds number, a definition that has stuck since,

$$Re = \frac{WD}{\nu}, \quad (2.21)$$

with  $\nu$  being the kinematic viscosity. The ratio between the Reynolds number and the KC number is referred to as  $\beta$  [39],

$$\beta = \frac{\text{Re}}{\text{KC}} = \frac{D^2}{\nu T}. \quad (2.22)$$

The hydrodynamic loads on complex subsea structures depend, in general, on both KC and Re. Due to the nature of oscillating flows, all subsea structures should be expected to depend on the KC number. Bluff bodies, without sharp edges, are in general Reynolds number dependent due to variations of flow-separation points. Consequently, the hydrodynamic loads can be sensitive to the scaling in experiments. Scale effects for the hydrodynamic coefficients of solid heave plates were discussed by Bezunartea-Barrio et al. [37]. The importance of scaling was found inferior to the effect of the KC number. They concluded that for practical purposes, the uncertainty of scale effects is less important than the uncertainty related to choosing the appropriate KC number [37].





## Chapter 3

# Experimental investigations

### 3.1 Facilities

The present experiments are conducted in a wave flume at the Marine technology center in Trondheim, Norway. At the Marine technology center, this wave flume is commonly referred to as Ladertanken (*en*: the Lader tank), due to Pål Lader who got the tank built and started performing experiments there in the late 1990s [40].

A simple sketch of Ladertanken is presented in Fig. 3.1. Ladertanken is a relatively narrow wave flume, 13.5 m long and 0.60 m wide. The applied water depth is 1.0 m. The narrow shape makes the tank suitable for facilitating near two-dimensional experiments. In the south<sup>1</sup> end of the tank, a wave flap can be used to generate waves. Alternatively, if the wave flap is not in use, a parabolic beach can be installed. The parabolic beach is installed such that it is approximately 2 mm below the mean free-surface. For the present configuration, this provides efficient damping of radiated waves. A similar beach is always used in the north<sup>2</sup> end of the tank.

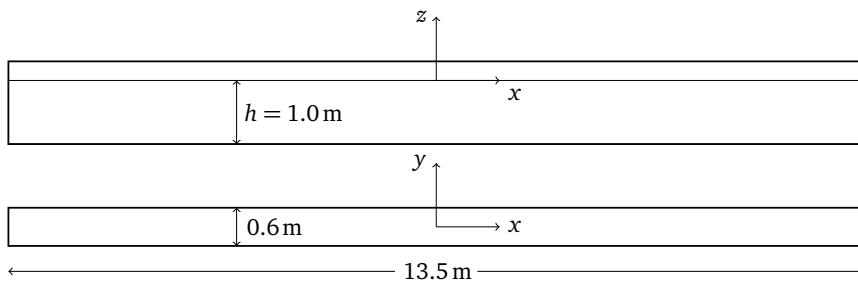


**Figure 3.1:** Dimensions of Ladertanken. Upper: Side view. Lower: Bird's eye view.

<sup>1</sup>The  $x$ -axis in Fig. 3.1 points in a direction approximately  $30^\circ$  east of true north, hence, the right edge of the tank in the sketch is referred to as the north end of the tank.

<sup>2</sup>See footnote 1.

Standard tap water is used in the tank. Depending on the season and the time of the day, the water temperature in the tank varies slightly. The water temperature is monitored with a basic thermometer. During cold winter nights, the minimum observed temperature is 19 °C, whereas during the summer, the water temperature reaches a maximum of 24 °C. This five degrees change in temperature yields slight variations in the density of water and approximately 10 % change in viscosity [41]. However, the experiments are performed in blocks with equal setup, typically lasting from a few days to a couple of weeks. Consequently, large temperature changes due to the seasons are not considered to affect the present experimental investigations.

Within each block of experiments, a number of experimental sets are performed, e.g. tests of different structure parts using the same tank setup. Each set consists of a range of oscillation periods and amplitudes. The total run time lasts, typically, from a few hours to one day. Some temperature variations during each set is expected, due to the indoor temperature difference between day and night.

## 3.2 Experimental setup

Ladertanken is equipped with a rig in which various models can be installed, such that experimental investigations of the models can be performed. The present experimental investigations include both forced oscillation experiments and incident wave experiments. In the forced oscillation experiments, the rig is forced to oscillate in otherwise calm water. In the incident waves experiments, the rig is fixed and the model experiences forces due to incident waves. A photo of the rig is presented in Fig. 3.2.

The rig is placed in the middle of the wave flume, with approximately equal distance from the south and north tank walls. The rig consists of an actuator which can move the rig in the vertical direction, a force transducer, a frame and two acrylic glass plates, cf. Fig. 3.2. This particular rig configuration was developed and installed for the present project<sup>3</sup>.

The acrylic glass plates consists of a large hole matrix such that various models can be installed and tested in multiple configurations. The acrylic glass plates are 420 mm wide, 1105 mm long and 6 mm thick. The mass of each acrylic glass plate is 3 kg. The gaps between the acrylic glass plates and the tank walls are 9 mm. The acrylic glass plates act as end-plates for the models, which yields a near two-dimensional setup, that is, water cannot flow between the installed model and the acrylic glass plates. The tested models are installed through the screw holes in the acrylic glass plates. Note that the sole purpose of the hole matrix is to be able to attach models at various positions. Yellow putty is used to fill holes that are not used, in order to ensure smooth surfaces on the acrylic glass plates.

In the intersection between the actuator and the frame, the force transducer

---

<sup>3</sup>Special thanks go to Trond Innset and Ole Erik Vinje who constructed and installed the present experimental rig.

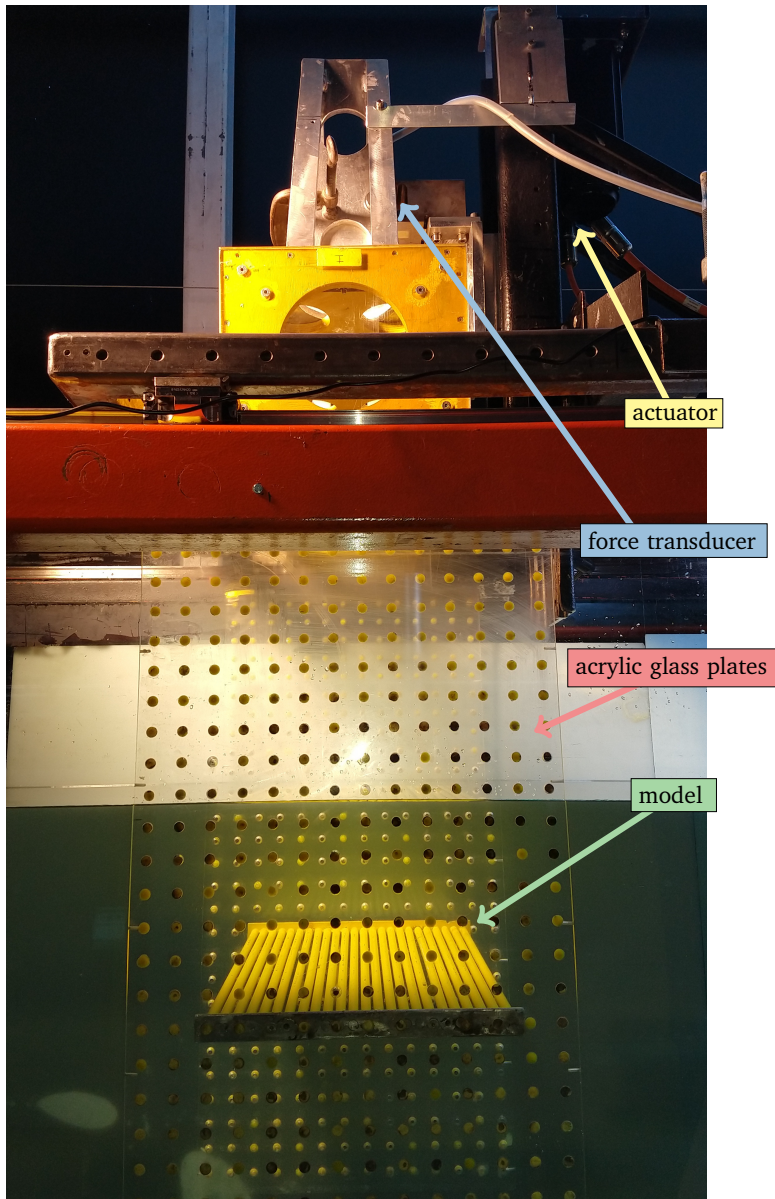


**Figure 3.2:** Photo of the experimental setup. Models can be installed between the two acrylic glass plates that are partly submerged. The acrylic glass plates are fastened to the yellow box and frame. Accelerometers are fastened to the frame.

measures the vertical force on the frame and the acrylic glass plates. Hence, if the rig is actuated, the measured force includes the force due to the moving frame and acrylic glass plates, in addition to the force on the model that is tested. In order to find the net force on the model, identical tests are performed without models fastened to the acrylic glass plates. The resulting force in these empty tests is subtracted, time-step by time-step, from the force measured in tests with a model,

$$F_{model} = F_{rig+model} - F_{rig}, \quad (3.1)$$

in order to obtain the net force on a model. Further, the dry mass of the model times the measured acceleration is subtracted from the force in order to find the hydrodynamic force on the model. Separate analyses were performed to assess the damping due to the rig and acrylic glass plates alone.

The software package Catman Easy by HBM is used for data acquisition of the experimental measurements [42]. The applied instrumental setup was carefully set up to achieve zero phase delay between the different signals, in order to obtain reliable hydrodynamic force coefficients. The vertical force, motions and wave elevation measurements are sampled at 200 Hz with Butterworth filtering at 20 Hz. The measurements are band-pass filtered around the basic harmonic of the oscillation when calculating the wave elevations, hydrodynamic coefficients and normalized hydrodynamic force amplitude. An example of the approach is presented in Fig. 3.3, in which the force and acceleration are presented for a typical high load case, illustrating the expected high-frequency noise of the measurements. Additional example plots from the experiments, including time-series and Fourier magnitude spectra, are provided in App. A. The measured signals are presented with blue color, the band-pass filtered signals with red. The acceleration is filtered around the first harmonic, whereas the force, which contains some contribution from higher-order components (mainly 3rd and 5th), is filtered around the first five harmonics.

Calibrations of the sensors are performed regularly to ensure high-quality measurements. All sensors are calibrated at the start of an experimental block. During longer lasting blocks, the sensor are calibrated, typically, on a biweekly schedule. Furthermore, all sensors are zero calibrated (removal of offset drift) before each set of an experimental block. Linear calibration curves are used for all sensors. The force transducer is calibrated by applying weights, representative for the forces measured in the experiments, to the rig and measuring the output in the data acquisition software. Based on the measured output, the calibration curve of the force transducer is adjusted in the software. The calibration factor and zero-crossing of the calibration curve is found based on the best linear fit from the weight tests. Similarly, the accelerometers are calibrated by physically turning them upside-down, on the side and the correct way while measuring the output in the data acquisition software. The calibration curve is then adjusted based on comparisons between the measured and expected ( $-g$ ,  $0$  and  $g$ ) output. Calibration of the wave probes is performed by physically adjusting the height of the sensors in water, reading the output and adjusting the calibration in the data

acquisition software. The tests are performed for several known heights, within a range representative for the waves of the experiments. The best linear fit from the tests is then used to determine the calibration curve.

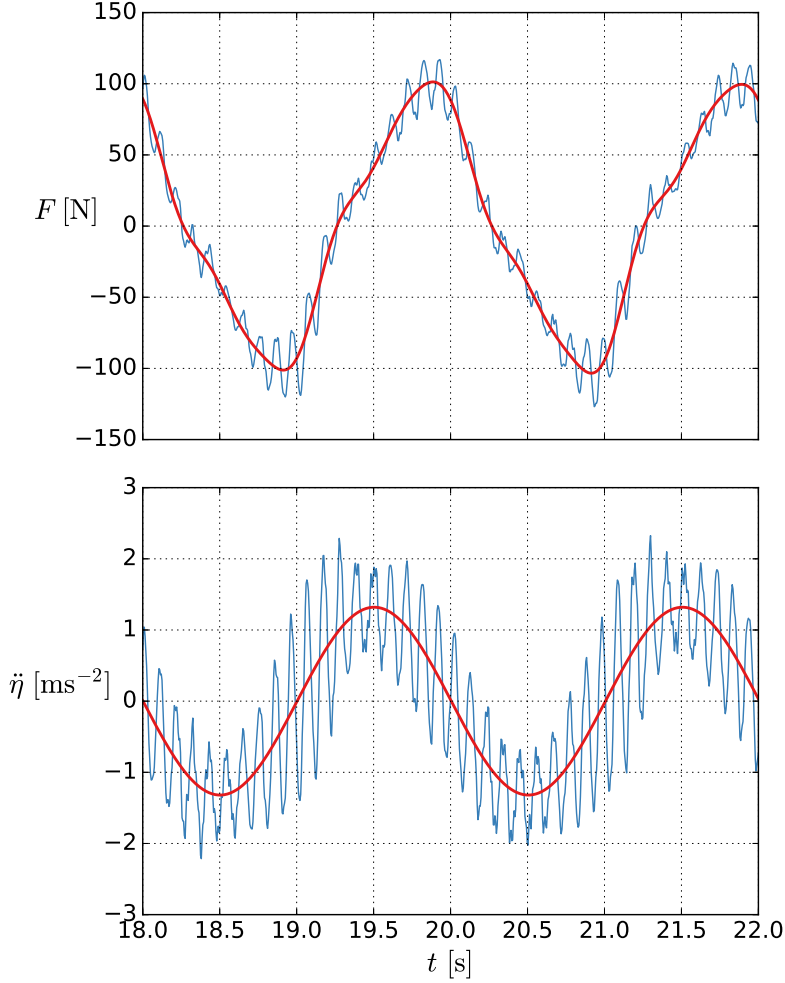


**Figure 3.3:** Measured (blue) and band-pass filtered (red) force and acceleration time-series from the experiments. The force and acceleration during two oscillation cycles of a typical high load case is presented; rig with perforated plate model C19 forced to oscillate with  $\eta_a = 13$  cm ( $KC = 2.82$ ),  $T = 2.0$  s. Additional example plots from the experiments are provided in App. A.

### 3.2.1 Forced oscillations

Ladertanken is well suited for performing forced oscillation experiments of two-dimensional models. A sketch of a typical setup is presented in Fig. 3.4. An harmonically oscillating signal is used to actuate the rig, such that the models oscillate in otherwise calm water. The vertical force and motions are measured on the rig. The oscillating rig and model will generate waves. Therefore, two parabolic beaches that damp out and avoid wave reflections, are installed in each end of the tank. The radiated waves are measured by wave probes installed downstream of the tank. The radiated waves are measured by wave probes installed downstream of the rig.

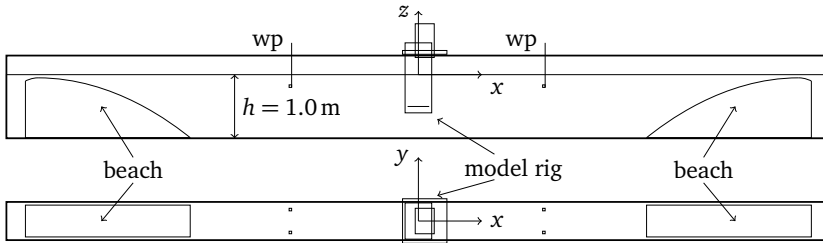


**Figure 3.4:** Sketch of the tank setup during forced oscillation tests. Parabolic beaches are placed on both sides of the tank to damp out and avoid reflection of radiated waves. Wave probes are placed far downstream of the rig to measure the radiated waves.

The actuator input signal, which is sampled at 50 Hz, consists of a range of sets. Each set has a prescribed amplitude and period of oscillation. Between each set there is 2-3 minutes of break (zero input) in order to ensure calm water conditions before each tested set. The signal is ramped linearly to and from the prescribed amplitude of motion at the beginning and end of a set. An implementation of the position of the rig and model before, during and after a set is presented in Code Listing 3.1.

Different input signals are used, but most of the forced oscillation experiments are based on a signal that consists of five periods of oscillation (1.00 s, 1.25 s, 1.50 s, 1.75 s, and 2.00 s) and a number of amplitudes of motion between 1.7 cm and 13 cm. In this input signal, each set consists of 20 oscillation cycles, of which five are used to ramp the signal from zero to the prescribed amplitude of motion, and five are used to ramp the signal back to zero. The presented force and coefficients are obtained for the eight oscillation cycles in the middle of the set, ignoring the ramp-in, ramp-out and the first and last oscillation cycle with full amplitude of motion. In Fig. 3.5, the first 60 s (top) and 4 minutes (bottom) of the input signal are presented. The total duration of this particular input signal, including all sets and breaks, is 15 hours. No exact scaling is set on the experimental models, however, they are typically of order 1:25-50 compared to full scale subsea structures. Consequently, the range of tested oscillation periods corresponds to

full scale (wave) periods in the range from approximately 5 s to 14 s. Limitations apply to the acceleration and motion of the actuator and rig, which is the reason for the applied range of amplitudes. Further, the smaller periods of oscillations are limited to smaller amplitudes within this range (1.7–13 cm) due to limitations on the applied accelerations of the actuator.

**Code listing 3.1:** Python code for obtaining the position of the rig and model before, during and after a set.

```
""" Signal used in forced oscillation experiments """
import numpy as np

def ramp_in(amp, period, time, time_break, n_r):
    """ Ramp in signal """
    amplitude = (time - time_break)/(n_r*period)*amp
    return amplitude*np.sin((2*np.pi/period)*(time - time_break))

def full_oscillation(amp, period, time, time_break):
    """ Full oscillation signal """
    return amp*np.sin((2*np.pi/period)*(time - time_break))

def ramp_out(amp, period, time, time_break, n_r, n_f):
    """ Ramp out signal """
    amplitude = (1 - (time - (time_break + (n_r + n_f)*period))/(n_r*period))*amp
    return amplitude*np.sin((2*np.pi/period)*(time - time_break))

for time in time_array:
    if time < time_break:
        eta = 0
    elif time >= time_break and time < time_break + n_r*period:
        eta = ramp_in(amp, period, time, time_break, n_r)
    elif time >= time_break + n_r*period and t < time_break + (n_r + n_f)*period:
        eta = full_oscillation(amp, period, time, time_break)
    elif (time >= time_break + (n_r + n_f)*period
          and time < time_break + (n_r + n_f + n_r)*period):
        eta = ramp_out(amp, period, time, time_break, n_r, n_f)
    else:
        eta = 0

# Description of variables:
# eta: position of the rig and model at time t.
# amp: prescribed amplitude of motion.
# n_r: number of ramp oscillation cycles.
# n_f: number of full oscillation cycles.
# period: prescribed period of oscillation.
# time: time.
# time_array: array of all time.
# time_break: break time before and after a set.
```

Some bugs were encountered during the first rounds of forced oscillation experiments. Initially, stiffeners fastened between the acrylic glass plates were used. The idea was that stiffeners would reduce vibrations and motions and increase the quality of the experiments. Instead, the opposite happened; the acrylic glass plates were likely to touch the walls of the tank if the stiffeners were used. The stiffeners were removed and new experiments were performed. Despite the acrylic glass plates only being 6 mm thick, vibrations and motions were not a problem without



stiffeners. When models are fastened to the acrylic glass plates, the stiffness of the rig is increased, but even in tests without models between the acrylic glass plates (empty tests), the acrylic glass plates of the rig oscillated without considerable high-frequency vibrations.

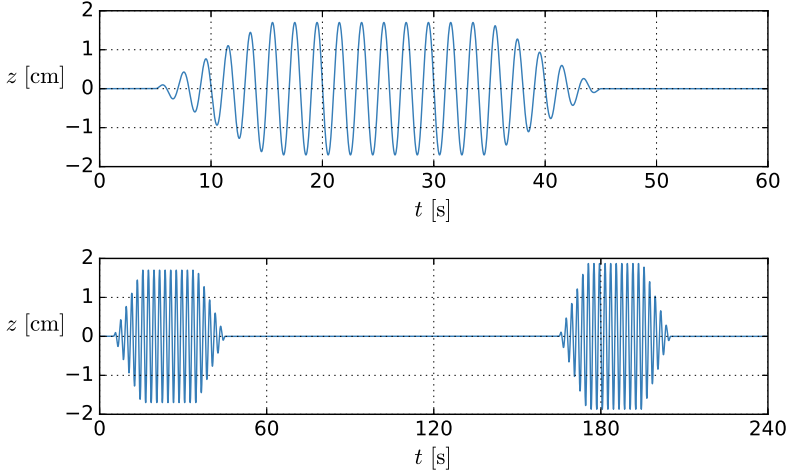


**Figure 3.5:** The first 60 s (top) and 4 minutes (bottom) of the input signal used in most forced oscillation experiments. The signal, which has a total duration of 15 hours, consists of multiple sets with breaks in between.

### 3.2.2 Forced oscillations with channel walls

Two walls were installed in the tank in order to test configurations forced to oscillate inside a channel. The channel walls were installed with 2 cm gaps to the acrylic glass plates. A photo of the setup is presented in Fig. 3.6. Two perforated plates were tested in oscillating channel flow. The purpose was to investigate how this would influence the hydrodynamic forces on the perforated plates when limiting the space for plate-end vortex generation. A priori, it was expected that the hydrodynamic force would consist of damping only.

In addition to tests of perforated plates, I tested a single square cylinder inside the oscillating channel. The purpose was to ensure that the channel wall setup was done correctly. This case was compared with forced oscillations of the same cylinder in open conditions, that is, without channel walls. In open conditions, the distance from the cylinder walls to the bottom and the free surface is the same as in the channel, 47 cm, but the distance to the side-walls of the tank is more than 6.5 m. As is the case for all the present forced oscillation experiments in open conditions, the models (perforated plates or cylinder) are forced to oscillate

vertically ( $z$ -direction) inside the channel.



**Figure 3.6:** Forced oscillation experiments inside a channel. Generation of plate-end vortices is limited due to the small gap from the plate-end to the channel wall.

Compared to the dimensions of the channel (width 0.46 m, height 1.0 m), the cylinder ( $D = 0.06$  m) is relatively small. Oscillating the cylinder vertically 0.5 m

from the free surface will only generate small disturbances on the free surface. Additionally, the channel walls are relatively far from the cylinder. Hence, if the setup is properly done, it is reasonable to expect that the effect of the channel walls, in terms of forces on the cylinder, is small. This can be seen from potential flow assumptions. As discussed by Faltinsen [6, p. 54], the potential flow added mass increases when a body is close to a wall [43]. However, the cylinder must be “quite close (...) before there is any influence” [6]. Therefore, one could expect slightly larger added mass coefficients in the channel than what is obtained when the channel walls are removed. Close inspection of the results presented by Greenhow and Ahn [43, Fig. 1] suggests that the increase in added mass is  $\approx 4\%$  when a circular cylinder is four radii from a wall. In the present experiment, the cylinder has a square cross-section—which has a potential flow added mass that is 1.51 times that of a circular cylinder [32, pp. 145–146]—and the distance to two walls is 7.7 radii. Therefore, the result presented by Greenhow and Ahn is not comparable to the present setup, however, it gives an idea of the order of magnitude of expected increase in added mass due to the channel walls. Moreover, since the space for the water to circumvent the cylinder is more limited in the channel compared to without channel walls, the flow velocity is increased close to the cylinder. This increases the damping. Consequently, both hydrodynamic coefficients are expected to increase slightly in the channel setup.

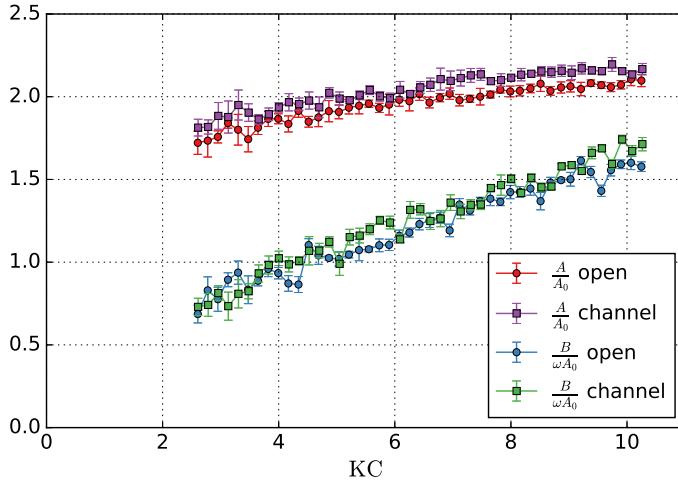


**Figure 3.7:** Test of the channel wall setup. A cylinder is forced to oscillate vertically ( $z$ -direction) with and without channel walls. In the channel, the added mass and damping coefficients are, on average, 4% larger than in open conditions.

The same input file was used in both settings; the period of oscillation was  $T = 2.0$  s and the amplitudes ranged from 2.5 cm to 10 cm. A total of 45 sets of

amplitudes were tested. Each set consists of 20 oscillation cycles of which five cycles are used to ramp the signal up, then follows 10 cycles with the prescribed amplitude of motion, before five cycles are used to ramp the signal down.

The added mass and damping coefficients from the square cylinder cases are presented in Fig. 3.7. The mean and standard deviations (error bars) are based on the eight cycles with the prescribed amplitude of motion in the middle of the set. The results in open and channel flow conditions are similar. As expected, the channel walls increases slightly the coefficients. For many KC numbers, the difference is within the standard deviations in coefficients for the different oscillation cycles.

On average, both coefficients are 4% larger in channel than in open conditions. The channel flow added mass coefficient is larger for 45/45 KC numbers, whereas the damping coefficient is larger for 31/45. The damping force is relatively small, which increases the uncertainty of the damping coefficients, a likely reason why there is a larger scatter for the damping coefficient than for the added mass coefficient.

The same comparison of channel and open conditions was done with the present numerical viscous solver. The numerically obtained differences in coefficients (channel vs. open conditions) were similar to those found in the experimental investigation (3% and 6% for, respectively, added mass and damping), giving further confidence in the experimental results. I concluded that the experimental setup of the oscillating channel was satisfactory.

### 3.2.3 Incident waves

Two models, both consisting of rows of cylinders, are tested in incident waves. The experiments are performed by fixing the model, installed in the rig, at given vertical positions. Sets of regular waves, of different wave amplitudes and periods, are then generated by the wave flap. Hence, the tested model is fixed and experiences incident waves. A sketch of the setup is presented in Fig. 3.8. A photo of one of the tested models placed 10 cm below the mean free-surface during a incident wave test is presented in Fig. 3.9.

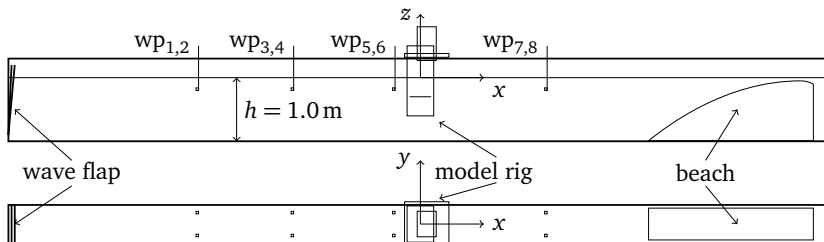


**Figure 3.8:** Sketch of the tank setup during incident wave tests. The positions of the wave flap, model rig, wave probes and beach are indicated.

Similar to the forced oscillation experiments, an input signal is used to actuate the wave flap. The implementation is similar to that presented in Code Listing 3.1. The input signal includes four wave periods (1.0 s, 1.1 s, 1.2 s and 1.3 s) and a range of flap amplitudes which yield wave amplitudes between 2.1 cm and 6.5 cm. Assuming an approximate scaling of the tested models of 1:25-50, the wave periods correspond to full scale wave periods of  $5\text{ s} \lesssim T \lesssim 9\text{ s}$ . Two periods of oscillation are used to ramp the signal to and from the prescribed wave flap amplitude (in Fig. 3.5, the presented input signal use five ramp periods). The vertical position of the models is varied from  $z = -30\text{ cm}$  to  $z = 5\text{ cm}$  ( $z = 0$  is the mean vertical coordinate of the free surface).

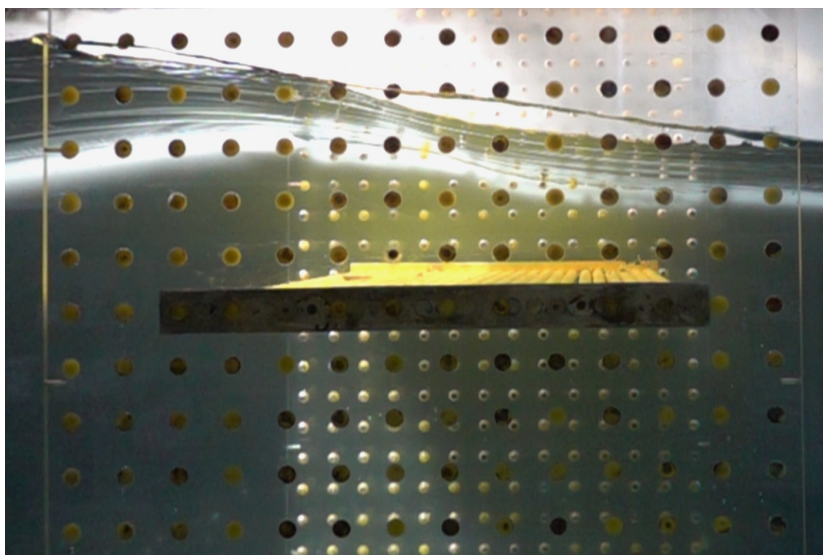


**Figure 3.9:** A perforated structure in incident waves. Yellow putty is used to fill the holes of the hole matrix of the acrylic glass plates that are not used to fasten the model, cf. Section 3.2.

Eight wave probes are installed in the tank during the incident wave tests, cf. Fig. 3.8. The wave profile above the model center is estimated based on the upstream wave probes. Wave probes 1-6 are used to estimate the wave celerity, and the measurements of wave probes 1-4 are used to estimate the wave profile above the geometrical center of the models. Special care is taken to ensure correct measurements of the horizontal distances between the upstream wave probes and the position of the geometrical center of the models, essential for calculating the correct wave celerity and phase of the wave at the position of the models.

### 3.3 Error sources and experimental uncertainty

A considerable amount of work is invested to ensure the general quality of the experiments and analysis, including minimizing the effect of random and bias error sources. Random errors are estimated by performing repetition tests and quantifying differences in the measured force and obtained coefficients from different oscillation/wave periods, e.g. by presenting both the mean and the standard deviations for a range of oscillation cycles. To minimize bias errors, several measures are taken, of which some are described in the following.

Different configurations (models and model placements) are tested by installing them through holes in the acrylic glass plates of the experimental rig. Consequently, the model rig is loosened and tightened between each configuration. This can yield small differences in the experimental conditions. The distance between the acrylic glass end-plates and the tank walls pose another challenge. In order to ensure similar conditions between several experimental trials, guiding plates and distance measuring are used when fastening the model rig.

In forced oscillation experiments, a common source of error is that the obtained hydrodynamic coefficients (added mass and damping) are sensitive to the sampling of signals. Problems arise if there is a phase delay between the measured signals that are larger than the sampling rate, or if the sampling rate is too small. If the force is almost in the exact phase as either the acceleration or the velocity, the accuracy of, respectively, the damping coefficient or added mass coefficient reduces. Three measures are highlighted in this context: 1) The sampling rate (200 Hz) is relatively high compared to the period of oscillations ( $1.00\text{ s} \leq T \leq 2.00\text{ s}$ ), to ensure that the time-series of the force and acceleration have fine resolutions. 2) The applied instrumental setup ensures that there is no phase difference between the sampled acceleration and force signals. 3) In addition to the hydrodynamic coefficients, the normalized force is presented. In cases where one of the coefficients dominates completely, the normalized force is emphasized and the uncertainty of the smaller coefficient is highlighted.

In the present experimental setup, the force difference between forced oscillation trials with and without models is used to obtain the net force on the model. Ideally, the only difference in this net force estimation is the force on the model, but the structural properties of the full model rig will be different than the empty rig, potentially influencing the force estimates. In addition to increasing the mass of the oscillating rig, the models will increase the structural stiffness of the rig since they are fastened to the lower parts of the acrylic glass plates, thereby forcing a constant distance between the plates. Contrary, the distance between the acrylic glass plates in the empty rig configuration depends on the fastening to the wooden box, at the top of the rig, only. A compromise is made between reducing the mass of the rig, which reduces the inertia force, and at the same time ensure sufficiently high rig stiffness. The acrylic glass plates are optimized with regards to limiting the size and mass, but at the same time ensuring large flexibility in test configurations.

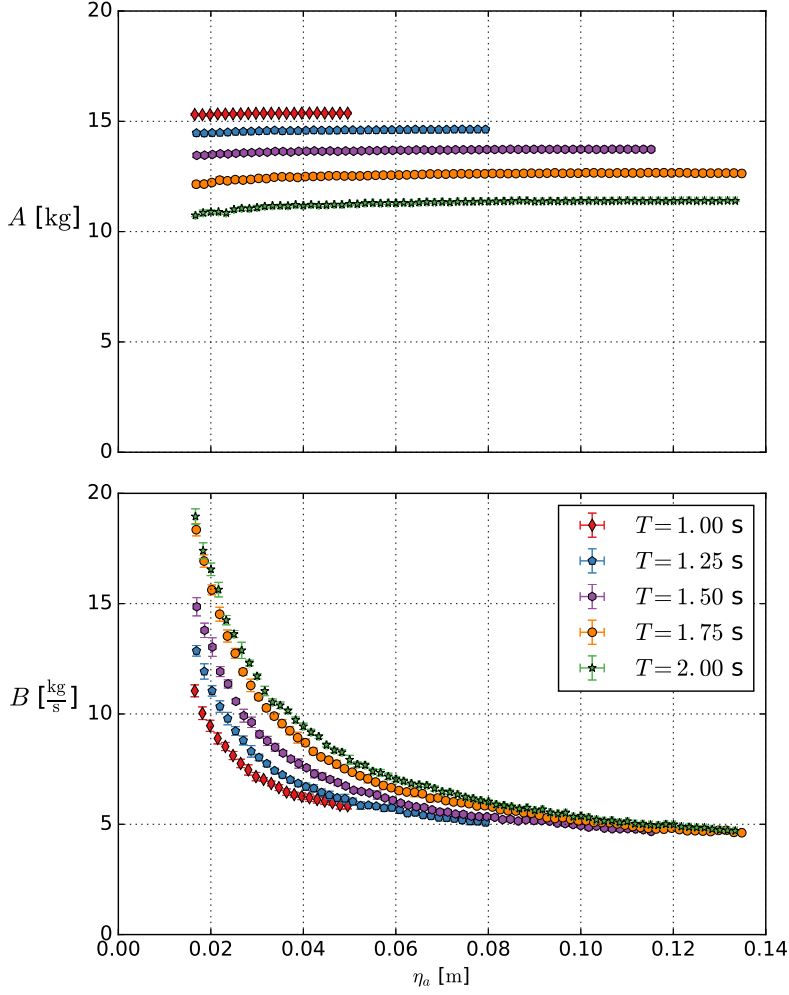


**Figure 3.10:** Measured force in empty rig trials decomposed in mass and damping terms, Eq. (3.2). The error bars indicate the variations of the force terms between oscillation periods.



If the net force on the model is very small relative to the force of the rig, the uncertainty of the present force estimation approach increases. The measured force during empty rig trials can be decomposed in mass and damping terms,

$$F_{empty} = A\ddot{\eta} + B\dot{\eta}. \quad (3.2)$$

In Fig. 3.10, the resulting  $A$  and  $B$  from empty rig trials of the commonly used input signal consisting of five oscillation periods is presented.

Compared to the measured total mass and damping in experiments with models, the empty rig results of Fig. 3.10 are small. However, for very small amplitudes of motion,  $\eta_a \lesssim 0.03$  m, the mass and damping terms in the empty rig trials can be of similar magnitude as those obtained for the models, e.g. for the configuration denoted as S28, the smallest tested amplitude yields  $A \approx 8$  kg and  $B \approx 50$ – $80$  kg s<sup>-1</sup> depending on the period of oscillation. The dry mass of this configuration is 1.79 kg. Consequently, the total inertia force (dry and added mass) of the model is of similar magnitude as the total inertia of the rig without models, whereas the net damping of the model is 3–7 times that of the empty rig (depending on the period of oscillation), cf. Fig. 3.10. For larger amplitudes of motion, the mass and damping forces of the models far exceed those found in empty rig trials.

Similar conclusions are drawn from comparison of the measured force amplitudes. For the smallest oscillation frequency,  $T = 2.0$  s, the force amplitude in experiments with models are typically 2–3 times that of the empty rig for the smallest tested oscillation amplitudes. For the largest oscillation amplitudes, the force amplitude in experiments with models are, typically, 6–15 times that of the empty rig force. Consequently, the accuracy of the present net force estimation is high for moderate and large oscillation amplitudes, but less certain for the smallest tested amplitudes of oscillation where the empty rig force, compared to the model force, is relatively large.

The results of Fig. 3.10 are plotted in terms of the mean value (marker) and the standard deviation (error bars) based on eight full oscillation cycles of the heaving actuator, cf. Section 3.2.1 and Fig. 3.5. In general, large standard deviations imply that there are large variations in the measured quantities between the oscillation/wave periods. These variations are either due to changes of the environmental conditions or due to experimental uncertainties. At the start of all experimental sets, the water in the tank is calm. As the rig and model starts to oscillate, some motion of the water in the tank must be expected. These water motions affect the measurements. Relevant examples are free-surface deflections (generation of waves) and the presence of the wake due to the previous oscillation of the model. By including error bars in the result plots, the uncertainty related to these effects is illustrated. For the specific case of the force terms in Fig. 3.10, the only fluid-structure interaction is due to the heaving acrylic glass plates, that is, the rig is empty. This effect is very limited. Consequently, the standard deviations give an indication of the precision of the experimental measurements. The error bars for  $A$  are hardly visible in Fig. 3.10. On average, the coefficient of variation (the standard deviation divided by the mean) of  $A$  is 0.4%. For  $B$ , the coefficient



of variation is 1.7%. Larger uncertainty in  $B$  is expected due to the force being dominated by mass when the rig is empty, i.e.,  $\frac{B}{\omega A} < 1$ , cf. Section 2.3.1.

Experimental uncertainties both increase and decrease when testing the models in incident waves. In terms of error sources, a benefit of this setup is that the model rig is fixed. Consequently, many of the above mentioned issues are not relevant. However, some new error sources appear, in particular related to the measurement of waves.

The results of the incident wave experiments are typically presented in terms of the normalized force on the models and the KC number. Both quantities depend on the measured wave elevation. To reduce possible errors, the wave probes are set up in pairs and calibrated regularly. Further, a total of eight wave probes are used, of which the six wave probes upstream of the rig are used to calculate the wave amplitude, cf. Fig. 3.8.

The normalization of force and amplitude also depend on the vertical position of the model. The position of the model is adjusted by the actuator before an experimental trial. The distance from the model to the free-surface, as well as the water depth, is manually checked before testing a new position of the model.

Slight variations of the water level in Ladertanken can occur from day to day, typically within 5 mm during 24 hours. This is related to leakage from the inlet and outlets of the tank. In the forced oscillation experiments, 5 mm change in water depth is unimportant and has no considerable effect on the measured force and obtained coefficients. Contrary, the incident wave experiments are sensitive to variations in water depth. However, a full experimental trial of a model in incident waves lasts four hours. Since the water depth is checked at the beginning of each experimental trial, the expected variations in water depth during the four hours are insignificant. Note that zero offset calibration is performed before all sets in both forced oscillations and incident waves. This limits the effect of sensor drift, related to e.g. water level variations, during long experimental trials.

### 3.4 List of experimentally tested configurations

I end this chapter by presenting a list of the models that are experimentally tested. The summary is provided in Table 3.1. All models are tested in forced oscillations. In addition, C19 and S28 are tested in incident waves.

The experimental studies include models that represent scaled simplifications of components of actual subsea structures. The models denoted P19, P28, C19 and S28 are perforated platelike structures. Perforated plates are typically used for protection structures like hatch covers, and are especially important for the loads of subsea structures. SPD15t, SPD30t and 2SP with varying gaps are models that consist of solid plates without and with gaps in between. Such models can be seen as simplifications of e.g. mudmats. Further, subsea structures are complex and consist of several members and types. How to account for interaction effects between different members of a subsea structure is one of the unsolved questions within hydrodynamics of complex structures in the wave zone. Hydrodynamic in-

teraction between various members is investigated experimentally with the studies of 5C, 2P28\_120+5C, 2P28\_120 and 2P28\_60. The models are introduced in more detail in the introduction to the results in Chapters 6–9.

**Table 3.1:** Experimentally tested models. The models are introduced in more detail in the result chapters.

Model	Description	Chapter(s)
P19	Ideal perforated plate with numerous holes. $D = 420$ mm, $\tau = 0.19$	6 and 9
P28	Ideal perforated plate with numerous holes. $D = 420$ mm, $\tau = 0.28$	6 and 9
C19	Perforated plate consisting of circular cylinders. $D = 298$ mm, $\tau = 0.19$	6 and 7
S28	Perforated plate consisting of square cylinders. $D = 360$ mm, $\tau = 0.28$	6 and 7
SPD15t	Solid plate, $D = 60$ mm, width-to-thickness $\frac{D}{t} = 15$	8 and 9
SPD30t	Solid plate, $D = 60$ mm, width-to-thickness $\frac{D}{t} = 30$	8
5C	Five circular cylinders of diameter 60 mm placed side-by-side with 30 mm gaps. Total width $D = 420$ mm	9
2P28_120+5C	Two times P28 placed in parallel 120 mm apart with 5C in between	9
2P28_120	Two times P28 placed in parallel 120 mm apart	9
2P28_60	Two times P28 placed in parallel 60 mm apart	9
2SP with varying gaps, $d_g$	Two solid plates of width $d = 60$ mm, thickness $t = 4$ mm, placed side-by-side with varying gaps: $d_g = 30$ mm, $d_g = 60$ mm, $d_g = 90$ mm and $d_g = 120$ mm	9



## Chapter 4

# Potential flow solver

A two-dimensional potential flow solver for infinite fluid conditions was implemented within the project. The purpose of the potential flow solver is to efficiently calculate the added mass of various bodies. The potential flow solver gives the added mass for  $KC \rightarrow 0$ . Added mass coefficients obtained by the potential flow solver provide useful support when evaluating the validity of other methods, in particular by comparing with results for small  $KC$  numbers in experiments and viscous flow solver simulations. Additionally, the potential flow solver is used to determine the variation in added mass of bodies during water entry by a von Kármán approach, in order to estimate the associated slamming force.

### 4.1 Implementation

A solution to the Laplace equation for the velocity potential, Eq. (2.3), can, by use of Green's identity, be constructed by a sum of source and doublet distributions placed on the boundaries of the domain, that is, by using a boundary element method (BEM). When determining the potential flow added mass of a body in infinite fluid, a distribution of sources is appropriate [6]. From the source distribution, the source strengths and thereby the velocity potential on the body is found. The added mass can then be determined from the linearized Bernoulli equation; numerically integrating the velocity potential times the normal vector for all elements.

The present implementation is similar to that described by Katz [44, p. 276] and Faltinsen [6, p. 103]. The implementation assumes that each discretized element of the body has a constant source strength that is evaluated in the center of each element, hence it is a constant-strength source method. This assumption dictates that a large number of sources are used in order to obtain accurate results.

#### 4.1.1 Basic structures

Two types of cross-sections, circular and rectangular, are used in the potential flow solver. By combining several basic structures side by side, these basic structures

can be used to model perforated plates.

When discretizing a circular cross-section, different implementations are possible. In the present potential flow solver, circular cross-sections are implemented such that the maximum radius of the discretized model corresponds to the radius of the exact circular cross-section. Hence, the area of the discretized circle is smaller than a true circle; when increasing the number of elements, the area of the circle will increase towards the area of a true circle. An illustration is given in Fig. 4.1.

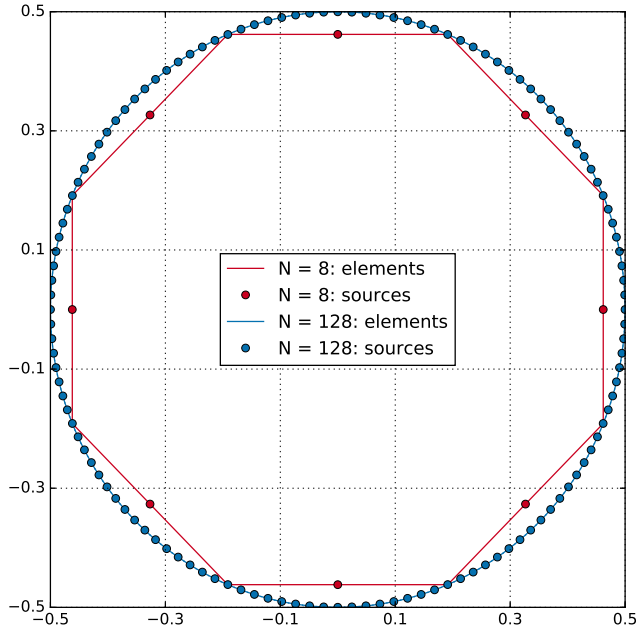


**Figure 4.1:** Discretizations with  $n_s = 8$  and  $n_s = 128$  sources, using the present potential flow solver, of a single circular cross-section with diameter equal 1.

#### 4.1.2 Perforated plates

Special care must be taken when modeling perforated plates with the potential flow solver. In the limit of zero KC, the added mass of a perforated structure will depend largely on the number of openings. As discussed by Molin [19], the potential flow added mass of a perforated flat plate will go to zero as the number of openings goes to infinity, independently on the perforation ratio of the plate.

Consequently, in order to get a realistic added mass of a perforated plate with the potential flow solver, the exact geometry of the plate—not just its perforation ratio—must be reproduced in the discretization. This is illustrated with an example presented in Table 4.1. The added mass of a perforated plate with perforation ratio  $\tau = 0.3$  is calculated with the potential flow solver using different number of openings. Included in the table is the relative difference to the relation for the added mass in the low-KC limit by DNVGL-RP-N103 [4, Section 3.3.4], Eq. (1.7). The expression by DNV GL is a function of the perforation ratio only. However, as stated above, the important parameter for  $KC \rightarrow 0$  is the number of openings, that is, the hole size relative to the plate size.

**Table 4.1:** Added mass of a thin plate ( $D = 100\tau$ ) with perforation ratio  $\tau = 0.3$  modeled with increasing number of holes,  $n_h$ , and corresponding hole size,  $l_h$ , to plate widths,  $D$ . The relative difference to Eq. (1.7) is included.

$n_h$	$\frac{l_h}{D}$	$\frac{A}{A_0}$	$\frac{ A - A_{Eq.(1.7)} }{A_{Eq.(1.7)}}$
1	0.3	0.284	17 %
2	0.15	0.207	40 %
4	0.075	0.144	58 %
8	0.0375	0.098	71 %
16	0.01875	0.071	79 %
32	0.009375	0.055	84 %
DNV GL		0.343	

#### 4.1.3 Double-body slamming approximation

In addition to calculating the potential flow added mass of various models, the potential flow solver is used to estimate the force on a body during water entry, which can be written [6, p. 299],

$$F = \frac{dA}{dt}w + A\frac{dw}{dt} + \rho g \Omega. \quad (4.1)$$

Here  $A$  is the added mass,  $w$  is the velocity of the body (here defined positive downwards),  $g = 9.81 \text{ ms}^{-2}$  and  $\Omega$  is the instantaneous submerged volume of the body. The three terms are, from left to right, the slamming force, the added mass force and the buoyancy force. The slamming force can be written in terms of the submergence,  $z$ ,

$$w\frac{dA}{dt} = w\frac{dA}{dz}\frac{dz}{dt} = \frac{dA}{dz}w^2. \quad (4.2)$$

A slamming coefficient,  $C_S$ , is then introduced,

$$\frac{dA}{dz}w^2 = \frac{1}{2}\rho C_S D w^2, \quad (4.3)$$

for the two-dimensional slamming force.

The double-body slamming approximation is based on the von Kármán approach which ignores the water rise-up. The added mass is estimated as half the added mass of a body consisting of the submerged part of the body and its mirror above the free-surface. The latter is justified if the velocity,  $w$ , is large such that the fluid accelerations are much larger than the acceleration due to gravity,  $g$ . From this assumption, the combined linearized free-surface condition, Eq. (2.7), will go towards  $\Phi = 0$  on  $z = 0$ . The problem can then be solved by considering the corresponding double-body problem in infinite fluid [6, pp. 43–44]. Consequently, the present potential flow solver can be used to calculate the double-body added mass, which is then halved to obtain the added mass of the actual body.

## 4.2 Verification

### 4.2.1 Added mass of basic structures

The potential flow solver is verified and checked for convergence for a single circular cross-section and a single square cross-section in infinite fluid. The results of the convergence study are presented in Table 4.2. Convergent results for both the circular cross-section and the square cross-section are obtained.

**Table 4.2:** Convergence study of potential flow solver. Added mass coefficients for a single circular cross-section and a single square cross-section calculated using an increasing number of sources to discretize the bodies. Analytical results: 1 and 1.513 for, respectively, a circular and a square cross-section [32, pp. 145–146].

Number of sources	Circular	Square
8	1.0908	1.6799
16	1.0671	1.5748
32	1.0386	1.5362
64	1.0205	1.5219
128	1.0105	1.5165
256	1.0053	1.5144
512	1.0027	1.5137
1024	1.0013	1.5134
2048	1.0007	1.5132

### 4.2.2 Water entry of a single circular cylinder

To verify the double-body slamming approximation, the water entry of a single circular cylinder at constant velocity is studied. The impact is discretized using 80 time-steps from right after the initial impact ( $z_w = \frac{1}{82}D$ ) to right before the cylinder is fully submerged ( $z_w = \frac{81}{82}D$ ). The double-body is discretized using 512

elements in each time-step. The slamming coefficient, cf. Eq. (4.3),

$$C_S = \frac{2}{\rho D} \frac{dA}{dz}, \quad (4.4)$$

is calculated based on the change in added mass for each time-step. The resulting slamming coefficient is presented as a function of the relative submergence,

$$\frac{wt}{D} = \frac{z_w}{D}, \quad (4.5)$$

with  $z_w$  being the wetted vertical coordinate.

The results are presented in Fig. 4.2. Linear extrapolation of the results for  $z_w = \frac{1}{82}D$  and  $z_w = \frac{2}{82}D$  yields  $C_S(t=0) = 3.19$  which is within 1.6% of the classical result by von Kármán,  $C_S(t=0) = \pi$  [45]. Faltinsen presented the added mass and slamming coefficient of a circular cylinder during water entry [6, Fig. 9.11, p. 300]. He used a potential flow solver. The present results are compared with the (digitized) results by Faltinsen, which serves as verification of the water entry module of the present potential flow solver.

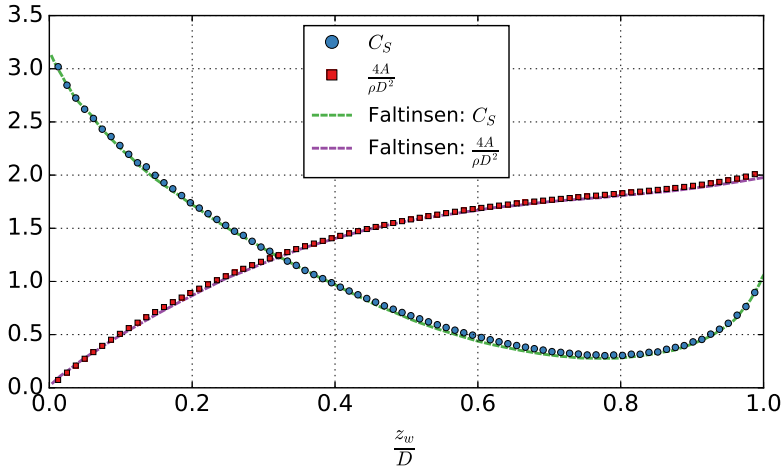


**Figure 4.2:** Slamming coefficient and added mass of a circular cross-section with diameter  $D$  during water entry. The  $x$ -axis indicates the relative submergence, that is,  $z_w$  is the wetted vertical coordinate which is equal to  $D$  when the cylinder is fully wet. The present results are compared with results by Faltinsen [6, Fig. 9.11, p. 300].





## Chapter 5

# Viscous flow solver

A two-dimensional viscous flow solver, based on the numerical solution of the continuity and Navier–Stokes equations, is implemented within the present project. The viscous flow solver is used to calculate loads on complex structures in different conditions, and to investigate different phenomena relevant for hydrodynamic loads on complex structures in the wave zone.

I use the abbreviation CFD, short for computational fluid dynamics, when referring to the viscous flow solver. Versteeg and Malalasekera define CFD as “the analysis of systems involving fluid flow, heat transfer and associated phenomena such as chemical reactions by means of computer-based simulations” [33, p. 1]. Following this definition, CFD could refer to any numerical solver of fluid flows, for example a potential flow solver. To distinguish between the two presently implemented numerical solvers—the viscous flow solver and the potential flow solver—I use the term BEM, short for boundary element method, when referring to the potential flow solver.

### 5.1 Governing equations

The presently implemented viscous flow solver is based on a fractional-step method, as that by Chorin [46], where the Navier–Stokes equation, Eq. (2.2), is split into two steps,

$$\frac{u_i^* - u_i^n}{\Delta t} = -u_j \frac{\partial u_i}{\partial x_j} + \nu \frac{\partial^2 u_i}{\partial x_j^2}, \quad (5.1)$$

$$\frac{u_i^{n+1} - u_i^*}{\Delta t} = -\frac{1}{\rho} \frac{\partial p}{\partial x_i}. \quad (5.2)$$

Standard index notation is used;  $u_i$  represents the velocity component in the  $x_i$  direction. For simplicity, the velocity components are referred to as  $u = u_1$  (horizontal direction) and  $w = u_2$  (vertical direction). Unless else is explicitly noted, the fluid density,  $\rho$ , and kinematic viscosity,  $\nu$ , are set to values similar to the water properties of 20° C,  $\rho = 1000 \text{ kg m}^{-3}$  and  $\nu = 1 \times 10^{-6} \text{ m}^2 \text{ s}^{-1}$ .  $n$  represents the present time-step,  $n + 1$  the next time-step, and  $*$  an auxiliary step.

Since the velocity field at  $n + 1$  is divergence free, cf. continuity Eq. (2.1), the divergence of Eq. (5.2) yields a Poisson equation for the pressure,  $p$ ,

$$\frac{\partial^2 p}{\partial x_i^2} = \frac{\rho}{\Delta t} \frac{\partial u_i^*}{\partial x_i}. \quad (5.3)$$

For each time-step, Eq. (5.1) is solved to find the tentative velocity field. Then Eq. (5.3) is used to determine the pressure, before the velocity field at  $n + 1$  is found from Eq. (5.2).

### 5.1.1 Domain decomposition

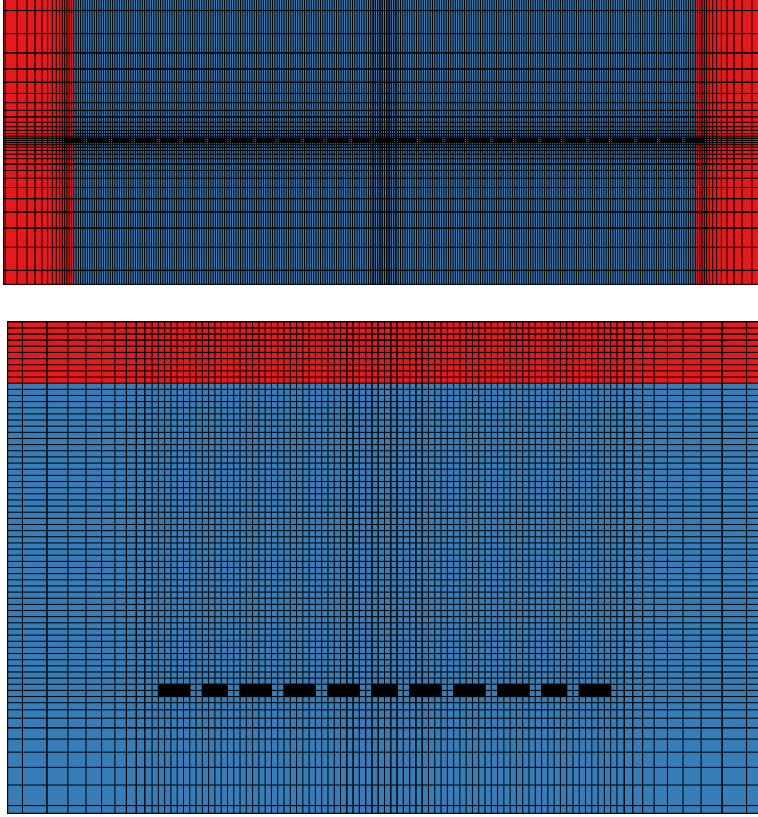


**Figure 5.1:** Illustrations of the domain decomposition principles in the modules *noEndVortex* (top) and *freeSurface* (bottom). The advection and diffusion terms are included in the blue regions; in the red regions they are omitted.

The viscous flow solver is implemented such that the numerical domains can be decomposed into regions with and without consideration of the advection and diffusion terms. This hybrid approach is similar to that by Kristiansen and Faltinsen [47]. In regions where the advection and diffusion terms are omitted,  $u_i^* = u_i^n$ . Consequently, the momentum equation is the linearized (no advection) Euler equation, and the pressure equation, Eq. (5.3), is a Laplace equation.

The domain decomposition technique is applied in two modules of the viscous flow solver, *noEndVortex* and *freeSurface*. Illustrations of the domain decompositions of the two modules are presented in Fig. 5.1. In the blue regions of the figures, the viscous flow solver is applied without modifications, whereas in the red regions, the advection and diffusion terms are omitted. Details on the two modules are given in the following.

In the first module, *noEndVortex*, simulation of perforated plates in oscillating flow are considered. The perforated plates consist of many small plate elements next to each other. The advection and diffusion terms are solved for all fluid cells in the domain that have horizontal coordinates between the center of the first and last plate elements. The terms are omitted for all other fluid cells. This allows for local flow separation through the openings between each plate element, while the global plate-end flow separation is not allowed.

The second module, *freeSurface*, is used in simulations of models in incident waves. For a few layers of cells close to the free-surface, the advection and diffusion terms are omitted. Kristiansen and Faltinsen [47] noted that no vorticity of significance should be advected into the part of the domain without consideration of the advection and diffusion terms. Sensitivity analyses of the intersection between the two parts of the domain are performed. Based on these, the intersection between the two parts of the domain is set to  $z = -0.05$  m such that there are 10 cell layers without advection and diffusion, cf. Fig. 5.1. An additional variable is included on the free-surface boundary ( $z = 0$ ), the wave elevation  $\zeta$ . The linearized kinematic free-surface condition, Eq. (2.5), yields a differential equation for the wave elevation,

$$\frac{\partial \zeta}{\partial t} = w; \quad z = 0, \quad (5.4)$$

with  $w$  being the vertical velocity component. Equation (5.4) is solved based on the vertical velocity in the previous step,

$$\frac{\zeta^{n+1} - \zeta^n}{\Delta t} = w^n - b \zeta_i^n. \quad (5.5)$$

A numerical beach is implemented through the function  $b(x)$  which is a third-order polynomial with non-zero values in the right part of the domain, and zero elsewhere. On the left boundary of the domain, a numerical wave flap generates waves. The new value of the wave elevation,  $\zeta^{n+1}$ , is used to determine the pressure. A boundary condition for the (net) pressure at the mean free-surface, needed to solve Eq. (5.3), is obtained by linearizing the Bernoulli equation, Eq. (2.4), and

define the atmospheric pressure  $p = p_a \equiv 0$ ,

$$p_a + \rho g z + \rho \frac{\partial \Phi}{\partial t} = p_a \equiv 0. \quad (5.6)$$

which gives the dynamic pressure used as boundary condition at the free-surface,

$$-\rho \frac{\partial \Phi}{\partial t} = \rho g \zeta. \quad (5.7)$$

### 5.1.2 Solution procedure summary

For clarity, the solution procedures of the viscous flow solver are outlined in the following. The solution procedure can be summarized in three steps in the simulations without waves:

1.  $u^n, w^n \rightarrow u^*, w^*$
2.  $u^*, w^* \rightarrow p^{n+1}$
3.  $u^*, w^*, p^{n+1} \rightarrow u^{n+1}, w^{n+1}$

In simulations with waves, the solution procedure consists of four steps:

1.  $u^n, w^n \rightarrow u^*, w^*$
2.  $\zeta^n, w^n \rightarrow \zeta^{n+1}$
3.  $u^n, w^n, u^*, w^*, \zeta^{n+1} \rightarrow p^{n+1}$
4.  $u^n, w^n, u^*, w^*, \zeta^{n+1}, p^{n+1} \rightarrow u^{n+1}, w^{n+1}$

Note that in the simulations of waves, steps 1 and 2 are independent on each other and can be solved in the opposite sequence.

## 5.2 Discretization

### 5.2.1 Grid

The equations are solved on a forward-staggered rectilinear<sup>1</sup> grid. The pressure is solved in the center of the cell. The horizontal and vertical velocity components are solved in the center of, respectively, the east and north faces of the pressure grid cells. In simulations with incident waves, the wave elevation is solved in the same point as the vertical velocity component, such that the top row of grid cells have the cell center in the vertical position  $z = -0.5\Delta z$  ( $z = 0$  is the free surface). An illustration of the forward-staggered approach is given in Fig. 5.2.

The grids consist, in general, of an inner fine region and an outer stretched region. This allows for a fine resolution around the models while limiting the computational time. In the inner fine region, which typically extends a few layers of cells outside the simulated model, all grid cells are of equal size. In the outer stretched region, the grid cells are geometrically stretched from the fine region

<sup>1</sup>A two-dimensional rectilinear grid is a tessellation by rectangles. In the case of zero stretching, the two-dimensional rectilinear grid consists of equally sized rectangles.

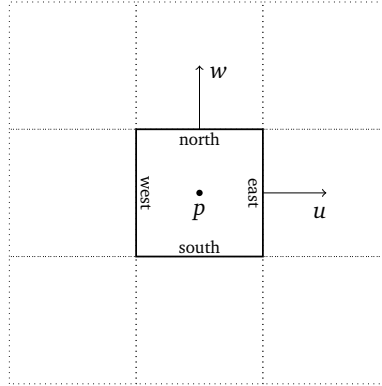


**Figure 5.2:** Forward-staggered grid arrangement. The horizontal,  $u$ , and vertical,  $w$ , velocity components are solved in the center of, respectively, the east and north cell faces.

grid cell size, towards the boundaries of the computational domain. The stretching will increase the cell sizes up to a given maximum value, typically set to 50 mm, beyond which a constant cell size is applied. Such relatively large cell sizes are justified by that the spatial variation of the flow is small far away from the body.

Based on sensitivity tests on stretching, the increase in adjacent cell size in the stretched regions is typically set to 20 %. Note that successful results are obtained by using even higher stretching, for example in simulations of a square cylinder in oscillating flow, the stretching can be more than 50 % without considerable influence on the force coefficients of the cylinder. However, when testing even larger stretching (up to 100 %), numerical stability issues were more likely to occur. As a conservative approach, I've limited the stretching to 20 % in the present simulations.

### 5.2.2 Spatial discretization schemes

Spatial discretizations in the CFD are of first, second and third orders. The solved equations are implemented such that their discretization schemes take into account the stretching of grid cells. The diffusion terms of Eq. (5.1), the pressure gradient terms of Eq. (5.2), as well as the terms of Eq. (5.3), are solved with second-order accurate central difference schemes unless else is explicitly highlighted. The nonlinear advection terms are linearized in time using the previous known velocity, that is,  $u_j^n$  of Eq. (5.1). The spatial discretization of the advection terms is performed using upwind schemes.

Three orders of accuracy are used to discretize the advection schemes. In addition to the classical first-order upwind scheme, which uses two data points, second-order and third-order accurate schemes are implemented. By including

more data points, the spatial accuracy of the advection could be improved. The applied second-order upwind scheme uses three data points, and includes information about the flow two cells upstream of the present. The third-order scheme uses four data points, two upstream and one downstream in addition to the present cell.

The presented CFD results are based on first-order accurate upwind schemes unless else is explicitly written. Due to the extended use of neighbor cells, there is a computational penalty with the higher-order schemes compared to the first-order upwind scheme. Consequently, there must be some kind of award, in terms of generally better results, to defend the use of higher-order schemes. However, despite increased spatial accuracy, a general increase in accuracy is not found compared to the first-order upwind scheme, when performing validation and verification simulations using the two higher-order advection schemes. Moreover, the stability of the first-order scheme, likely due to the effect of false diffusion [33, p. 150], is found to be superior to the tested higher-order schemes.

### 5.2.3 Time-stepping

Various methods are used for the temporal discretization. Equation (5.1) is solved by a first-order implicit scheme (backwards Euler), a second-order two-point scheme (Crank–Nicholson), and second- and fourth-order explicit Runge–Kutta schemes. Due to its simplicity and physically satisfactory behavior [48, pp. 56–58], the first-order implicit scheme is used as default. A first-order forward scheme is always used to find the velocity field at  $n + 1$  from the auxiliary field (\*) and pressure gradient in Eq. (5.3).

In incident wave simulations, first-, second- and fourth-order forward Runge–Kutta schemes are used to find the wave elevation at  $n + 1$  in Eq. (5.4). The first-order scheme, i.e., the forward Euler scheme, is used as default. Note that Eq. (5.1) is solved using the first-order implicit scheme in these simulations as well, cf. step 1 in Section 5.1.2.

In simulations of oscillating and orbital flows, as well as in simulations with incident waves, the time-step size is chosen based on requirements for a minimum temporal resolution, 200 time-steps per oscillation period, and a maximum CFL number equal to 1 in all cells of the domain,

$$\Delta t = \min \left( \frac{T}{200}, \left( \frac{\Delta x}{u}, \frac{\Delta z}{w} \right) \right). \quad (5.8)$$

Since the maximum values of  $\frac{\Delta x}{u}$  and  $\frac{\Delta z}{w}$  are not known prior to simulation, the actual implementation of the time-step size is set based on the velocity amplitude of the simulation,  $W$ , and the smallest cell size,  $h$ ,

$$\Delta t = \min \left( \frac{T}{200}, c \frac{h}{W} \right), \quad (5.9)$$

with  $c$  being a constant that ensures the requirement of CFL less than or equal to one, in all cells, is fulfilled throughout the simulation. The maximum CFL number

is calculated in each time-step. The code is implemented such that a warning message will appear if a CFL number larger than one is obtained in a time-step, such that  $c$  can be reduced and the simulation can be restarted. From trial-and-error, the value of  $c$  is, typically, set between 0.2 and 0.4. A constant time-step is preferred with respect to post-processing.

### 5.3 Boundary conditions

Different sets of boundary conditions are used to simulate different types of flow. Cavity flow conditions, presented in Section 5.3.1, are used only during the validation and verification of the CFD. Oscillating flow conditions, in which the prescribed vertical velocity and acceleration oscillate harmonically, are simulated in “infinite fluid”, that is, with the boundaries far from the simulated models, presented in Section 5.3.2, and in a channel flow arrangement, presented in Section 5.3.3. Simulations with orbital flow conditions, presented in Section 5.3.4, use oscillating conditions for the velocities and accelerations in both the vertical and horizontal directions. Finally, in Section 5.3.5, the boundary conditions used for simulating incident waves are presented.

#### 5.3.1 Cavity flow

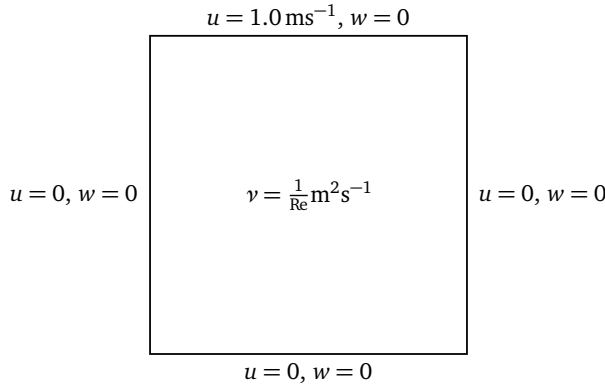


**Figure 5.3:** Cavity flow setup. The top lid is moving with a constant horizontal velocity. The kinematic viscosity is set based on the simulated Reynolds number.

An illustration of the boundary conditions in the cavity flow problem is presented in Fig. 5.3. The prescribed velocity at the boundaries are zero except for the top boundary where the tangential velocity is set to  $u = 1.0 \text{ ms}^{-1}$ . The domain size is fixed to  $1.0 \text{ m} \times 1.0 \text{ m}$ . Different Reynolds numbers are tested by changing



the prescribed kinematic viscosity of the simulation,

$$\nu = \frac{UL}{\text{Re}} = \frac{1}{\text{Re}} \text{m}^2 \text{s}^{-1}. \quad (5.10)$$

The resolution of the grids are based on a prescribed number,  $N$ , of cells in each direction. A constant and equal cell size,  $h$ , is used in both directions, that is,

$$h = \Delta x = \Delta z = \frac{1}{N} \text{m}. \quad (5.11)$$

### 5.3.2 Oscillating flow

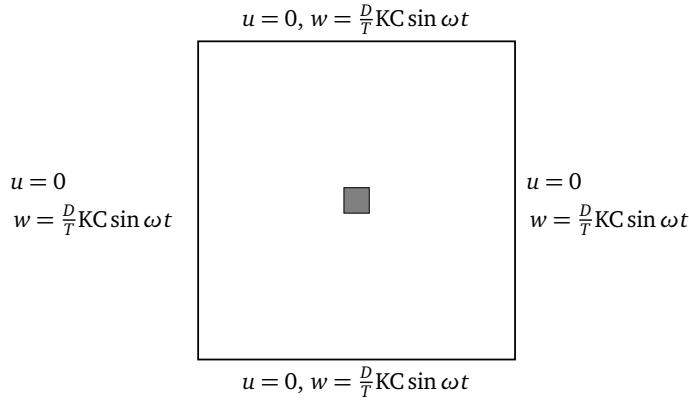


**Figure 5.4:** Oscillating flow setup. The ambient vertical velocity component is oscillating harmonically at the boundaries. The simulated model is placed in the center of the numerical domain.

The boundary conditions in oscillating flow are illustrated in Fig. 5.4. In oscillating flow conditions, the velocity field at the boundaries of the computational domain is set to a prescribed oscillating vertical velocity based on a prescribed velocity amplitude,  $W$ , which from Eq. (2.19) can be written in terms of the KC number, the period of oscillation,  $T$ , and the characteristic width of the structure,  $D$ ,

$$u = 0, \quad (5.12)$$

$$w = \frac{D}{T} KC \sin \omega t. \quad (5.13)$$

The period of oscillation (and corresponding circular frequency  $\omega = \frac{2\pi}{T}$ ) is set to  $T = 1.0 \text{ s}$  to yield similar Reynolds numbers as in the experiments, although the Reynolds number is expected not to be of importance since the cylinders have sharp edges.

Appropriate boundary conditions for the pressure gradient are obtained from the Navier–Stokes equation assuming uniform flow,

$$\frac{\partial p}{\partial x} = -\rho \frac{\partial u}{\partial t} = 0, \quad (5.14)$$

$$\frac{\partial p}{\partial z} = -\rho \frac{\partial w}{\partial t} = -\rho \omega \frac{D}{T} KC \cos \omega t. \quad (5.15)$$

No-slip conditions are used on the boundaries of the discretized models,

$$u = w = 0, \quad \frac{\partial p}{\partial x} = \frac{\partial p}{\partial z} = 0. \quad (5.16)$$

### 5.3.3 Oscillating channel flow

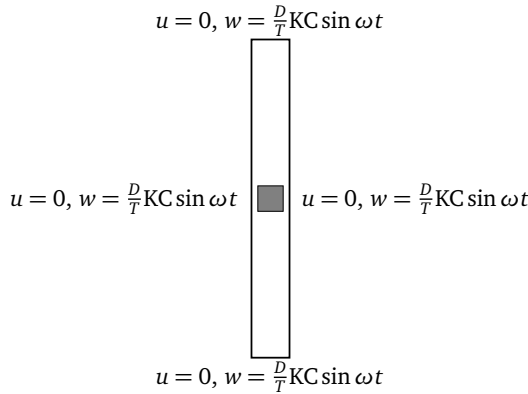


**Figure 5.5:** Oscillating channel flow setup. Equal setup and boundary conditions as in oscillating flow, except that the sidewalls are placed next to the model.

Oscillating channel flow represents a special case of oscillating flow. The boundary conditions are equal in both cases, but the sidewalls are placed closer to the model, as illustrated in Fig. 5.5.

### 5.3.4 Orbital flow conditions

The boundary conditions in orbital flow are illustrated in Fig. 5.6. Except for non-zero horizontal prescribed velocities and accelerations, the orbital flow simulations are performed in the exact same manner as the oscillating flow simulations. The following velocity conditions are set on the boundaries of the computational

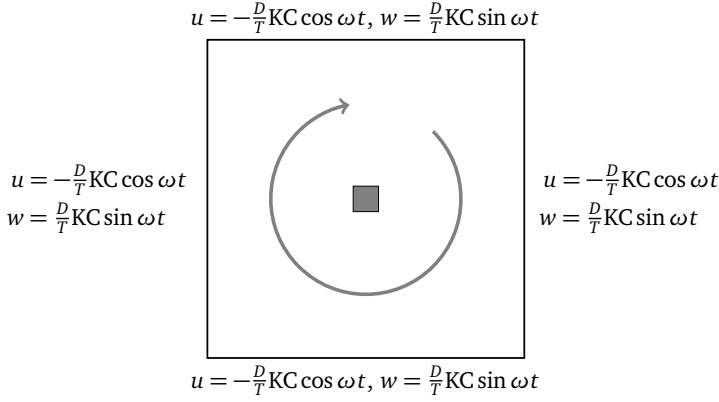


**Figure 5.6:** Orbital flow setup. The ambient horizontal and vertical velocity components are oscillating harmonically at the boundaries. The gray arrow indicates the change of direction of flow with time. The simulated model is placed in the center of the numerical domain.

domains,

$$u = -\frac{D}{T}KC \cos \omega t, \quad (5.17)$$

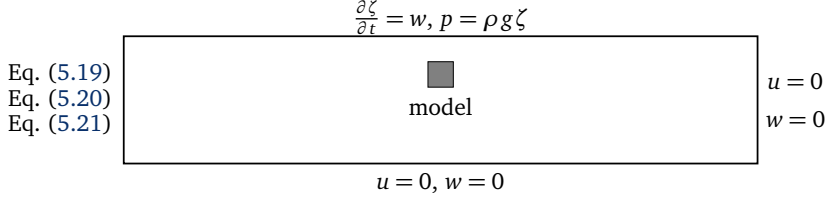
$$w = \frac{D}{T}KC \sin \omega t, \quad (5.18)$$

with corresponding appropriate boundary conditions for the pressure gradient based on the prescribed accelerations.

In orbital flow, the horizontal and vertical velocity components vary harmonically in time, but have no spatial variations. Thus, orbital flow conditions may be regarded as a limit of linear wave theory, where the wave is long compared to the model and the model is deeply submerged, such that there is no interaction with a free surface. Consequently, orbital flow simulations may be regarded as a first step towards simulations in waves. A benefit of this approach is that the simulations can be set up similar to oscillating flow conditions.

### 5.3.5 Incident waves

Simulations of incident waves are performed in a numerical wave tank that consists of the free surface, a wave flap and two solid boundaries. A sketch of the setup is presented in Fig. 5.7. The right and bottom wall of the tank is modeled as solid walls with no-slip boundary conditions. A harmonically oscillating horizontal velocity is prescribed at the left boundary of the computational domain, to mimic the wave flap of the experiments. The wave flap is modeled using a prescribed

**Figure 5.7:** Incident wave setup.

harmonically oscillating horizontal velocity with amplitude  $U$ ,

$$u = \begin{cases} U \sin \omega t \frac{z+h_f}{h_f}, & z \geq z_{FS} - h_f \\ 0, & z < z_{FS} - h_f. \end{cases} \quad (5.19)$$

$$w = 0 \quad (5.20)$$

$$\frac{\partial p}{\partial x} = -\rho \frac{\partial u}{\partial t} = \begin{cases} -\rho \omega U \cos \omega t \frac{z+h_f}{h_f}, & z \geq z_{FS} - h_f \\ 0, & z < z_{FS} - h_f. \end{cases} \quad (5.21)$$

The wave flap is hinged 0.9 m below the free surface in the experimental investigations (the water depth is 1.0 m), and the same flap design is used in the numerical simulations, i.e.,  $h_f = 0.9$  m ( $z_{FS} = 0$ ).

An appropriate boundary condition for the pressure gradient at the free-surface boundary ( $z = 0$ ) is taken from a first-order spatial backwards differential of Eq. (5.7),

$$\frac{\partial p}{\partial z} = \frac{\rho g \zeta - p_c}{0.5 \Delta z_c}, \quad (5.22)$$

with  $p_c$  being the pressure in the cell center of the grid cell next to the top boundary.  $\Delta z_c$  is the vertical grid cell size of the cell next to the top boundary.

The incident wave simulations are performed for a simplified model of S28, cf. Table 3.1. Numerical stability issues are experienced in trials attempting to simulate the physical model in waves. The issues are avoided by using a simplified model of the S28 structure, denoted R28. R28 has the same perforation ratio, thickness and width as S28, but the number of cylinders is 11 instead of the 26 of the original model. Consequently, the plate elements (cross-sections) are rectangular, not squares, hence R instead of S. By using larger plate elements, a coarser grid can be applied, which increases the numerical stability of the simulation. Although they represent two different models, comparing R28 simulations and S28 experiments is an acceptable approach for most KC numbers. Later in the text, the sensitivity to the number of holes used to model a perforated plate is investigated in forced heave simulations.

Considerable time was invested in debugging the incident wave simulations of S28. I tested decreasing the time-step size and increasing the order of the time-stepping, using a fourth order Runge–Kutta scheme, but still experienced unstable

simulations with the original S28 model. Note that these stability issues are not experienced in simulations using oscillating and orbital flow conditions. Therefore, the problems are suspected to be related to the hybrid domain coupling and free-surface modeling. The fine region grid size must be 2 mm in order to have two grid cells between each cylinder of S28. In the coarser model (R28), the smallest grid size is 5 mm. Using larger grid cell sizes increases the general stability in terms of smaller CFL and increased numerical damping. Additionally, since a stretched grid is applied, the differences between grid sizes in the  $x$ - and  $z$ -directions are generally smaller, and less stretching is required.

## 5.4 Validation and verification

Confidence in the numerical viscous solver is obtained by simulating and comparing cases where there exist previous experimental, numerical or analytical results. In Section 5.4.1, simulations of the lid-driven cavity flow are compared with previous numerical studies [49, 50]. In Section 5.4.2, the hydrodynamic force on a square section in oscillating flow is compared with previous experimental [51] and numerical investigations [52, 53]. In Section 5.4.3, the added mass due to flow through openings in a channel is compared with analytical expressions [54].

### 5.4.1 Cavity flow

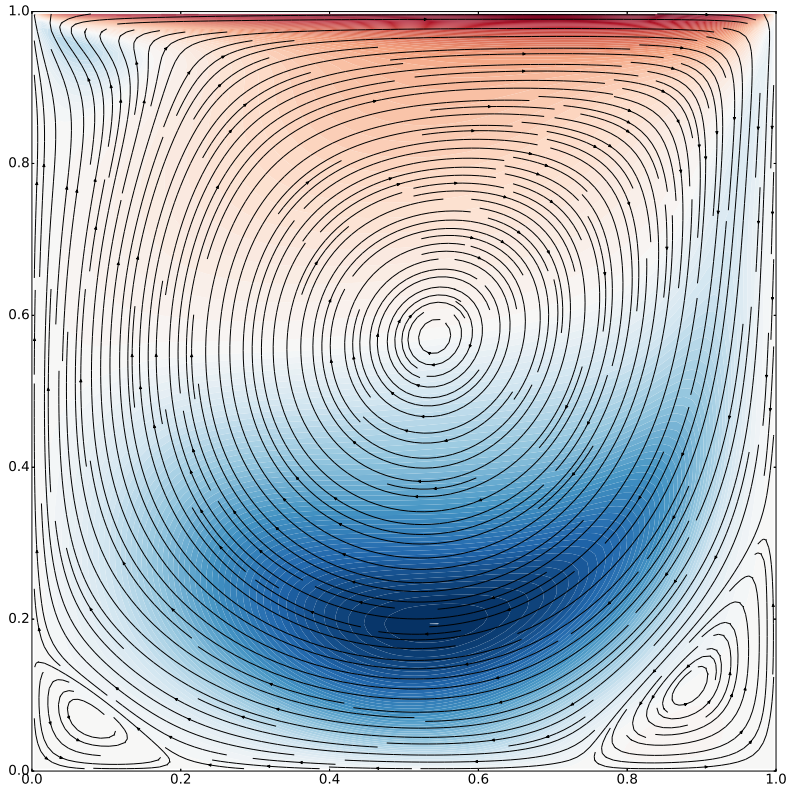


**Figure 5.8:** Streamline plot of cavity flow at  $Re = 1000$  with  $160 \times 160$  grid cells. The horizontal velocity at the top boundary is  $u = 1.0 \text{ ms}^{-1}$ . The `RdBu_r` colormap in Matplotlib [55] is used to indicate the horizontal velocity component, from  $-1.0 \text{ ms}^{-1}$  (blue) to  $1.0 \text{ ms}^{-1}$  (red).

Simulations of the lid-driven cavity flow problem are performed to verify the numerical viscous flow solver against previous numerical implementations of the continuity and Navier–Stokes equations. Unlike the more complex validation and verification cases, the cavity flow problem has three features that makes it an ideal case to verify the implementation of the governing equations: 1) An easy setup with simple, time-independent, boundary conditions. 2) The end result is easy to obtain without extensive post-processing, that is, the steady-state coordinates of the vortices. 3) The case has been tested in many previous studies. Consequently, a satisfactory result in the cavity flow problem gives the developer confidence in the implementation of the governing equations. Contrary—and in contrast to more complex validation and verification cases, where an unsatisfactory result can come from numerous sources—if an unsatisfactory result is obtained, the developer has a good indication that something is not right with the implementation of the governing equations.

The cavity flow problem has been simulated for three different Reynolds numbers,  $Re = 100$ ,  $Re = 400$  and  $Re = 1000$ . A CFL number of 1 is used in all simulations, and the simulations are run to steady-state. The simulations use a grid that has  $160 \times 160$  equally sized grid cells. The results, in terms of position of vortices, found from inspections of minimum absolute velocity, are compared to the investigations by Schreiber and Keller [50] and Vanka [49], which have performed simulations with the same Reynolds numbers and with grids that are of similar resolutions as the present. The sensitivity to the grid cell size is inspected by simulating  $Re = 100$  with three grids;  $80 \times 80$ ,  $160 \times 160$  and  $320 \times 320$ .

The cavity flow results are presented in Tables 5.1, 5.2 and 5.3, for respectively,  $Re = 100$ ,  $Re = 400$  and  $Re = 1000$ . The present results are compared to the results by Schreiber and Keller [50] and Vanka [49]. The grid sensitivity is presented in Table 5.4. Additionally, a streamline plot of  $Re = 1000$  is presented in Fig. 5.8.

Satisfactory results are obtained for the simulated cavity flows when comparing the position of the vortices to those reported in previous studies. Minor differences are found, likely related to differences in grids and implementations. Increasing the grid density from  $160 \times 160$  to  $320 \times 320$  grid cells for the cavity flow at  $Re = 100$ , changes the position of vortices by 0.2%. However, the grid dependence, and need for finer grids, is expected to increase with increasing Reynolds number [49], which is a likely cause for the general trend of increasing differences to previous studies when increasing the Reynolds number.

**Table 5.1:** Cavity flow results at  $Re = 100$ . Result presentation: Horizontal coordinate, vertical coordinate (distance to present result). PV: Primary vortex, BR: Bottom right vortex, BL: Bottom left vortex.

	$160 \times 160$	Vanka [49]	Schreiber and Keller [50]
PV	0.615625, 0.740625	0.6188, 0.7375 (0.004)	0.61667, 0.74167 (0.001)
BR	0.946875, 0.059375	0.9375, 0.0563 (0.010)	0.94167, 0.05000 (0.011)
BL	0.034375, 0.034375	0.0375, 0.0313 (0.004)	0.03333, 0.02500 (0.009)

**Table 5.2:** Cavity flow results at  $Re = 400$ . Result presentation: Horizontal coordinate, vertical coordinate (distance to present result). PV: Primary vortex, BR: Bottom right vortex, BL: Bottom left vortex.

	$160 \times 160$	Vanka [49]	Schreiber and Keller [50]
PV	0.565625, 0.615625	0.5563, 0.6000 (0.018)	0.55714, 0.60714 (0.012)
BR	0.896875, 0.115625	0.8875, 0.1188 (0.010)	0.88571, 0.11429 (0.011)
BL	0.046875, 0.040625	0.0500, 0.0500 (0.010)	0.05000, 0.04286 (0.004)

**Table 5.3:** Cavity flow results at  $Re = 1000$ . Result presentation: Horizontal coordinate, vertical coordinate (distance to present result). PV: Primary vortex, BR: Bottom right vortex, BL: Bottom left vortex.

	$160 \times 160$	Vanka [49]	Schreiber and Keller [50]
PV	0.540625, 0.571875	0.5438 0.5625 (0.010)	0.52857, 0.56429 (0.014)
BR	0.884375, 0.109375	0.8625 0.1063 (0.022)	0.86429, 0.10714 (0.020)
BL	0.084375, 0.065625	0.075 0.0813 (0.018)	0.08571, 0.07143 (0.006)

**Table 5.4:** Cavity flow grid refinement results at  $Re = 100$ . Result presentation: Horizontal coordinate, vertical coordinate (distance to  $160 \times 160$  result, cf. Table 5.1).

	$80 \times 80$	$320 \times 320$
PV	0.60625, 0.74375 (0.010)	0.6171875, 0.7421875 (0.002)
BR	0.94375, 0.05625 (0.004)	0.9453125, 0.0609375 (0.002)
BL	0.04375, 0.03125 (0.010)	0.0328125, 0.0359375 (0.002)



### 5.4.2 Square in oscillating flow

Oscillating flow of a facing square is one of the simpler studies of a body in an oscillating flow, and thus an ideal validation case for an oscillating flow solver. Bearman et al. [51] studied the facing square section in oscillating flow at a ratio between the Reynolds number and KC number, Eq. (2.22),

$$\beta = \frac{D^2}{\nu T} = 213, \quad (5.23)$$

which is used in the present setup as well; the period of oscillation is  $T = 1.0$  s, the length of the square is  $D = 0.1$  m, and the kinematic viscosity is set to fulfill Eq. (5.23). In addition to the experimental results by Bearman et al. [51], results from previous studies using a Navier–Stokes solver [52] and a vortex-in-cell method [53] are included in the comparison.

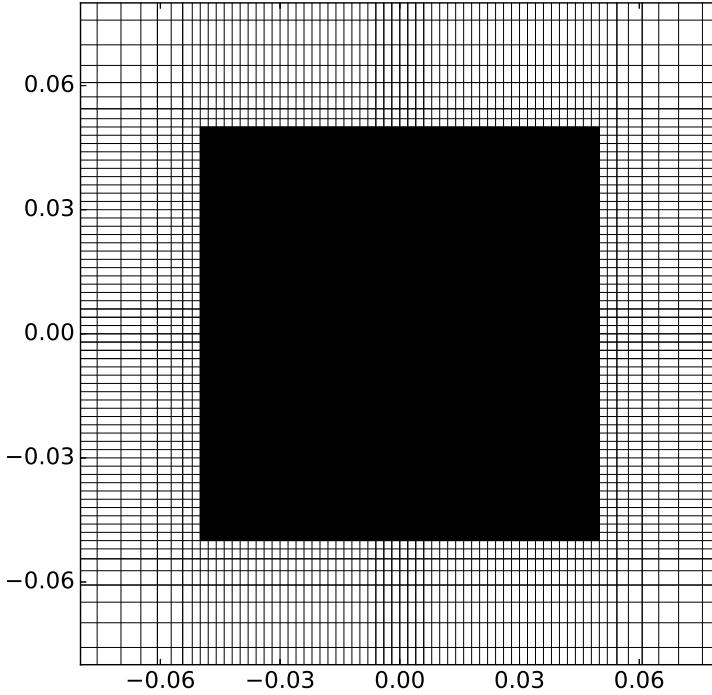


**Figure 5.9:** Fine region of grid used to simulated a square in oscillating flow.

The tested square cross-section has sides that are  $D = 100$  mm long. The fine region is defined to be  $104 \text{ mm} \times 104 \text{ mm}$ . A constant grid cell size of  $\frac{\Delta x}{D} = \frac{\Delta z}{D} = 0.02$  is used in the fine region. The grid is then stretched with a stretching parameter 20% until the maximum grid cell size of  $\frac{\Delta x_{\max}}{D} = \frac{\Delta z_{\max}}{D} = 0.5$  is reached. The total domain size is  $2 \text{ m} \times 2 \text{ m}$  ( $\frac{l}{D} = 20$ ) and the total number of grid cells is 10 956. Additionally, to verify that the boundaries of the domain do not influence the solution, a second simulation with domain size  $4 \text{ m} \times 4 \text{ m}$  ( $\frac{l}{D} = 40$ , 21 836 grid cells) is performed. A plot of the fine region of the grid close to the square is presented in Fig. 5.9.

The results are presented in terms of the added mass coefficient including the Froude–Krylov contribution,  $C_M$ , and the quadratic damping coefficient,  $C_D$ , for comparison with the previous investigations, that is, the force is decomposed as

$$F = (A + \rho V)\ddot{\eta} + B_q \dot{\eta} |\dot{\eta}|, \quad C_M = \frac{A + \rho V}{A_0}, \quad C_D = \frac{B_q \pi D}{2A_0}, \quad (5.24)$$

cf. the discussion of Section 2.3.

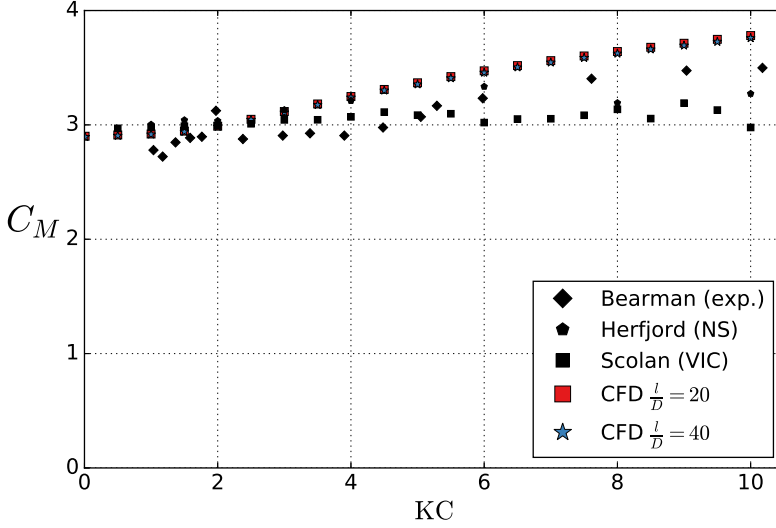


**Figure 5.10:** Added mass coefficient including the Froude–Krylov contribution,  $C_M$ , of a facing square in oscillating flow. Comparisons with studies by Bearman et al. [51] (exp.: experiments), Herfjord [52] (NS: Navier–Stokes solver), and Scolan and Faltinsen [53] (VIC: vortex-in-cell method).

The results are presented in Figs. 5.10 and 5.11. The differences between  $\frac{l}{D} = 20$  and  $\frac{l}{D} = 40$  are by and large negligible. In general, the present results are acceptable; main trends are consistent with the previous studies, although the

present numerical solver yields somewhat higher values of  $C_M$  for  $KC > 3$  than what was earlier observed. The  $C_D$  values are also, in general, somewhat high compared to the previous studies. There are notable differences between the different studies; experimental vs. numerical, solver technique, grid and cell sizes, number of oscillation periods, etc., and some variation in the resulting coefficients is expected.

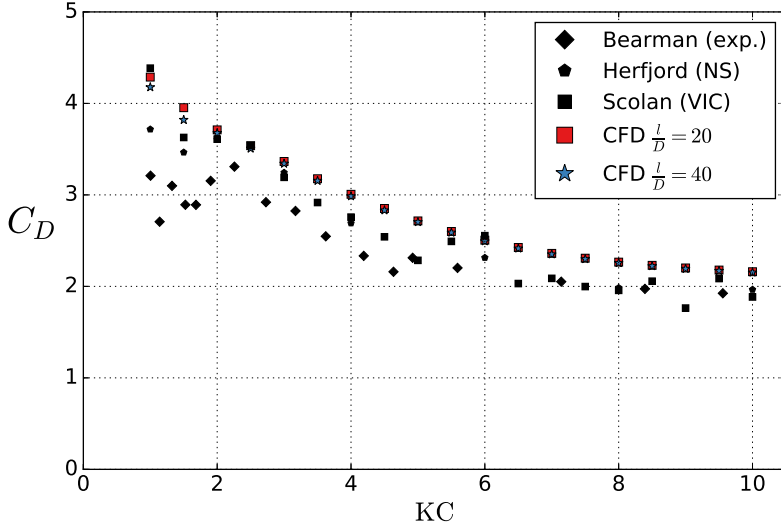


**Figure 5.11:** Quadratic damping coefficient,  $C_D$ , of a facing square in oscillating flow. Comparisons with studies by Bearman et al. [51] (exp.: experiments), Herfjord [52] (NS: Navier–Stokes solver), and Scolan and Faltinsen [53] (VIC: vortex-in-cell method).

The smallest simulated  $KC = 0.01$  yields  $C_M = 2.901$  ( $\frac{l}{D} = 20$ ) and  $C_M = 2.894$  ( $\frac{l}{D} = 40$ ), cf. intersection with  $y$ -axis in Fig. 5.10. This is slightly larger (4%) than the analytical  $C_M = 2.786$  ( $\frac{4.754}{\pi} + \frac{4}{\pi}$ ) for  $KC \rightarrow 0$  [32, pp. 145–146]. A reason for this discrepancy is due to the Reynolds number in the simulation. For  $KC \rightarrow 0$ , the form drag goes to zero, but the friction drag depends on  $\beta$  [35]. The quadratic damping coefficient is presented in Fig. 5.11, but the linear damping coefficient is also calculated. For  $KC = 0.01$ ,  $\frac{B}{\omega A_0} = 0.173$  ( $\frac{l}{D} = 20$ ) and  $\frac{B}{\omega A_0} = 0.175$  ( $\frac{l}{D} = 40$ ). In an additional simulation of  $KC = 0.01$  ( $\frac{l}{D} = 20$ ), the Reynolds number is increased by a factor 100 such that  $\beta = 21300$ . This reduces the friction drag. As a consequence, the damping coefficient is considerably decreased, that is,  $\frac{B}{\omega A_0} = 0.053$ . At the same time, the inertia coefficient is reduced to  $C_M = 2.805$ , which is only 0.7% larger than the analytical  $C_M = 2.786$ .

### 5.4.3 Oscillating flow through openings in a channel

The next step towards simulation of perforated plates is the simulations of oscillating flow through openings in a channel. This case is presented by Molin [19]. Simulations are performed with the viscous flow solver for very small KC numbers. The resulting added mass coefficients are compared to the analytical expression for the added mass due to potential flow through an opening in a channel by Morse and Ingard [54, p. 487],

$$A = \rho \frac{\pi}{4} D^2 \frac{8}{\pi^2} \ln \left( \frac{1}{2} \tan \left( \frac{\pi d}{4D} \right) + \frac{1}{2} \cot \left( \frac{\pi d}{4D} \right) \right). \quad (5.25)$$

Here  $d$  is the width of the opening and  $D$  the width of the channel. The expression can be written in terms of the perforation ratio,

$$\tau = \frac{d}{D}, \quad (5.26)$$

and normalized with a reference added mass,  $A_0$ , here set to the added mass of a solid plate of width  $D$ ,

$$\frac{A}{A_0} = \frac{8}{\pi^2} \ln \left( \frac{1}{2} \tan \left( \frac{\pi \tau}{4} \right) + \frac{1}{2} \cot \left( \frac{\pi \tau}{4} \right) \right). \quad (5.27)$$

The expression for one opening can be extended to the case of  $n_h$  equal openings,

$$\frac{A}{A_0} = \frac{8}{n_h \pi^2} \ln \left( \frac{1}{2} \tan \left( \frac{\pi \tau}{4} \right) + \frac{1}{2} \cot \left( \frac{\pi \tau}{4} \right) \right). \quad (5.28)$$

Two comparisons are performed. First, simulations of a single opening with varying perforation ratios are compared to Eq. (5.27). Second, simulations of  $\tau = 0.5$  are performed with increasing number of openings.

All simulations are set up with  $KC = \frac{WT}{D} = 0.01$ ,  $\beta = 1.6 \times 10^5$ , based on the width of the channel,  $D$ . The openings are discretized by using 320 grid cells across the channel width and one grid cell across the opening height. The channel length is  $\frac{l}{D} = 5$ , and the total number of grid cells is 32480.

The results are presented in Fig. 5.12. The trend predicted with the analytical expression is well captured by the numerical simulations. Some differences between the analytical method and the numerical simulations are highlighted; 1) the thickness of the opening(s),  $\frac{t}{D} = \frac{1}{320}$ , is finite, 2) the length of the channel,  $\frac{l}{D} = 5$ , is limited, and 3) the KC number is small, but not infinitesimal. These factors are likely reasons why the numerical simulations yield slightly larger added mass. Additionally, as discussed in Section 5.4.2, the friction drag for  $KC \rightarrow 0$  increases the force coefficients compared to analytical methods.

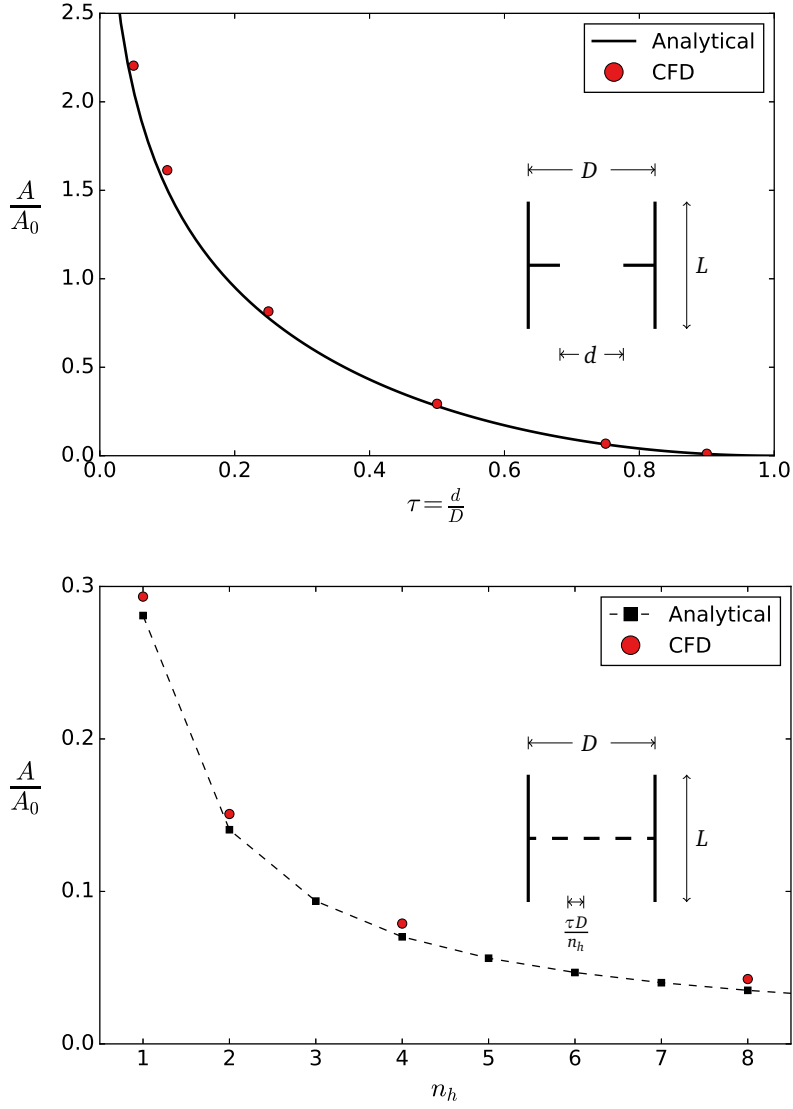


**Figure 5.12:** 2D channel flow added mass coefficient. Top: As function of the perforation ratio,  $\tau = \frac{d}{D}$ , due to oscillating flow through a single slit. Bottom: As function of the number of openings,  $n_h$ , due to oscillating flow through a series of openings for  $\tau = 0.5$ . Both:  $KC = 0.01$ . Comparisons with analytical expressions of Eqs. (5.27) and (5.28).

## 5.5 Modeling perforated structures

Perforated structures are modeled using a number of structure elements consisting of solid cells, with fluid cells between each structure element. The total dimensions and perforation ratio of the perforated structure is set equivalent to that of the physical structure. Consider as an example a perforated plate of width  $D$ , thickness  $t$  and perforation ratio  $\tau$ . The perforated plate is modeled as a number of smaller solid plates, of thickness  $t$ , that are placed next to each other such that the total width is  $D$ , and the sum of the width of the fluid cells between the plate elements match the perforation ratio,

$$\sum \Delta x_{fluid} = \tau D \quad (5.29)$$

Compared to using special porosity-cells, where the governing equations take into account the perforation ratio of the structure, the present approach has the advantage that the governing equations are solved in the fluid cells between each structure element directly, without need for empirical correlations and modifications to account for the porosity. Additionally, the number of cells in the domain, and consequently computational time, is reduced, since there is no flow in the solid cells of the perforated structure, hence, they are not part of the numerical domain.

A potential drawback of the present approach is that the force on the plate can be sensitive to the discretization of the perforated structure, i.e., the number of solid elements used to model the structure and the number of fluid cells between each solid element. In the limit of zero KC, the number of plate elements is the important parameter for the added mass of a perforated plate, cf. Section 4.1.2. Sensitivity studies to the number of plate elements and the number of fluid cells between each plate element, is carried out and presented in the following.

### 5.5.1 Grid sensitivity

In order to investigate the grid sensitivity of perforated plates in the viscous flow solver, simulations are performed using three grid refinements for a perforated plate, keeping all other parameters constant. The fine regions of the three grids are presented in Figs. 5.13 and 5.14.

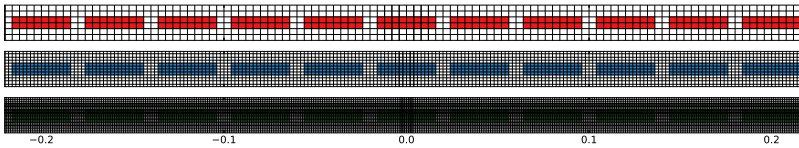


**Figure 5.13:** Grid cell size sensitivity study: The fine region of the three grids.

The grid sensitivity is performed for a fictitious plate that resembles the plates that have been tested experimentally in the present study. The width of the plate

is 432 mm and the thickness is 8 mm. The total width of the plate holes is 80 mm, such that the perforation ratio is  $\tau = \frac{80}{432} = 0.186$ . The plate is modeled with 11 equally sized plate elements, each having a width of 32 mm. This allows for testing of three different fine region grid cell sizes,  $\Delta = 4$  mm, 2 mm and 1 mm. The total domain sizes are  $6 \text{ m} \times 6 \text{ m}$  and the number of grid cells are 33 904 ( $\Delta = 4$  mm), 54 428 ( $\Delta = 2$  mm) and 95 296 ( $\Delta = 1$  mm). The time-step sizes in the simulations are set based on the finest grid, by varying  $c$  in Eq. (5.9);  $c = 0.25$  ( $\Delta = 1$  mm),  $c = 0.125$  ( $\Delta = 2$  mm) and  $c = 0.0625$  ( $\Delta = 4$  mm).

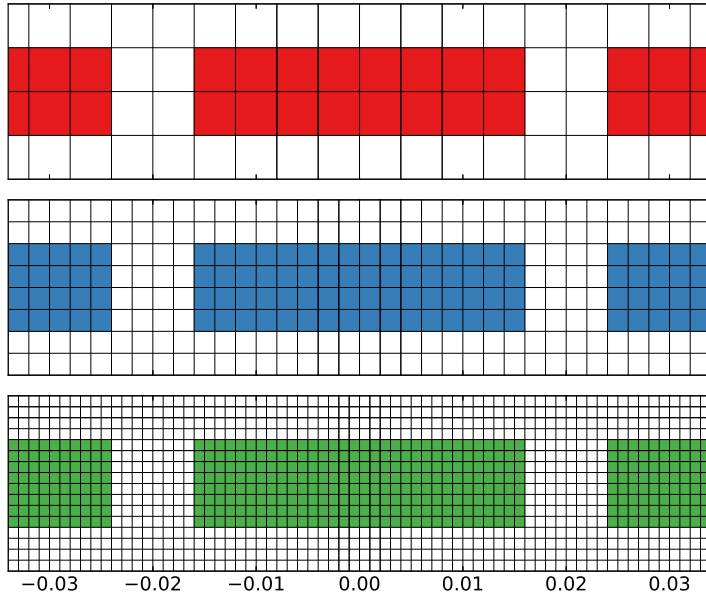


**Figure 5.14:** Grid cell size sensitivity study: A zoomed-in section of the fine region grid illustrating the discretization of the three grids close to a plate element.

The results, in terms of added mass and damping coefficients, from the grid size sensitivity are presented in Fig. 5.15. The hydrodynamic coefficients are nearly insensitive to the grid cell size within the tested range of  $\Delta$ . The coarsest grid has only two grid cells in each opening between the plate elements. Nevertheless, such an approach seems sufficient when it comes to modeling perforated plates in the viscous flow solver. Similar findings were made by Firoozkoobi [56], who studied sloshing in rectangular tanks equipped with a slat screen, that is, a perforated platelike structure used to damp the fluid motions in the tank. The screens had perforation ratios  $\tau = 0.21$  and  $\tau = 0.53$ . In numerical simulations using OpenFOAM, the pressure forces on the slat screens were “very similar” [56] when using two grid cells in the perforated openings of the screens, compared to using six grid

cells. A feasible major part of the (quite surprising) fact that only two elements are sufficient is the use of rectilinear grids. As a consequence, the separation points are fixed, i.e., the rectilinear grid yields sharp corners, and the boundary layer flow does not need to be captured.

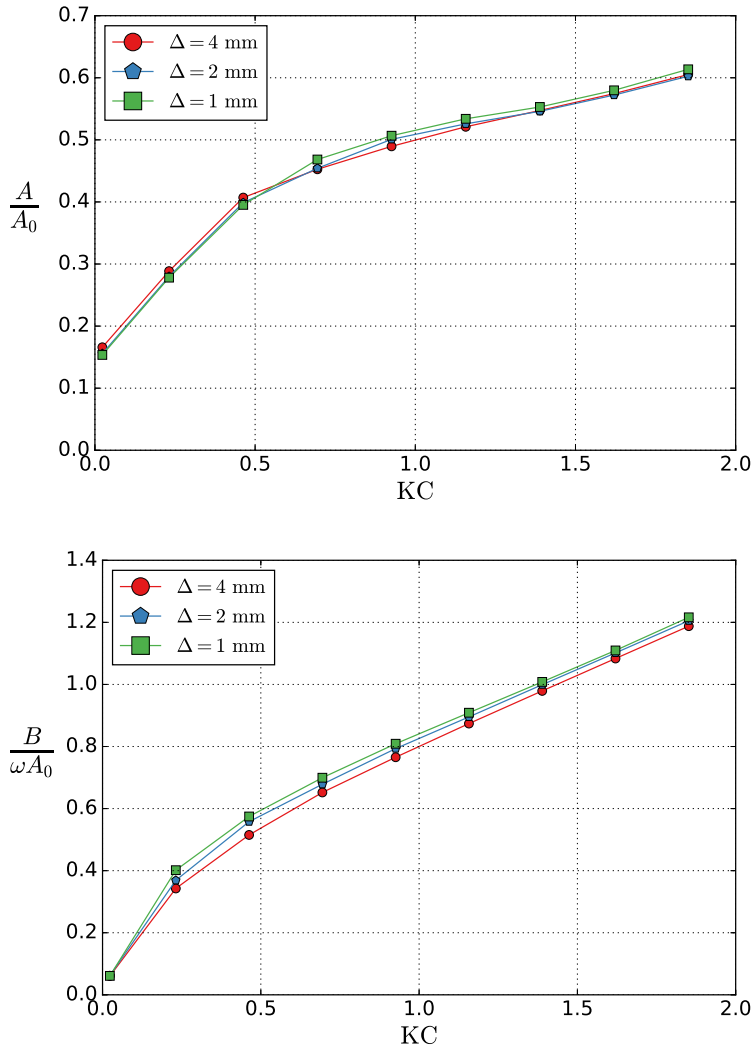


**Figure 5.15:** Grid size sensitivity study: Added mass and damping coefficients for a perforated plate ( $\tau = 0.185$ ) with three different grid cell sizes in the fine region close to the plate.  $\beta = 186\,624$ .



### 5.5.2 Hole size sensitivity

A hole size sensitivity study is performed to investigate the sensitivity of the number and size of holes used to model a perforated plate with perforation ratio  $\tau = 0.186$ . Five different hole size configurations are simulated. Details on the number and size of holes is given in Table 5.5. Illustrations of the plates are presented in Fig. 5.16.

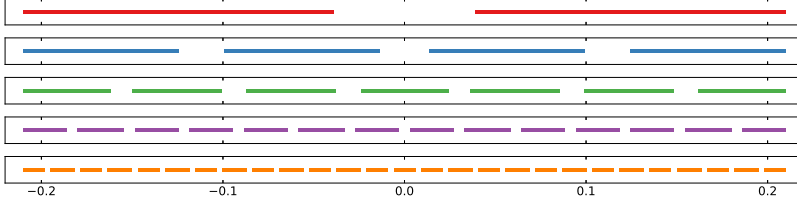


**Figure 5.16:** Hole size sensitivity study: The five configurations of plate elements.

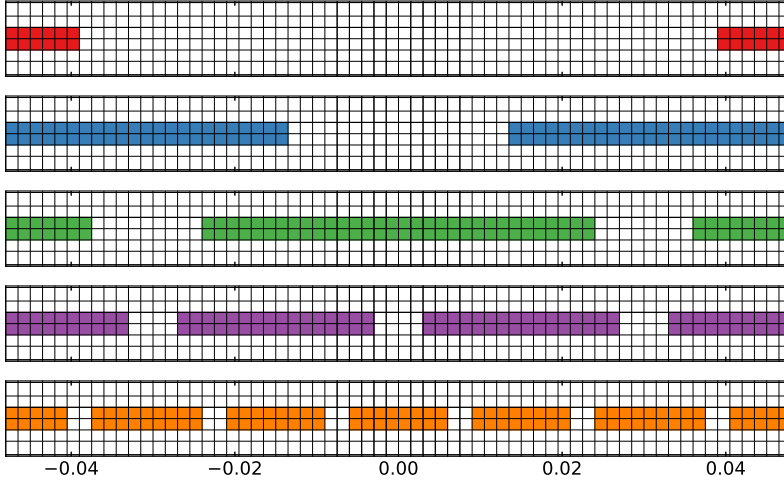


**Figure 5.17:** Zoomed-in sections of the fine region grids, cf. Fig. 5.16, illustrating the discretization of the five configurations of plate elements.

The simulated perforated plate has dimensions  $D = 420$  mm and  $t = 3$  mm. In the fine region close to the perforated plate, the grid cell size is  $\Delta x = \Delta z = 1.5$  mm, that is, the width of the perforated plate covers 280 grid cells. 228 of these are solid cells and 52 are fluid cells, hence the perforation ratio is  $\tau = \frac{52}{228} = 0.186$ . Zoomed-in sections of the fine region grids are presented in Fig. 5.17. Outside the fine region, the grid is stretched towards the boundaries of the domain. The

stretching factor in the stretched region is 1.2. Total domain size is  $6\text{ m} \times 6\text{ m}$ , and the total number of grid cells is 63 688.

**Table 5.5:** Hole size sensitivity study: Relevant parameters.  $n$ : Number of plate elements,  $n_h$ : Number of holes,  $l_h$ : Hole size.

$n$	$n_h \times l_h$
2	$1 \times 78\text{ mm}$
4	$2 \times 25.5\text{ mm}$ and $1 \times 27\text{ mm}$
7	$2 \times 12\text{ mm}$ and $4 \times 13.5\text{ mm}$
14	$13 \times 6\text{ mm}$
27	$26 \times 3\text{ mm}$

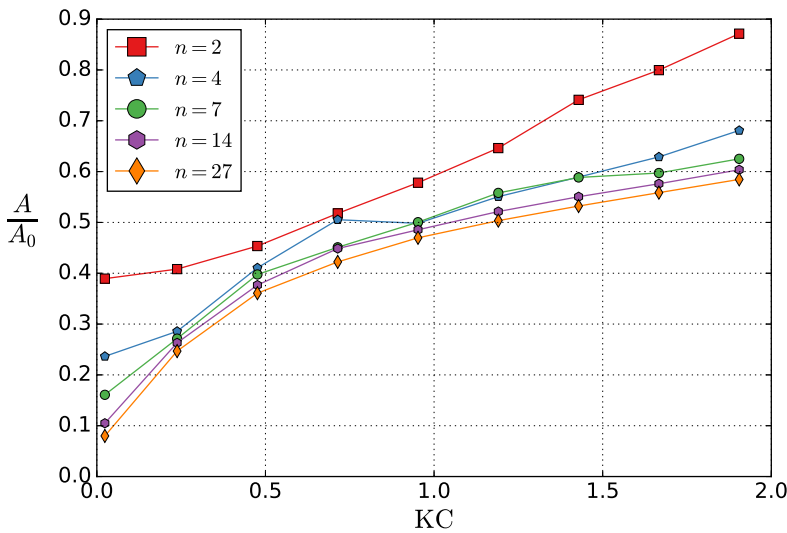


**Figure 5.18:** Hole size sensitivity study: Added mass coefficients for a perforated plate ( $\tau = 0.186$ ) with five different hole sizes.  $\beta = 176\,400$ .

The results are presented in Figs. 5.18 and 5.19. The number of plate elements is a considerable factor for the smallest KC numbers. This is consistent with the results of the potential flow solver, cf. Table 4.1. Additionally, dependence on the number of plate elements (number of holes)—for very small KC numbers—was demonstrated for the case of oscillating flow through openings in a channel, cf. Section 5.4.3. For  $KC \geq 0.23$ , the differences between the different configurations are (perhaps surprisingly) small. An exception is the plate with two plate elements (one large hole), which differ, quite considerably, from the other configurations for all KC numbers. The results seem to converge when increasing the number of

plate elements; only minor differences are found when increasing the number of plate elements from  $n = 14$  to  $n = 27$ . The added mass coefficient decreases, in general, with increasing number of plate elements for all KC numbers. The damping coefficient increases for increasing number of plate elements for  $KC < 0.93$  and decreases for increasing number of plate elements for  $KC > 0.93$ . However, for all plates with  $n \geq 4$ , only small differences are found in the damping coefficient.

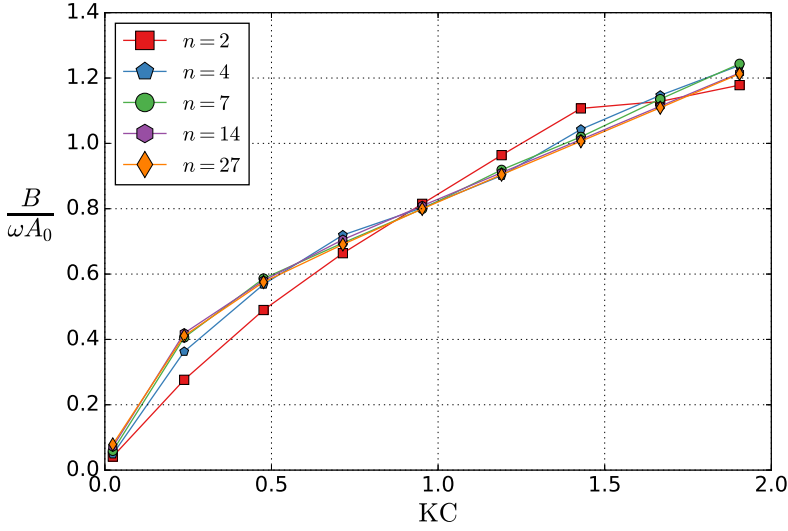


**Figure 5.19:** Hole size sensitivity study: Damping coefficients for a perforated plate ( $\tau = 0.186$ ) with five different hole sizes.  $\beta = 176\,400$ .

As for the coarsest grid in the grid sensitivity, Section 5.5.1, there are only two fluid cells between each plate element for the  $n = 27$  model. Such a perforated plate model technique seems to be sufficient compared to using more fluid elements between each plate element.

### 5.5.3 Domain decomposition intersection

In simulations of perforated structures in incident waves, a hybrid approach, in which the domain is decomposed into two parts, is applied, cf. Section 5.1.1. The sensitivity of the intersection between the two domain parts is investigated for the R28 plate. The model is placed at  $z_m = -0.3$  m. Above the plate, a constant grid cell size of  $\Delta = 0.005$  m is used. Simulations are performed using intersections  $z = -0.075$  m,  $z = -0.050$  m and  $z = -0.025$  m. Thus, the number of cell layers without advection and diffusion is 15 ( $z = -0.075$  m), 10 ( $z = -0.050$  m) and

5 ( $z = -0.025$  m). The configuration with 10 cell layers without advection and diffusion is illustrated in the bottom subplot of Fig. 5.1.

The resulting force amplitude from the simulations is presented in Fig. 5.20. Similar results are obtained for the different intersections. Small differences are found for the largest tested KC numbers. However, both KC and  $F_a$  are slightly shifted, such that the trends, in terms of force amplitude as function of KC, are similar. Unless else is explicitly noticed, the intersection between the two parts of the domain is set to  $z = -0.050$  m in the present numerical simulations of models in incident waves.

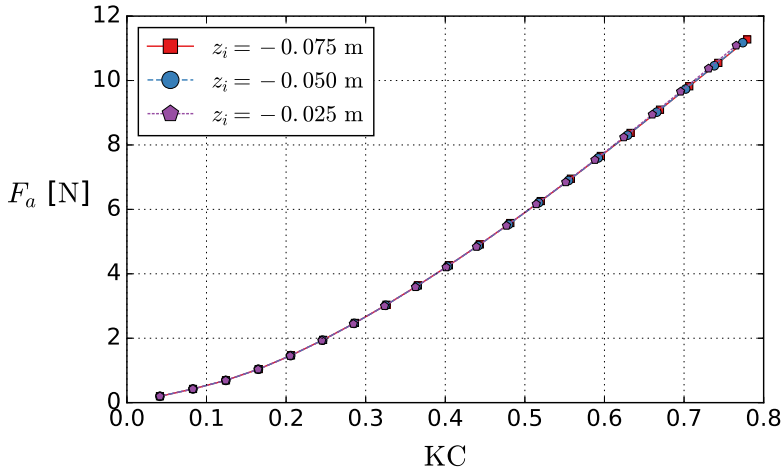


**Figure 5.20:** Sensitivity to the intersection line between the two parts of the domain in simulations of R28 placed at  $z_m = -0.3$  m in incident waves. The wave period is  $T = 1.6$  s.



## Chapter 6

# Perforated structures in oscillating flow

In the sections of this chapter, results from tests and simulations of single perforated platelike structures in oscillating flow conditions are presented. Experiments of four different perforated plate models are investigated. The experimental models are placed in the middle of the tank—with equal distance (0.5 m) to the tank bottom and to the free surface—and forced to oscillate vertically. Viscous flow solver simulations are performed for numerical models of three of these structures. Two of the experimental models are *ideal* perforated plates consisting of numerous holes. The results for the ideal perforated plates are presented first. Then, the results for two *real* perforated plates—consisting of a limited amount of cylinders placed in a row—are presented. Comparisons and discussions are given towards the end of the chapter.

### 6.1 Ideal perforated plates

#### 6.1.1 Experimental models

Two (almost) ideal perforated plates are experimentally investigated. The perforation ratios of the plates are  $\tau = 0.19$  and  $\tau = 0.28$ . I refer to these plates as P19 and P28, P being short for perforated plate and the numbers referring to the perforation ratio ( $\tau = 0.19$  and  $\tau = 0.28$ ). The plates are almost ideal in the sense that they are very thin and consist of numerous small holes, such that the added mass of the plates in the low KC limit is almost zero, cf. discussion on ideal vs. real perforated plates in Sections 1.4.2 and 1.4.4. Photos of the ideal perforated plate models are presented in Fig. 6.1.

Two identical plates were made for each perforation ratio. Each plate is  $D = 420$  mm wide and  $t = 3$  mm thick. The length of the plates in the lateral direction is  $L = 570$  mm, such that the plates fit in the experimental rig, cf. Section 3.2. The material used to construct the plates were obtained from Fish Tech AS [57, 58]. The holes on the plates have diameters 2 mm ( $\tau = 0.19$ ) and 3 mm ( $\tau = 0.28$ ).

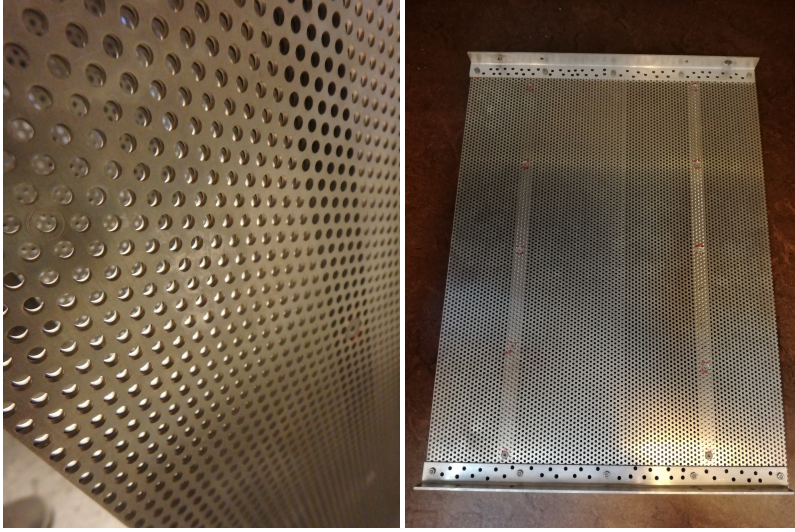


**Figure 6.1:** Photos of the ideal perforated plate models.

The arrangement of the holes is visible in Fig. 6.1. Fastening profiles are used on the plates, in order to be able to attach them to the acrylic glass plates of the experimental rig, cf. Section 3.2. Additionally, two 20 mm wide aluminum angle sections are fastened along the length span (tank width direction) of the plates, 9 cm from each end. These L-shaped stiffeners ensures minimal bending even for the higher amplitudes and oscillation frequencies tested. Due to stiffeners and fastening profiles, the perforation ratios of the constructed plate models are somewhat lower than that of the perforated materials. The perforated materials have perforation ratios 0.2267 (P19) and 0.326 (P28) [57, 58]. Consequently, the use of stiffeners and fastening profiles reduces the effective perforation ratio of the structures by 16 % (P19) and 14 % (P28).

### 6.1.2 Numerical models

Numerical models of the two experimentally investigated ideal perforated plates, P19 and P28, are simulated. The dimensions of the numerical plates correspond to the experiments,  $D = 420$  mm and  $t = 3$  mm. The numerical perforated plate models consist of several plate elements with small gaps in between. Based on the findings of the hole and grid size sensitivities, Section 5.5, I use 27 plate elements in the numerical models of P19 and P28.

A fine region of grid cells is used in the vicinity of the plates. The grid cell sizes are constant equal to  $\Delta = \Delta x = \Delta z = 1.5$  mm in the fine region. Thus, 280 grid cells cover the width of the plates. For P19, 52 grid cells are open fluid cells, while 78 grid cells are open fluid cells in the P28 model. The fine regions of the

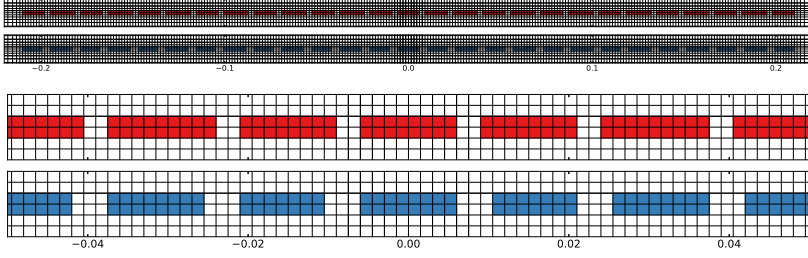


**Figure 6.2:** The fine regions of the numerical models of P19 and P28 (top subplot). A zoomed in section of the fine regions is presented in the bottom subplot.

two perforated plate models are presented in Figs. 6.2.

Outside the fine region, the grid cells are geometrically stretched towards the boundaries of the numerical domain. The stretching is 20% until a maximum grid cell size of 50 mm is reached. The total domain size is 6 m × 6 m, and the total number of grid cells are 63 688 (P19) and 63 740 (P28). The minor difference between the two is due to the difference in perforation ratio and thereby number and size of plate elements.

### 6.1.3 Results

Examples of force time-series are presented in Fig. 6.3. The plots show the measured raw force with P19 and P28 inside the experimental rig. The period of oscillation is  $T = 2.0$  s and the amplitude corresponds to  $KC = 1.42$ . Clearly, the force is largest for the smallest perforation ratio.

Note that the plots in Fig. 6.3 show the measured raw forces, and that in order to obtain the net forces on the models, the force is filtered and the filtered force in empty rig experiments is subtracted time-step by time-step. In order to obtain hydrodynamic coefficients, the Fourier averaging procedure of Eqs. (2.16) and (2.17) is applied for the eight periods of oscillation in the middle of the set (ramp in and out and the first and last full oscillation cycles are omitted). The (dry) inertia force of the model is subtracted from the total inertia in order to obtain the added mass coefficient.

Plots of the normalized force on P19 and P28 in numerical simulations at  $KC = 1.43$  are presented in Fig. 6.4. The numerical results show that the force is largest on the plate with smallest perforation ratio. Note that there is no rig in the numerical simulations, hence the forces are the net forces on the plates, and no empty-rig subtraction is needed. However, since the numerical simulations are of fixed models with oscillating flow conditions at the boundaries of the numerical domain, the Froude–Krylov force is subtracted for comparisons with the experiments of oscillating models in calm water.

The experimental results in this chapter are presented for five oscillation peri-



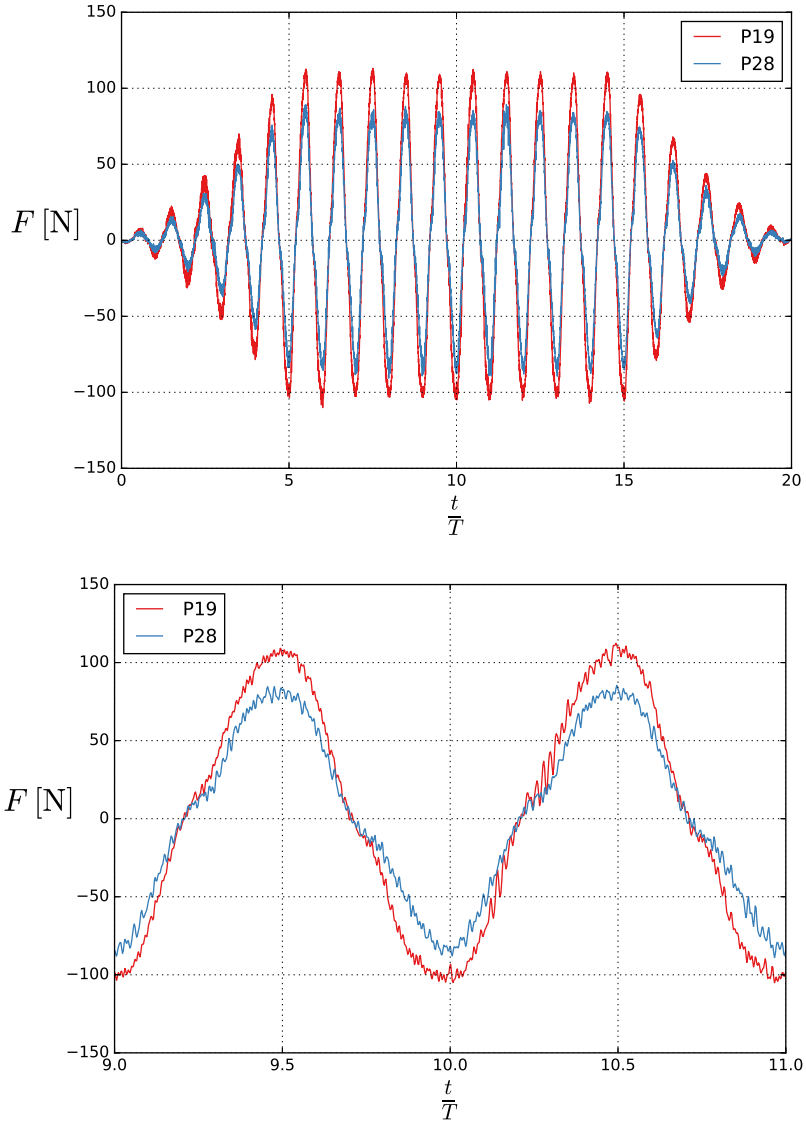


**Figure 6.3:** Example of force measurements from experiments of P19 and P28. The figures show the raw, unfiltered force during a full experimental test set with five oscillation cycles of ramp-in, 10 full oscillation cycles and five oscillation cycles of ramp-out (top) and the two full oscillation cycles in the middle of the set (bottom). The example is for  $KC = 1.42$ ,  $T = 2.0$  s.

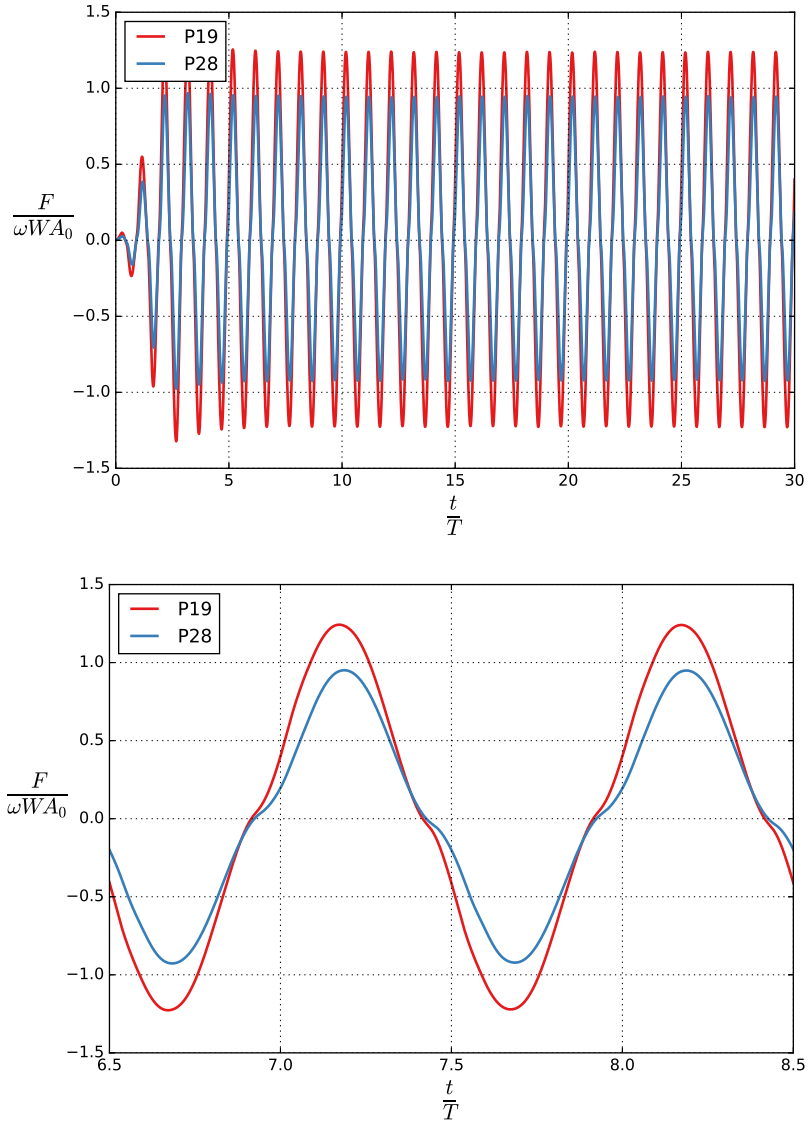


**Figure 6.4:** Example of normalized force during numerical simulations of P19 and P28 at  $KC = 1.43$ . The figures show the numerical ramp-in followed by 28 full oscillation cycles (top). The normalized force for  $6.5T \leq t \leq 8.5T$  is presented in the bottom subplot. The last 25 full oscillation cycles are used to calculate forces and coefficients.

ods, cf. Section 3.2.1. I use the same markers to indicate the periods of oscillations in all figures. The markers are presented with and without error bars in Fig. 6.5. These markers are also used for forced oscillation experiments in other chapters. To keep the legends simple, I label only one of the markers in each result figure, and refer the reader to Fig. 6.5 for a description of the period of oscillation.

◆	$T = 1.00$ s	◆	$T = 1.00$ s
●	$T = 1.25$ s	◆	$T = 1.25$ s
●	$T = 1.50$ s	◆	$T = 1.50$ s
●	$T = 1.75$ s	◆	$T = 1.75$ s
★	$T = 2.00$ s	◆	$T = 2.00$ s

**Figure 6.5:** Markers used to present results of different periods of oscillation from forced oscillation experiments. The right plot includes error bars, which are used to indicate the standard deviation. The standard deviation is calculated based on the values from each of the considered full oscillation cycles, cf. Section 3.2.1.

The added mass and damping coefficients of P19 and P28 are presented in Figs. 6.6 and 6.7. Added mass coefficients of the CFD models, calculated with the potential flow solver, are included. The potential flow solver added mass coefficients are in line with the viscous flow solver results.

The experimental results are presented for five periods of oscillation. Within the range of tested periods of oscillation, there is not much period dependence for neither P19 nor P28. However, some differences are visible, in particular for P19 at the highest KC numbers. A likely reason is free-surface interaction and wave generation which increases with increasing KC and is dependent on the period of oscillation. Due to the smaller perforation ratio, forcing P19 to oscillate moves more water and disturbs the free surface more than for P28.

There is in general good agreement between experimental and numerical results. The agreement is particularly good for the added mass of P19. For P28, there is up to  $\approx 15\%$  discrepancy. But remember the difference between the physical plates and the numerical models. The experimental and numerical results agree that for a given KC number, the perforation ratio is the main parameter for the hydrodynamic force coefficients of ideal perforated plates. Both coefficients are highly dependent on the amplitude of motion, and increase with increasing KC in both the experiments and the numerical simulations.

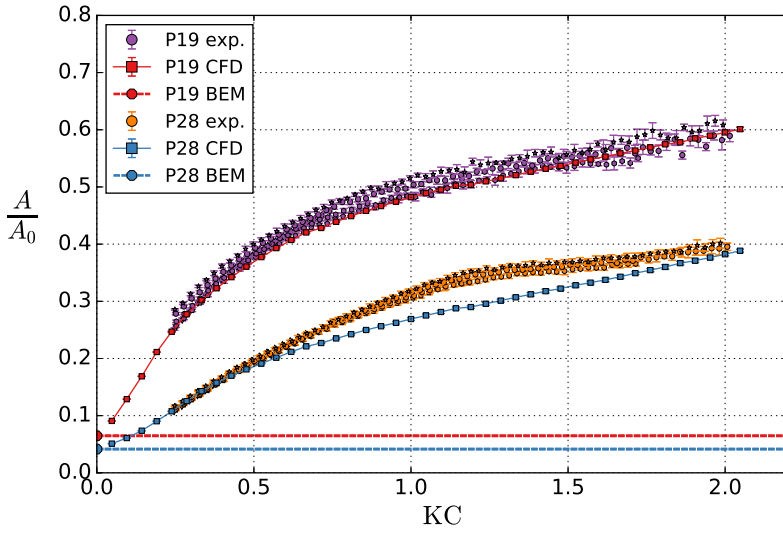


**Figure 6.6:** Added mass coefficients from experimental investigations and numerical simulations of P19 and P28.

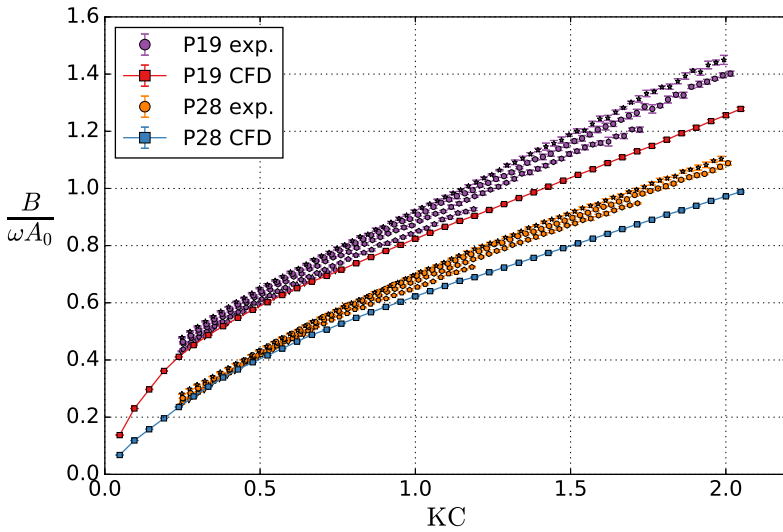


**Figure 6.7:** Damping coefficients from experimental investigations and numerical simulations of P19 and P28.

## 6.2 Perforated structures consisting of cylinders

### 6.2.1 Experimental models

Two perforated structures that consist of cylinders aligned in a row, with openings between the cylinders that makes the structure perforated, are experimentally investigated. The first model consists of 24 circular cylinders of 10 mm diameter. The total width of this structure is  $D = 298$  mm, such that the perforation ratio is  $\tau = 0.19$ . I use the abbreviation C19 (circular,  $\tau = 0.19$ ) to refer to this model. The circular cylinders, made from aluminum, have wall-thicknesses of 2 mm. The second model consists of 26 cylinders with square cross-sections of lengths 10 mm. The structure is  $D = 360$  mm wide, and has a perforation ratio of  $\tau = 0.28$ . This model is denoted S28 (square,  $\tau = 0.28$ ) in the text. The square cylinders are made from aluminum and have wall-thicknesses of 1 mm. Photos of the two models are presented in 6.8. Sketches are presented in Fig. 6.9.

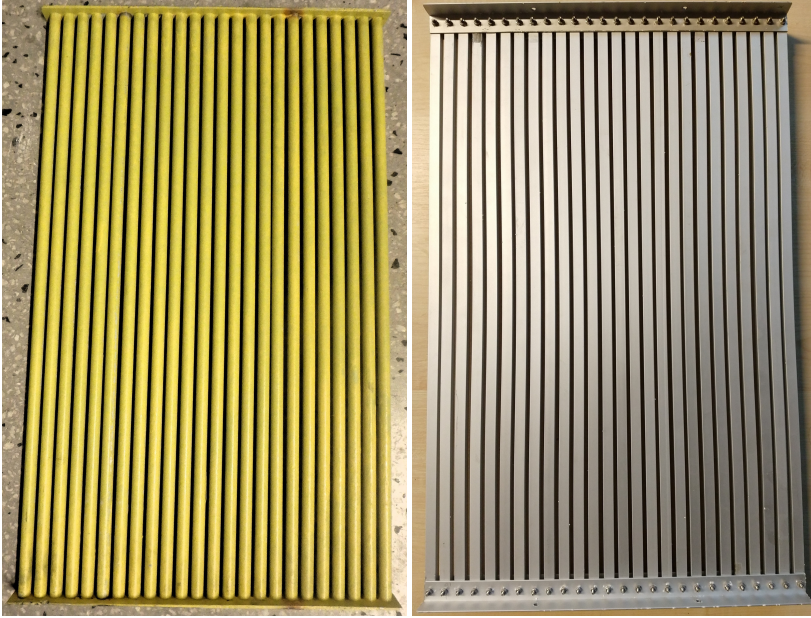


**Figure 6.8:** Photos of the perforated structures that consist of rows of cylinders, C19 (top) and S28 (bottom). C19 consists of 24 circular cylinders. S28 consists of 26 cylinders with square cross-sections. The perforation ratios are  $\tau = 0.19$  (C19) and  $\tau = 0.28$  (S28).

Contrary to the *ideal* perforated plates P19 and P28 (numerous holes,  $\frac{D}{t} = 140$ ), C19 and S28 are *real* perforated plates in the sense that the number of openings is limited and that they have a considerable thickness (C19:  $\frac{D}{t} = 29.8$ , S28:  $\frac{D}{t} = 36$ ).

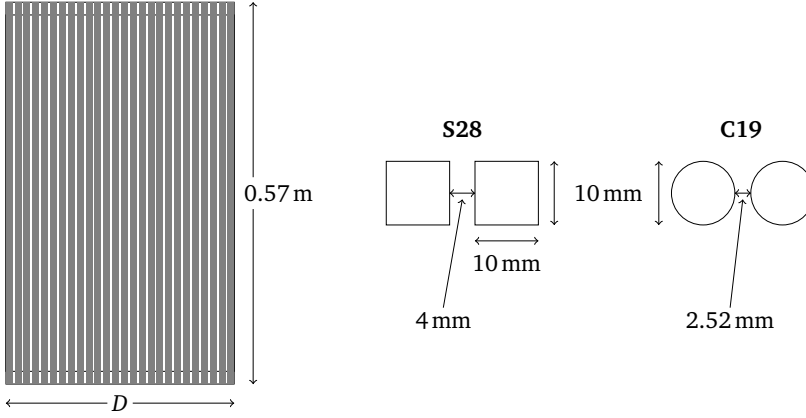


**Figure 6.9:** Schematic sketches of S28 and C19.  $D = 0.298$  m and the number of cylinders is 24 for C19, whereas  $D = 0.360$  m and the number of cylinders is 26 for S28.

The structures are forced to oscillate in otherwise calm water using the same test series as for P19 and P28. Since C19 and S28 are somewhat narrower than P19 and P28, the KC range is shifted a little upwards. Representative time-series and spectra from the experiments of C19, including low and high KC numbers for the smallest and largest periods of oscillation, are provided in App. A.

### 6.2.2 Reynolds numbers

The forces on blunt bodies without sharp edges, such as the circular cylinders of the C19 plate, must be expected to be Reynolds number dependent due to the lack of fixed flow-separation points. The relevant Reynolds and KC numbers are local, that is, they are based on the width of each cylinder,  $d$ . The local Reynolds number is

$$\text{Re}_d = \frac{Wd}{\nu}. \quad (6.1)$$

The local KC number,  $\text{KC}_d$ , is

$$\text{KC}_d = \frac{WT}{d}. \quad (6.2)$$

The range of amplitudes and periods of oscillation in the forced oscillation tests corresponds to  $7.4 \leq \text{KC}_d \leq 85$  and  $5.3 \times 10^2 \leq \text{Re}_d \leq 4.9 \times 10^3$ . The effective local Reynolds and KC numbers will be larger due to the flow restriction, caused by the row of cylinders, which will increase the speed of the flow around each cylinder. Using a simple control volume analysis for C19, the increase can be estimated to  $\frac{1}{\tau} \approx 5$ , that is,  $37 \lesssim \text{KC}_d \lesssim 425$  and  $2.7 \times 10^3 \lesssim \text{Re}_d \lesssim 2.5 \times 10^4$ . These estimated  $\text{KC}_d$  and  $\text{Re}_d$  numbers are likely conservative since the flow will

circumvent the plate. Nevertheless, even if the range of Reynolds numbers are extended to include somewhat smaller values than  $2.7 \times 10^3$ , the drag coefficient for a smooth circular cylinder varies only slightly in this Reynolds number range. One may expect similar behavior for the present model. For moderate to large KC numbers, the global wake, i.e., that shed from the two cylinders at the ends of the model, is expected to dominate the hydrodynamic force on the plate. Therefore, the effect of the placement of the separation point on each cylinder is expected to be negligible.

### 6.2.3 Numerical modeling of S28

In addition to the experimental investigations of the real perforated plates, numerical simulations using the viscous flow solver are conducted for S28. The numerical model of S28 is exactly equal to the two-dimensional cross-section of the experimentally tested model.

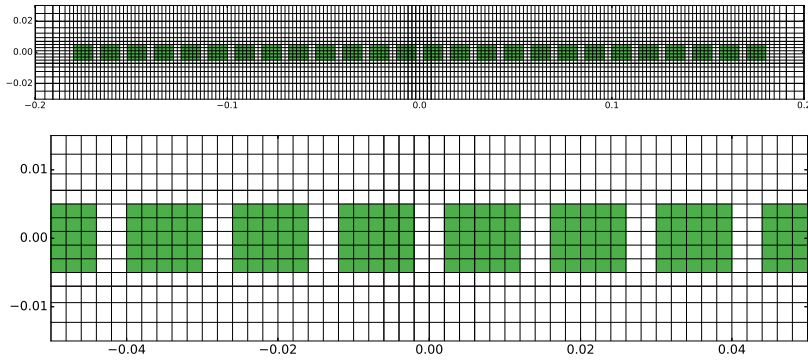


**Figure 6.10:** Fine region grid of S28 (top). A zoomed-in section of the fine region grid is presented in the bottom subplot.

A fine region of grid cells is used in the vicinity of the plate. The fine region is presented in Fig. 6.10. The grid cell sizes are constant equal to  $\Delta = \Delta x = \Delta z = 2\text{ mm}$  in the fine region. Each of the 26 cylinders are modeled using five grid cells in both directions. Two grid cells are used along the opening between two consecutive cylinders. Consequently, the width ( $D = 360\text{ mm}$ ), thickness ( $t = 10\text{ mm}$ ) and perforation ratio ( $\tau = \frac{100\text{ mm}}{360\text{ mm}} = 0.28$ ) of the numerical model is exactly equal to the experimentally tested model.

Outside the fine region, the grid cells are geometrically stretched towards the boundaries of the numerical domain. The stretching is 20% until a maximum grid cell size of 50 mm is reached. The total domain size is  $6\text{ m} \times 6\text{ m}$ , and the total number of grid cells are 48 630.

## 6.2.4 Results

The pressure distribution on the perforated plate S28 is investigated using BEM and CFD and compared with BEM of a corresponding solid plate. The presently investigated perforated plates consist of small cylinders placed next to each other. Numerically, the perforated plates are modeled as a series of small two-dimensional plate elements with openings between them. In Fig. 6.11, I compare the pressure distribution on the plate elements in BEM and CFD. For a given  $\frac{x}{D}$  along the plate, I present the pressure loss, that is, the upstream pressure minus the downstream pressure. The pressure loss is normalized using the maximum and minimum pressure losses along the plate. By utilizing the present normalization, using the maximum and minimum pressure from each calculation, it is possible to visualize and compare the difference between a solid plate and a perforated plate.

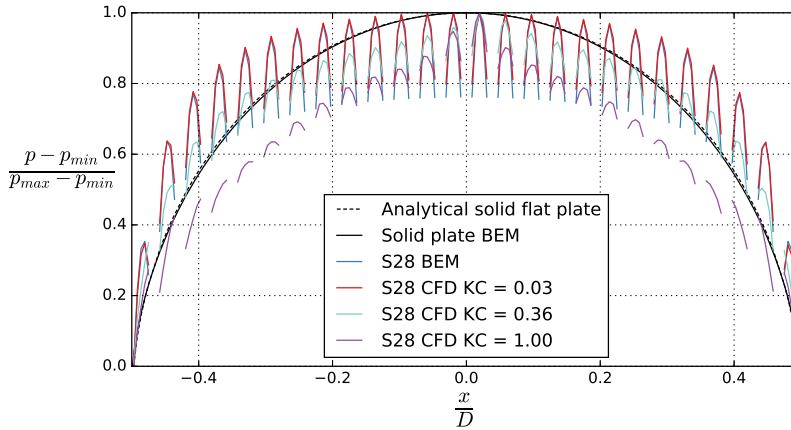


**Figure 6.11:** Pressure loss distribution on the S28 perforated plate with BEM and CFD. The pressure loss, that is, the upstream pressure minus the downstream pressure, is normalized using the maximum and minimum pressure losses on the plate. The BEM result for a corresponding solid plate ( $\frac{D}{t} = 36$ ), and the analytical expression for a solid flat plate, Eq. (6.3), are included for comparison.

The distribution of sources in the BEM matches the number of cells in the CFD. In the CFD, the sides of each plate element of S28 have five grid cells, cf. Fig. 6.10. Therefore, the calculated pressure loss is based on the five grid cells above and below each plate element. In the BEM, each plate element is modeled using five sources along each side of the element, and the pressure loss is presented for the five sources above and below each plate.

Potential flow results are presented for both the S28 model and a corresponding solid plate. The analytical velocity potential for a flat plate yields a reversed



U-shaped pressure distribution over the plate [6, pp. 285–286],

$$p = \rho \frac{\partial w}{\partial t} \sqrt{\frac{D^2}{4} - x^2}, \quad -\frac{D}{2} < x < \frac{D}{2}. \quad (6.3)$$

The global pressure loss distribution predicted by the BEM for S28 has the same characteristic reversed U-shape. Further, the pressure loss distribution over each plate element also follows the same shape.

Included in Fig. 6.11 are CFD results from the forced oscillation simulations at three KC numbers. The pressure on the plate is obtained at the time-instant  $\frac{t}{T} = 30.00$ , that is, when the prescribed ambient acceleration is at its maximum, and the prescribed ambient velocity is zero. For the smallest KC number, the difference between the pressure predicted by the CFD and BEM is hardly visible. This serves as further verification of the CFD. The variations in pressure loss on each plate element are, in general, smaller when the KC number is increased, that is, the significance of the local reversed U-shapes are decreased. Hence, the wake behind each plate element results in a more uniform pressure distribution, similar to the near uniform base drag pressure profile in the wake of a cylinder. For the very last plate elements, that is, the plate-ends, instead of a local reversed U-shape, the normalized pressure loss distribution is similar to that of the solid plate at the corresponding locations. The similarity with the solid plate at the plate-ends increases with increasing KC number.

Added mass and damping coefficients for C19 and S28 are presented in Fig. 6.12. The number of openings are similar for the two configurations (C19: 23, S28: 25), but the cross-section of the cylinders is different (C19: circular, S28: square). As a result, the potential flow added mass is similar for C19 ( $\frac{A}{A_0} = 0.0780$ ) and S28 ( $\frac{A}{A_0} = 0.0799$ ), despite different perforation ratios. The experimentally obtained added mass coefficients agree with the potential flow solver when extrapolating towards  $KC \rightarrow 0$ . For S28, the potential flow solver result is in line with the viscous flow solver results. Both coefficients increase with increasing KC for C19 and S28. There is in general small period dependence, but some dependency to the period of oscillation is found for the larger KC numbers. Similar was found for the ideal perforated plates; a likely reason is free-surface interaction and wave generation which increases with increasing KC and is dependent on the period of oscillation. For a given KC number, the coefficients for C19 ( $\tau = 0.19$ ) are larger than those for S28 ( $\tau = 0.28$ ). This is consistent with the results for the ideal perforated plates; for a given KC, the perforation ratio is the most important parameter for the hydrodynamic force coefficients of perforated plates.

The experiments and CFD are in general in good agreement. The added mass coefficients agree well for all tested KC numbers, while the damping coefficients are slightly overpredicted by the viscous flow solver. A possible reason for the small discrepancy is that in the CFD, the structure elements have sharp-edged corners exactly equal  $90^\circ$ , whereas the square sectional tubes (type: Alberts 4004338473518 [59]), used in the physical model, have slightly blunted edges. Blunting of the edges leads to less sharp corners, a possible reason for reduced damping.

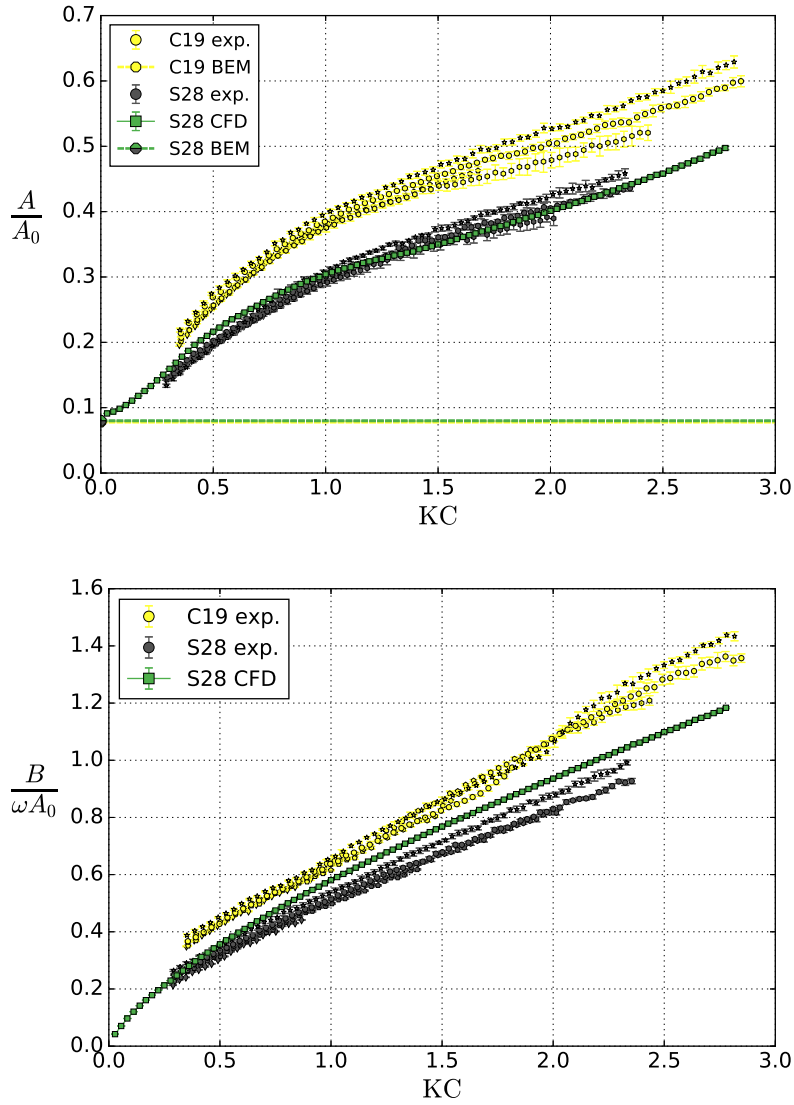


**Figure 6.12:** Added mass and damping coefficients from experimental investigations and numerical simulations of C19 and S28.

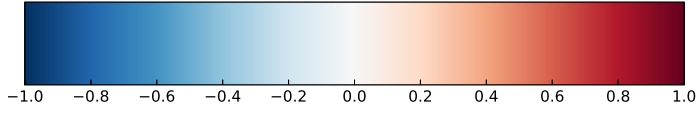


**Figure 6.13:** Colormap for contours in streamline plots.

One of the advantages of the numerical viscous flow solver is the ability to easily visualize and observe features of the flow field. In Figs. 6.14 and 6.15, streamline plots from the simulations of S28 are provided. The colormap for the contours, cf. Fig. 6.13, represents the vertical velocity. The applied colormap is the diverging Matplotlib colormap named `RdBu_r` [55], which is presented in Fig. 6.13. Normalization of the colormap is made against three times the prescribed amplitude of the velocity at the boundaries, that is, the darkest blue ( $-1.0$  in Fig. 6.13) corresponds to  $w = -3\frac{D}{T}KC$  and the darkest red ( $1.0$  in Fig. 6.13) corresponds to  $w = 3\frac{D}{T}KC$ . The flow field is visualized for the simulation of  $KC = 1.0$  at six time-steps during an oscillation cycle, from  $t = 29.1T$  to  $t = 29.6T$ . Corresponding plots zoomed in on a section of the model are provided in Figs. 6.16 and 6.17. The plots illustrate the local flow separation from each plate element, the speed-up of flow through the openings of the perforated plate, and the generation of global plate-end vortices.

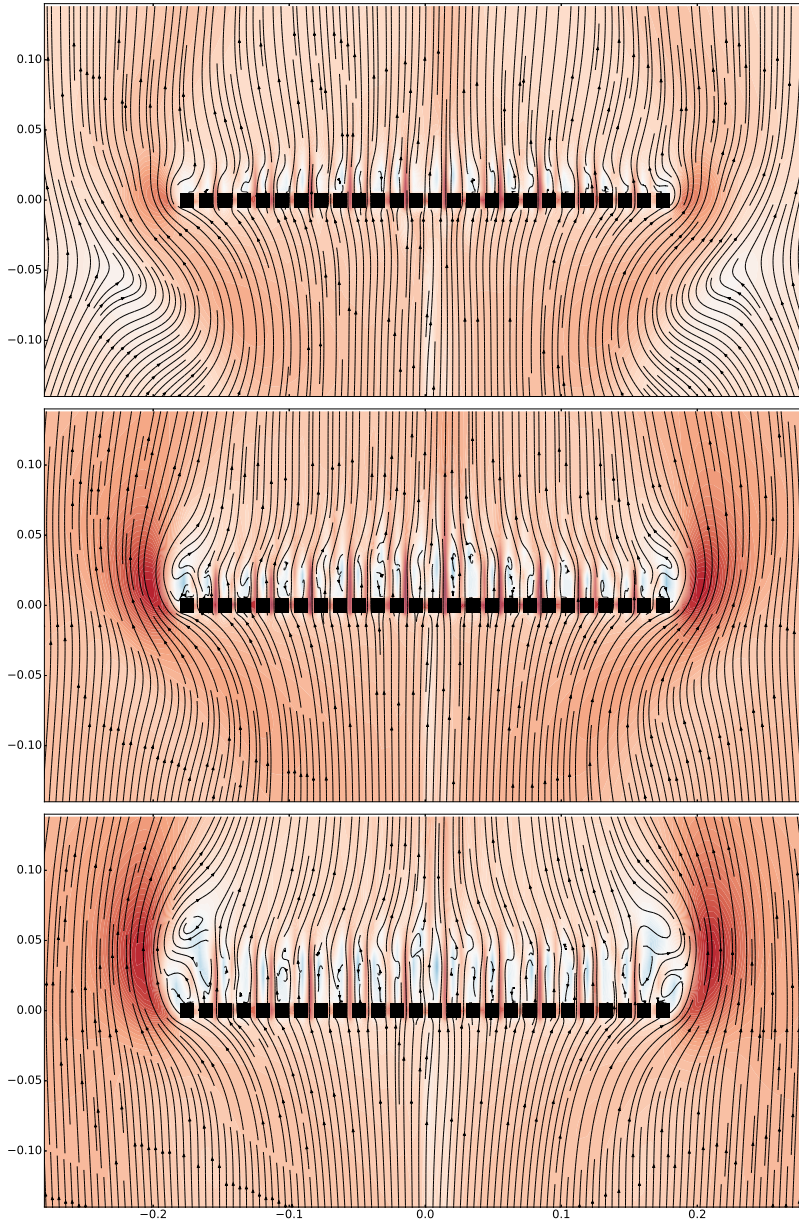


**Figure 6.14:** Streamline plots of S28 at  $KC = 1.0$ . Time-steps:  $t = 29.1T$  (top),  $t = 29.2T$  (middle),  $t = 29.3T$  (bottom). Color contours applied to the vertical velocity (red: positive, blue: negative).

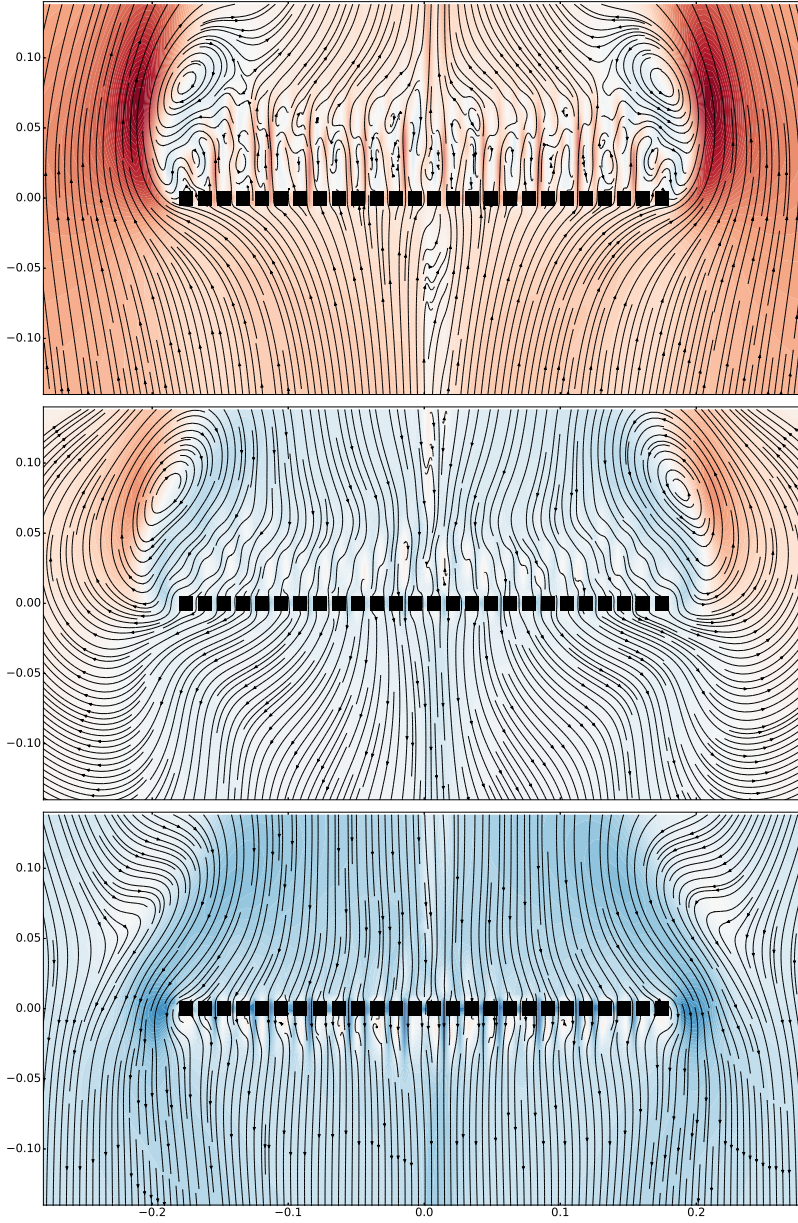


**Figure 6.15:** Streamline plots of S28 at  $KC = 1.0$ . Time-steps:  $t = 29.4T$  (top),  $t = 29.5T$  (middle),  $t = 29.6T$  (bottom). Color contours applied to the vertical velocity (red: positive, blue: negative).



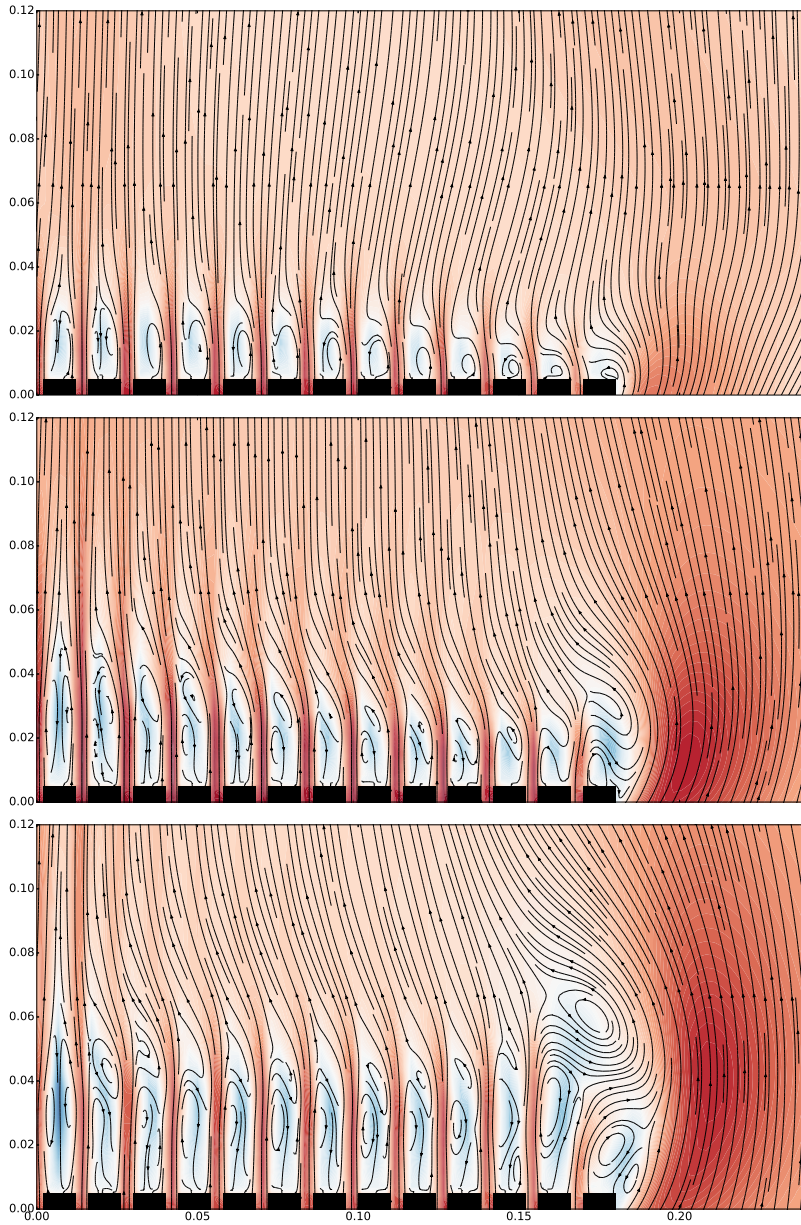


**Figure 6.16:** Streamline plots of upper right part of S28 at  $KC = 1.0$ . Time-steps:  $t = 29.1T$  (top),  $t = 29.2T$  (middle),  $t = 29.3T$  (bottom). Color contours applied to the vertical velocity (red: positive, blue: negative).

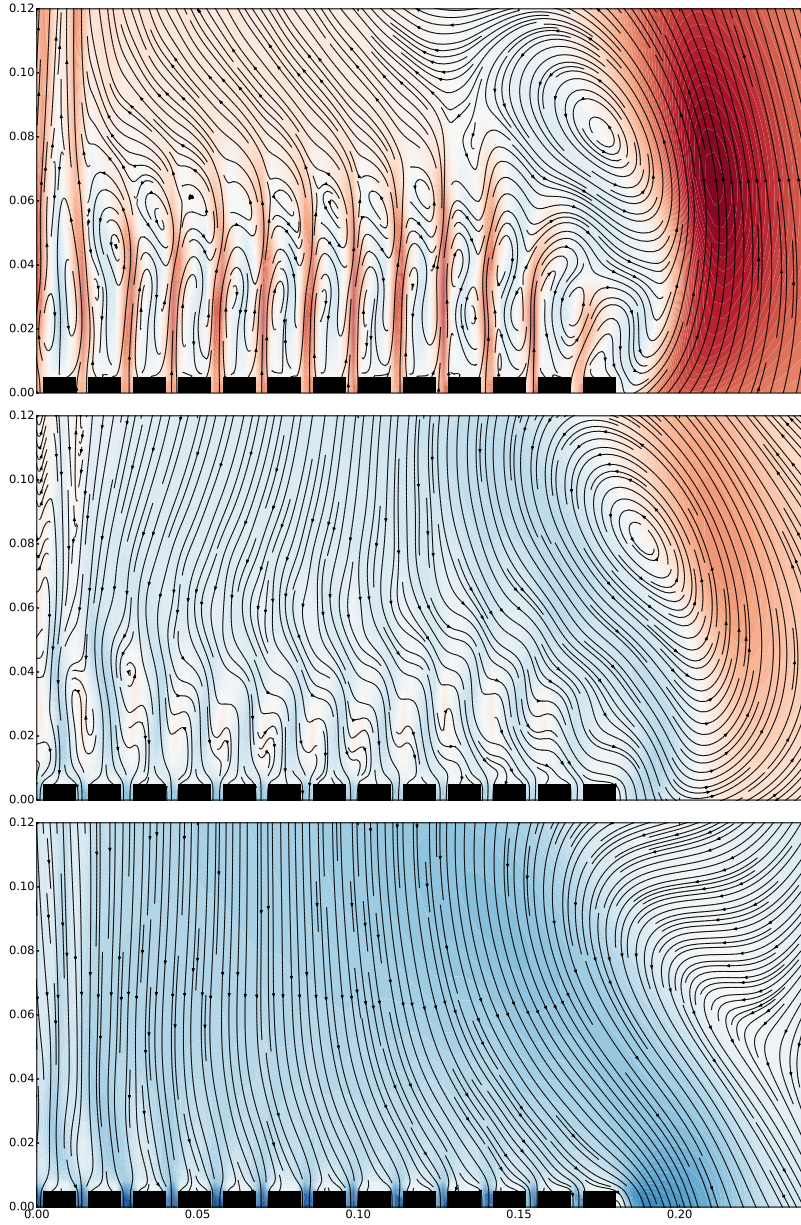


**Figure 6.17:** Streamline plots of upper right part of S28 at  $KC = 1.0$ . Time-steps:  $t = 29.4T$  (top),  $t = 29.5T$  (middle),  $t = 29.6T$  (bottom). Color contours applied to the vertical velocity (red: positive, blue: negative).

## 6.3 Comparing different perforated plates

### 6.3.1 Added mass and damping

The experimentally obtained hydrodynamic coefficients for P19, P28, C19 and S28 are presented in Figs. 6.18 and 6.19. These plots serve as comparison of ideal and real perforated plates. In the introduction of the thesis, I presented the method by Molin and the finding that if a perforated plate is infinitely thin, the potential flow added mass goes to zero as the number of openings goes to infinite, no matter the perforation ratio [19]. P19 and P28 represent almost ideal perforated plates. I also noted a relation in DNV GL RP-N103 which suggests that real perforated plates, relevant for subsea structures, with finite thickness and finite number of openings, have considerable potential flow added masses. C19 and S28 are examples of models of real perforated plates. The present comparison between the two types is particularly useful since the perforation ratio is equal for P19 and C19, and for P28 and S28.

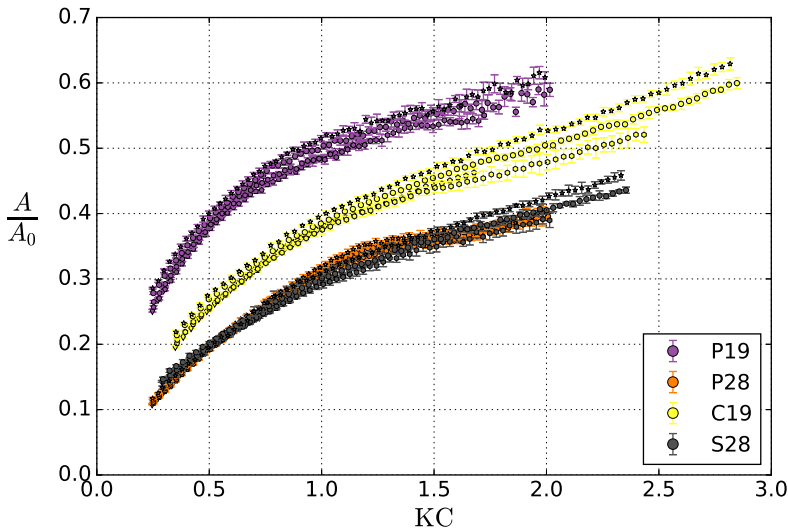


**Figure 6.18:** Added mass coefficients from experimental investigations of P19, P28, C19 and S28.

Unlike an ideal perforated plate, a real perforated plate will have a considerable added mass in the low KC limit due to the limited number of perforations or openings. The smallest experimentally tested KC numbers,  $KC \approx 0.25$ , are too large to highlight this effect; all four structures have considerable added mass at  $KC \approx 0.25$ . Note that for a structure with characteristic width equal to 10 m,  $KC = 0.25$  corresponds to an oscillation amplitude of 0.4 m (wave height 0.8 m),



hence  $KC = 0.25$  is quite small even for large structures.

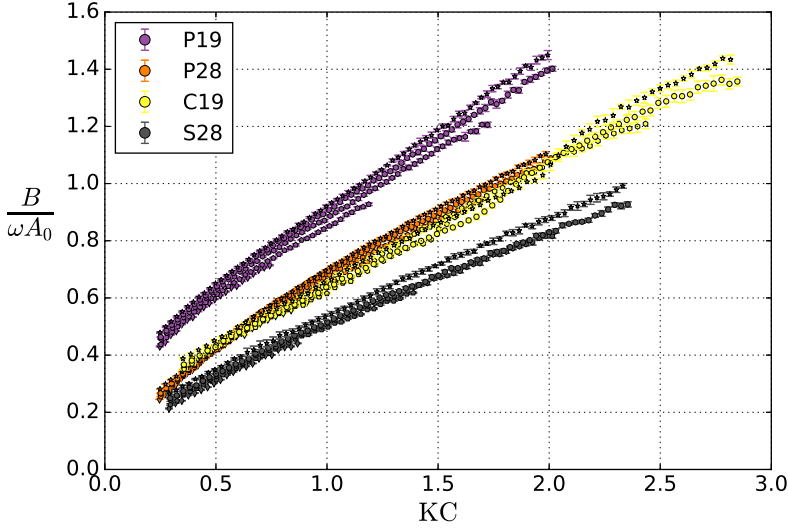


**Figure 6.19:** Damping coefficients from experimental investigations of P19, P28, C19 and S28.

The results in Figs. 6.18 and 6.19 illustrate that for a given perforation ratio, the type of perforated structure—in particular the type of openings on the structure—is important for the hydrodynamic forces on the structure. The damping coefficients are, in general, smaller for the real structures, C19 and S28, than for the ideal perforated plates, (respectively) P19 and P28. The added mass is reduced for C19 compared to P19, but not for S28 compared to P28. The circular elements of C19 give weaker flow separation compared to when the openings have sharp edges. Consequently, one should expect the hydrodynamic forces on the model to reduce. In Molin's method—where the hydrodynamic coefficients are functions of  $KC_{\text{por}}$ , cf. Section 1.4.2—this is similar to a change of the discharge coefficient,  $\mu$ , due to change of the geometry of the openings. Accordingly, both coefficients are reduced for C19 compared to P19. Contrary, for S28 compared to P28, the damping is considerably reduced, but the added mass is by and large unchanged. Slight blunting of the edges of S28 may be part of the explanation for reduced damping, cf. discussion in Section 6.2.4. Note that for the smallest  $KC$  numbers, the damping is similar for S28 and P28, whereas for increasing  $KC$ , there is a difference in slope (larger for P28) of the damping coefficient as function of  $KC$ . Increasing  $KC$  increases the importance of the global plate-end flow separation. The plate-ends are very sharp for P28. For S28, the outermost cylinder on each side forms the plate-end.

### 6.3.2 Hydrodynamic force ratio

Within the range of KC numbers tested, the hydrodynamic force on the four perforated plates is dominated by damping. This is illustrated in Fig. 6.20. The ratio between the two forces is typically within  $1.5 < \frac{B}{\omega A} < 2.5$ . Due to squaring of terms, the effect on the hydrodynamic force amplitude is large even for  $\frac{B}{\omega A} = 1.5$ , that is, for  $\frac{B}{\omega A} = 1.5$ , damping alone is 83 % of the hydrodynamic force amplitude, cf. Eq. (2.15) and the example in Section 2.3.1.

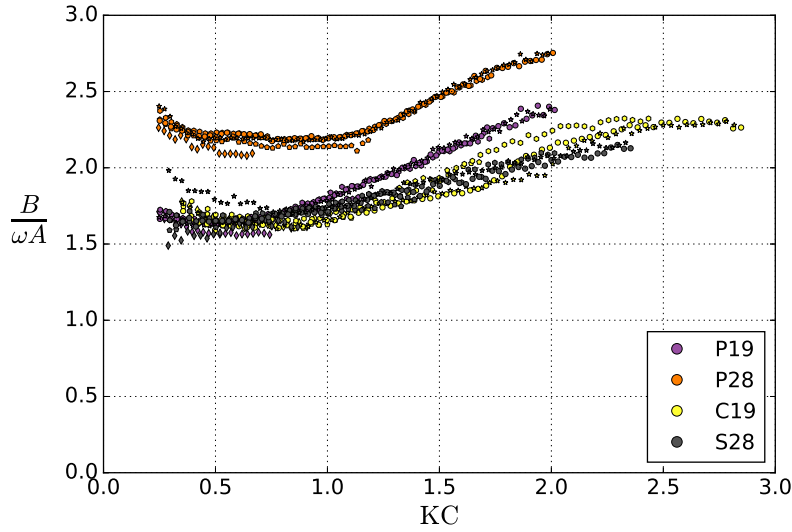


**Figure 6.20:** The ratio between the damping force and the added mass force for P19, P28, C19 and S28.

The hydrodynamic force ratio depends on both the perforation ratio and the type of openings. The results for P19 and P28 indicate that the hydrodynamic force ratio increases with increasing perforation ratio. A reduction in damping dominance is found for S28 compared to P28. As discussed in Section 6.3.1, this is due to reduced damping of S28 compared to P28, not increase in added mass. There is also a reduction for C19 compared to P19 for  $KC > 1$ , but here the differences are smaller. Both coefficients are smaller for C19 than for P19, but the relative importance, that is, the hydrodynamic force ratio, is not considerably affected.

### 6.3.3 Importance of cylinder type

The two ideal perforated plates are similar in all aspects except for the perforation ratio, however, the difference between the real perforated plates, C19 and S28, is both the perforation ratio and the shape of the cylinders. Consequently, it is hard to know which factor is more important for the change in hydrodynamic coefficients—change of perforation ratio or change of cylinder shape. Figures 6.18 and 6.19 give some answers in this regard, since the change in perforation ratio is equal between the ideal and the real perforated plates, that is,  $\tau = 0.19$  and  $\tau = 0.28$ .

To further investigate the effect of cylinder shape, viscous flow solver simulations, and potential flow added mass calculation, are performed for a numerical model which is similar to C19, but with square, not circular, cylinders. This model is denoted S19. The potential flow added mass of S19 is calculated with the BEM using 128 sources per cylinder, in total 3072, equivalent to the number of sources used for C19. The viscous flow solver simulations are set up similar to those of S28, P19 and P28. The total domain size is  $6 \text{ m} \times 6 \text{ m}$ , the fine region grid cell size is  $1.25 \text{ mm}$ , the plate width is  $297.5 \text{ mm}$  and the total number of grid cells in the domain is 59 904. The fine region grid of S19 is presented in Fig. 6.21.

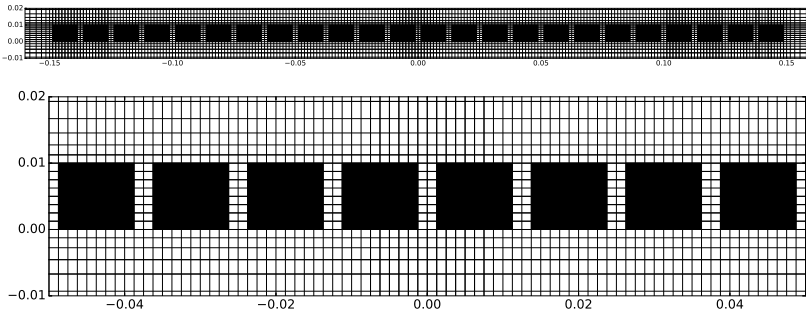


**Figure 6.21:** Fine region grid of S19 (top). A zoomed-in section of the fine region grid is presented in the bottom subplot.

Note the minor difference in the distance between adjacent cylinders in S19 ( $2.5 \text{ mm}$ ) compared to C19 ( $2.52 \text{ mm}$ , to two decimal places), cf. Fig. 6.9. In order to use a constant grid cell size in the fine region of S19, the distance between each cylinder is set to  $2.5 \text{ mm}$  in the numerical simulation. Consequently, there is a slight difference in the width of the plates and the perforation ratio,  $D = 298 \text{ mm}$ ,  $\tau = 0.1946$  (C19) versus  $D = 297.5 \text{ mm}$ ,  $\tau = 0.1933$  (S19). However, these differences are very small and within the expected error of measuring the correct width of C19. Needless to say, these minor differences are without importance for the present comparison.

Comparing different types of results (numerical and experimental), to investigate the effect of plate type and cylinder shape, is supported by the viscous flow

solver results of P19, P28 and S28, which are generally good compared to the experiments. However, I stress the added uncertainty of such an approach.<sup>1</sup>

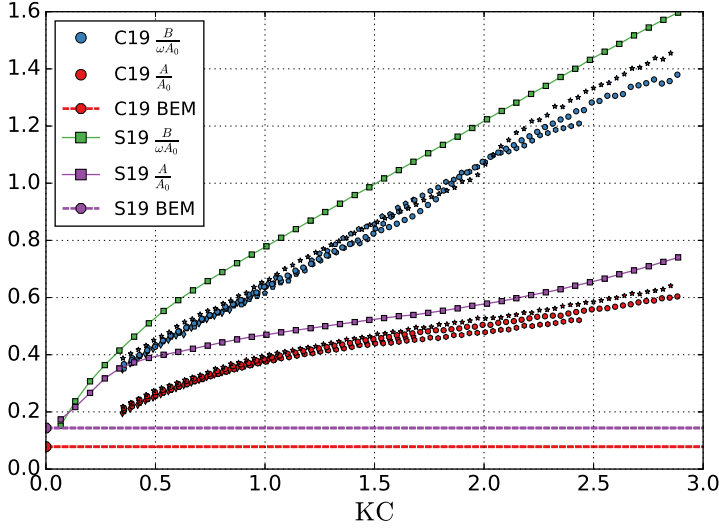


**Figure 6.22:** Added mass and damping of the numerical simulations of S19 compared with the experimental investigations of C19.

The results from the simulations of S19 are compared with the experimental results of C19 in Fig. 6.22. The added mass coefficient for S19 calculated with the potential flow solver is  $\frac{A}{A_0} = 0.1438$ . Both coefficients are larger for S19 than for C19 for corresponding KC numbers throughout the whole range of considered KC numbers. Based on the good agreement between the experimental and numerical results for S28, the considerable differences between S19 and C19 must be, by and large, a result of different cylinder shapes.

In the semi-analytical method by Molin for calculating the hydrodynamic coefficients of perforated plates, the effect of different types of openings of a perforated plate is expressed through the discharge coefficient,  $\mu$ . The discharge coefficient is inversely proportional to the resistance coefficient [19]. In the case that the resistance is due to the drag of a cylinder, the discharge coefficient is inversely proportional to the drag coefficient. For a single cylinder of diameter  $d = 0.01$  m, in the range of Reynolds numbers considered in the experimental investigations, cf. Section 6.2.2, the drag coefficient of a square cylinder is considerably larger than that of a circular cylinder. Consequently, the drag coefficient for the row

<sup>1</sup>One may say that this is a comparison of apples and oranges, but with the particularly good numerical and experimental accordance of S28 in mind, this is rather a comparison between Pink Lady and Granny Smith.

of square cylinders is likely considerably larger than that of the row of circular cylinders, although one must be careful with superposing the results due to the small distance between the cylinders, which gives speed-up of flow (increases the Reynolds number) and considerable interaction effects.

In Molin's original method without drag correction due to plate-end flow separation [19], the hydrodynamic coefficients only depend on the porous KC number, Eq. (1.3), which can be written

$$KC_{\text{por}} = KC \frac{1 - \tau}{2\pi\mu\tau^2}, \quad (6.4)$$

hence increasing the drag coefficient (decreasing the discharge coefficient) is equivalent to increasing the KC number. The results of Fig. 6.22 is consistent with the analysis of discharge coefficients since both coefficients increase with KC for both C19 and S19, and, for a given KC number, the coefficients are larger for S19 than for C19. This is in particular true for the added mass of small KC numbers. However, the potential flow solver added mass calculated for S19 is almost twice that of C19,  $\frac{A}{A_0} = 0.1438$  versus  $\frac{A}{A_0} = 0.0780$ . Therefore, it is likely that the large relative differences in added mass for small KC numbers is partly due to the difference in potential flow added mass of the two structures. Smaller relative differences for larger KC numbers can be an indication that the effect of plate-end flow separation is more important than the type of cylinder shape (and, for the added mass coefficients, potential flow effects) when the KC number is increased.

#### 6.3.4 Additional remarks

The agreement between the experimental and numerical results presented in this chapter is generally quite good. Geometrically, the most important difference between the experimental and numerical models is the lateral, that is, into the plane, extent of the models. The experimental models have no lateral variations, and the use of end-plates makes the setup of the experiments close to two-dimensional. However, the flow around these models at the considered Reynolds numbers must be expected to be turbulent and by nature three-dimensional. Therefore, it may be somewhat surprising that the numerical viscous flow solver is this well able to predict the loads of the experiments, considering that it is a two-dimensional direct numerical simulation (DNS) solver, i.e., the governing equations are solved without any turbulence model. Two effects are highlighted in this respect. 1) Rectilinear grids yield sharp corners; the separation points are fixed and the boundary layer flow does not need to be captured. Similarly, the experimentally tested models that are simulated numerically consist of sharp-edged holes (P19 and P28) or of cylinders with square cross-sections (S28), and have sharp-edged plate-ends. 2) The wake flow downstream of the perforated plates is barely developed before the flow reverses; the simulated KC numbers are relatively small and the dissipation of the wake is less important than for higher KC numbers. For solid flat plates, Singh [60] denotes  $KC < 3$  as the symmetric region. Compared to higher

KC numbers, the plate-end vortices are weak and do not interact, that is, a *symmetric* pair of vortices is developed. A similar behavior can be expected for the plate-end vortices of (relatively dense) perforated plates. The use of first order upwind schemes introduces a diffusion-like error known as false diffusion [33, p. 150]. A consequence is that the transported properties become smeared. The numerical dissipation might coincidentally have similar dissipation effect of the wake as (physical) turbulent dissipation. For large KC numbers with more developed wake flow, i.e.,  $KC > 3$ , the accuracy of the solver should be expected to decrease. However, for perforated plates relevant for subsea structures, the KC numbers are limited, e.g for a 10 m wide hatch cover,  $KC = 3$  is equivalent to a wave height of 9.5 m(!).

As a first attempt to study the effect of wake dissipation and sensitivity of the prescribed Reynolds number, numerical simulations with considerably larger values of the kinematic viscosity,  $\nu$ , were conducted. The resulting force from these simulations were almost insensitive to even large changes in the kinematic viscosity. An exception is for very small Reynolds numbers due to friction drag, cf. discussion in Section 5.4.2.

The present findings are in line with previous studies on the effect of Reynolds numbers and need for considering the three-dimensionality of turbulence for circular disks in oscillating flow. Tian et al. [61] studied the effects of Reynolds numbers on the hydrodynamic characteristics of solid circular disks. The hydrodynamic coefficients of the disks were not considerably affected by even large variations of the Reynolds number. Note that the study was limited to three relatively modest KC numbers,  $KC = 0.2$ ,  $KC = 0.6$  and  $KC = 1.0$ . However, for the present investigations, these KC numbers are relevant. They highlighted that even though the flow becomes non-axisymmetric and turbulent for relatively small Reynolds numbers (corresponding to  $\beta \geq 8 \times 10^3$ ), the effect of turbulence gets averaged over the disk. As a consequence, hydrodynamic coefficients can be calculated based on axisymmetric flow assumptions, even for large Reynolds numbers where the flow in reality is highly turbulent and three-dimensional [61]. This noteworthy result supports the finding that a relatively simple two-dimensional DNS solver may be able to yield reliable force estimates for structures in flows that in reality are highly turbulent and three-dimensional.

## 6.4 On the importance of plate-end flow separation

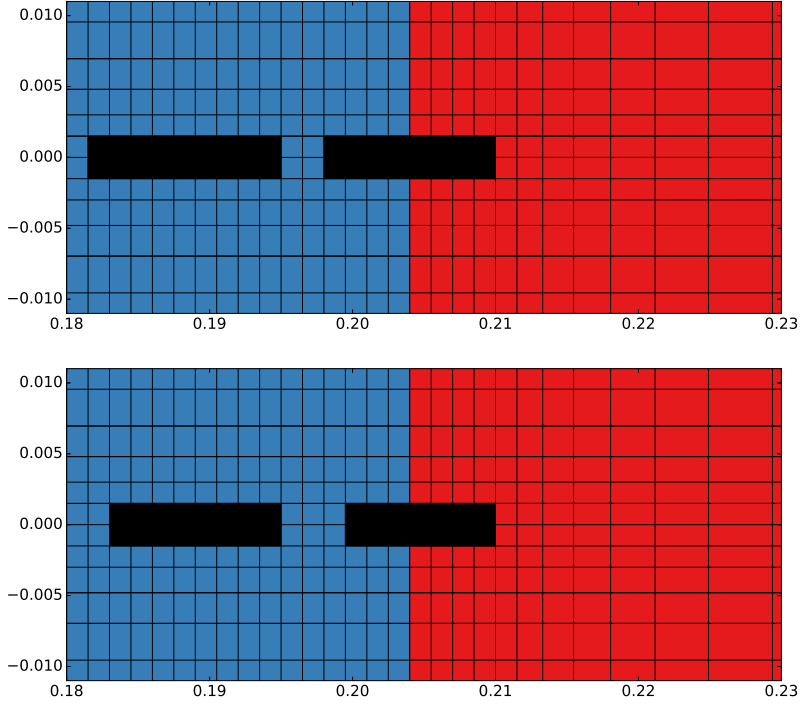


**Figure 6.23:** Last plate elements of the P19 (top) and P28 (bottom) plates in simulations where the domain is decomposed in regions with (blue) and without (red) solution of the advection and diffusion terms.

Several studies have suggested that the plate-end flow separation is important for the hydrodynamic coefficients of perforated plates [9, 18–20, 25]. To investigate the effect of plate-end flow separation, further numerical studies of the ideal perforated plates P19 and P28 are performed. These numerical studies are equal to the viscous flow solver studies presented in Section 6.1.2, except that the numerical domains are decomposed into regions with and without advection and diffusion terms, cf. Section 5.1.1. The advection and diffusion terms are solved for cells with horizontal coordinates between the center of the first and last plate elements. For all other cells of the numerical domains, the advection and diffusion terms are omitted. Illustrations are presented in Fig. 6.23, in which the boundary between the two domain parts on the right plate-end is presented. As a consequence of omitting the advection and diffusion terms on the plate-ends, no plate-end flow separation occur. This allows for studying the force on the perfo-

rated plates due to local flow separation through the openings between the plate elements, without allowing the global plate-end flow separation.

The resulting hydrodynamic coefficients of the numerical simulations are presented in Fig. 6.24. Compared with the viscous flow solver (CFD) results, the *noEndVortex* module increases the added mass and reduces the damping. The same has been observed in previous studies that have compared the semi-analytical method by Molin with and without plate-end flow separation [9, 18, 20].

When there is no flow separation at the plate-ends, there is a distinct maximum peak in the damping coefficients. In the semi-analytical method by Molin, in infinite fluid domains, the peak in the damping coefficient occurs for the KC number where the added mass and damping coefficients intersect [19]. Similar results are obtained when using the *noEndVortex* module, although the coefficients are not exactly equal. For  $\tau = 0.19$ , the maximum damping coefficient,  $\frac{B}{\omega A_0} = 0.40$ , is at  $KC = 0.43$  when the added mass coefficient is  $\frac{A}{A_0} = 0.48$ . For  $\tau = 0.28$ , the maximum damping coefficient,  $\frac{B}{\omega A_0} = 0.38$ , is at  $KC = 0.95$  when the added mass coefficient is  $\frac{A}{A_0} = 0.43$ . Both plates yield larger added mass than damping at this KC number. One contribution is that, unlike the method by Molin, the perforated plates have finite thickness and finite number of openings, and, consequently nonzero potential flow added mass.

The peak in damping does not occur in experiments or CFD when the flow is allowed to separate at the plate ends, cf. for example Fig. 6.19. Contrary, the damping coefficients continue to increase with increasing KC number. A consequence of this is that the damping coefficients are largely underpredicted for large KC numbers if the plate-end flow separation is not taken into account. The discrepancy increases with decreasing perforation ratio. As an example, the damping coefficients at  $KC = 2.0$  in simulations without plate-end flow separation are largely underpredicted and only  $\frac{0.135}{1.256} = 11\%$  ( $\tau = 0.19$ ) and  $\frac{0.308}{0.972} = 32\%$  ( $\tau = 0.28$ ) of the corresponding damping coefficients with plate-end flow separation. For the same KC number, the added mass coefficients are  $\frac{0.899}{0.595} = 151\%$  ( $\tau = 0.19$ ) and  $\frac{0.647}{0.382} = 169\%$  ( $\tau = 0.28$ ) of the corresponding CFD result.

The effect of plate-end flow separation is quantified for all KC numbers in Fig. 6.25. The hydrodynamic coefficients of P19 and P28 obtained in the simulations without plate-end flow separation are divided by the corresponding viscous flow solver results. Clearly, the effect of plate-end flow separation depends on KC; for very small KC numbers, the effect is negligible for both coefficients and both perforation ratios, whereas for all other KC numbers, the effect is crucial for the coefficients. Further, the effect of plate-end flow separation depends on the perforation ratio. An example is the relative increase in added mass for  $KC > 0.5$ , which is larger for  $\tau = 0.28$  than for  $\tau = 0.19$ . Interestingly, the relative difference in damping is smaller for  $\tau = 0.28$  than for  $\tau = 0.19$  for all these KC numbers. Consequently, if using the method by Sandvik et al. to account for plate-end flow separation in Molin's method, cf. Sections 1.4.2 and 1.4.3, determining  $\alpha$  can be difficult for two reasons: 1)  $\alpha$  is likely to depend on the perforation ratio. 2) The



best-fit of  $\alpha$  to the added mass coefficient is likely different than the best fit of  $\alpha$  to the damping coefficient.

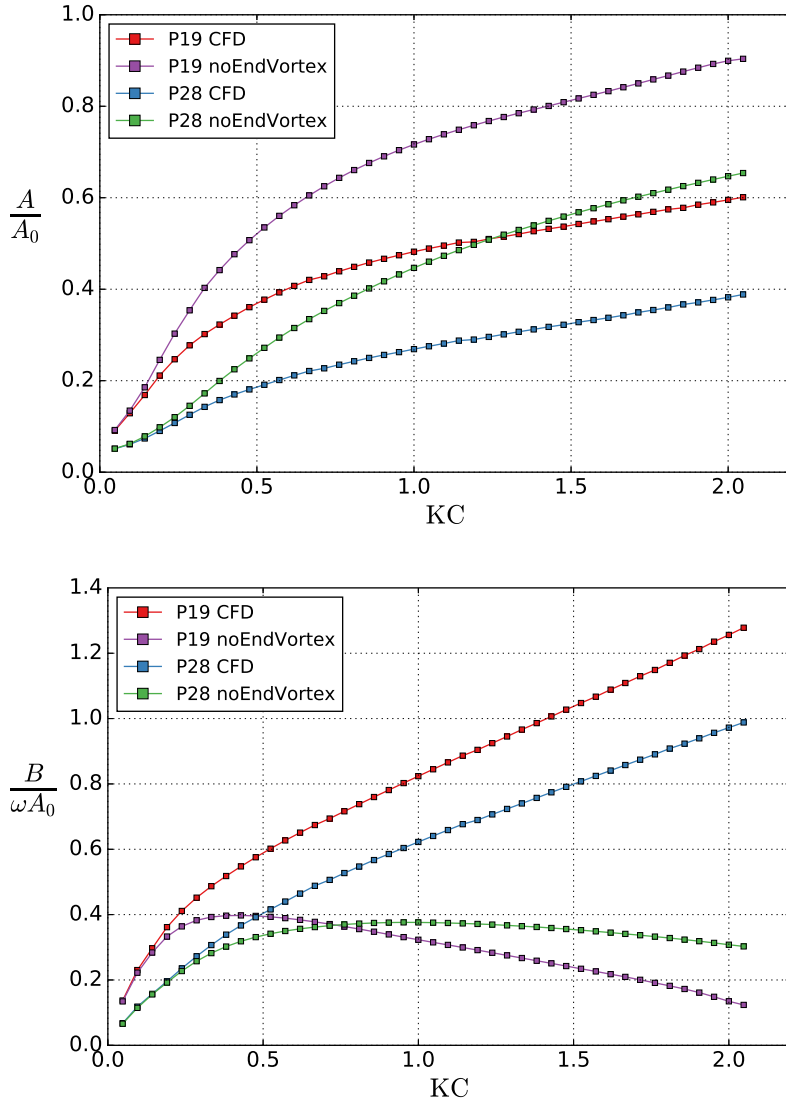


**Figure 6.24:** Added mass and damping coefficients of P19 and P28 with and without plate-end flow separation.

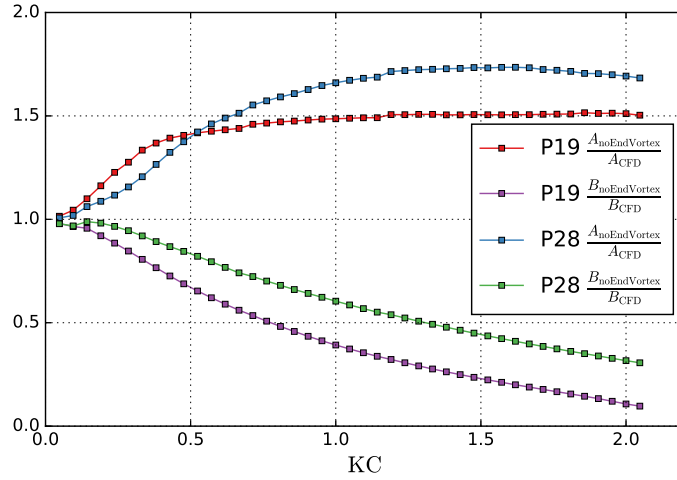


**Figure 6.25:** Relative magnitude of added mass and damping coefficients between the simulations without plate-end flow separation and the CFD.

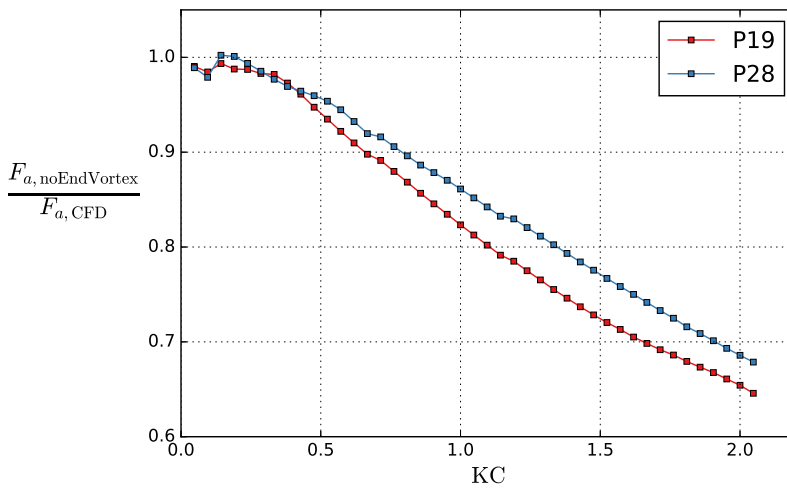


**Figure 6.26:** Relative magnitude of the normalized force amplitude between the simulations without plate-end flow separation and the CFD.

In Fig. 6.26, the difference in the normalized force amplitude, i.e., the sum of the coefficients squared, Eq. (2.12), is presented for P19 and P28. Note that the  $y$ -axis is from 0.6. If the plate-end vortices are neglected, the normalized force amplitude is reduced. The reduction increases with  $KC$  and is, in general, larger for  $\tau = 0.19$  than for  $\tau = 0.28$ . Since the damping is underestimated and the added mass is overestimated in simulations without plate-end flow separation, the effect on the normalized force amplitude is less than the effect on the individual coefficients. Nevertheless, the normalized force amplitude is considerably underestimated if the plate-end flow separation is not taken into account, increasingly so with increasing  $KC$ .

I end this chapter by presenting streamline plots of P19 and P28 in simulations with and without plate-end flow separation. The comparisons are presented in Figs. 6.27 (P19) and 6.28 (P28). The streamline plots are obtained for  $KC = 1.0$  at  $t = 29.36T$ , that is, when the prescribed ambient velocity is positive upwards and 36% into the oscillation cycle. The colormap for the contours, cf. Fig. 6.13, represents the vertical velocity. Normalization of the colormap is made against two times the prescribed amplitude of the velocity at the boundaries, that is, the darkest blue ( $-1.0$ ) in Fig. 6.13 corresponds to  $w = -2\frac{D}{T}KC$  and the darkest red ( $1.0$ ) corresponds to  $w = 2\frac{D}{T}KC$ . Clearly, not taking into account the plate-end flow separation changes the flow patterns completely.

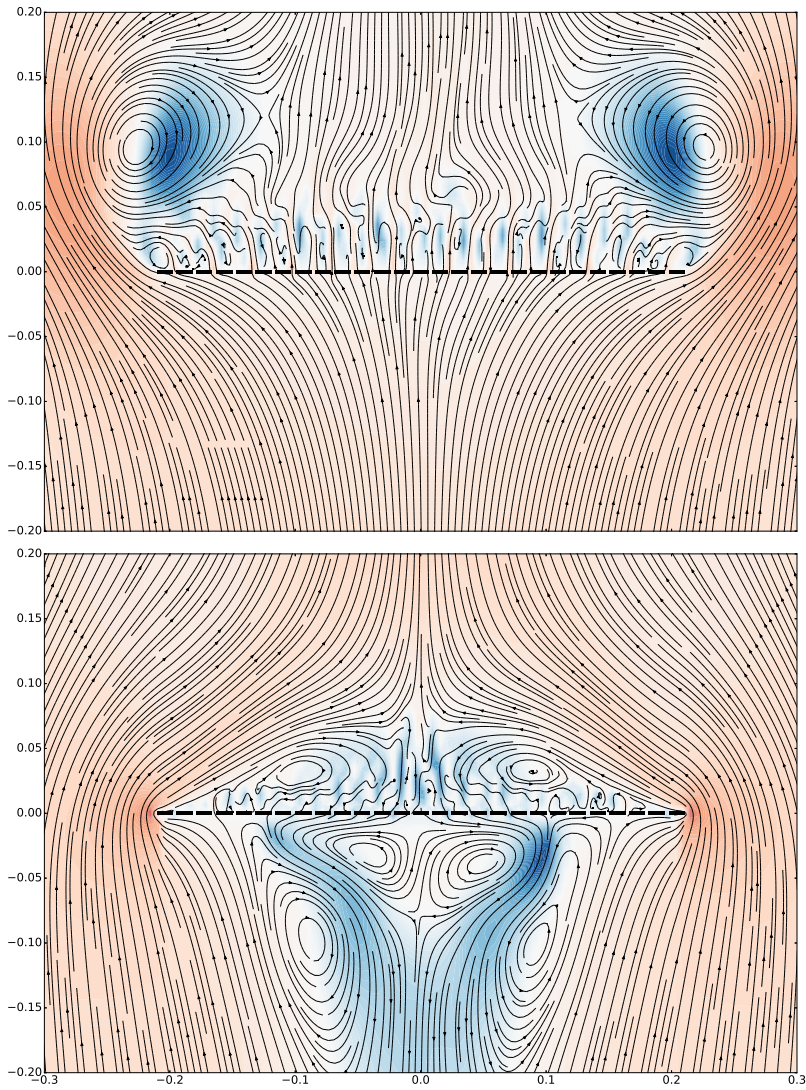


**Figure 6.27:** Streamline plots of P19 at  $KC = 1.0$  obtained at  $t = 29.36T$ . Comparison between simulations using the viscous flow solver (top) and the hybrid method without plate-end flow separation (bottom). Color contours applied to the vertical velocity (red: positive, blue: negative).

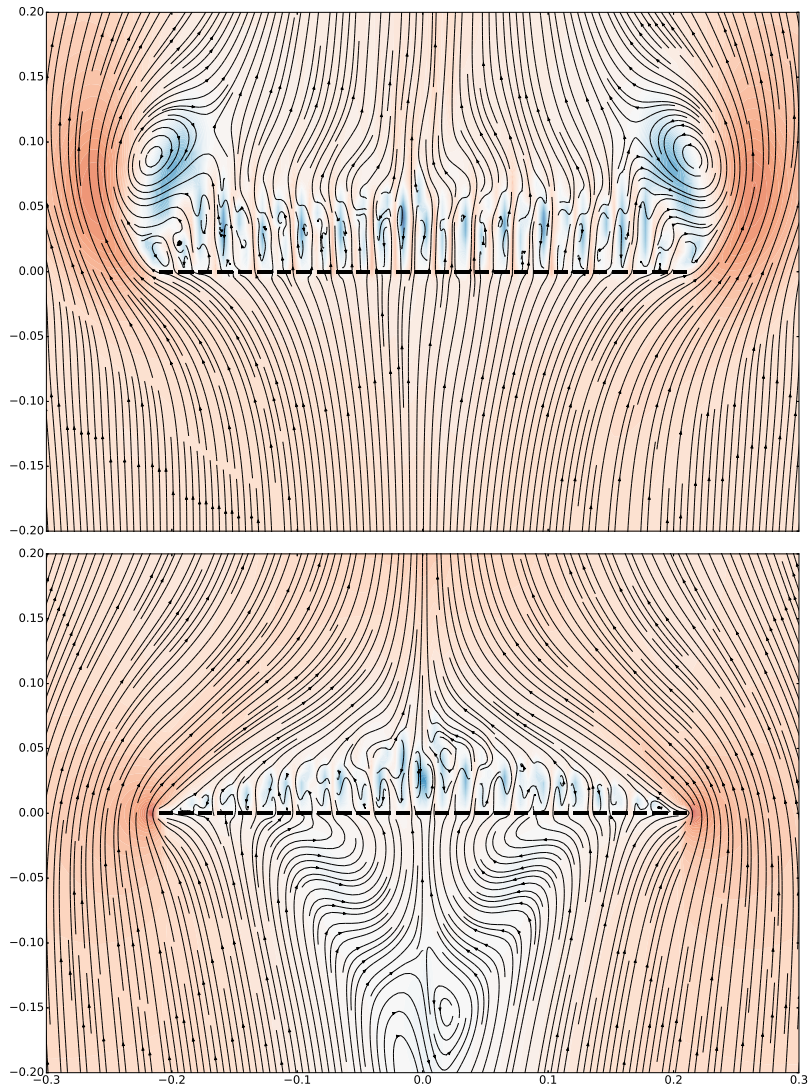


**Figure 6.28:** Streamline plots of P28 at  $KC = 1.0$  obtained at  $t = 29.36T$ . Comparison between simulations using the viscous flow solver (top) and the hybrid method without plate-end flow separation (bottom). Color contours applied to the vertical velocity (red: positive, blue: negative).

## Chapter 7

# Perforated structures in waves

Experimental investigations and numerical simulations of perforated structures in waves are presented in this chapter. The experiments are performed on two perforated plates consisting of rows of cylinders. The models are fixed in the experimental rig and subjected to incident waves. These models were introduced in Section 6.2 and are referred to as C19 and S28.

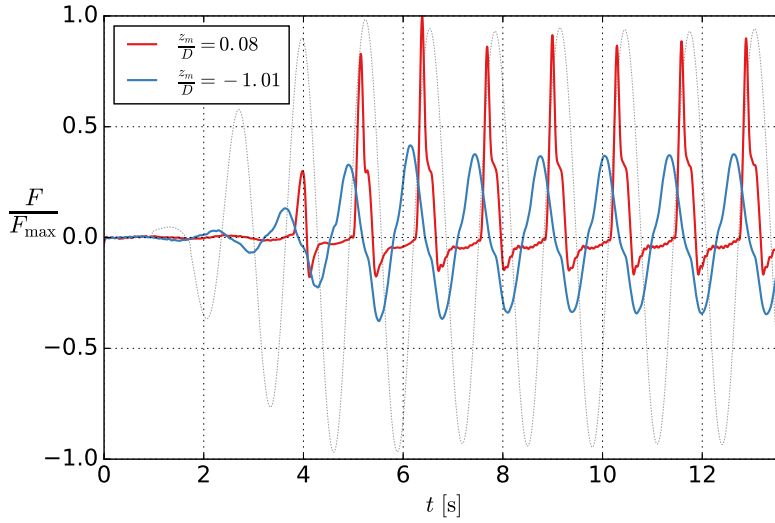


**Figure 7.1:** Example of force time-series of C19 fixed in incident waves: Nondimensional force on the C19 model placed at  $z_m = 2.5$  cm ( $\frac{z_m}{D} = 0.08$ ) and  $z_m = -30$  cm ( $\frac{z_m}{D} = -1.01$ ). Wave parameters:  $\zeta_a = 5.4$  cm,  $T = 1.3$  s. The nondimensional wave elevation at the rig center is presented with dotted line. The forces are, in this figure, made nondimensional based on the maximum force during the  $z_m = 2.5$  cm set.

A range of wave amplitudes, wave periods and vertical distances to the mean free-surface is presented. The experiments are performed for varying wave parameters  $T = 1.0$  s,  $1.1$  s,  $1.2$  s and  $1.3$  s, and a range of amplitudes between  $2.1$  cm and  $6.5$  cm. The wave parameters are chosen due to four main reasons: 1) To obtain a relatively wide range of KC numbers and wave periods, such that the sensitivity to KC and wave period/length can be investigated. 2) Limitations to the wave-flap and tank facilities; due to the length of the parabolic beach and the wave flume, longer waves are not feasible. 3) To ensure that the waves are regular, linear and not too steep. This limits the wave amplitudes and KC numbers, as well as the lower bound of the wave periods. 4) To ensure similar conditions as in the corresponding forced oscillation experiments, that is, the scaling, KC numbers and Reynolds numbers are similar to that of the forced oscillation experiments. The forced oscillation experiments of C19 and S28 (the models tested in waves) are performed for oscillation periods  $1.0 \text{ s} \leq T \leq 2.0 \text{ s}$  and oscillation amplitudes between  $1.7 \text{ cm} \leq \eta_a \leq 13 \text{ cm}$ . These oscillation periods correspond to full scale (wave) periods  $5 \text{ s} \lesssim T \lesssim 14 \text{ s}$ , cf. Section 3.2.1. Assuming the same scaling (1:25-50), the wave tests correspond to full scale wave periods  $5 \text{ s} \lesssim T \lesssim 9 \text{ s}$ . Note that in the wave tests, the KC and Reynolds numbers depend on the vertical position of the models,  $z_m$ .

**Table 7.1:** Tested wave parameters: Amplitudes, periods and corresponding (inverse) wave steepnesses.

	$T = 1.0 \text{ s}$		$T = 1.1 \text{ s}$		$T = 1.2 \text{ s}$		$T = 1.3 \text{ s}$	
	$\zeta_a$	$\frac{\lambda}{2\zeta_a}$	$\zeta_a$	$\frac{\lambda}{2\zeta_a}$	$\zeta_a$	$\frac{\lambda}{2\zeta_a}$	$\zeta_a$	$\frac{\lambda}{2\zeta_a}$
1	2.1 cm	38	2.5 cm	38	2.9 cm	38	3.4 cm	38
2	2.2 cm	36	2.6 cm	36	3.1 cm	36	3.6 cm	36
3	2.3 cm	34	2.8 cm	34	3.3 cm	34	3.8 cm	34
4	2.4 cm	32	2.9 cm	32	3.5 cm	32	4.1 cm	32
5	2.6 cm	30	3.1 cm	30	3.7 cm	30	4.3 cm	30
6	2.8 cm	28	3.4 cm	28	4.0 cm	28	4.6 cm	28
7	3.0 cm	26	3.6 cm	26	4.3 cm	26	5.0 cm	26
8	3.3 cm	24	3.9 cm	24	4.7 cm	24	5.4 cm	24
9	3.5 cm	22	4.3 cm	22	5.1 cm	22	5.9 cm	22
10	3.9 cm	20	4.7 cm	20	5.6 cm	20	6.5 cm	20

**Table 7.2:** Ratio of wavelength to width for C19 and S28.

	$T = 1.0 \text{ s}$	$T = 1.1 \text{ s}$	$T = 1.2 \text{ s}$	$T = 1.3 \text{ s}$
C19	$\frac{\lambda}{D} = 5.25$	$\frac{\lambda}{D} = 6.35$	$\frac{\lambda}{D} = 7.51$	$\frac{\lambda}{D} = 8.74$
S28	$\frac{\lambda}{D} = 4.33$	$\frac{\lambda}{D} = 5.23$	$\frac{\lambda}{D} = 6.20$	$\frac{\lambda}{D} = 7.21$

A presentation of all test sets is given in Table 7.1. Ratios of the wavelength to the characteristic dimensions of the two models are presented in Table 7.2.

The vertical position of the models,  $z_m$ , is varied from  $z_m = -30$  cm to  $z_m = 5$  cm, that is, from 30 cm below the mean free-surface to 5 cm above. A list of the tested vertical positions, and corresponding ratio of the vertical position to the characteristic dimensions of the two models, is presented in Table 7.3.

**Table 7.3:** Ratio of vertical position to width for C19 and S28.

	$z_m$	C19 $\frac{z_m}{D}$	S28 $\frac{z_m}{D}$
Section 7.1	5 cm	0.17	0.14
	2.5 cm	0.08	0.07
	0 cm	0	0
	-2.5 cm	-0.08	-0.07
	-5 cm	-0.17	-0.14
Section 7.2	-10 cm	-0.34	-0.28
	-15 cm	-0.50	-0.42
	-20 cm	-0.67	-0.56
	-25 cm	-0.84	-0.69
	-30 cm	-1.01	-0.83

An example of force time-series is presented in Fig. 7.1. The time-series are extracted for  $T = 1.3$  s,  $\zeta_a = 5.4$  cm. The force on the C19 model is presented for model position  $z_m = 2.5$  cm and  $z_m = -30$  cm. Clearly, both the magnitude and characteristics of the forces are highly dependent on the vertical position of the model. I return to the set of  $T = 1.3$  s,  $\zeta_a = 5.4$  cm throughout the chapter, and use the force time-series of C19 to present, qualitatively, some differences of the load characteristics at varying vertical positions.

The measured force in the experiments is obtained from the force transducer which is located in the intersection between the model rig and the actuator, cf. Section 3.2. Hence, the measured force includes the force on the rig and the model. In the forced oscillation tests, the measured force in tests without models is subtracted, time-step by time-step, in order to obtain a good estimate for the net force on the model. However, unlike in forced oscillation tests, there is no inertia force since the rig is fixed in the incident wave tests. Furthermore, the only parts of the rig that are in water and subjected to waves are the two acrylic glass plates. Therefore, a different approach is used in the incident wave tests to obtain the net force on the model. Since the two acrylic glass plates are relatively thin (6 mm), and their position is fixed, the main contribution to the force on the rig is due to varying buoyancy as the wave elevation varies. The corresponding buoyancy force, based on the measured wave elevation, is subtracted time-step by time-step, from the measured force on the rig and model. This gives an estimate of the net force on the model. Note that only the varying buoyancy force on the acrylic glass plates is subtracted. Consequently, in cases where the model may go in and out of water, the presented force includes the variation in buoyancy of the model. Furthermore, the effect of varying buoyancy of the acrylic glass plates on the forces



is small, and whether or not this contribution is subtracted does not affect any conclusions.

The forces on the models as functions of the vertical position of the models,  $z_m$ , for six of the tested wave amplitudes are presented in Figs. 7.2 (C19) and 7.3 (S28). The wave period is  $T = 1.3$  s for all the presented wave amplitudes. In the top subplots, the maximum unfiltered force is presented, while the amplitudes of the band-pass filtered forces using the first five harmonics, FFT5, are presented in the bottom subplots. Both forces are made nondimensional based on the wave frequency, the wave amplitude, and the reference added mass of the plates, that is,  $A_0$  from Eq. (2.11). Hence, the normalization is—for a given model—equal for all submergences. This allows for a direct comparison of how the magnitude of the wave force depends on the vertical position of a model. Since the wave velocity reduces with water depth, the inflowing velocity on the models will reduce with decreasing  $z_m$ . Consequently, one should expect the force to reduce with decreasing  $z_m$  for vertical positions that are below the mean free-surface. The force amplitude on both models decrease, in general, with decreasing  $z_m$  below the mean free-surface. Furthermore, consistent with the oscillating flow results presented in Section 6.2, the force increases with decreasing perforation ratio, that is, the force is larger on C19 than on S28.

Both the maximum unfiltered force,  $F_{\max}$ , and the amplitudes of the band-pass filtered forces using the first five harmonics,  $F_{a,\text{FFT5}}$ , are included in Figs. 7.2 and 7.3. A large difference between the two could indicate one or several of the following: 1) Considerable high-frequency noise in the measurements; 2) A large difference between the magnitude of the force maximum and the force minimum; 3) Higher-order nonlinear effects are important. Closer investigations of time-series from the measurements reveal that 1) is relevant for all submergences, in particular when the model is fully submerged, and when the wave amplitude and corresponding force are small such that the background noise is relatively large (compared to other test sets with larger wave amplitudes). High frequency noise can typically contribute to a difference between the unfiltered maximum and the filtered force amplitude of 20 %.

As the models are placed closer to the mean free-surface, the difference between  $F_{\max}$  and  $F_{a,\text{FFT5}}$  increases. This is due to both 2) and 3). In cases close to the mean free-surface, the dynamics of the force is, in general, not well captured by the FFT5-filter. When a model is installed close to the mean free-surface, depending on the wave parameters, the model may go in and out of water. Consequently, higher-order nonlinear effects can be important for the forces on the models. Contrary, when the model is fully submerged and (relatively) far from the mean free-surface, higher-order nonlinear effects are less important, and the FFT5-filter is more appropriate. Furthermore, close to the mean free-surface, the force amplitude is asymmetrical, with, typically, a larger maximum positive peak than negative peak, due to differences between the water-entry and the water-exit forces. This is in fact opposite to that of water entry and exit of a rectangular body, where the water exit load can be of larger magnitude.

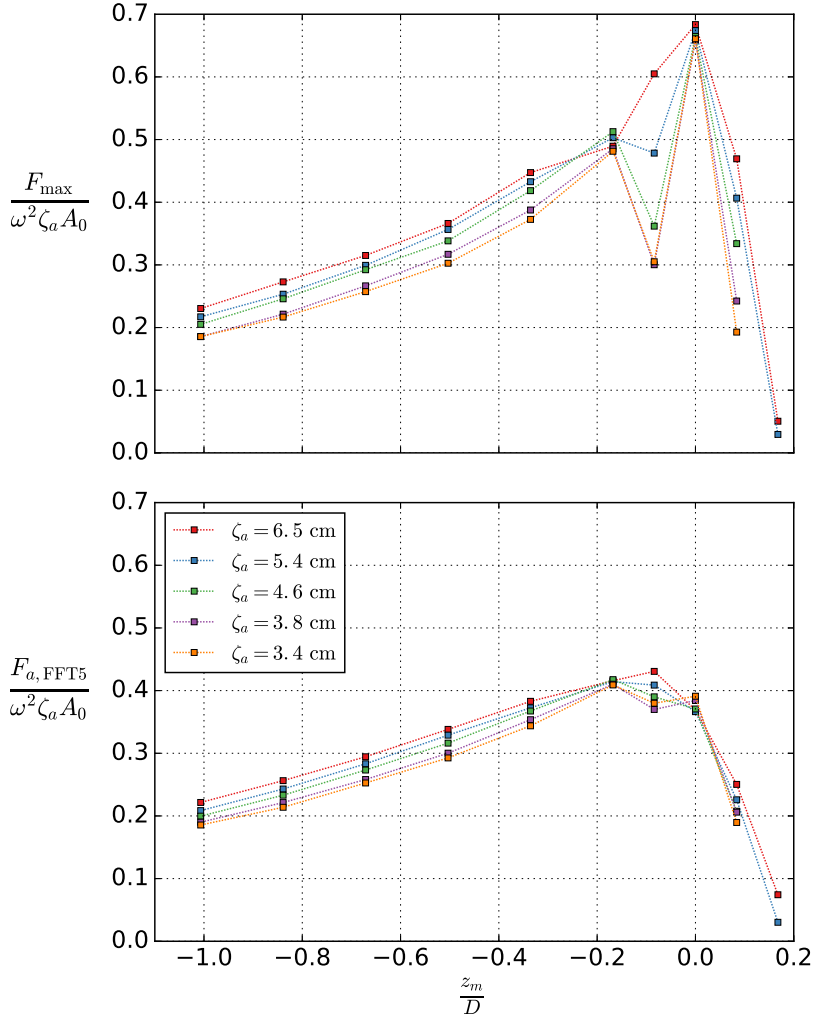


**Figure 7.2:** Normalized forces as function of the submergence of C19 for six of the tested wave amplitudes. The maximum measured raw force (Butterworth filtered at 20 Hz) and the amplitude of the band-pass filtered force using the first five harmonics are presented.  $T = 1.3$  s,  $-0.30 \text{ m} \leq z_m \leq 0.05 \text{ m}$ .

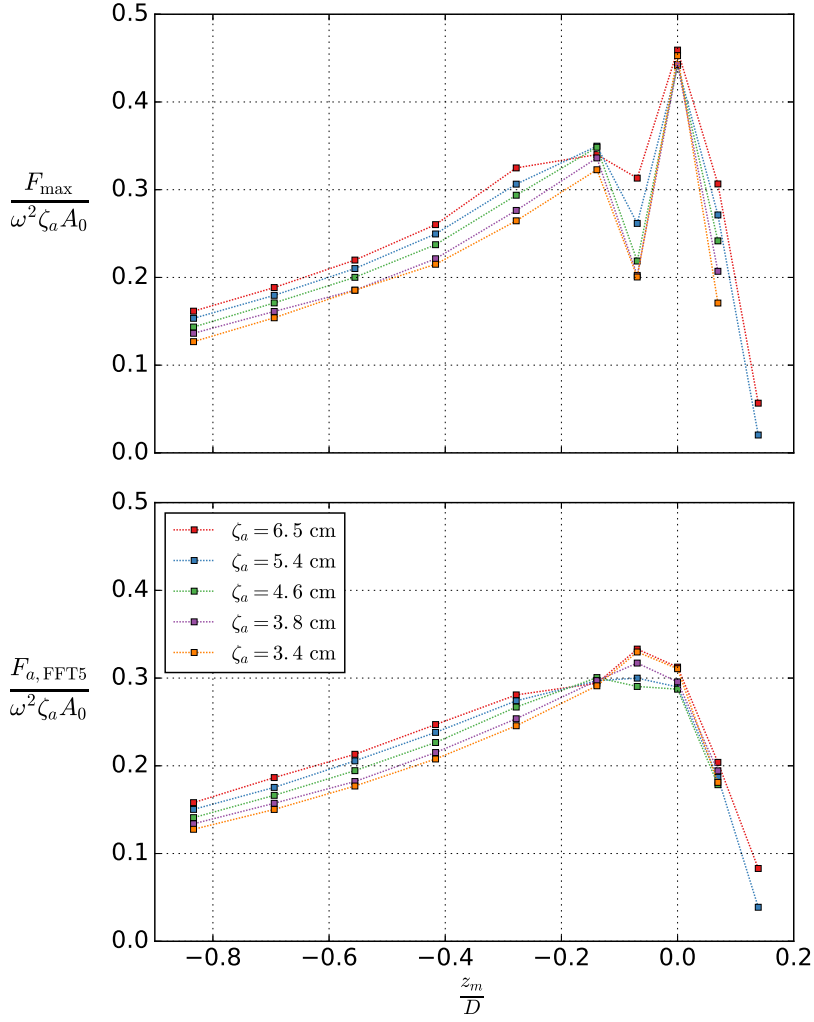


**Figure 7.3:** Normalized forces as function of the submergence of S28 for six of the tested wave amplitudes. The maximum measured raw force (Butterworth filtered at 20 Hz) and the amplitude of the band-pass filtered force using the first five harmonics are presented.  $T = 1.3$  s,  $-0.30 \text{ m} \leq z_m \leq 0.05 \text{ m}$ .

Considering the large number of test sets, and that the two models are tested in 10 different vertical positions, clear and effective result presentation is a challenge. Therefore, I included only six of the total 56 test sets in Figs. 7.2 and 7.3. In the following, I make a distinction between experiments where the models can go in and out of water, and experiments where the models are fully submerged. In Section 7.1, the experiments for model positions  $-5\text{ cm} \leq z_m \leq 5\text{ cm}$  are presented. Then, in Section 7.2, the experiments for model positions  $-30\text{ cm} \leq z_m \leq -10\text{ cm}$  are presented. In the latter cases, the force on the model is, qualitatively, similar to that of tests without waves or free-surface, for example in forced oscillations or orbital flow conditions. The main focus in this chapter is on the experimental investigations, but numerical results are also presented. Comparisons with numerical simulations are presented in Section 7.4. The simulations are performed for a numerical model of S28 and numerical models similar to S28, but with other open-area ratios. I also compare the results in incident waves with simulations of forced oscillations and orbital flow conditions.

## 7.1 Partly submerged—water entry and exit

The experimental results for model positions  $-5.0\text{ cm} \leq z_m \leq 5.0\text{ cm}$  are presented in the following. This close to the mean free-surface, the model may go in and out of water, depending on the vertical position and the wave parameters. Consequently, higher-order nonlinear effects can be important for the forces on the plates.

The force is zero calibrated at the beginning of each time-series. For  $z_m = 2.5\text{ cm}$  and  $z_m = 5.0\text{ cm}$ , the complete model is out of water at the beginning of the time-series. Consequently, the model will get a positive force contribution due to buoyancy when the model gets wet. For  $z_m = -2.5\text{ cm}$  and  $z_m = -5.0\text{ cm}$ , the model is initially fully submerged and the buoyancy force is included when doing the zero calibration. Lastly, for  $z_m = 0$ , the zero calibration includes buoyancy of half the model.

In Fig. 7.4, the force on C19 during two wave periods for  $z_m = 2.5\text{ cm}$  (top) and  $z_m = 0$  (bottom) with wave parameters  $T = 1.3\text{ s}$ ,  $\zeta_a = 5.4\text{ cm}$  is presented. A low-pass filter (cutoff at 12 Hz) is applied to filter out high-frequency noise in the force measurements. The wave elevation and forces are made nondimensional based on the maximum values during each set. Note that the wave elevation is estimated for the center of the model, hence the model starts to get wet some time-steps before the wave elevation is equal to  $z_m$ . The force is characterized by a large peak which occurs during the initial water entry when the wave hits the model. After the initial peak, the force reduces somewhat during the phase when the model is fully wetted. Further, as the wave passes the model, the water exit gives a negative contribution to the force. Compared to the magnitude of the water entry peak, the magnitude of the negative peak is small. Note that the maximum peak force is largest for  $z_m = 0$  which is the critical position in terms of maximum peak force for both C19 and S28, cf. Figs. 7.2 and 7.3.

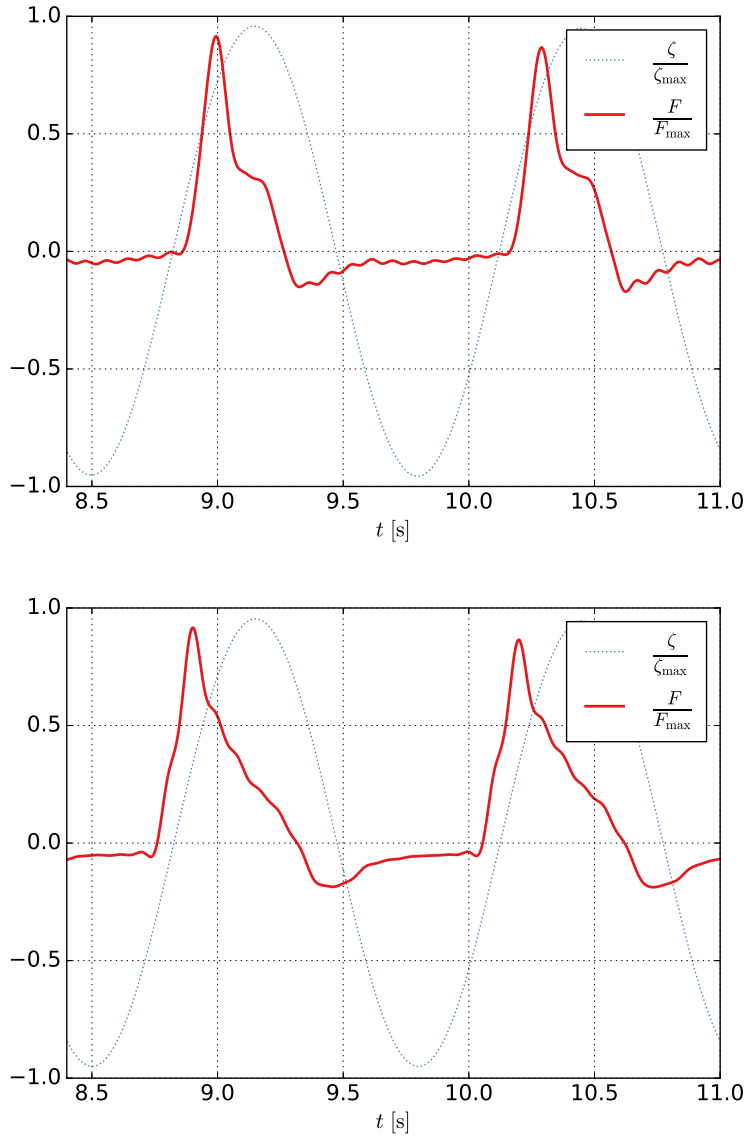


**Figure 7.4:** Nondimensional force and wave elevation (at model center) in test of C19 placed at  $z_m = 2.5$  cm (top) and  $z_m = 0$  (bottom). Wave parameters:  $\zeta_a = 5.4$  cm,  $T = 1.3$  s. The wave elevation and forces are made nondimensional based on the maximum during each set.

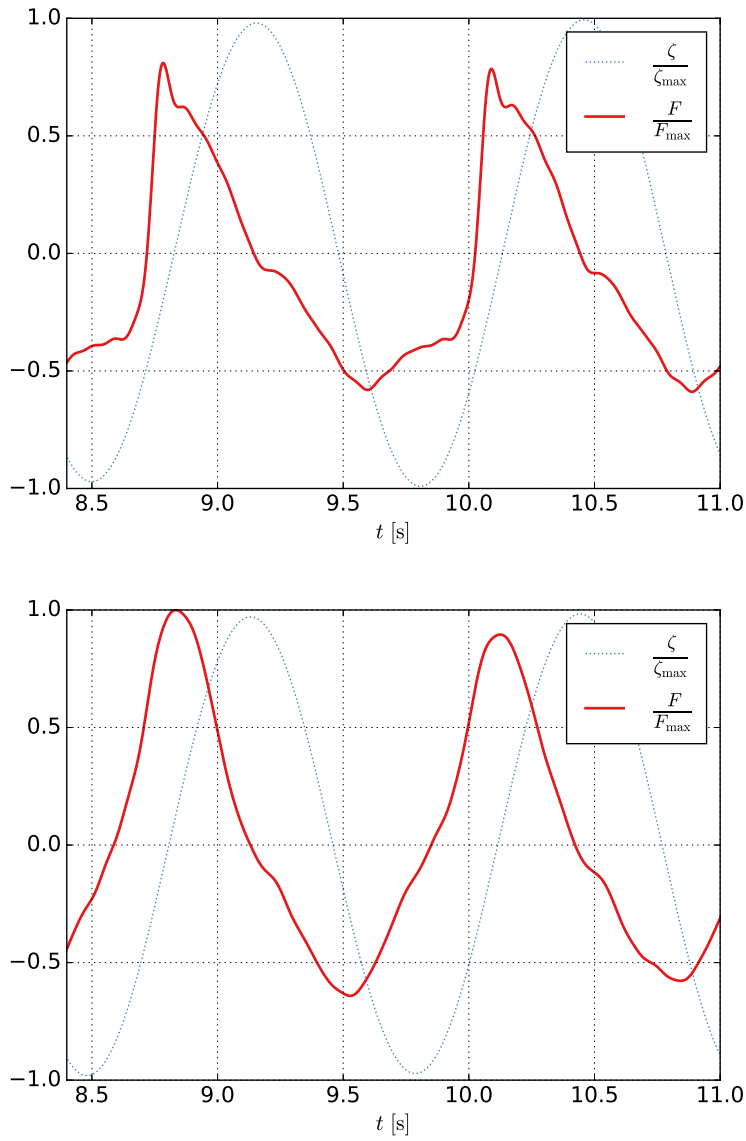


**Figure 7.5:** Nondimensional force and wave elevation (at model center) in test of C19 placed at  $z_m = -2.5$  cm (top) and  $z_m = -5.0$  cm (bottom). Wave parameters:  $T = 1.3$  s,  $\zeta_a = 5.4$  cm. The wave elevation and forces are made nondimensional based on the maximum during each set.

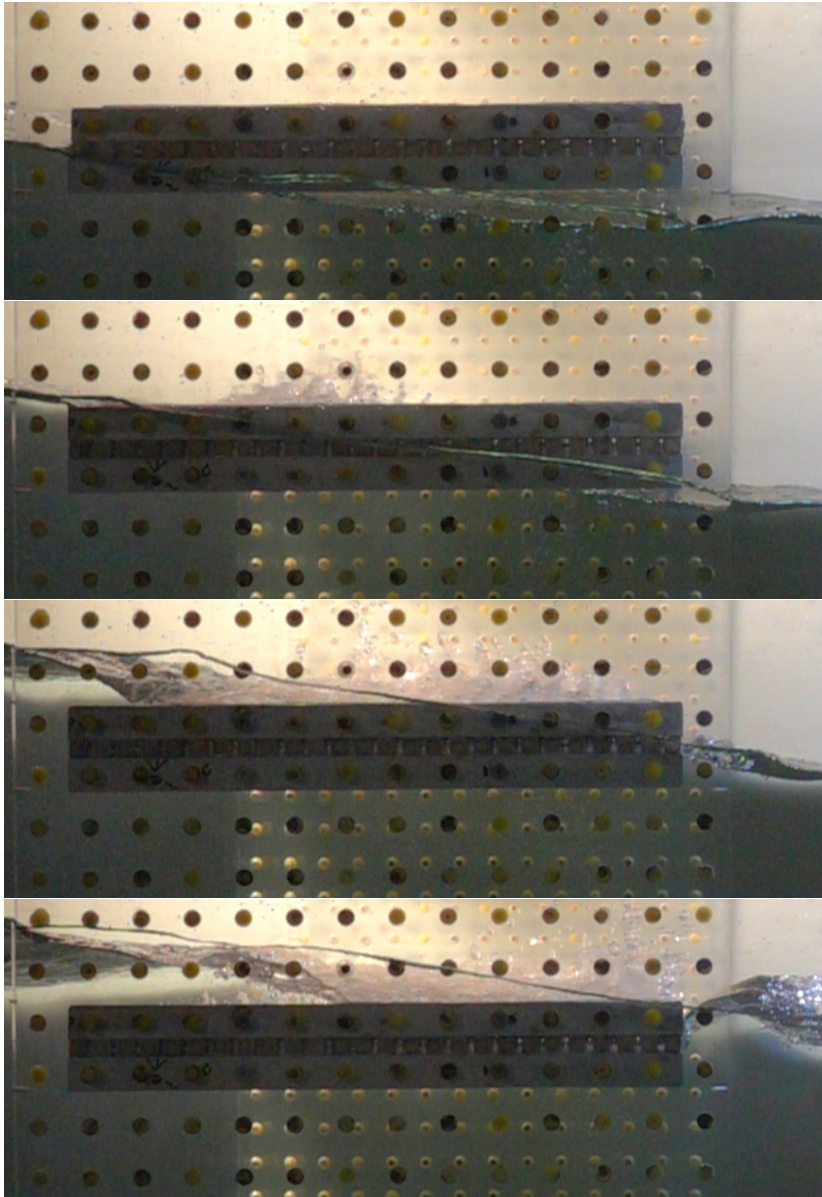


**Figure 7.6:** Photos of S28 at  $z_m = 0$  during water entry of the largest incident wave,  $\zeta_a = 6.5$  cm,  $T = 1.3$  s. The time increases from top to bottom in time-steps  $\Delta t = 0.1T$ .

In Fig. 7.5, force plots of C19 placed at  $z_m = -2.5$  cm (top) and  $z_m = -5.0$  cm (bottom), subjected to incident waves with wave parameters  $T = 1.3$  s,  $\zeta_a = 5.4$  cm, are presented. For  $z_m = -2.5$  cm, when the wave elevation is at its minimum, the model is dry and experiences a negative force due to water exit and loss of buoyancy. Note that the force is zero calibrated before each test set, hence the considerable negative force at minimum wave elevation compared to when the model is zero calibrated when dry as for e.g.  $z_m = 2.5$  cm. As the wave elevation rises, the model enters water, but the relative magnitude of the wave slamming force is not as severe as for  $z_m = 0$ , since the velocity of the wave is relatively small during the impact.

The force on C19 for  $z_m = -5.0$  cm is presented in the bottom subplot of Fig. 7.5. Since  $\zeta_a - z_m = 0.4$  cm this configuration is on the borderline of being fully submerged during the full wave period. Instead of distinct water entry and exit phases, the force resembles that of fully submerged conditions. Note, however, that there is still a considerable difference between the magnitudes of the maximum peak force and the minimum peak force at  $z_m = 5$  cm.

Photos of S28 at  $z_m = 0$  are presented in Fig. 7.6. The photos are taken at four time-steps during the wave slamming of the largest incident wave,  $\zeta_a = 6.5$  cm,  $T = 1.3$  s. The wave slamming causes the water to accelerate and form small jets through the perforated openings of the plate. Jets are seen above the plate in the second and third photo due to flow through the openings. In the last photo, the flow separation at the right plate-end is visible.

### 7.1.1 Force as function of KC





































In the following, the results for all test sets with models close to the mean free-surface are presented. I use five colors, one for each vertical position, and four markers, one for each wave period, in the result figures. The complete legends are presented in Fig. 7.7.

The normalized forces on the models are presented as functions of the KC number. For all positions below the mean free-surface, i.e.,  $z_m < 0$ , the KC numbers are estimated based on the measured incident wave amplitude and the vertical distance from the mean free-surface to the structure, using linear wave theory, Eq. (2.20). Further, the characteristic velocity,  $W$ , used to normalize the force, takes into account the vertical position and is calculated as  $\frac{D}{T}KC$ . Since all vertical positions are relatively close to the mean free-surface, the reduction in KC due to submergence is limited, and similar plots are obtained if the effect of submergence is excluded. However, when the models are placed further below the mean free-surface, taking into account the reduced velocity will, in general, reduce the spread between the results for different submergences. For consistency, I have used this normalization in the result plots for models close to the mean free-surface as well.

In Figs. 7.8 (C19) and 7.9 (S28), the maximum and minimum magnitudes of the force are presented. The measured force is sampled at 200 Hz with Butter-



worth filtering at 20 Hz. Additionally, a low-pass filter with cutoff frequency 12 Hz is applied to avoid influence from high-frequent noise. Both the maximum peak and the minimum peak are presented, due to large differences in the magnitudes of the water entry and water exit force.

	$\frac{z_m}{D} = 0.17, T = 1.2 \text{ s}$		$\frac{z_m}{D} = 0.14, T = 1.2 \text{ s}$
	$\frac{z_m}{D} = 0.17, T = 1.3 \text{ s}$		$\frac{z_m}{D} = 0.14, T = 1.3 \text{ s}$
	$\frac{z_m}{D} = 0.08, T = 1.0 \text{ s}$		$\frac{z_m}{D} = 0.07, T = 1.0 \text{ s}$
	$\frac{z_m}{D} = 0.08, T = 1.1 \text{ s}$		$\frac{z_m}{D} = 0.07, T = 1.1 \text{ s}$
	$\frac{z_m}{D} = 0.08, T = 1.2 \text{ s}$		$\frac{z_m}{D} = 0.07, T = 1.2 \text{ s}$
	$\frac{z_m}{D} = 0.08, T = 1.3 \text{ s}$		$\frac{z_m}{D} = 0.07, T = 1.3 \text{ s}$
	$\frac{z_m}{D} = 0, T = 1.0 \text{ s}$		$\frac{z_m}{D} = 0, T = 1.0 \text{ s}$
	$\frac{z_m}{D} = 0, T = 1.1 \text{ s}$		$\frac{z_m}{D} = 0, T = 1.1 \text{ s}$
	$\frac{z_m}{D} = 0, T = 1.2 \text{ s}$		$\frac{z_m}{D} = 0, T = 1.2 \text{ s}$
	$\frac{z_m}{D} = 0, T = 1.3 \text{ s}$		$\frac{z_m}{D} = 0, T = 1.3 \text{ s}$
	$\frac{z_m}{D} = -0.08, T = 1.0 \text{ s}$		$\frac{z_m}{D} = -0.07, T = 1.0 \text{ s}$
	$\frac{z_m}{D} = -0.08, T = 1.1 \text{ s}$		$\frac{z_m}{D} = -0.07, T = 1.1 \text{ s}$
	$\frac{z_m}{D} = -0.08, T = 1.2 \text{ s}$		$\frac{z_m}{D} = -0.07, T = 1.2 \text{ s}$
	$\frac{z_m}{D} = -0.08, T = 1.3 \text{ s}$		$\frac{z_m}{D} = -0.07, T = 1.3 \text{ s}$
	$\frac{z_m}{D} = -0.17, T = 1.0 \text{ s}$		$\frac{z_m}{D} = -0.14, T = 1.0 \text{ s}$
	$\frac{z_m}{D} = -0.17, T = 1.1 \text{ s}$		$\frac{z_m}{D} = -0.14, T = 1.1 \text{ s}$
	$\frac{z_m}{D} = -0.17, T = 1.2 \text{ s}$		$\frac{z_m}{D} = -0.14, T = 1.2 \text{ s}$
	$\frac{z_m}{D} = -0.17, T = 1.3 \text{ s}$		$\frac{z_m}{D} = -0.14, T = 1.3 \text{ s}$

**Figure 7.7:** Legends for result figures: C19 (left) and S28 (right).

The results for both models indicate large differences in the magnitudes of the maximum and minimum normalized forces for the vertical positions close to the mean free-surface.  $z_m = 0$  yields, in general, the largest maximum normalized forces. These findings are consistent with the examples presented in Figs. 7.4 and 7.5. Both structures have the largest absolute minimum normalized forces when the plates are installed at  $z_m = -2.5$  cm. This is due to water exit and loss of buoy-

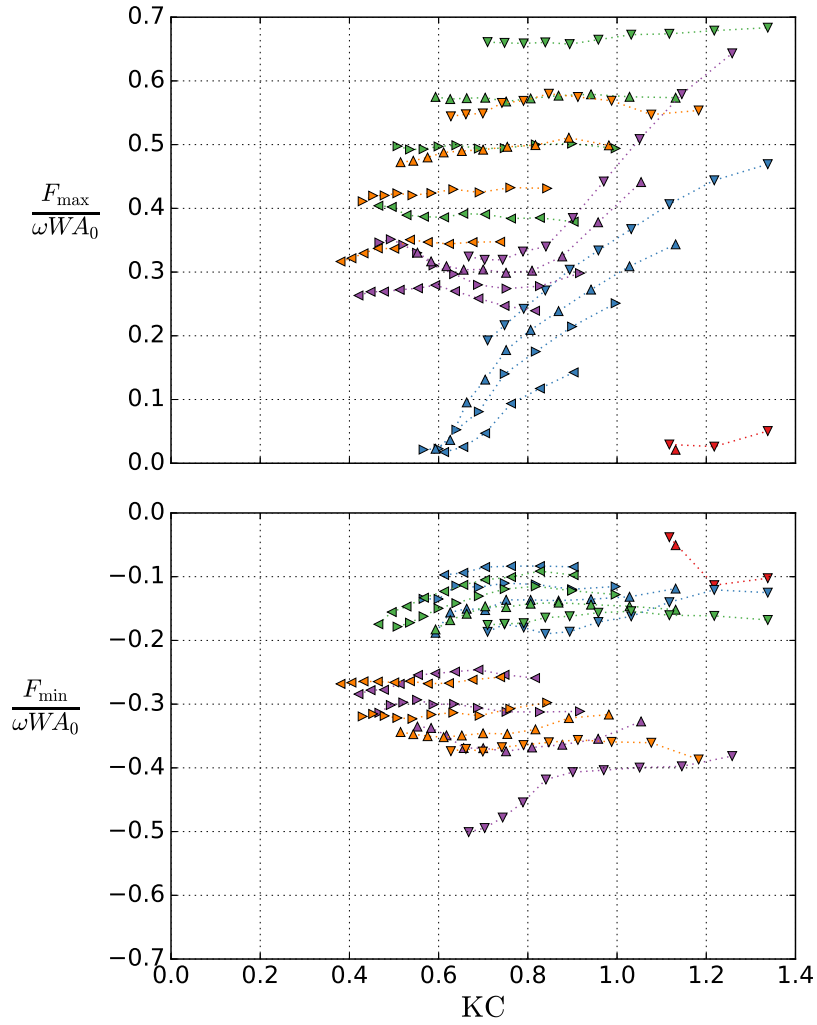


**Figure 7.8:** Normalized force as function of  $KC$  for C19. Different colors indicate different vertical positions,  $z_m$ . Different markers indicate different wave periods. Legend in Fig. 7.7.

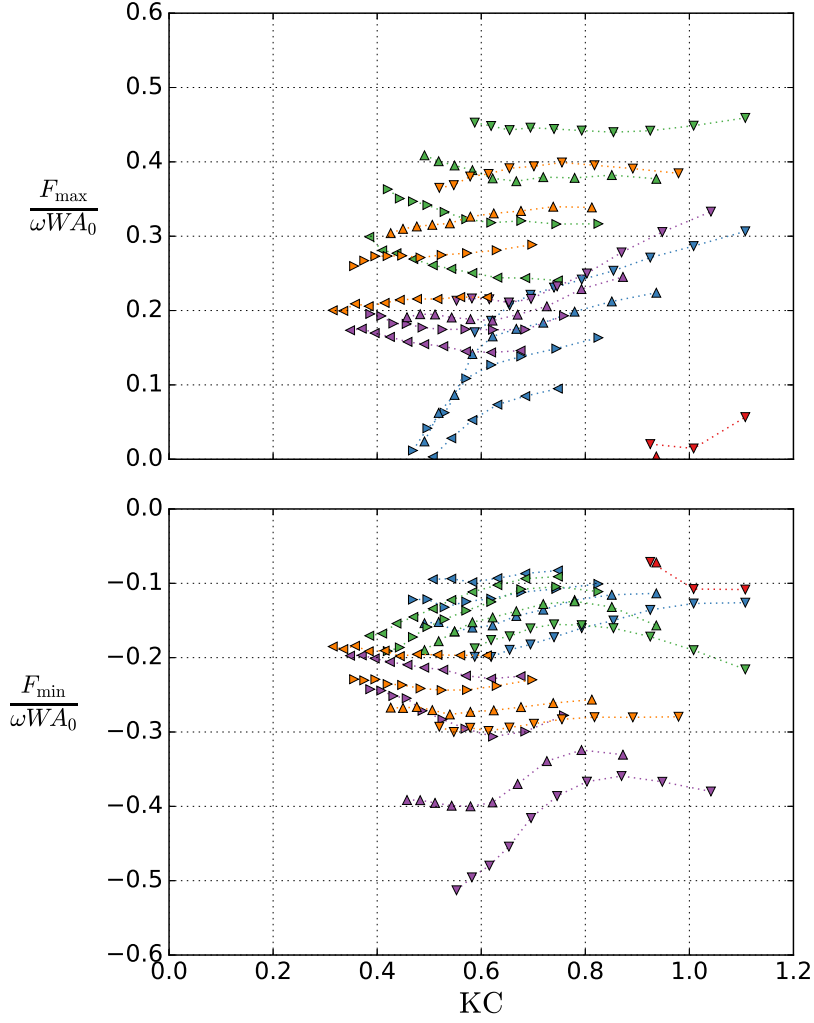


**Figure 7.9:** Normalized force as function of KC for S28. Different colors indicate different vertical positions,  $z_m$ . Different markers indicate different wave periods. Legend in Fig. 7.7.

ancy when the wave trough is below  $z_m$ . In relative terms, the effect is largest for the smallest wave amplitudes that completely dry up the models (C19:  $T = 1.3$  s,  $0.6 \lesssim KC \lesssim 0.8$ . S28:  $T = 1.2$  s and  $1.3$  s,  $0.4 \lesssim KC \lesssim 0.6$ ). However, this is due to the fact that the normalized force is made non-dimensional with the characteristic velocity, which, for a given  $z_m$  and  $T$ , increases linearly with increasing  $KC$ . In dimensional terms (i.e., Newton), the maximum absolute negative forces are not within these narrow  $KC$  ranges, but instead similar for all waves that completely dry up the models.

Contrary to the forced oscillation results, the results presented in Figs. 7.8 and 7.9 are highly period dependent, with generally larger magnitudes for longer waves. A potential reason can be sensitivity to  $\frac{\lambda}{D}$ . However, compared to the characteristic dimensions of the plates, all tested waves are relatively long, cf. Table 7.2.

### 7.1.2 Water entry force with BEM

The water entry force is predicted with a von Kármán approach using the potential flow solver, cf. Section 4.1.3. In the experiments, C19 at  $z_m = 0$  with wave period  $T = 1.3$  s yields the largest forces. This scenario is simulated with the von Kármán approach. Four amplitudes are tested,  $\zeta_a = 4.1$  cm, 4.3 cm, 5.4 cm and 6.5 cm, that is, series 4, 6, 8 and 10, cf. Table 7.1. Sensitivity to the number of sources used to discretize the model is tested for  $\zeta_a = 5.4$  cm.

Three important assumptions are made to model the impact between the model and the incident wave in the potential flow solver. 1) The impact between the wave and the model is simplified as an impact acting normally on the model, that is, each cylinder of C19 is similarly wetted at equal time. This can be thought of as a long-wave approximation. Hydrodynamic interaction between the cylinders is included. 2) No flow separation is considered. 3) The velocity of the impact is assumed constant throughout the impact. Consequently, the added mass term of Eq. (4.1) is zero. The force on the model simplifies to

$$F = \frac{dA}{dz} w^2 + \rho g \Omega L, \quad (7.1)$$

with  $\Omega$  being the two-dimensional instantaneous submerged part of the cross-section of the 24 cylinders of C19. The lateral length of the model is  $L = 0.57$  m in order to have comparable three-dimensional force with the experimental investigations. Since the model is placed at  $z_m = 0$ , the vertical velocity is assumed constant equal  $w = \omega \zeta_a$ .

The duration of the impact,  $\delta t$ , is estimated as the time from the first cylinder starts to get wet in the experiments, to the last cylinder is fully wet,

$$\delta t = \frac{\arcsin\left(\frac{0.5d}{\zeta_a}\right) - \arcsin\left(\frac{-0.5d}{\zeta_a}\right) + kD}{\omega}. \quad (7.2)$$

Here  $d$  is the diameter of the cylinders,  $d = 1.0$  cm,  $k = \frac{2\pi}{\lambda}$  is the wave number and  $D = 298$  mm is the width of the C19 model. The number of time-steps in

the simulations is fixed such that the sampling rate is 200 Hz, that is, equal to the sampling rate of the experimental investigations. This corresponds to 36-40 time-steps. A summary of the parameters used in the simulations is given in Table 7.4.

**Table 7.4:** Parameters in water entry BEM simulations of C19. The velocity of the simulations is  $w = \omega \zeta_a$ .  $n_t$  is the number of time-steps,  $n_{s,cyl}$  the number of sources per cylinder (24 cylinders in total) and  $z_m$  is the mean position of the model.

$\zeta_a$	$T$	$n_t$	$n_{s,cyl}$	$z_m$
4.1 cm	1.3 s	40	160	0
4.6 cm	1.3 s	39	160	0
5.4 cm	1.3 s	38	20, 40, 80, 160, 320	0
6.5 cm	1.3 s	36	160	0

A sensitivity study of the number of sources used to model each cylinder is performed. The parameters used in the simulations correspond to the parameters used for  $\zeta_a = 5.4$  cm, cf. Table 7.4. Note that the buoyancy force is calculated from geometrical considerations and insensitive to the number of sources. Therefore, the sensitivity study is performed for the slamming coefficient,  $C_S$ , Eq. (4.3). The slamming coefficient is here normalized based on the diameter of each cylinder of C19,  $d = 1.0$  cm,

$$C_S = \frac{2}{\rho d} \frac{dA}{dz}. \quad (7.3)$$

This makes it easy to compare with superposition of the results for 24 individual cylinders with diameter  $d$ . The slamming coefficient of one cylinder was presented in Section 4.2.2.

The results of the sensitivity study are presented in Fig. 7.10. The results of superposition of 24 single cylinders, cf. Section 4.2.2, is included for comparison. The variations in added mass, and consequently smoothness of the slamming coefficient along the relative submergence,  $\frac{z_w}{d}$ , increase with increasing number of sources. Based on the results,  $n_s = 24 \times 160 = 3840$  is used in the rest of the simulations.

The results in Fig. 7.10 highlight the need for considering the hydrodynamic interaction between the cylinders. However, in the first time-step, the results for C19 and superposition of 24 single cylinders are similar. If the coefficient for C19 in the first time-step is divided by 24 (the total number of cylinders),  $C_S(t = 0)$  is within 3 % of the classical result by von Kármán,  $C_S(t = 0) = \pi$  [45]. Contrary to the results for one cylinder, where the maximum peak in  $C_S$  occurs at the initial time of impact, the maximum peak for C19 in the simulations is when  $z_w \approx 0.5d$ . This is due to potential flow interaction between the cylinders, which gives the largest variations in added mass when each cylinder is approximately 50 % wet. The importance of hydrodynamic interaction between the cylinders can be estimated by the impulse of the slamming force. The impulse of the slamming force

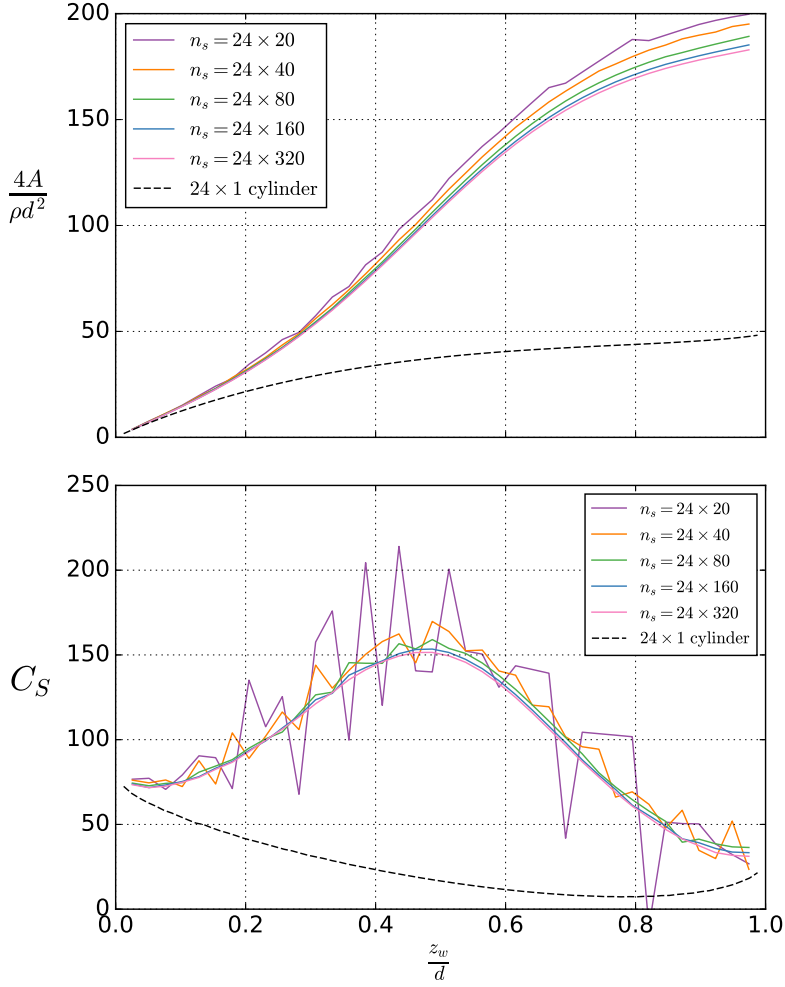


**Figure 7.10:** Added mass and slamming coefficient of C19 as function of the relative submergence. Numerical results using varying number of sources,  $n_s$ , in BEM. Normalization against one cylinder. Comparison with superposition of 24 single cylinders, cf. Section 4.2.2.

is proportional to the impulse of the slamming coefficient,

$$I_{C_S} = \int_{t=0}^{t=\frac{d}{w}} C_S dt = \frac{1}{w} \int_{z_w=0}^{z_w=d} C_S dz_w. \quad (7.4)$$

Since the added mass is zero before the cylinders start to get wet, the difference in impulse is proportional to the difference in added mass when the cylinders are fully wet, cf. Eq. (7.3). For a single cylinder,  $I_{C_S} = 1.05 \frac{d}{w}$ , hence superposition of 24 cylinders yields  $I_{C_S} = 25 \frac{d}{w}$ . The impulse of C19 yields  $I_{C_S} = 96 \frac{d}{w}$  which is almost four times the result of superposition 24 individual cylinders. The results of the top subplot of Fig. 7.10 indicate some variation in the impulse between the different discretizations of C19. An alternative illustration of the difference in impulse between 24 single cylinders and C19 discretized using  $n_s = 3840$  is presented in Fig. 7.11.

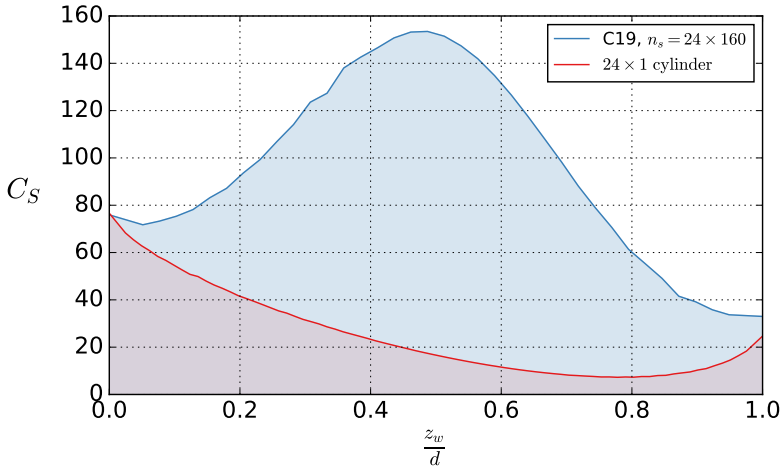


**Figure 7.11:** Illustration of difference in impulse between C19 and superposition of 24 single cylinders, cf. Section 4.2.2.

Results for the four simulated wave amplitudes in BEM are compared with the corresponding experimental results in Figs. 7.12 and 7.13. The experimental results are presented in terms of the mean and standard deviation of the measured force for the last five wave periods, cf. Fig 7.1. The experimental force is presented for the first half wave period,  $0 \leq t < 0.5T$ , where  $t = 0$  refers to the initial water entry of the first cylinder of the model and  $T = 1.3$  s. Contrary, the predicted water entry load by the von Kármán approach is presented during the water entry phase only, since the potential flow simulations end when the cylinders are fully wetted.

The potential flow solver water entry module provides acceptable estimates of the maximum peak force for all considered wave amplitudes, in particular for

the largest wave amplitude  $\zeta_a = 6.5$  cm where the peak force in BEM is within 5% of the experiment. However, there is a considerable phase difference between the force in the BEM and in the experiments. This is related to the assumption of normal impact in BEM, in which all cylinders are wetted at the same time. Contrary, in the experiments, the cylinders are wetted at different times.

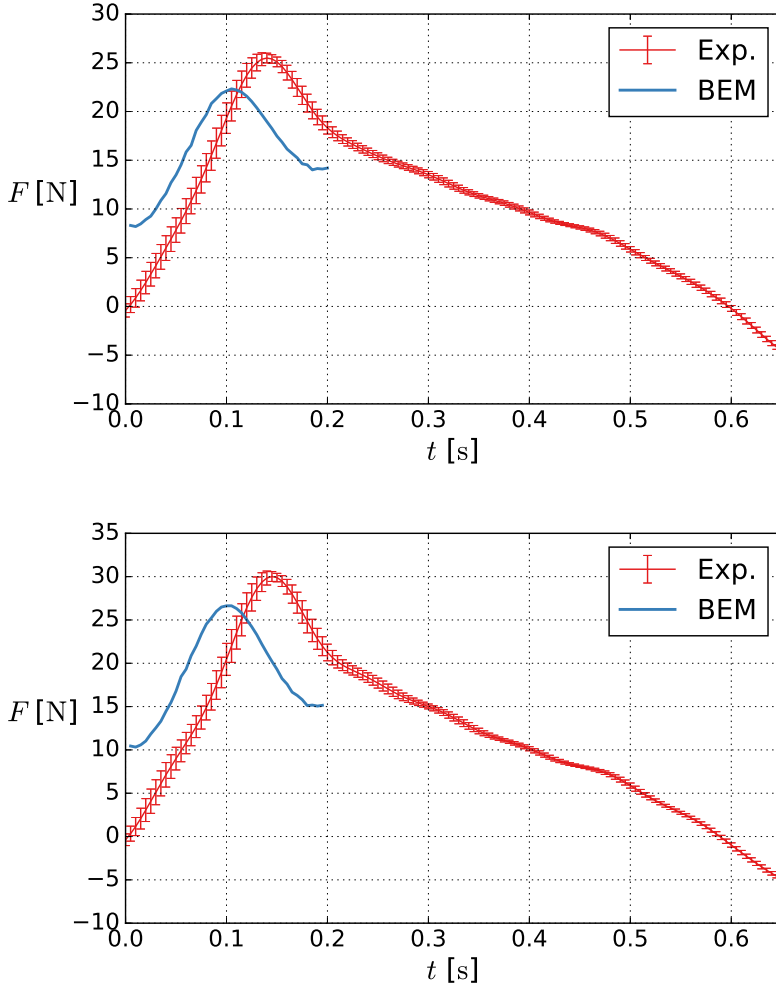


**Figure 7.12:** Force on C19 placed at  $z_m = 0$  from initial water entry of model due to incident wave. Wave parameters  $T = 1.3$  s,  $\zeta_a = 4.1$  cm (top) and  $\zeta_a = 4.6$  cm (bottom). The experimental results are presented in terms of the mean and standard deviation of the measured force for five wave periods.



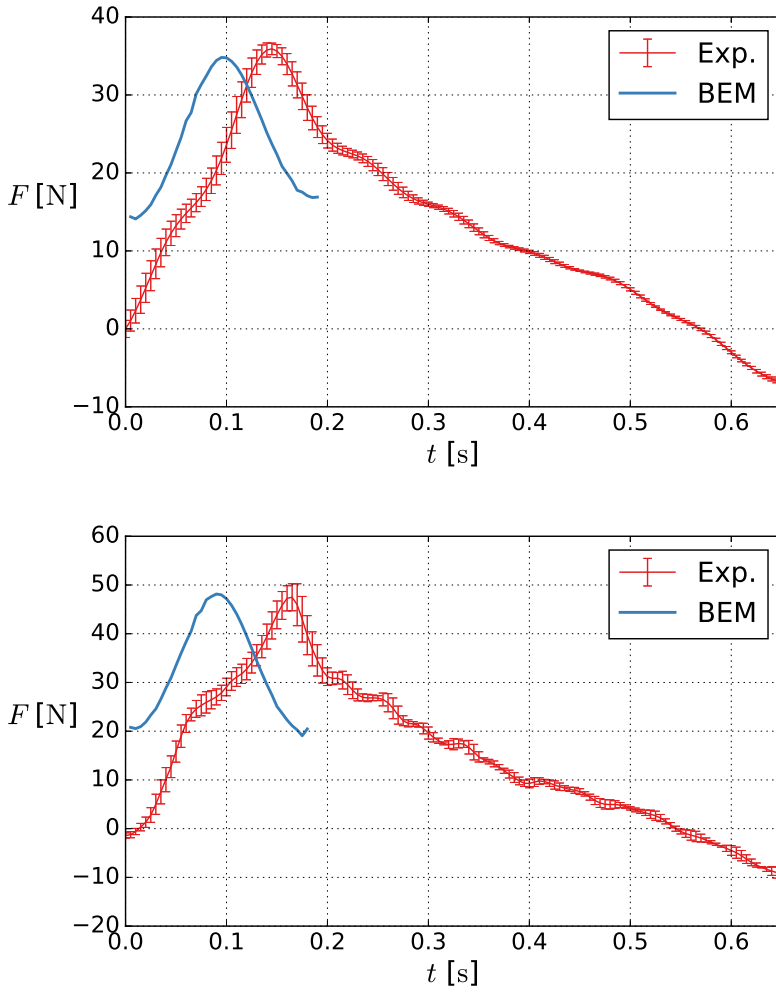


**Figure 7.13:** Force on C19 placed at  $z_m = 0$  from initial water entry of model due to incident wave. Wave parameters  $T = 1.3$  s,  $\zeta_a = 5.4$  cm (top) and  $\zeta_a = 6.5$  cm (bottom). The experimental results are presented in terms of the mean and standard deviation of the measured force for five wave periods.

## 7.2 Fully submerged

In Fig. 7.14, plots of the nondimensional wave amplitude and forces for C19 at  $z_m = -10$  cm (top) and  $z_m = -30$  cm (bottom) are presented. The wave parameters are  $\zeta_a = 5.4$  cm,  $T = 1.3$  s. The bottom subplot is a zoomed-in section of the blue line in Fig. 7.1, but with different scaling of the force.

The band-pass filtered forces including the first, FFT1, and first five, FFT5, harmonics are included in Fig. 7.14. The FFT5 filter seems appropriate for both cases, in particular for  $z_m = -30$  cm. For  $z_m = -10$  cm, the effect of filtering is somewhat reduced, in particular, there is a considerable difference between the force maximum and force minimum. Nevertheless, the first order filter includes a considerable part of the forces; the force magnitudes calculated with the FFT1 filter is 94% ( $z_m = -30$  cm) and 89% ( $z_m = -10$  cm) of the magnitudes of the corresponding FFT5 filtered forces. It may be surprising that the load characteristics are this well captured by the basic harmonics since the wave trough is less than 5 cm from the model when  $z_m = -10$  cm.

The experimental results for all test sets for model positions  $-30 \text{ cm} \leq z_m \leq -10 \text{ cm}$  are presented in the following. The legends for the result figures are presented in Fig. 7.15. Compared to vertical positions close to the mean free-surface, there is less difference between the maximum peak magnitude, the minimum peak magnitude and the amplitude of the band-pass filtered forces, when the models are fully submerged. Therefore, the amplitude of the band-pass filtered forces (FFT1 and FFT5) are used to present the results for the fully submerged positions.

The results are presented in Figs. 7.16 (C19) and 7.17 (S28). Consistent with previous results, the force amplitude is in general larger for C19 than for P28. The normalized force amplitudes increases with increasing KC. Some period dependence is noted, in particular for larger KC numbers and for increasing wave steepnesses. For a given KC number, increasing the wave period—which increases  $\frac{\lambda}{D}$  and  $\frac{\lambda}{2\zeta_a}$ —increases, in general, the normalized force amplitude. The variations in the flow over the plates are larger when  $\frac{\lambda}{D}$  is small, which is a likely explanation. The sensitivity to the vertical position is, in general, small when the depth dependence of the velocity is included in the normalization of the force amplitude. This is in particular true for the longest waves. However, there is a tendency that the normalized force is slightly larger when the distance from the free-surface is increased, given a fixed KC number.

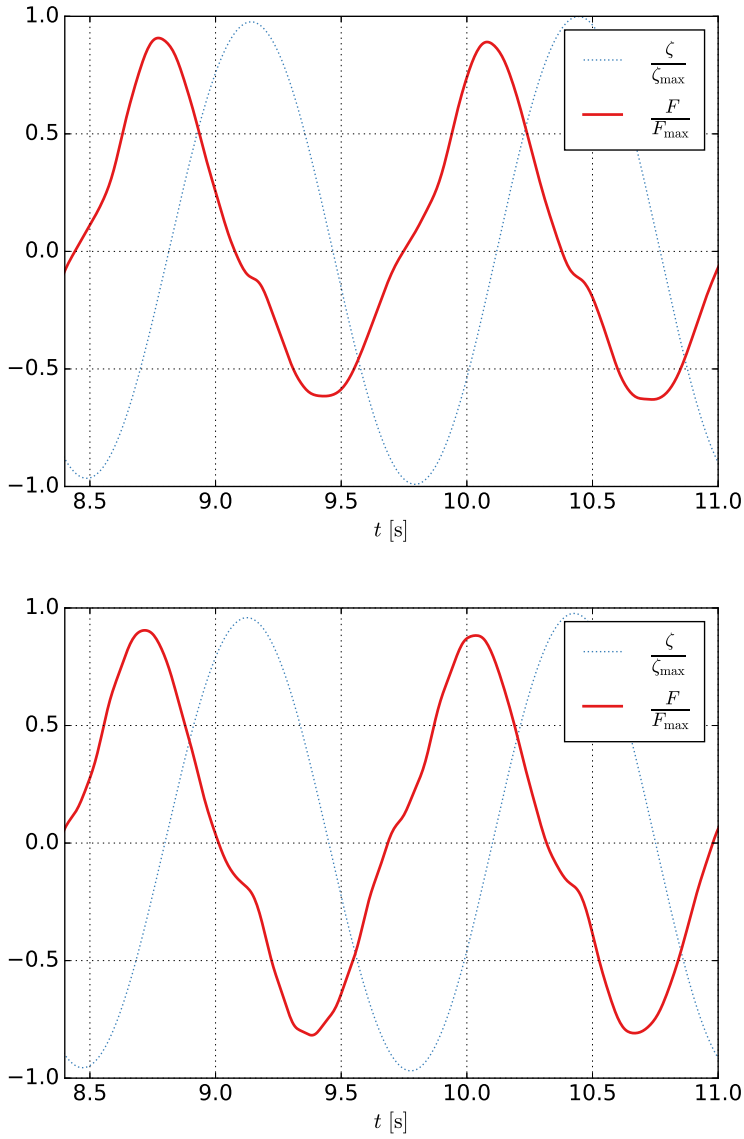


**Figure 7.14:** Nondimensional force and wave elevation (at model center) in test of C19 placed at  $z_m = -10$  cm (top) and  $z_m = -30$  cm (bottom). Wave parameters:  $\zeta_a = 5.4$  cm,  $T = 1.3$  s. The wave elevation and forces are made nondimensional based on the maximum during each set.

	$\frac{z_m}{D} = -0.34, T = 1.0 \text{ s}$		$\frac{z_m}{D} = -0.28, T = 1.0 \text{ s}$
	$\frac{z_m}{D} = -0.34, T = 1.1 \text{ s}$		$\frac{z_m}{D} = -0.28, T = 1.1 \text{ s}$
	$\frac{z_m}{D} = -0.34, T = 1.2 \text{ s}$		$\frac{z_m}{D} = -0.28, T = 1.2 \text{ s}$
	$\frac{z_m}{D} = -0.34, T = 1.3 \text{ s}$		$\frac{z_m}{D} = -0.28, T = 1.3 \text{ s}$
	$\frac{z_m}{D} = -0.50, T = 1.0 \text{ s}$		$\frac{z_m}{D} = -0.42, T = 1.0 \text{ s}$
	$\frac{z_m}{D} = -0.50, T = 1.1 \text{ s}$		$\frac{z_m}{D} = -0.42, T = 1.1 \text{ s}$
	$\frac{z_m}{D} = -0.50, T = 1.2 \text{ s}$		$\frac{z_m}{D} = -0.42, T = 1.2 \text{ s}$
	$\frac{z_m}{D} = -0.50, T = 1.3 \text{ s}$		$\frac{z_m}{D} = -0.42, T = 1.3 \text{ s}$
	$\frac{z_m}{D} = -0.67, T = 1.0 \text{ s}$		$\frac{z_m}{D} = -0.56, T = 1.0 \text{ s}$
	$\frac{z_m}{D} = -0.67, T = 1.1 \text{ s}$		$\frac{z_m}{D} = -0.56, T = 1.1 \text{ s}$
	$\frac{z_m}{D} = -0.67, T = 1.2 \text{ s}$		$\frac{z_m}{D} = -0.56, T = 1.2 \text{ s}$
	$\frac{z_m}{D} = -0.67, T = 1.3 \text{ s}$		$\frac{z_m}{D} = -0.56, T = 1.3 \text{ s}$
	$\frac{z_m}{D} = -0.84, T = 1.0 \text{ s}$		$\frac{z_m}{D} = -0.69, T = 1.0 \text{ s}$
	$\frac{z_m}{D} = -0.84, T = 1.1 \text{ s}$		$\frac{z_m}{D} = -0.69, T = 1.1 \text{ s}$
	$\frac{z_m}{D} = -0.84, T = 1.2 \text{ s}$		$\frac{z_m}{D} = -0.69, T = 1.2 \text{ s}$
	$\frac{z_m}{D} = -0.84, T = 1.3 \text{ s}$		$\frac{z_m}{D} = -0.69, T = 1.3 \text{ s}$
	$\frac{z_m}{D} = -1.01, T = 1.0 \text{ s}$		$\frac{z_m}{D} = -0.83, T = 1.0 \text{ s}$
	$\frac{z_m}{D} = -1.01, T = 1.1 \text{ s}$		$\frac{z_m}{D} = -0.83, T = 1.1 \text{ s}$
	$\frac{z_m}{D} = -1.01, T = 1.2 \text{ s}$		$\frac{z_m}{D} = -0.83, T = 1.2 \text{ s}$
	$\frac{z_m}{D} = -1.01, T = 1.3 \text{ s}$		$\frac{z_m}{D} = -0.83, T = 1.3 \text{ s}$

Figure 7.15: Legends for result figures: C19 (left) and S28 (right).

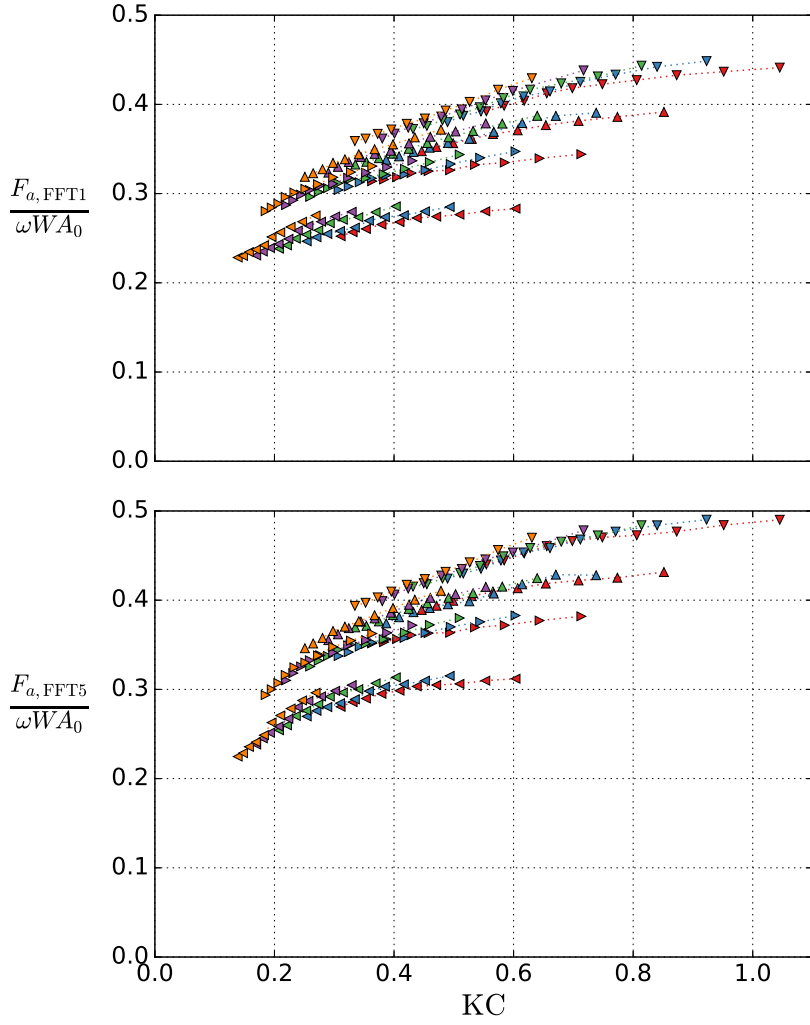


**Figure 7.16:** The normalized force amplitudes on C19 in incident waves for  $-30 \text{ cm} \leq z_m \leq -10 \text{ cm}$ . The results are based on the band-pass filtered force using the first, FFT1, and first five, FFT5, harmonics. Legend in Fig. 7.15.

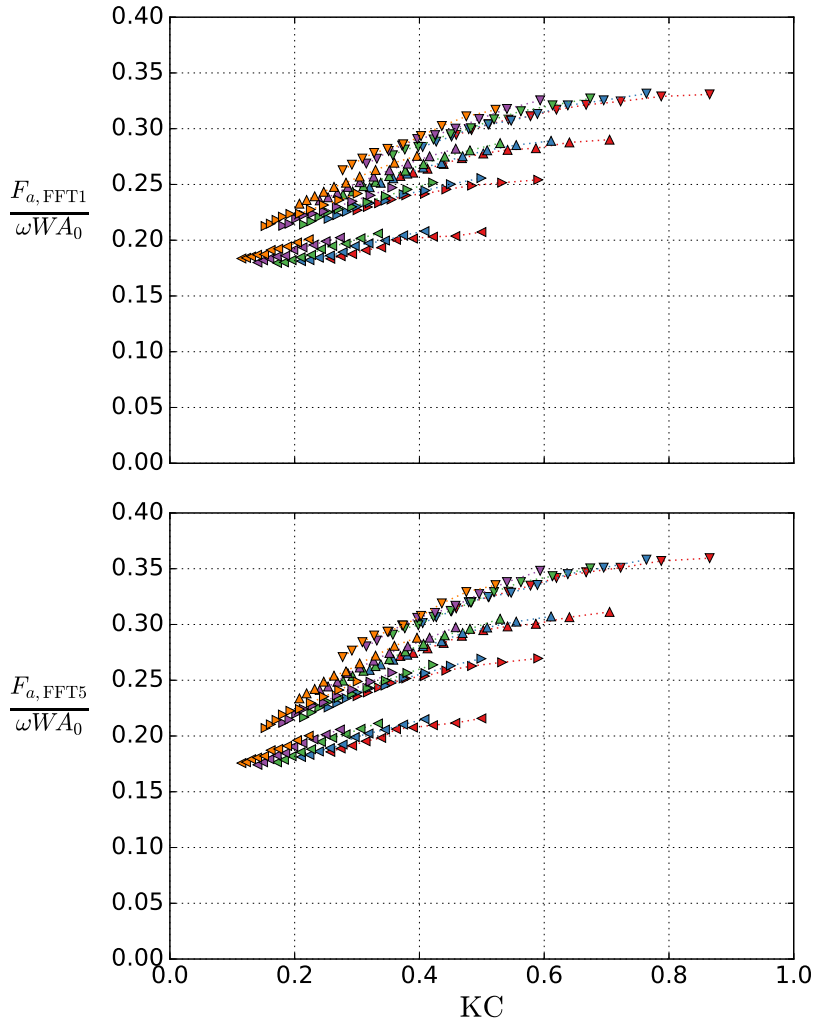


**Figure 7.17:** The normalized force amplitudes on S28 in incident waves for  $-30\text{ cm} \leq z_m \leq -10\text{ cm}$ . The results are based on the band-pass filtered force using the first, FFT1, and first five, FFT5, harmonics. Legend in Fig. 7.15.

### 7.3 Comparing incident waves and forced oscillations

The normalized force amplitudes in experiments of fully submerged models in incident waves, presented in Section 7.2, are compared with the forced oscillation experiments presented in Section 6.2. In the forced oscillation experiments, the normalized force amplitude is based on the obtained added mass and damping coefficients, cf. Fig. 6.12. In order to compare the two methods, the Froude–Krylov contributions are added in the forced oscillation experiments, that is,

$$\frac{F_a}{\omega W A_0} = \sqrt{\left(\frac{A + \rho V}{A_0}\right)^2 + \left(\frac{B}{\omega A_0}\right)^2}. \quad (7.5)$$

Here the amplitude of the vertical velocity component is

$$W = \omega \eta_a = \frac{D}{T} KC. \quad (7.6)$$

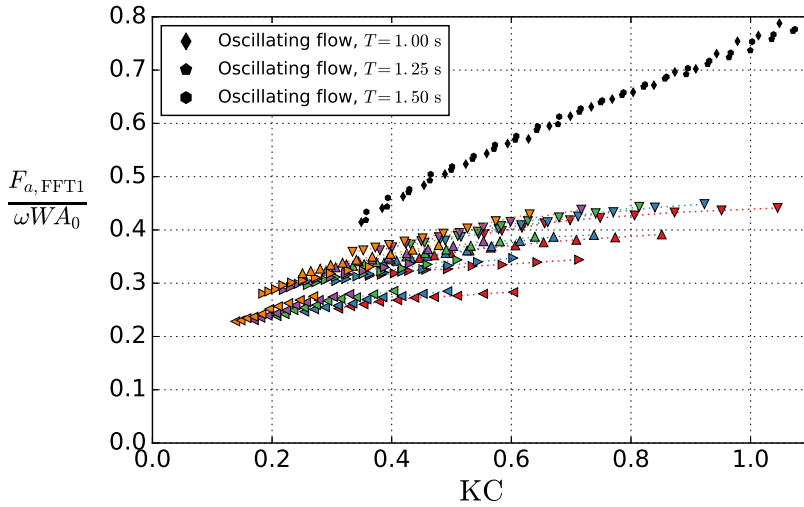


**Figure 7.18:** Experimentally obtained normalized force amplitude for C19. Incident wave results (legend in Fig. 7.15) compared with forced oscillations (black markers).

The normalized force amplitudes are presented in Figs. 7.18 (C19) and 7.19 (S28). The legends for the incident wave results are given in Fig. 7.15. For consistency, the three smallest periods of oscillation, that is,  $T = 1.00$  s,  $T = 1.25$  s and  $T = 1.50$  s, are considered, in order to have similar conditions as the incident wave experiments ( $1.0 \text{ s} \leq T \leq 1.3 \text{ s}$ ). However, note that the dependence on the period of oscillation is small in the forced oscillation experiments, in particular for  $KC < 1.1$  which is presently considered.

The normalized force on the models in incident waves is considerably smaller compared to when the models are forced to oscillate. An exception is for the smallest tested KC numbers in forced oscillations, in which the forces are similar to those experienced in waves. Contrary, for the largest considered KC numbers in incident waves, there is a 60-70% increase in force when the models are forced to oscillate.

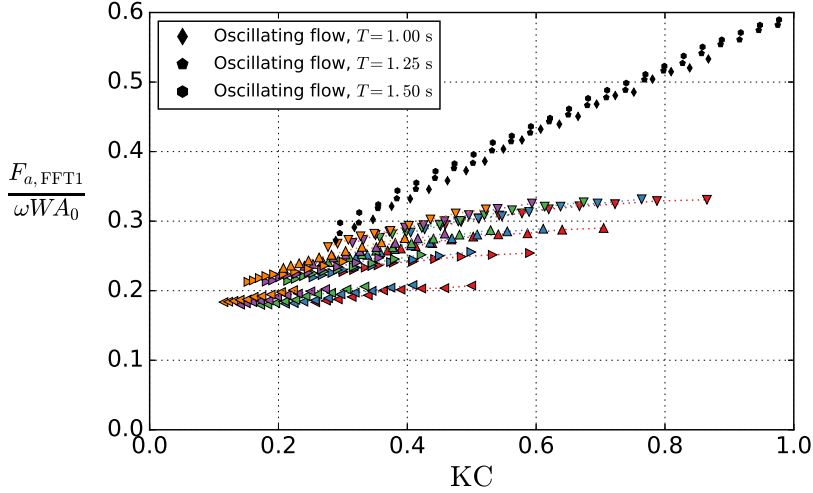


**Figure 7.19:** Experimentally obtained normalized force amplitude for S28. Incident wave results (legend in Fig. 7.15) compared with forced oscillations (black markers).

A possible reason for the large difference in force between incident waves and forced oscillations is the presence of a nonzero horizontal velocity component in waves. In oscillating flow, the interaction between the harmonically oscillating plate and the fluid generates large plate-end vortices on both sides of the plate. Flow visualization with the viscous flow solver reveals that the flow is near symmetric with large similar plate-end vortices on both sides of the plate, cf. Figs. 6.14 and 6.15. In waves, it is likely that the nonzero horizontal velocity component breaks this symmetry; for example that the plate-end vortices are advected away from the plate. Another source of difference is the free surface.

In order to study the effect a nonzero horizontal velocity component has on the force on a perforated plate, orbital flow simulations of S28 are performed. A numerical study using S28 is particularly useful considering the good agreement between the numerical and experimental results, cf. Fig. 6.12. The orbital flow simulations use the same setup as for oscillating flow of S28, the only difference is the boundary conditions, that is, the ambient harmonically oscillating flow has nonzero horizontal component in the orbital flow simulations, cf. Section 5.3.4.



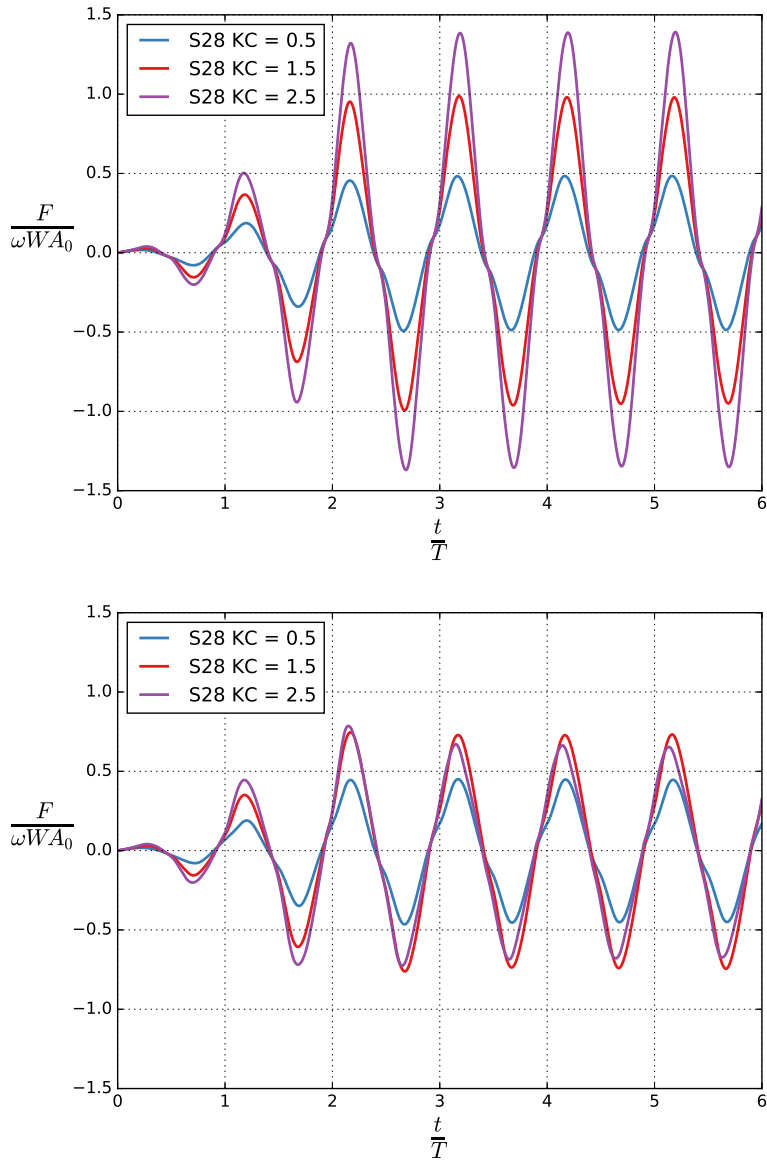


**Figure 7.20:** Normalized force on S28 during the first six oscillation cycles for  $KC = 0.5$ ,  $1.5$  and  $2.5$  from numerical simulations of oscillating (top) and orbital (bottom) flow conditions.

In Fig. 7.20, the normalized vertical force time-series on the S28 plate is presented for three KC numbers,  $KC = 0.5, 1.5$  and  $2.5$ , for oscillating and orbital flow conditions. The normalized force is plotted against time for the first six periods of oscillation, including the ramp. In oscillating flow, the normalized force increases with increasing KC. For  $KC = 0.5$ , the magnitude of the force in orbital flow is similar to that of oscillating flow, whereas for  $KC = 1.5$  and  $KC = 2.5$ , the force is considerably larger in oscillating flow. Note in particular that the normalized force in orbital flow conditions in fact reduces from  $KC = 1.5$  to  $KC = 2.5$ .

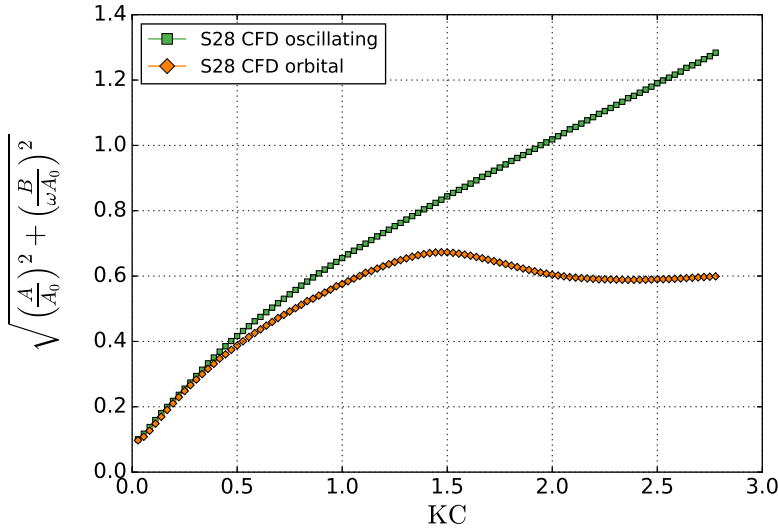


**Figure 7.21:** Normalized force amplitude, i.e., the square root of the sum of the normalized added mass and damping coefficients squared, from numerical simulations of oscillating and orbital flow conditions for S28. The reduction in force in orbital compared to oscillating flow for high KC numbers is due to reduction of both the added mass and the damping.

The normalized force amplitude as function of KC is presented in Fig. 7.21. The results supports the observations of Fig. 7.20. In general, the normalized force amplitude in orbital and oscillating flow is similar for small KC numbers, whereas there is a relative decrease in orbital flow for increasing KC numbers. It is particularly interesting that there is a clear reduction in the normalized force amplitude for  $KC \gtrsim 1.6$ . Note that the KC number is defined based on the amplitude of the vertical velocity in both simulation types. Hence, the normalized force amplitude is smaller, even though the absolute velocities,  $\sqrt{u^2 + w^2}$ , are larger in orbital than in oscillating flow conditions for a given KC number.

Flow visualizations, comparing the orbital and oscillating flow fields, at  $KC = 0.5, 1.5$  and  $2.5$ , are analyzed. Streamline plots are presented in Figs. 7.22–7.24.

The colormap for the contours, cf. Fig. 6.13, represents the vertical velocity. Normalization of the colormap is made against two times the prescribed amplitude of the velocity at the boundaries in the case of  $KC = 2.5$ , that is, the darkest blue ( $-1.0$ ) in Fig. 6.13 corresponds to  $w = -5\frac{D}{T}$  and the darkest red ( $1.0$ ) corresponds to  $w = 5\frac{D}{T}$ . The plots are zoomed in on the plates at a time-instant  $0.26T$  into an oscillation period ( $w = \frac{D}{T}KC\sin\omega t$ ). Hence, at this time-instant, the boundary conditions are approximately equal in oscillating and orbital flow conditions; the vertical velocity is  $w \approx W$ , while the horizontal velocity is  $u \approx 0$  (exactly  $u = 0$  in oscillating flow conditions).

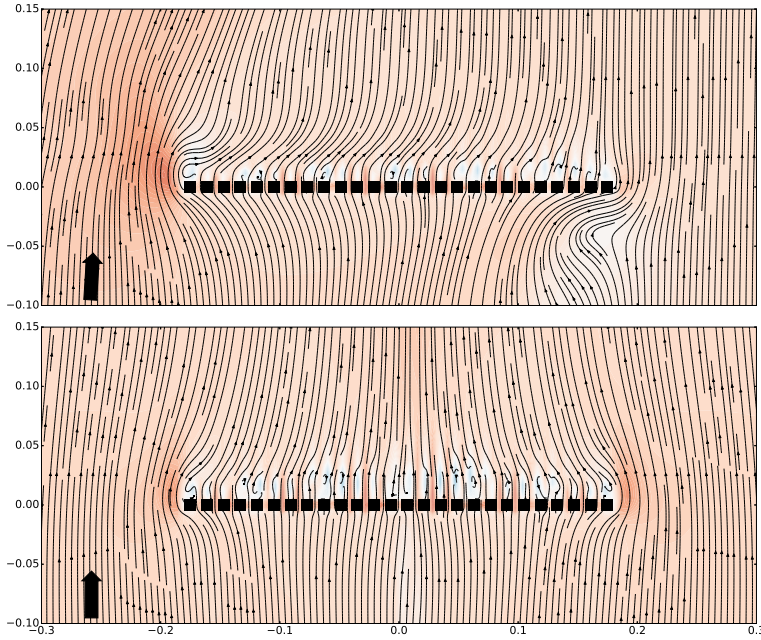


**Figure 7.22:** Streamline plots of S28 with orbital (top) and oscillating (bottom) flow conditions at  $KC = 0.5$ . The time-instant is  $0.26T$  into an oscillation period ( $w = \frac{D}{T}KC\sin\omega t$ , orbital:  $u = -\frac{D}{T}KC\cos\omega t$ , oscillating:  $u = 0$ ). Color contours applied to the vertical velocity (red: positive, blue: negative).

The flow visualizations at  $KC = 0.5$  are presented in Fig. 7.22. The normalized force amplitude is reduced by 7% in orbital compared to oscillating flow conditions at  $KC = 0.5$ . In both orbital and oscillating flow conditions, local wakes downstream of each plate element of the perforated structure are observed. The local wakes are of similar magnitude as the global vortical structures caused by flow separation at the plate-ends.

Corresponding flow visualizations at  $KC = 1.5$  are presented in Fig. 7.23. Here, the normalized force amplitude is 20% less in orbital than in oscillating flow con-

ditions. The importance of the flow separation at the plate-ends, relative to the local flow separation at each plate element, is increased compared to  $KC = 0.5$ . In both flow conditions, there is a significant global wake formation downstream of the left plate-end, but only the oscillating flow has a similar wake downstream of the right plate-end. A reduction in flow velocity is observed upstream of the right plate-end in orbital flow.

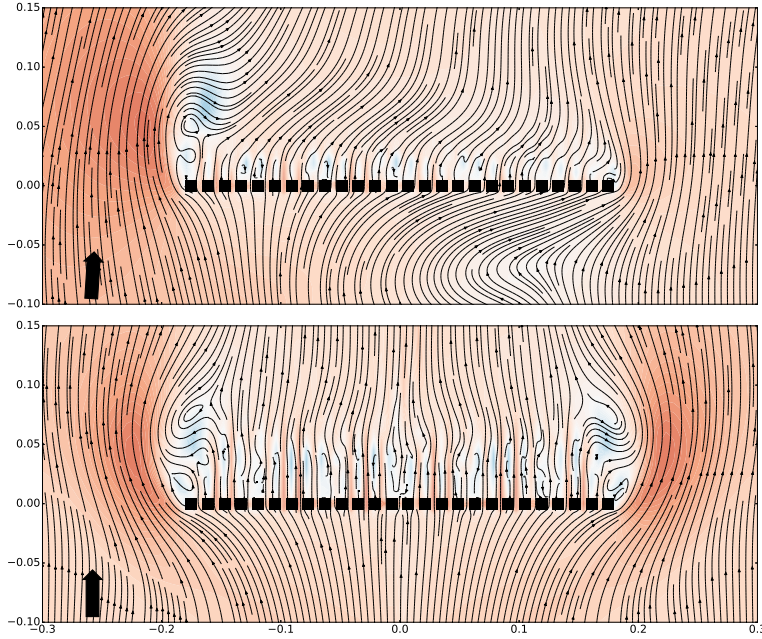


**Figure 7.23:** Streamline plots of S28 with orbital (top) and oscillating (bottom) flow conditions at  $KC = 1.5$ . The time-instant is  $0.26T$  into an oscillation period ( $w = \frac{D}{T}KC \sin \omega t$ , orbital:  $u = -\frac{D}{T}KC \cos \omega t$ , oscillating:  $u = 0$ ). Color contours applied to the vertical velocity (red: positive, blue: negative).

As the  $KC$  number is further increased to  $KC = 2.5$ , Fig. 7.24, the extent of the global vortical structures from the plate-ends is considerably larger than the local vortical structures in the wakes behind each plate element. The reduction in the normalized force amplitude is 50 % in orbital compared to oscillating flow conditions. A large plate-end vortex is observed on the left side only in orbital conditions, whereas a symmetric pattern is seen in oscillating flow. The fact that there is only one vortex rather than two, creating low pressure, might explain the lower force amplitude.

The numerical study of orbital versus oscillating flow explains, to some degree, why the force is smaller in incident waves than in forced oscillations. In particular, the presence of a non-zero horizontal velocity component in the or-

bital flow simulations affects the global flow separation, important for the force on the structure. However, in the incident wave experiments, the force is considerably reduced compared to forced oscillation experiments even for  $KC \approx 0.5$ , whereas in the numerical simulations for corresponding  $KC$  numbers, the normalized force is only slightly reduced in orbital compared to oscillating flow. Possible reasons are free-surface effects and  $\frac{\lambda}{D}$ . The experimental results indicate that both parameters affect the force; the normalized force amplitude reduces with reduced distance to the free-surface and reduced  $\frac{\lambda}{D}$ . Orbital flow represents an idealization of the orbital motion of waves, without free-surface effects. Further, since there are no spatial variations, that is, the ambient flow is equal along the width of the plate, orbital flow conditions can be thought of as a long-wave approximation,  $\frac{\lambda}{D} \rightarrow \infty$ . Consequently, the orbital flow results support the findings from the experimental investigations of incident waves, although there are additional effects that must matter.

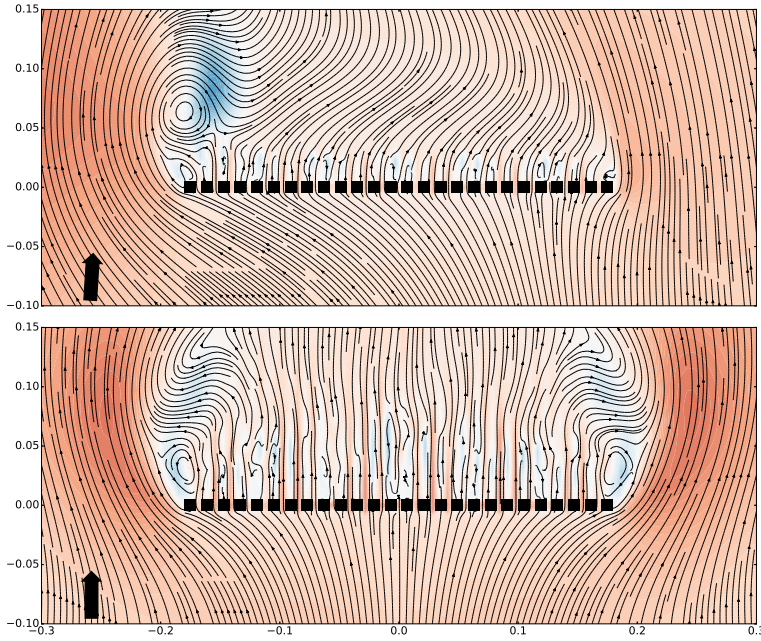


**Figure 7.24:** Streamline plots of S28 with orbital (top) and oscillating (bottom) flow conditions at  $KC = 2.5$ . The time-instant is  $0.26T$  into an oscillation period ( $w = \frac{D}{T} KC \sin \omega t$ , orbital:  $u = -\frac{D}{T} KC \cos \omega t$ , oscillating:  $u = 0$ ). Color contours applied to the vertical velocity (red: positive, blue: negative).

## 7.4 Numerical simulations of incident waves

Numerical simulations of incident waves are performed with the hybrid CFD, that is, the *freeSurface* module of the viscous flow solver, cf. Section 5.1.1, for a simplified model of S28. The simplified model, denoted R28, consists of 11 rectangular cylinders instead of the 26 square cylinders of S28. This difference is due to numerical stability in the simulations, cf. discussion in Section 5.3.5. The fine region grid of R28 is presented in Fig. 7.25.

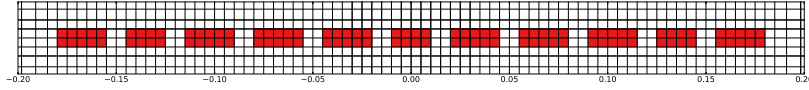


**Figure 7.25:** Fine region grid of R28, a simplified model of S28 consisting of 11 rectangular cross-sections instead of the 26 square cross-sections of S28, cf. Fig 6.10. The perforation ratio of R28 is equal to S28,  $\tau = 0.28$ .

In Fig. 7.26, the hybrid CFD numerical wave tank results of R28 are presented. The CFD includes numerical simulations of R28 at  $z_m = -0.30$  m ( $\frac{z_m}{D} = -0.83$ ) including linearized free-surface conditions, as well as orbital flow simulations of R28. The experimental results with S28 placed at  $z_m = -0.30$  m are included for comparison. There is in general good agreement between the numerical simulations of incident waves and the experiments.

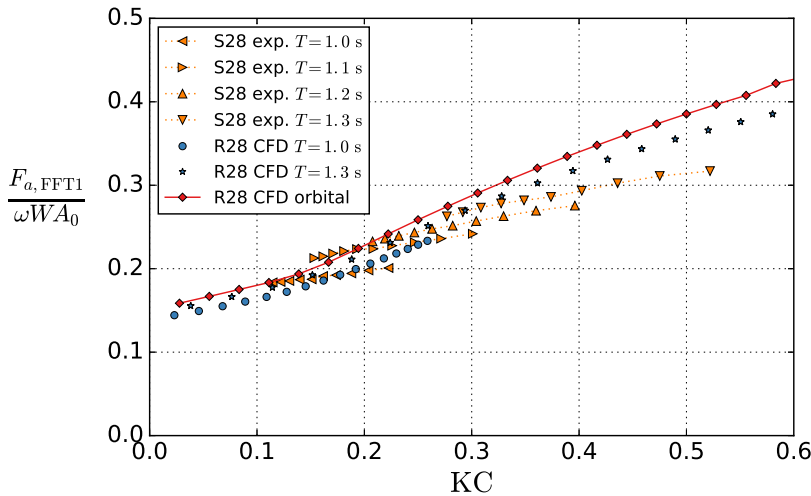


**Figure 7.26:** The normalized force amplitudes in incident waves for  $\frac{z_m}{D} = -0.83$ . Experimental results for S28 compared with numerical simulations of R28. Orbital flow simulations of R28 are included for comparison.

The orbital flow simulations of R28 are included in Fig. 7.26 as well. For  $KC \gtrsim 0.4$ , the force is overpredicted in orbital flow relative to the experiments and CFD with waves. However, for  $KC \lesssim 0.4$ , the force is very similar to that in waves. This is interesting from a practical point of view, since the orbital flow simulations are significantly less cumbersome.

A general trend in the experimental results is that the normalized force amplitude, for a given  $KC$  number, decreases for decreasing wave period. This is found for both experimentally tested model, C19 and S28, cf. Figs. 7.16 and 7.17. Similar tendencies are observed in the incident wave simulations of R28, with  $T = 1.0$  s yielding smaller normalized force amplitudes than  $T = 1.3$  s, for a given  $KC$ .

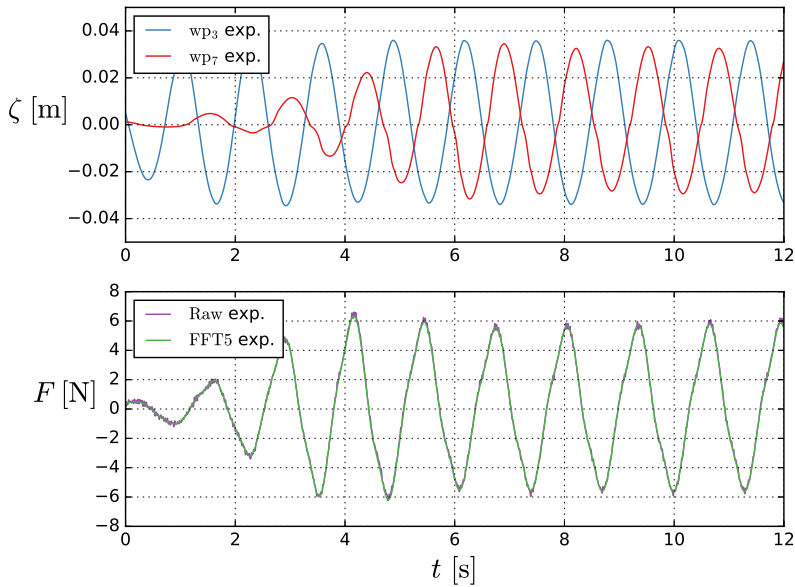


**Figure 7.27:** Examples of time-series extracted from the experimental investigations of S28. The wave elevations 2 m upstream ( $wp_3$ ) and 2 m downstream ( $wp_7$ ) of the model is presented, in addition to the raw and filtered (first five harmonics—FFT5) force.  $T = 1.3$  s,  $KC = 0.29$ .

Examples of time-series extracted from the experiments are presented in Fig. 7.27. The measured wave elevations, 2 m upstream and 2 m downstream of the rig, and the force on the model are presented for the case of S28 placed at  $z_m = -0.3$  m with wave parameters  $T = 1.3$  s and  $\zeta_a = 0.036$  m ( $\frac{\lambda}{H} = 36$ ). In addition to the raw measurements, the force filtered around the first five harmonics (FFT5) is presented. Higher harmonics are observed in the downstream wave measurements.

In Fig. 7.28, the numerical counterpart of the experimental time-series is pre-



sented. Due to the hybrid numerical approach with linear free-surface conditions, the higher harmonics of the wave profiles in the experiments cannot be reproduced in the CFD. Contrary, the force on the plate, which is solved in the Navier–Stokes part of the domain, contains higher harmonics, similar to those in the experiments. Consequently, most of the nonlinearity in the force must be associated with the quadratic pressure jump on the plate. There is generally good agreement between the numerical simulation and the experiment.

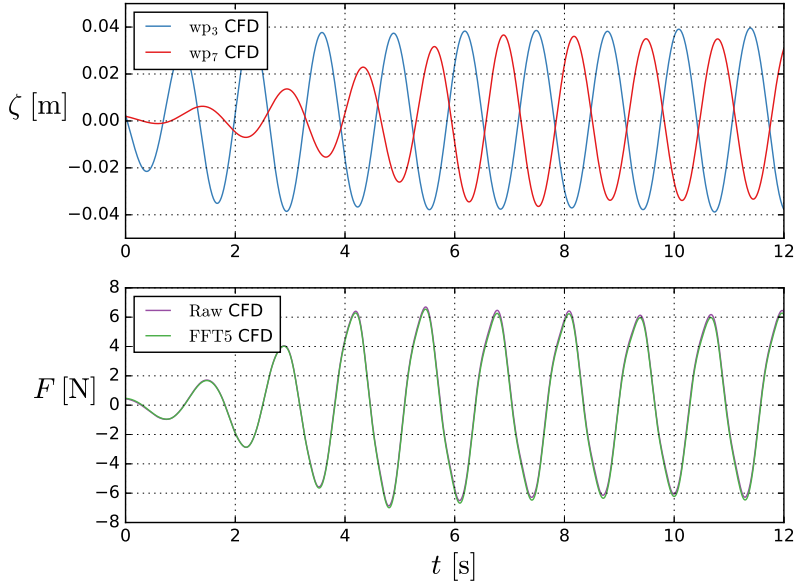


**Figure 7.28:** Examples of time-series extracted from the numerical simulations of S28. The wave elevations 2 m upstream ( $wp_3$ ) and 2 m downstream ( $wp_7$ ) of the model is presented, in addition to the raw and filtered (first five harmonics—FFT5) force.  $T = 1.3$  s,  $KC = 0.29$ .

In addition to the incident wave simulations of R28, two similar models with perforation ratios  $\tau = 0.19$  and  $\tau = 0.36$  are simulated. The models are denoted, respectively, R19 and R36. The fine region grids of R19 and R36 are presented in Fig. 7.29. The fine region grid of R28 is included for comparison. Two wave periods are simulated,  $T = 1.3$  s ( $\frac{\lambda}{D} = 7.21$ ) and  $T = 1.6$  s ( $\frac{\lambda}{D} = 10.4$ ). By simulating longer waves, larger  $KC$  numbers are obtained.

The normalized force amplitudes from the incident wave simulations are compared with corresponding orbital flow simulations in Fig. 7.30. Similar to previous results, the force increases with decreasing perforation ratio. The orbital flow simulations yield results that are similar to the incident wave simulations, in particular for R36. In general, the accordance is better when the waves are long and



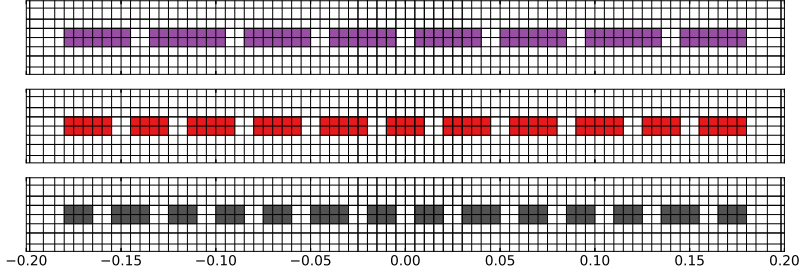


**Figure 7.29:** Fine region grid of R19 (top), R28 (middle) and R36 (bottom).

when the perforation ratio is high. A denser perforated plate means stronger fluid-structure interaction; more flow must circumvent the plate, the global plate-end flow separation and the local flow-separation through the perforated openings are stronger. Thus, a larger pressure difference over the plate as consequence, which potentially interacts more with the free surface. Consequently, the flow is more likely to interfere with the free-surface for decreasing perforation ratio in incident waves, whereas in orbital flow, the flow conditions are forced on all boundaries.

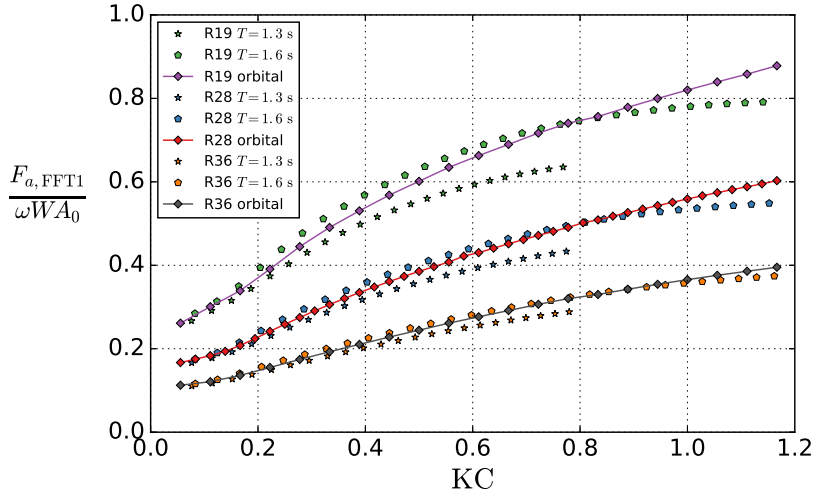


**Figure 7.30:** The normalized force amplitudes in simulations of incident waves and orbital flow of R19, R28 and R36. The submergence is  $z_m = -30$  cm, that is,  $\frac{z_m}{D} = -0.83$ .

## Chapter 8

# A semi-analytical method for forces on perforated plates

A simple method for calculating the hydrodynamic force of perforated plates in oscillating flow is presented in this chapter. The method is based on curve-fitting the results of a large numerical study, on the effect of perforation ratio and KC number on the hydrodynamic coefficients of perforated plates, to expressions similar to those by Graham for solid plates [22]. In Section 8.1, a summary of the analytical method by Graham is given. Graham's analysis is for small KC numbers. The applicability of the method for higher KC numbers is discussed. Comparisons are made with present numerical and experimental results. Details and results of the numerical study is presented in Section 8.2. In Section 8.3, the numerical study is compared with calculations using the semi-analytical method by Molin. The expressions and details of the new curve-fits are then given in Section 8.4. The method is based on a two-dimensional analysis using two-dimensional results. In Section 8.5, the hydrodynamic forces estimated by the obtained expressions are compared with previous three-dimensional experiments.

### 8.1 Graham's plate in oscillating flow

In his analysis of the hydrodynamic forces on sharp-edged objects at low KC numbers [22], Graham presents the following relations for the hydrodynamic force on a solid flat plate in oscillating flow,

$$F = \frac{\pi}{4} \rho C_M D^2 \ddot{\eta} + \frac{1}{2} \rho C_D D \dot{\eta} |\dot{\eta}|, \quad C_M = a_0 + a_1 KC^{\frac{2}{3}}, \quad C_D = b_1 KC^{-\frac{1}{3}}. \quad (8.1)$$

The theoretical analysis yielded  $a_1 = 0.25$  and  $b_1 = 11.8$ . For a solid flat plate,  $a_0 = 1$ . Equation (8.1) can be expressed accordingly to Eq. (2.8), that is, with an added mass coefficient and a linear damping coefficient. Since the plate considered by Graham is flat, the inertia term yields  $\frac{A}{A_0} = C_M$ ,

$$\frac{A}{A_0} = a_0 + a_1 KC^{\frac{2}{3}}. \quad (8.2)$$

The motions are oscillating harmonically. Consequently, the quadratic damping term yields the following equivalent linearized damping coefficient,

$$\frac{B}{\omega A_0} = \frac{b_1}{\pi^2} KC^{\frac{2}{3}}. \quad (8.3)$$

Graham's method was compared with experimental results by Singh [60], which yielded somewhat smaller coefficients,  $a_1 = 0.2$  and  $b_1 = 8.0$  [22]. Note that this curve-fit was based on a limited amount of experimentally tested KC numbers, and that the results by Singh do not agree with results for flat plates by Keulegan and Carpenter [38]. According to Singh, the reason for the discrepancies is likely due to differences in experimental setup and geometry of the plates [60]. Contrary to the results by Singh, the results by Keulegan and Carpenter show that the added mass coefficient increases with increasing KC numbers up to a local maximum of  $C_M \approx 2.5$  for  $KC \approx 7$ . Assuming that the plate by Keulegan and Carpenter was thin, such that  $C_M \approx \frac{A}{A_0}$ , the coefficient in the added mass expression would need to be  $a_1 = 0.41$  in order to have  $C_M = 2.5$  at  $KC = 7$ . However, the analysis by Graham is applicable for small KC numbers; when  $KC = 7$ , the amplitude of motion is larger than the plate width, hence, this is not a small KC number for a flat plate.

In order to analyze the applicability of the method by Graham, simulations and experiments of flat plates are compared to the analytical expressions. Graham states that his analysis yields force expressions that are applicable for small KC. For practical purposes, it is important to assess how small KC must be in order to get acceptable force estimates with the method.

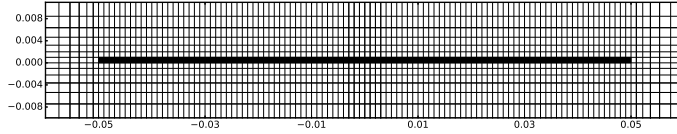


**Figure 8.1:** Fine region of grid used to simulated a solid plate in oscillating flow.

A solid flat plate has been simulated with the viscous flow solver and compared with the analytical results by Graham [22]. A plot of the fine region of the grid close to the plate is presented in Fig. 8.1. The simulated plate is  $D = 100 \text{ mm} \times t = 1 \text{ mm}$ , that is  $\frac{D}{t} = 100$ . A constant grid cell size of  $\Delta x = \Delta z = 1 \text{ mm}$  is used in the fine grid region close to the plate, which is defined to be  $102 \text{ mm} \times 3 \text{ mm}$ . The grid is then stretched with a stretching parameter 20% until the maximum grid cell size of  $\Delta x_{\max} = \Delta z_{\max} = 50 \text{ mm}$  is reached. The total domain size is  $2 \text{ m} \times 2 \text{ m}$  and the total number of grid cells is 13 298.

In addition to the comparison with the analytical method by Graham, I have included results from present experimental investigations of two solid plates<sup>1</sup>. This

<sup>1</sup>Special thanks go to Frøydis Solaas and Mia Abrahamsen-Prsic who led the experimental study.

experimental study was conducted in a collaboration project within CRI MOVE. We presented the results at the International Conference on Offshore Mechanics and Arctic Engineering (OMAE) in 2019 [62].



**Figure 8.2:** Side and top view of the experimentally tested plate. The plate is  $D = 60$  mm wide,  $t = 4$  mm thick ( $\frac{D}{t} = 15$ ) and has a lateral length of  $L = 570$  mm. Photo by Frøydis Solaas.

In the experiments, solid plate elements of width  $D = 60$  mm are installed in the rig and forced to oscillate. A photo of the plate elements is presented in Fig. 8.2. To ensure sufficient stiffness, the plate elements are  $t = 4$  mm thick and made from steel. An estimate of the maximum deflection is obtained from elementary beam theory for static loads [63], assuming quasi-static behavior of the plate, i.e., the oscillation period is far from the wet natural period of the plate. For a fixed beam of width  $D$  and length  $L$ , subjected to a uniformly distributed force  $F$ , the maximum deflection is

$$\delta z_{\max} = \frac{1}{384} \frac{FL^3}{EI}. \quad (8.4)$$

Here  $E = 2 \times 10^{11}$  Pa is the Young modulus of steel and  $I = \frac{1}{12} t^3 D$  is the moment of inertia. Thus, for the tested plate element,  $EI = 64 \text{ Nm}^2$  and

$$\delta z_{\max} = 7.5 \times 10^{-6} \text{ mN}^{-1} F. \quad (8.5)$$

The force depends on the tested KC number and period of oscillation,  $T$ . The maximum force during the experiments of a single plate element is approximately  $F = 40$  N. Consequently,  $\delta z_{\max} = 0.3$  mm. Equation (8.4) is a theoretical estimate based on a fixed beam. A more conservative approach is to assume that the beam is allowed to rotate at the ends. The maximum deflection is then five times the estimate of Eq. (8.4), that is,  $\delta z_{\max} = 1.5$  mm. The present arrangement is between these two configurations, cf. Fig. 8.2. Furthermore, the time-series of force and acceleration were investigated; we did not find signs of plate vibrations. We concluded from this that the stiffness of the plate elements is satisfactory.

Two solid plate configurations are experimentally investigated. In the first, a single plate element is forced to oscillate, hence  $\frac{D}{t} = 15$ . In the second, two plate elements are placed next to each other without any gap in between, acting as

a single solid plate of  $\frac{D}{\tau} = 30$ . The experiments are performed similarly to the other forced oscillation experiments in the thesis, cf. Chapter 3. An exception is for  $\frac{D}{\tau} = 30$  in which only one period of oscillation,  $T = 2.00$  s, is tested. For more details on these experiments, I refer to the cited conference paper [62].

The results are presented in Fig. 8.3. Clearly, the assumption of small KC numbers in Graham's method is important for the added mass coefficient. The numerical results agree well with the theory by Graham for  $KC < 3$ . For larger KC numbers, the theory by Graham underpredicts the added mass coefficient compared to the numerical results. Curve-fitting to the expressions of Eqs. (8.2) and (8.3) yields  $a_1 = 0.228$  and  $b_1 = 10.41$ , when considering the viscous flow solver results for  $KC \leq 3$ . Note that due to the finite thickness of the numerically simulated plate, the limiting added mass coefficient for  $KC \rightarrow 0$  is slightly larger than 1.

As discussed for the experimental results by Keulegan and Carpenter, the value of  $a_1$  in Eq. (8.2) depends on the range of KC numbers considered. The coefficients  $a_1$  and  $b_1$ , in Eqs. (8.2) and (8.3), for different ranges of KC numbers lower than a given  $KC_{\max}$ , are presented in Tables 8.1 and 8.2. In these curve-fits, the potential flow added mass, calculated with the present potential flow solver, is used to find  $a_0$ , in order to reduce the effect of difference in  $\frac{D}{\tau}$ . The potential flow solver added mass coefficients are  $a_0 = 1.026$  ( $\frac{D}{\tau} = 100$ ),  $a_0 = 1.066$  ( $\frac{D}{\tau} = 30$ ) and  $a_0 = 1.107$  ( $\frac{D}{\tau} = 15$ ). If the KC range is limited to the smallest KC numbers, Graham's analytical  $a_1 = 0.25$  is close to the present experimental and numerical results.

**Table 8.1:** Graham's flat plate: Curve-fitted  $a_1$  from CFD and experimental results for varying KC number ranges up to a given  $KC_{\max}$ . Graham's analytical result for low-KC:  $a_1 = 0.25$ .

KC <sub>max</sub>	CFD $\frac{D}{\tau} = 100$	Exp. $\frac{D}{\tau} = 30$	Exp. $\frac{D}{\tau} = 15, T = 2.00$ s
1.0	0.211	0.196	-
1.5	0.209	0.220	-
2.0	0.211	0.243	0.187
2.5	0.215	0.279	0.225
3.0	0.228	0.328	0.276
3.5	0.256	0.373	0.330
4.0	0.313	0.404	0.373
4.5	0.351	0.436	0.394
5.0	0.384	0.459	0.415

The experimental results agree, in general, well with the numerical results for  $KC < 5$ . Some differences should be expected due to the differences in  $\frac{D}{\tau}$ . In the experiments, the bottom wall of the tank and the free surface may also influence the coefficients, although  $\frac{D}{h} = \frac{0.06\text{m}}{1.0\text{m}} = 0.06$  ( $\frac{D}{\tau} = 15$ ) and  $\frac{D}{h} = \frac{0.12\text{m}}{1.0\text{m}} = 0.12$  ( $\frac{D}{\tau} = 30$ ). The plates are installed in the rig with equal distance to the free surface and the bottom wall of the tank, i.e., the distance is half the water depth,  $0.5h$ . For  $KC > 5$ , the experimentally obtained added mass coefficient decreases

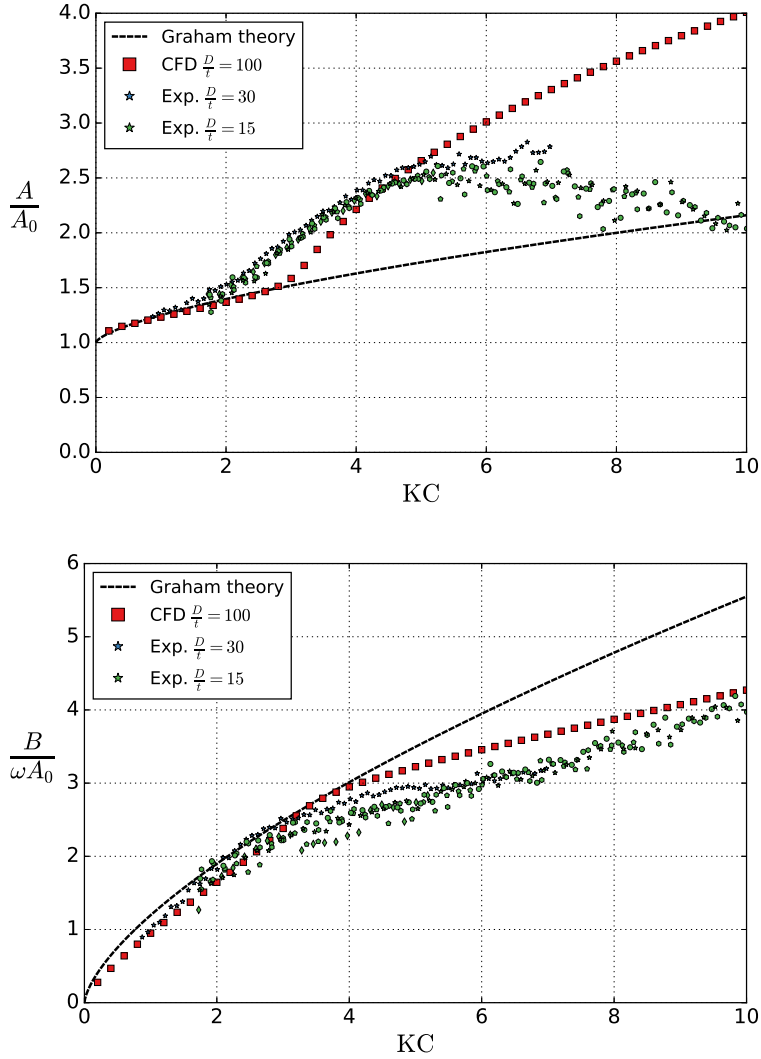


**Figure 8.3:** Added mass and damping coefficients of a solid plate in oscillating flow. Comparison between the analysis by Graham [22] using Eqs. (8.2) and (8.3) and present numerical and experimental results. Five periods of oscillation are tested for  $\frac{D}{t} = 15$ , cf. Fig. 6.5.

with increasing KC. Contrary, the numerically obtained added mass coefficient continues to increase.

The damping coefficient is less sensitive to the applied range of KC numbers. All considered KC ranges yield somewhat smaller  $b_1$  than what was analytically found by Graham. However, the present experimentally and numerically obtained  $b_1$  coefficients are considerably larger than the experiments result by Singh,  $b_1 = 8.0$ . Note that the KC number range for which this was based on, was quite modest.

**Table 8.2:** Graham's flat plate: Curve-fitted  $b_1$  from CFD and experimental results for varying KC number ranges up to a given  $KC_{\max}$ . Graham's analytical result for low-KC:  $b_1 = 11.8$ .

$KC_{\max}$	CFD $\frac{D}{t} = 100$	Exp. $\frac{D}{t} = 30$	Exp. $\frac{D}{t} = 15, T = 2.00\text{ s}$
1.0	9.07	9.73	-
1.5	9.38	10.26	-
2.0	9.76	10.82	10.47
2.5	10.00	11.29	10.42
3.0	10.41	11.54	10.52
3.5	10.72	11.49	10.47
4.0	11.01	11.35	10.26
4.5	11.07	11.16	10.15
5.0	11.07	10.94	10.01

Based on the present results, the method by Graham seems appropriate for predicting the hydrodynamic coefficients of solid plates in oscillating flow for  $KC < 3$ . For  $KC > 3$ , the added mass coefficient is, in general, underestimated with Graham's method compared to the present viscous flow solver and experimental results. This is consistent with previous experimental results by Keulegan and Carpenter [38]. Interaction between the two plate-end vortices is expected for the higher KC numbers. As a consequence, one of the vortices grows larger and quicker than the other, hence, Singh [60] refers to  $4 < KC < 7$  as the asymmetric region. For even higher KC numbers, "very strong vortices, sometime occupying the width of the plate, are formed" [60].

The hydrodynamic force on a solid plate is dominated by damping for higher KC numbers ( $KC \gtrsim 2$ ), cf.  $y$ -axes in Fig. 8.3. All considered results—numerical, experimental and analytical—agree on this. Graham's analytical method predicts the intersection between the damping and added mass as

$$\frac{B}{\omega A} = \frac{\frac{b_1}{\pi^2} KC^{\frac{2}{3}}}{a_0 + a_1 KC^{\frac{2}{3}}} = 1 \quad \rightarrow KC = 1.1. \quad (8.6)$$

Consequently, even though the added mass coefficient from Graham's method is not accurate for  $KC > 3$ , the predicted normalized force amplitude can be acceptable since the force is dominated by damping. The normalized force amplitude is

presented in Fig. 8.4. The analysis by Graham gives similar force as the experimental and numerical results for  $KC < 5$ . For higher  $KC$  numbers, the analytical and numerical force estimates are similar; both methods overestimate the results of the experiments.

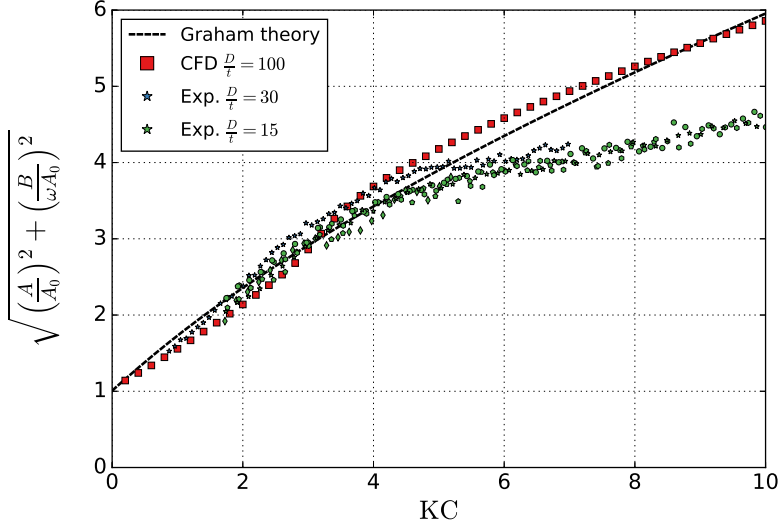


**Figure 8.4:** Normalized force amplitude of a solid plate in oscillating flow. Comparison between the analysis by Graham [22] using Eqs. (8.2) and (8.3) and present numerical and experimental results. Five periods of oscillation are tested for  $\frac{D}{T} = 15$ , cf. Fig. 6.5.

The comparison of experimental and numerical results suggests that the accuracy of the viscous flow solver is limited for high  $KC$  numbers. The viscous flow solver is a fully two-dimensional code of DNS type. No turbulence modeling is included. 3D effects and correlation length may matter, but they are not investigated further. As the flow velocity increases, these simplifications are less appropriate, cf. the discussion in Section 6.3.4. Nevertheless, the range of  $KC$  numbers that are relevant for subsea lifting operations is limited. Within a more limited (and relevant)  $KC$  range, the present investigations suggest that the viscous flow solver—as well as the analytical method by Graham for solid plates—are efficient and useful tools.



## 8.2 Numerical study on the perforation effect

A large numerical study on the effect of the perforation ratio and KC number on the force coefficients of perforated plates, in oscillating flow, is performed. The study is based on numerical simulations with the presently implemented viscous flow solver. Ten perforation ratios, from  $\tau = 0.05$  to  $\tau = 0.50$  in steps of  $\tau = 0.05$ , are simulated. Additionally, corresponding solid plates ( $\tau = 0$ ) are simulated. The simulations are performed for oscillation amplitudes corresponding to  $0.002 \leq KC \leq 2.2$ . These ranges of  $\tau$  and KC cover typical conditions for perforated plate structures used in marine operations.

**Table 8.3:** Discretization of plate models I and II. Plate width ( $D$ ), width-to-thickness ( $\frac{D}{t}$ ), width-to-hole-size ( $\frac{D}{l_h}$ ), width-to-cell size in the fine grid region close to the plate ( $\frac{D}{\Delta}$ ), domain size to plate width ( $\frac{l}{D}$ ), and total number of grid cells in the domain.

Model	$D$	$\frac{D}{t}$	$\frac{D}{l_h}$	$\frac{D}{\Delta}$	$\frac{l}{D}$	Cell count
I	0.42 m	140	140	280	14.3	74 268
II	0.36 m	120	80	240	16.7	67 860

Two different numerical perforated plate models, I and II, with different numerical grids, widths and number of fluid cells in the openings, are tested for each perforation ratio, in order to increase the confidence in the results, and to investigate the numerical uncertainty of different modeling of the same plate perforation. Details of plate models I and II are given in Table 8.3. The numerical modeling is similar to that of the perforated plates that were thoroughly investigated and validated against dedicated experiments in Chapter 6. Illustrations of the plate element setup are presented in Figs. 8.5 and 8.6.

Examples of flow fields are provided in Figs. 8.7 and 8.8. Here, streamline plots for simulations with plate model I at  $KC = 0.95$  are provided for  $\tau = 0$  (top),  $\tau = 0.20$  (middle) and  $\tau = 0.40$  (bottom). The red-blue colormap presented in Fig. 6.13 is used to indicate the vertical velocity. Normalization of the colormap is made against three times the prescribed amplitude of the velocity at the boundaries, that is, the darkest blue ( $-1.0$  in Fig. 6.13) corresponds to  $w = -3\frac{D}{l}KC$  and the darkest red ( $1.0$  in Fig. 6.13) corresponds to  $w = 3\frac{D}{l}KC$ . The plots are zoomed in on the plates at a time-instant 41 % into an oscillation period; the velocity at the boundaries is set to  $w = \frac{D}{l}KC \sin \omega t$ . Note that the flow is globally deflected towards the sides of the plate even for high perforation ratios, similar to that for a solid plate. Vortices due to plate-end flow separation are easily observed for  $\tau = 0.20$ . Figure 8.8 presents a closer view of the perforated plates presented in Fig. 8.7, with streamline representations zoomed in on the right end of the plates. The closer view reveals vortical structures behind each plate element at the scale of the plate element lengths for all perforation ratios.

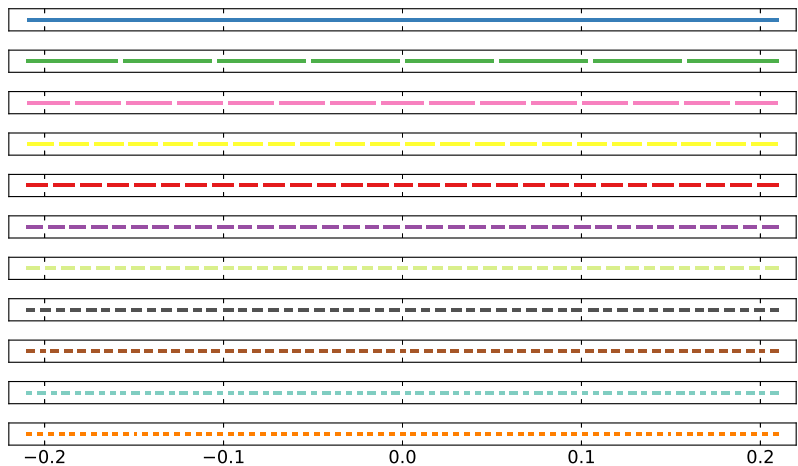


Figure 8.5: Plate models type I.

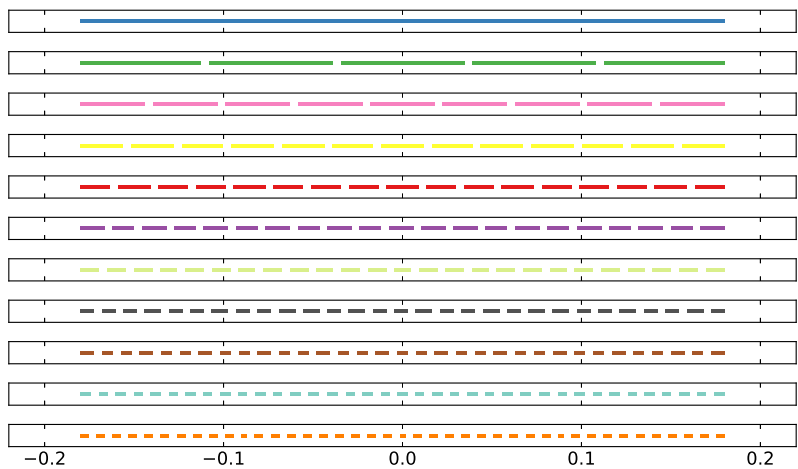
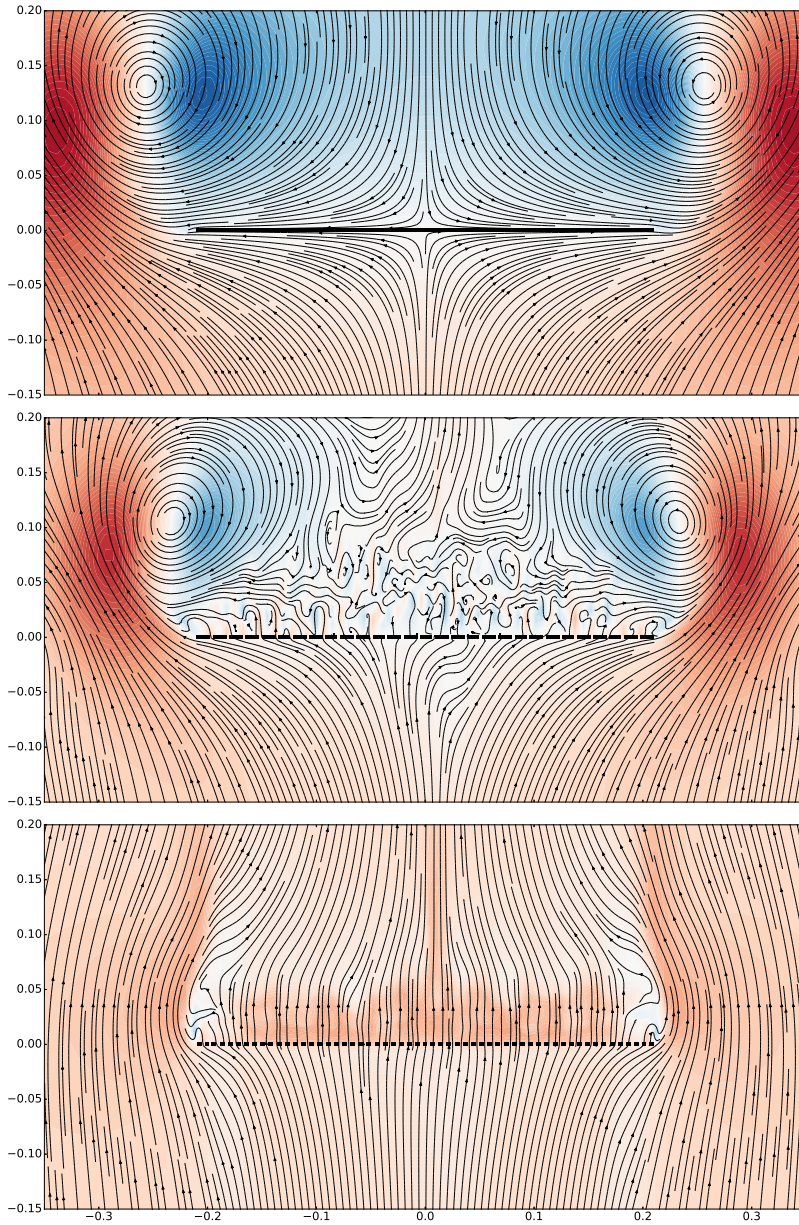
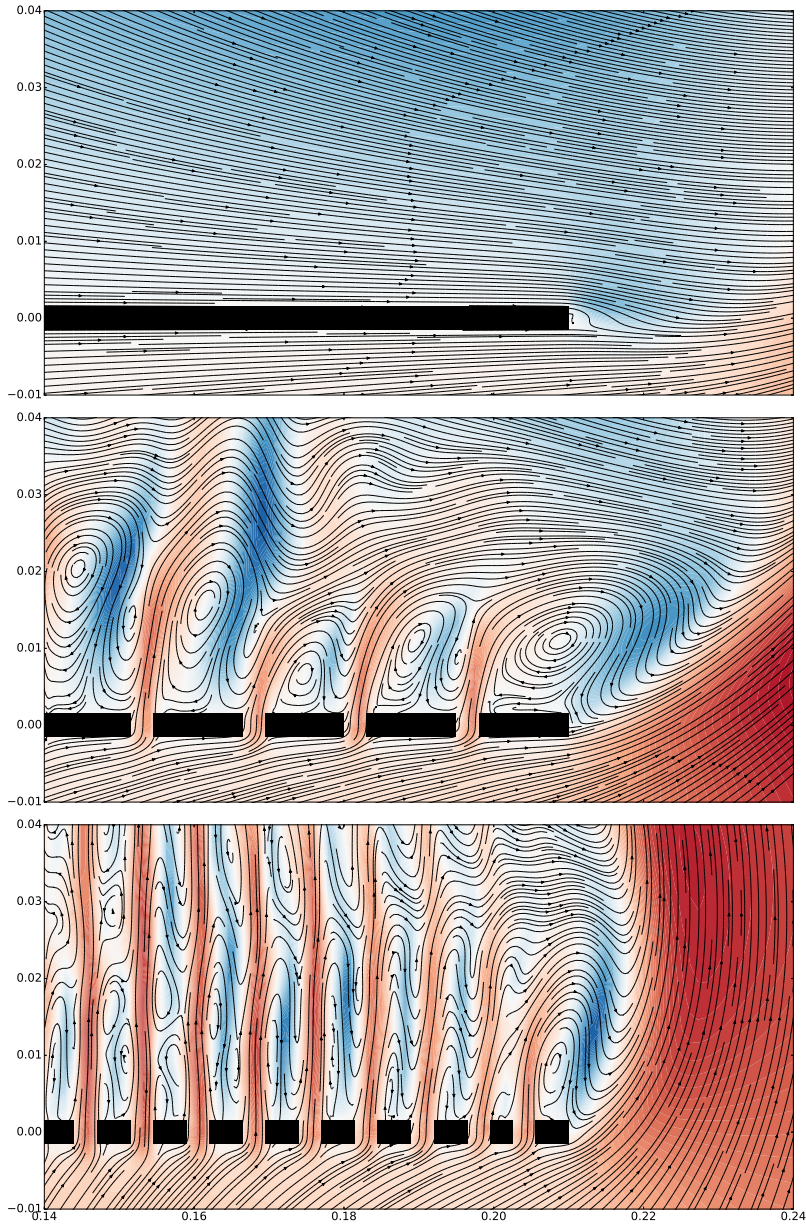


Figure 8.6: Plate models type II.



**Figure 8.7:** Streamlines for  $\tau = 0$  (top),  $\tau = 0.20$  (middle) and  $\tau = 0.40$  (bottom) at  $KC = 0.95$ . Color contours applied to the vertical velocity (red: positive, blue: negative).



**Figure 8.8:** Streamlines zoomed in on the upper right plate-ends of  $\tau = 0$  (top),  $\tau = 0.20$  (middle) and  $\tau = 0.40$  (bottom) at  $KC = 0.95$ . Color contours applied to the vertical velocity (red: positive, blue: negative).

Added mass and damping coefficients obtained in the numerical simulations are presented in Figs. 8.9 and 8.10. There are small differences between the results of plate models I and II. The added mass clearly increases with decreasing perforation ratio. The largest rate of absolute changes in  $A$  appear for  $\tau \lesssim 0.20$ . For the damping,  $B$ , there is a more steady rate of absolute change with decreasing perforation ratio. Notably,  $\tau = 0.05$ ,  $\tau = 0.10$ ,  $\tau = 0.15$  and  $\tau = 0.20$  all yield larger damping coefficients than the solid plate for a range of low KC numbers. For increasing KC, the damping coefficients are largest for the solid plates. The perforated plates yield larger damping than the solid plates for  $KC < 0.36$  ( $\tau = 0.20$ ),  $KC < 0.69$  ( $\tau = 0.15$ ),  $KC < 0.97$  ( $\tau = 0.10$ ) and  $KC < 1.31$  ( $\tau = 0.05$ ). The fact that the damping at small KC numbers can be larger for dense perforated plates than for corresponding solid plates, is consistent with previous studies [16, 23, 25], cf. Section 1.4.5.

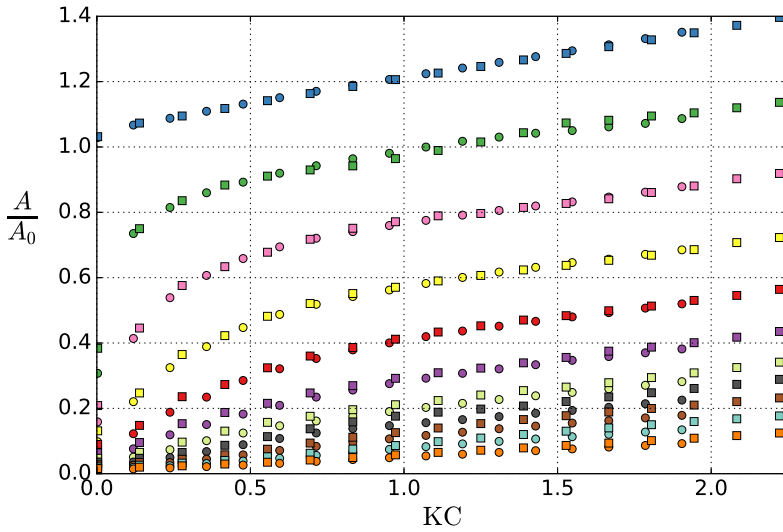


**Figure 8.9:** Added mass coefficients for numerically simulated perforated plates. Circular markers: Model I. Square markers: Model II.

The ratio between the damping force and added mass force is presented in Fig. 8.11. For practical values of the KC number, perforation ratios larger than  $\tau = 0.10$  are found to be damping dominant. Even the densest perforated plate,  $\tau = 0.05$ , is damping dominant for  $KC > 0.95$ . The flat solid plate is damping dominant for  $KC \geq 1.43$ .

The normalized force amplitude is presented in Fig. 8.12. The hydrodynamic force amplitude increases with decreasing perforation ratio and increasing KC number. Due to the importance of the damping force, the results are similar to the

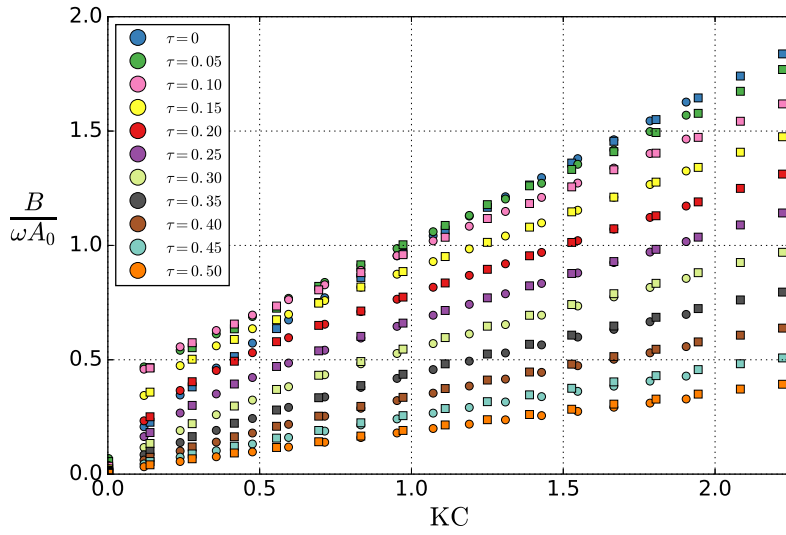


**Figure 8.10:** Damping coefficients for numerically simulated perforated plates. Circular markers: Model I. Square markers: Model II.

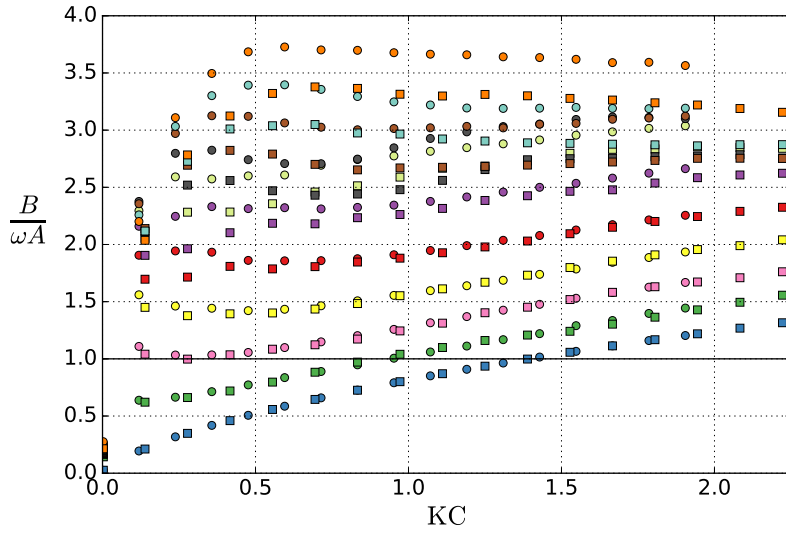


**Figure 8.11:** Ratio between damping force and added mass force for numerically simulated perforated plates. Circular markers: Model I. Square markers: Model II. Legend in Fig. 8.10.



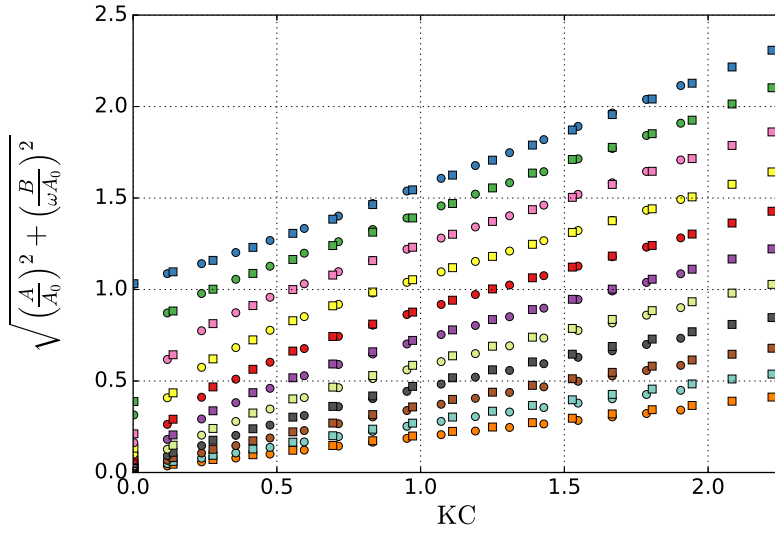


**Figure 8.12:** Normalized force amplitude for numerically simulated perforated plates. Circular markers: Model I. Square markers: Model II. Legend in Fig. 8.10.

damping coefficients alone, Fig. 8.10. However, an importance differences is that the force amplitude, for a given KC number, always increases when the perforation ratio decreases.

### 8.3 Comparison with Molin's method

Calculations using Molin's semi-analytical method [19], including drag correction, for added mass and damping coefficients of perforated structures, are performed. Ten perforated plates are considered, with perforation ratios equal to that of the numerical study, that is, from  $\tau = 0.05$  to  $\tau = 0.50$  in steps of  $\tau = 0.05$ . Further, the same range of KC numbers is considered as in the numerical study, that is,  $0.002 \leq KC \leq 2.2$ , cf. Section 8.2.

In the method by Molin when including a drag correction term as proposed by Sandvik et al. [9], the added mass and damping coefficients are functions only of  $\tau$ , KC,  $\mu$  and  $\alpha$ , cf. Sections 1.4.2 and 1.4.3. Hence,  $\tau$ , KC,  $\mu$  and  $\alpha$  are the only input parameters when performing calculations using this method. Two of these parameters, the perforation ratio,  $\tau$ , and the KC number, are (at least in the present context) trivial, since they define the considered case. Contrary, the drag correction coefficient,  $\alpha$ , and the discharge coefficient,  $\mu$ , are (in general) unknown and must be set in advance of the calculation. The discharge coefficient,  $\mu$ , which relates the pressure loss to the relative velocity through the perforated

openings [19], is a function of the local geometry of the plate openings. As an example,  $\mu$  will differ between a plate that has sharp-edged holes, and a plate that consists of circular cylinders in a row. The drag correction coefficient,  $\alpha$ , is proportional to the drag coefficient and drag force due to plate-end flow separation. Sandvik et al. [9] were inspired by the analytical results for solid plates by Graham [22], and a similar model for the drag force was applied, that is, the drag correction coefficient,  $\alpha$ , is equivalent to  $b_1$  in Eq. (8.1). In his analytical study, Graham found that for a *solid* plate,  $b_1 = \alpha = 11.8$  [22]. Consequently, the appropriate value of  $\alpha$  for a *perforated* plate is  $0 < \alpha < 11.8$ , cf. discussion in Section 1.4.3.

For the present comparison, calculations are performed for a range of  $\mu$  and  $\alpha$ . For each perforation ratio, 24 different values of  $\alpha$  ranging from  $\alpha = 0.5$  to  $\alpha = 12.0$ , with increments of 0.5, are tested. Further, for each combination of  $\tau$  and  $\alpha$ , calculations are performed for 15 discharge coefficients, ranging from  $\mu = 0.3$  to  $\mu = 1.0$  with increments of 0.05. The choice of discharge coefficients are made based on resistance coefficients provided by Blevins [21, pp. 314–315], which correspond to discharge coefficients in the range  $0.35 < \mu < 0.65$  for the present perforation ratios, and by statements by Molin et al. [17–19], where it is commented that the discharge coefficient is usually  $0.3 < \mu < 1.0$ .

Taking into account the 10 different perforation ratios, the 24 values of  $\alpha$  and the 15 discharge coefficients, a total of 3600 semi-analytical calculations are performed. A summary of the calculation variables is provided in Table 8.4.

**Table 8.4:** Calculation variables in study using Molin's method

Parameter	Min value	Max value	Increment
$\tau$	0.05	0.50	0.05
$\alpha$	0.05	12.0	0.05
$\mu$	0.30	1.0	0.05

In order to compare effectively the results of the semi-analytical calculations with the viscous flow solver results, only the best fitting results of the various combinations of  $\alpha$  and  $\mu$  are provided. Hence, from the 360 calculations (24  $\alpha$  times 15  $\mu$ ) for each perforation ratio, only the best fit is presented. The best fit is determined by calculating the mean relative difference,  $\overline{d_r}$ , between the results of the semi-analytical method and the viscous flow solver for the range of KC considered,  $0.002 \leq KC \leq 2.2$ . For each perforation ratio, the combination of  $\alpha$  and  $\mu$  that corresponds to the smallest mean relative difference is presented. Three results are provided for each plate perforation, the combination of  $\mu$  and  $\alpha$  that yields the smallest relative difference for 1) the added mass coefficient, 2) the damping coefficient, and 3) the square root of the sum of the coefficients squared, that is, the normalized force amplitude.

The results from calculations with Molin's semi-analytical method are presented in Tables 8.5 and 8.6. The presented mean relative difference ( $\overline{d_r}$ ) and correlation coefficient ( $r$ ) are between the CFD results and the semi-analytical



**Table 8.5:** The combination of  $\mu$  and  $\alpha$  that yields the best fit with the added mass and damping coefficients of the CFD results. Mean relative difference ( $\overline{d_r}$ ) and correlation coefficient ( $r$ ) between semi-analytical best fits and CFD results.

$\tau$	Best added mass fit				Best damping fit			
	$\mu$	$\alpha$	$\overline{d_r}$	$r$	$\mu$	$\alpha$	$\overline{d_r}$	$r$
0.05	0.30	0.5	10 %	0.869	1.00	10.5	17 %	0.999
0.10	0.95	2.0	10 %	0.975	1.00	9.5	6 %	0.997
0.15	0.85	4.5	11 %	0.983	0.95	9.0	3 %	0.998
0.20	0.75	5.5	13 %	0.982	0.85	8.0	4 %	0.998
0.25	0.65	6.5	16 %	0.972	0.80	7.5	5 %	0.998
0.30	0.55	7.0	18 %	0.958	0.80	7.0	5 %	0.999
0.35	0.45	7.0	19 %	0.947	0.75	5.5	6 %	0.998
0.40	0.45	6.5	20 %	0.953	0.75	4.5	6 %	0.999
0.45	0.45	5.5	21 %	0.968	0.75	3.0	7 %	0.997
0.50	0.40	6.0	23 %	0.944	0.80	3.5	8 %	0.998

**Table 8.6:** The combination of  $\mu$  and  $\alpha$  that yields the best fit with the normalized force amplitude of the CFD results. Mean relative difference ( $\overline{d_r}$ ) and correlation coefficient ( $r$ ) between combined semi-analytical best fit and CFD results.

$\tau$	$\mu$	$\alpha$	$\overline{d_r}$	$r$
0.05	0.50	12.0	3 %	0.999
0.10	0.95	11.5	5 %	0.998
0.15	0.85	10.0	6 %	0.998
0.20	0.80	9.0	7 %	0.998
0.25	0.80	8.0	8 %	0.998
0.30	0.75	7.0	8 %	0.998
0.35	0.75	7.0	9 %	0.999
0.40	0.75	6.0	9 %	0.999
0.45	0.75	5.0	10 %	0.998
0.50	0.75	0.5	10 %	0.997

method for the same KC numbers as was simulated in the CFD. Two observations are highlighted in the following. 1) There are no generic values of  $\mu$  and  $\alpha$ , and it is not obvious how these parameters should be chosen. Nonetheless, the drag correction coefficient,  $\alpha$ , is found to decrease with increasing perforation ratio. This is consistent with weaker plate-end flow separation for increasing perforation ratio. Note that the best fit for the added mass coefficient is not obtained for decreasing  $\alpha$  with increasing  $\tau$ . The resistance coefficients for a perforated plate with square edges provided by Blevins [21, p. 314] suggests that  $\mu$  should increase from  $\mu = 0.35$  for the smallest perforation ratio,  $\tau = 0.05$ , to  $\mu = 0.50$  for the largest perforation ratio,  $\tau = 0.5$ . However, the present results found the best fit when  $\mu$  is larger than 0.5, without consistent dependence on the perforation ratio. 2) The best fit to both added mass and damping is in general not found for a single combination of  $\mu$  and  $\alpha$ . Most noticeable are the inconsistent trends in  $\alpha$ . For smaller perforation ratios, the best fit to the damping coefficient is found with a larger  $\alpha$  than what gives the best fit for the added mass coefficient. This behavior is opposite for higher perforation ratios, that is, for the largest perforation ratios, the added mass best fit is found with a larger  $\alpha$  than the damping best fit. A similar problem has previously been observed when comparing the semi-analytical method to experimental results; when comparing the semi-analytical method with experiments of a perforated disk with a perforation ratio of  $\tau = 0.20$ , Molin et al. [18] found that  $\alpha = 6$  was needed to get a good fit for the damping coefficient, but this would underestimate the added mass coefficient. The results by An and Faltinsen [20], comparing the semi-analytical method with experimental results of two rectangular perforated plates of perforation ratios  $\tau = 0.08$  and  $\tau = 0.16$ , yielded a similar conclusion. However, since the hydrodynamic force on perforated plates in oscillating flow is, in general, dominated by damping, inconsistent dependence on  $\alpha$  for the added mass coefficient is less important than for the damping coefficient.

## 8.4 Semi-analytical method inspired by Graham

The results of the numerical study using the viscous flow solver are combined with the expressions for the hydrodynamic coefficients of solid plates by Graham, in order to develop simple expressions for the force coefficients of perforated plates. The method is semi-analytical in the sense that it is based on Graham's analytically derived expressions for solid plates, but with the parameters curve-fitted to the present results for perforated plates. A benefit of the method by Graham is that the analytical expressions are very simple to use. In Section 8.1, good agreement between Graham's method and present numerical and experimental results of solid plates was demonstrated. In Section 8.2, a large numerical study of perforated plates was presented. In the following, the parameters of Eqs. (8.2) and (8.3), that yields the best curve-fit to the simulated perforated plates are provided.

For each perforation ratio, the resulting parameters,  $a_0$ ,  $a_1$  and  $b_1$ , are presented in Table 8.7. A simple code for obtaining the added mass and damping

coefficients for a given  $\tau$  and KC is given in Code listing 8.1. In Table 8.7, the mean relative difference ( $\overline{d_r}$ ) and correlation coefficient ( $r$ ) are obtained based on the normalized force amplitude. The results of the CFD are compared to the estimated result using the curve-fits applied to the same KC numbers as was simulated in the CFD. A visual comparison of the curve-fits to the viscous flow solver results is presented in Fig. 8.13.

**Table 8.7:** Coefficients in Eqs. (8.2) and (8.3) when curve-fitted to the present CFD results. The mean relative difference ( $\overline{d_r}$ ) and correlation coefficient ( $r$ ) are based on comparing the normalized force amplitude estimated with the curve-fits and the CFD results.

$\tau$	$a_0$	$a_1$	$b_1$	$\overline{d_r}$	$r$
0.00	1.000	0.216	10.1	2%	0.998
0.05	0.748	0.230	10.1	2%	0.999
0.10	0.498	0.252	9.58	3%	0.998
0.15	0.281	0.271	8.72	4%	0.998
0.20	0.132	0.261	7.67	3%	0.998
0.25	0.055	0.222	6.57	2%	0.999
0.30	0.017	0.181	5.48	3%	0.999
0.35	0.000	0.156	4.44	6%	0.999
0.40	0.000	0.120	3.49	10%	0.998
0.45	0.000	0.087	2.69	12%	0.995
0.50	0.000	0.057	2.04	13%	0.994

The applied functional relationship, i.e., Eqs. (8.2) and (8.3), seems to provide a reasonable model. A deficiency is that the damping coefficients are underestimated for the densest perforated plates at low KC numbers, cf. discussions in Sections 1.4.5 and 8.2. Moreover, for  $\tau \geq 0.35$ , there is a considerable increase in the mean relative difference between the curve-fits and the CFD results. This is consistent with the fact that the analysis by Graham only takes the plate-end flow separation into account, that is, Eqs. (8.2) and (8.3) were developed for solid—not perforated—plates. Plate-end flow separation is important for perforated plates as well, but the effect is less important for increasing perforation ratio as more flow can pass through the perforated openings. The streamline plots of Fig. 8.7 illustrate the differences in flow for different perforation ratios; clearly, the plate-end vortices are weaker when the perforation ratio increases.

The curve fits for the perforated plates are based on results for both plate models I and II for  $0.24 \leq KC \leq 2.2$ . The results from the smallest KC numbers are ignored when performing the curve fitting for the perforated plates. The reason is that plate-end flow separation is not of importance for small KC numbers and Graham's flat plate theory should not be expected to be representative. In reality, the low limit KC in the method should depend on  $\tau$  since increasing the KC number and/or decreasing the perforation ratio increases the importance of the plate-end flow separation, cf. Section 6.4. For instance from Fig. 6.24,  $\tau = 0.19$ :  $KC_{\text{low}} \simeq 0.2$

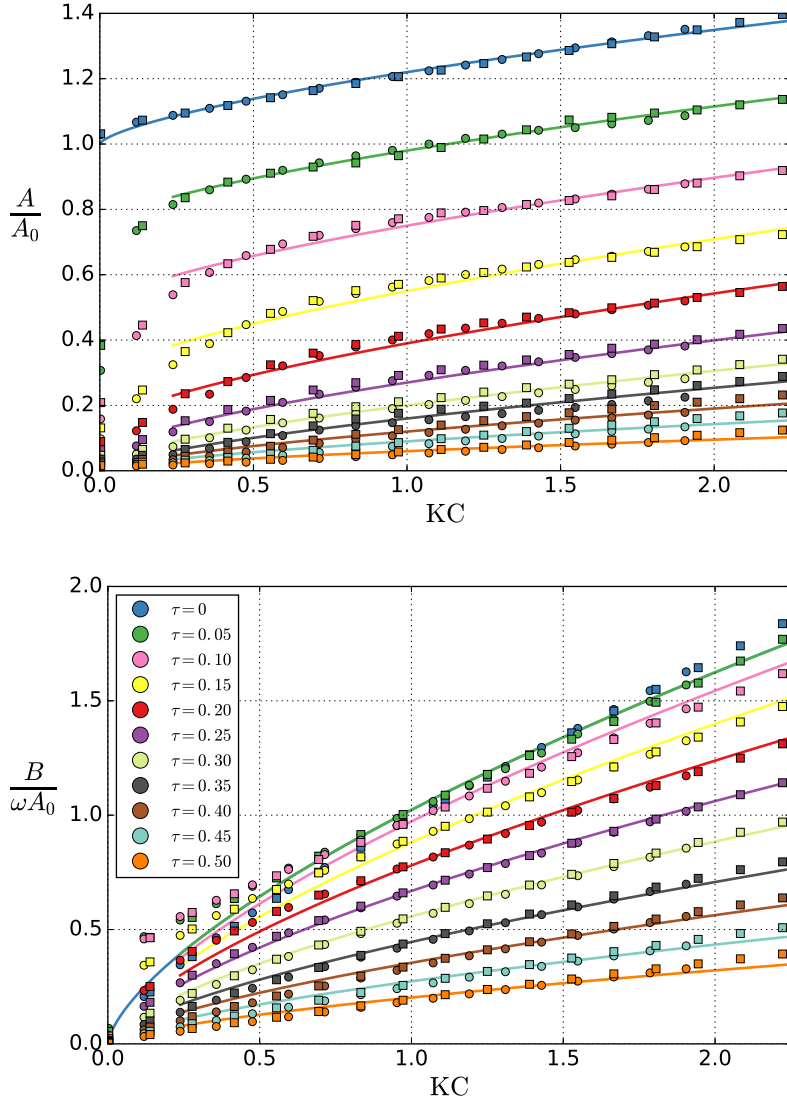


**Figure 8.13:** Added mass (top) and damping (bottom) coefficients. Markers represent present CFD and curves are based on curve-fit of the CFD results to Eqs. (8.2) and (8.3). Curve-fit coefficients presented in Table 8.7. Circular markers: Model I. Square markers: Model II.

and  $\tau = 0.28$ :  $KC_{\text{low}} \simeq 0.3$ . When using a constant low limit of  $KC_{\text{low}} = 0.24$ , there is a considerable mean relative difference between the curve-fits and the CFD results for the highest perforation ratios. In order to have smaller mean relative difference than 5%, the low limit KC must be  $KC_{\text{low}} = 0.28$  ( $\tau = 0.35$ ),  $KC_{\text{low}} = 0.56$  ( $\tau = 0.4$ ),  $KC_{\text{low}} = 0.83$  ( $\tau = 0.45$ ) and  $KC_{\text{low}} = 0.97$  ( $\tau = 0.5$ ). Note that for very small KC numbers, i.e.,  $KC \rightarrow 0$ , the number of holes on the plate is the important parameter for the (added mass) force. If a value for the added mass in the low-KC limit is needed, one should use an alternative approach, e.g. a source method calculation, cf. Section 4.1.2.

Compared to the semi-analytical method by Molin, a benefit of the proposed model is its simplicity. No advanced calculations are needed, and the estimated force depends only on  $\tau$  and KC, not  $\mu$  and  $\alpha$ . Even from the large range of  $\tau$ ,  $\mu$  and  $\alpha$  considered (3600 combinations), consistent trends and clear recommendations of use are not obtained, in particular for  $\mu$ . However, since the present method does not take a discharge coefficient into account, and is based on simulations using rectilinear grids (sharp edges), the method will be conservative for perforated structures without sharp edges, cf. Section 6.3.3.

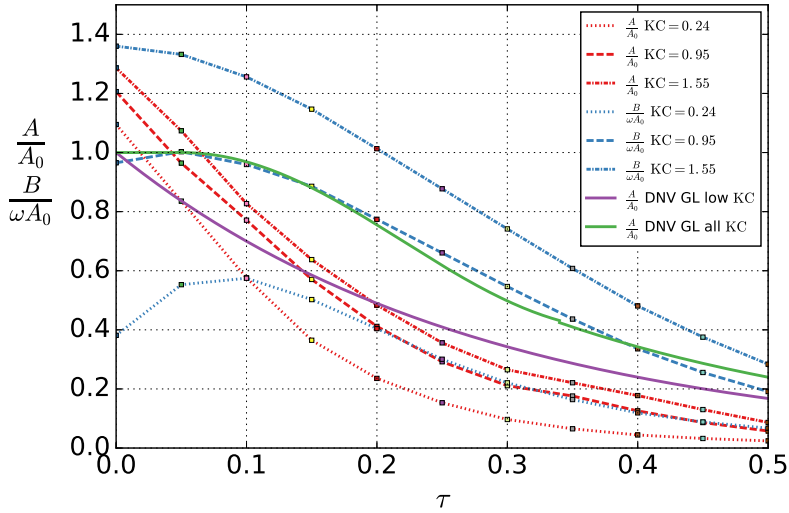


**Figure 8.14:** Added mass and damping coefficients as functions of perforation ratio for three KC numbers in the present numerical study. Comparisons with the recommended practice by DNV GL [4], cf. Section 1.4.4.

In Section 1.4.4, methods for estimating the effect of perforation, provided by DNV GL [4], are presented. Compared to the recommended practice by DNV GL, a strength of the proposed method is that estimates for both the added mass and

damping coefficients of perforated plates are obtained. The results of the numerical study highlight the importance of damping. Experimental studies presented in Chapter 6 support the numerical findings. Furthermore, the present expressions are functions of KC. The hydrodynamic force and coefficients of perforated plates are highly KC dependent. An illustration is presented in Fig. 8.14. The present results are plotted for three KC numbers. Both  $\tau$  and KC are important, e.g. for  $\tau = 0.25$ , the damping coefficient at  $KC = 0.95$  is more than twice that at  $KC = 0.24$ .

**Code listing 8.1:** Python code for obtaining added mass and damping coefficients for a given perforation ratio and KC number using the semi-analytical method.

```
""" Semi-analytical force model: 0 < tau < 0.5, 0.2 < KC < 2.2 """

import numpy as np

def coefficient_interpolation(tau):
    """ Interpolation of curve-fits """
    taus = np.linspace(0, 0.5, 11)
    a_0s = [1.000, 0.748, 0.498, 0.281, 0.132,
            0.055, 0.017, 0.000, 0.000, 0.000, 0.000]
    a_1s = [0.216, 0.230, 0.252, 0.271, 0.261,
            0.222, 0.181, 0.156, 0.120, 0.087, 0.057]
    b_1s = [10.1, 10.1, 9.58, 8.72, 7.67,
            6.57, 5.48, 4.44, 3.49, 2.69, 2.04]
    a_0 = np.interp(tau, taus, a_0s)
    a_1 = np.interp(tau, taus, a_1s)
    b_1 = np.interp(tau, taus, b_1s)
    return a_0, a_1, b_1

def coefficients_from_tau_kcn(tau, kcn):
    """ Added mass and damping for a given tau and KC number """
    a_0, a_1, b_1 = coefficient_interpolation(tau)
    return a_0 + a_1*kcn**(2/3.0), b_1/np.pi**2*kcn**(2/3.0)

# Example of use: Coefficients for a given perforation ratio and KC number
A_A0, B_OMEGAA0 = coefficients_from_tau_kcn(tau=0.24, kcn=1.5)
```

## 8.5 Comparison with 3D experiments

The coefficients in the semi-analytical method, presented in Table 8.7, are based on the two-dimensional analytical investigation by Graham and two-dimensional numerical viscous flow solver results of perforated plates. In the following, the applicability of the method to predict the force on three-dimensional perforated structures is investigated. The present verification includes experimental investigations of five structures by Sandvik et al. [9] and two structures by An and Faltinsen [20]. Parameters of the three-dimensional studies are presented in Table 8.8.

Sandvik et al. [9] performed three-dimensional experimental model tests of a realistic protection roof structure, consisting of rows of circular cylinders surrounded by an outer bumper frame. The perforation ratio of the structure as a

**Table 8.8:** Parameters in experimental studies by An and Faltinsen [20] and Sandvik et al. [9]; perforation ratios, aspect ratios, and periods of oscillation in the experiments. The aspect ratio is the length divided by the width. The width of the structures is used as the characteristic length ( $D$ ) in the KC number.

$\tau$	Aspect ratio	$T$	Reference
0.08	1.4	1.5 s, 2.0 s, 2.5 s, 3.0 s	An and Faltinsen [20]
0.16	1.4	1.5 s, 2.0 s, 2.5 s, 3.0 s	An and Faltinsen [20]
0.16	2.0	1.5 s, 2.0 s	Sandvik et al. [9]
0.25	2.0	1.5 s, 2.0 s	Sandvik et al. [9]
0.27	1.3	6 s, 10 s	Sandvik et al. [9]
0.375	1.1	6 s, 10 s	Sandvik et al. [9]
0.47	1.1	6 s, 10 s	Sandvik et al. [9]

whole is  $\tau = 0.27$ . Two similar roof models with perforation ratios  $\tau = 0.375$  and  $\tau = 0.47$  were also tested. In addition to the roof structures, two simpler hatch covers, also consisting of rows of cylinders, but without outer bumper frames, were investigated. The simpler hatch covers have perforation ratios  $\tau = 0.25$  and  $\tau = 0.16$ . Photos of one of the roofs and one of the simpler hatch covers are presented in Fig. 8.15. The experimental results for these structures, as well as the photos in Fig. 8.15, were provided by Frøydis Solaas, co-author of the referred study.



**Figure 8.15:** Photos of two of the structures experimentally investigated by Sandvik et al. [9]. The poster Hatch 18 refers to the number of cylinders. Photos from Frøydis Solaas.

An and Faltinsen [20] investigated experimentally three-dimensional plates with sharp-edged circular holes. The plates are 520 mm long and 365 mm wide. The plates consist of many holes and are relatively thin with thickness equal to 5 mm. Consequently, the plates are almost ideal. An and Faltinsen tested two plates. The plates are similar except for the number of holes which is 192 and 384. Each hole has diameter 10 mm. Thus, the perforation ratios are  $\tau = 0.08$  and  $\tau = 0.16$ . The latter is particularly useful in the present comparison, since one of the structures by Sandvik et al. also has perforation ratio  $\tau = 0.16$ . Hence, these structures have equal perforation ratios, but different shapes—20 circular

cylinders (Sandvik,  $\tau = 0.16$ ) versus 384 sharp-edged holes (An,  $\tau = 0.16$ ).

The normalized force amplitudes are presented in Figs. 8.16 and 8.17. The semi-analytical expressions are given with solid lines. The experimental results by An and Faltinsen [20] are presented with four rotations of triangle markers (four different periods of oscillation), while the results by Sandvik et al. [9] are given with circular and square markers (two different periods of oscillation). Note that the reference added mass,  $A_0$ , differ between 2D and 3D; Sandvik et al. estimated the potential flow added mass taking into account the aspect ratio and using a correction factor [64], while An and Faltinsen performed potential flow calculations of a corresponding solid plate to determine  $A_0$ .

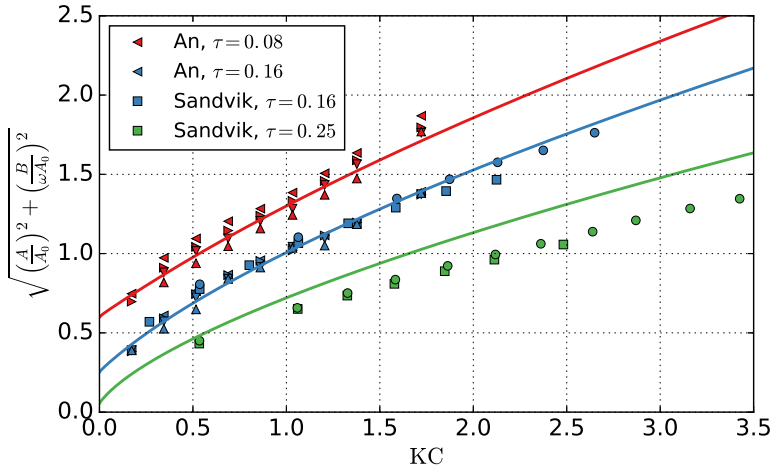


**Figure 8.16:** Normalized force amplitude of three-dimensional perforated plates [9, 20]. The different markers indicate different periods of oscillation. Comparisons with the semi-analytical method (solid lines), Table 8.7.

The agreement between the semi-analytical method and the previous three-dimensional experimental investigations is, in general, reasonable, keeping in mind that the models are 3D, while the method is based on two-dimensional ideal plates. Good agreement is obtained for  $\tau = 0.08$  and  $\tau = 0.16$ . For higher perforation ratios, the semi-analytical method overpredicts the force. An exception is for  $\tau = 0.47$ , in which the semi-analytical method agrees well with the experimental investigations.

It is not surprising that there are discrepancies. One obvious candidate is the geometry of the members. In the roof model with  $\tau = 0.27$ , all members are cylindrically shaped with circular cross-sections. For this case, the semi-analytical method overpredicts considerably. The plates by An and Faltinsen have circular sharp-edged holes, which is more consistent with the present CFD model. Further,



one may expect weaker global vortex structures shed from the plate ends when the structure edge is not sharp. The roof models have bumper frames with circular cylinders. The hatch covers ( $\tau = 0.25$  and  $\tau = 0.16$ ) have sharp edges along the two short sides. The plates by An ( $\tau = 0.08$  and  $\tau = 0.16$ ) have sharp edges along all four sides. Nevertheless, in terms of geometry, Sandvik's roofs of  $\tau = 0.375$  and  $\tau = 0.47$  are very similar, yet the semi-analytical method is poor for  $\tau = 0.375$  and good for  $\tau = 0.47$ .

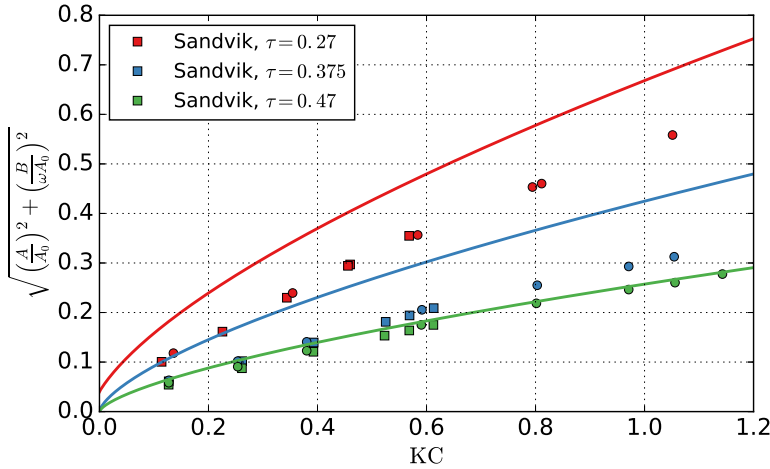


**Figure 8.17:** Normalized force amplitude of three-dimensional perforated plates [9, 20]. The different markers indicate different periods of oscillation. Comparisons with the semi-analytical method (solid lines), Table 8.7.

Another candidate is three-dimensionality of the geometry. One would expect this to give effects most pronounced for length-to-width aspect ratios of 1. The aspect ratios are given in Table 8.8. However, there is no clear trend in the presented data that higher aspect ratios provide better comparison with the semi-analytical model. For instance, the plate with aspect ratio 1.4 (An  $\tau = 0.16$ ) agrees better than the hatch cover with aspect ratio of 2.0 (Sandvik  $\tau = 0.25$ ).

There is in general reasonable agreement between the semi-analytical method—which is based on Graham's two-dimensional analysis and two-dimensional numerical simulations—and the three-dimensional experiments. As elaborated earlier, plate-end flow separation is important for the hydrodynamic force on perforated plates. The flow separation will occur on two sides of a two-dimensional plate, and on four sides of a three-dimensional plate. Nevertheless, the predicted force on the plates using the two-dimensional method agrees reasonable when comparing with the three-dimensional experiments. Two effects are highlighted in this respect. 1) Interaction between the flow separation from the four sides in

3D is more dominant than the interaction from flow separation at the two sides in 2D. 2) The flow has more freedom to circumvent the plate in 3D. This is illustrated in the sketch in Fig. 8.18. The flow will separate on the sides 1 and 2 in the two-dimensional case, and from sides 1, 2, 3 and 4, including their corners, in the three-dimensional case. However, the freedom to flow in the intermediate quadrants A, B, C and D without separation is only possible in 3D.

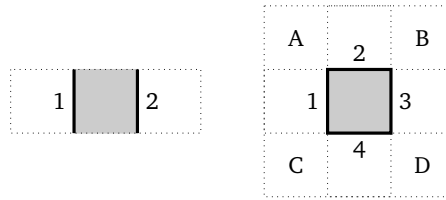


**Figure 8.18:** Explanation of parameters used in discussion of 2D (left) vs 3D (right) plate flow. The flow will separate at the plate-ends in both cases (numbered edges), but is allowed to circumvent the plate without separation in 3D (A, B, C and D).



## Chapter 9

# Interaction effects

One of the unsolved questions within hydrodynamics of complex structures in the wave zone is how and when interaction effects influence the forces on a complex structure. In the recommended practice for modeling and analysis of marine operations, DNV GL notes that for subsea structures, “interaction effects between members caused by flow restrictions can cause a significant increase in the added mass and damping” [4, Section 3.3.3]. Thus, according to DNV GL, estimating the hydrodynamic force coefficients of a subsea structure based on superposition of each member can lead to an underestimation of the actual total force. At worst, this can increase the probability of unsafe operations with risk for equipment and personnel.

In this chapter I present some new results in this regard, and highlight some aspects of interaction effects relevant for subsea structures. The results are obtained from experimental and numerical methods in forced oscillation conditions. Results from numerical simulations of orbital flow conditions are included as well. The focus in this chapter is mostly on interaction between different members, for example wake effects. I’ve also included results from the type of interaction effect that is due to the presence of a boundary (wall) close to the model.

### 9.1 Simplified subsea structure

A simplified subsea structure is experimentally investigated. The simplified subsea structure consists of two ideal perforated plates of  $\tau = 0.28$ , identical to P28 presented in Section 6.1. In general, I refer to models consisting of two perforated plates of  $\tau = 0.28$  as 2P28. The plates are placed in parallel with a gap distance of 120 mm, that is, 2P28\_120. Between the two perforated plates, five circular cylinders (5C) are installed. The perforated plates may be thought of as simplifications of the top and bottom covers of a subsea module, while the cylinders represent simplifications of equipment on the module. The cylinders have equal radius  $R = 30$  mm. The wall-to-wall distance between each cylinder is 30 mm, such that the total width of the cylinders is  $5 \times 60 \text{ mm} + 4 \times 30 \text{ mm} = 420 \text{ mm}$ .

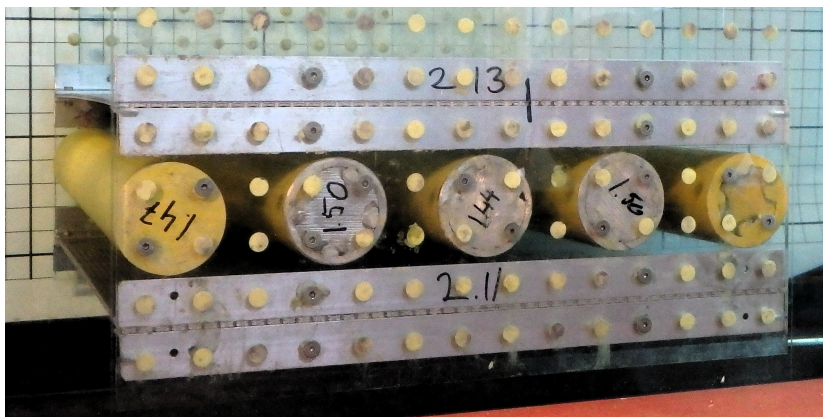


**Figure 9.1:** Photo of 2P28\_120+5C, a simplified subsea structure model. Between two perforated plates of  $\tau = 0.28$ , five circular cylinders are installed. The width of the model is  $D = 420$  mm, the gap distance between the two perforated plates is 120 mm.

The full model is referred to as 2P28\_120+5C. A photo of the model is presented in Fig. 9.1.

Examples of time-series from the experimental investigations of 2P28\_120+5C are presented in Fig. 9.2. The measured raw, unfiltered force and acceleration are presented for one set (combination of period and amplitude of oscillation) of the experimental investigations. Both quantities are made nondimensional by their maximum values during the set. Clearly, there is a phase delay between the first harmonic of the acceleration and force, indicating that the force consists of both added mass and damping terms. Note that the force coefficients are obtained for the eight oscillation cycles in the middle of the set, ignoring the ramp-in, ramp-out and the first and last oscillation cycle with full amplitude of motion. Furthermore, both signals are filtered around the basic harmonics; the acceleration is band-pass filtered from  $0.7T$  to  $1.3T$ , while the force is filtered from  $0.7T$  to  $5.3T$ . The filtered force and acceleration are included with dotted lines in the bottom plot of Fig. 9.2.

The obtained added mass and damping coefficients of 2P28\_120+5C are presented in Fig. 9.3. Included in the figure are the coefficients from experimental investigations of the five cylinders without perforated plates, 5C, as well as the two perforated plates without cylinders between them, 2P28\_120. Interestingly, the force coefficients are, in general, larger for the two parallel perforated plates without cylinders than when the cylinders are included. An exception is the added mass coefficient for small  $KC$  numbers. However, the hydrodynamic force ratio of both 2P28\_120 and 2P28\_120+5C are dominated by damping (cf. the values of the vertical axes), and the increased added mass of 2P28\_120+5C is more than compensated for by a smaller damping coefficient. This becomes clearer by study-

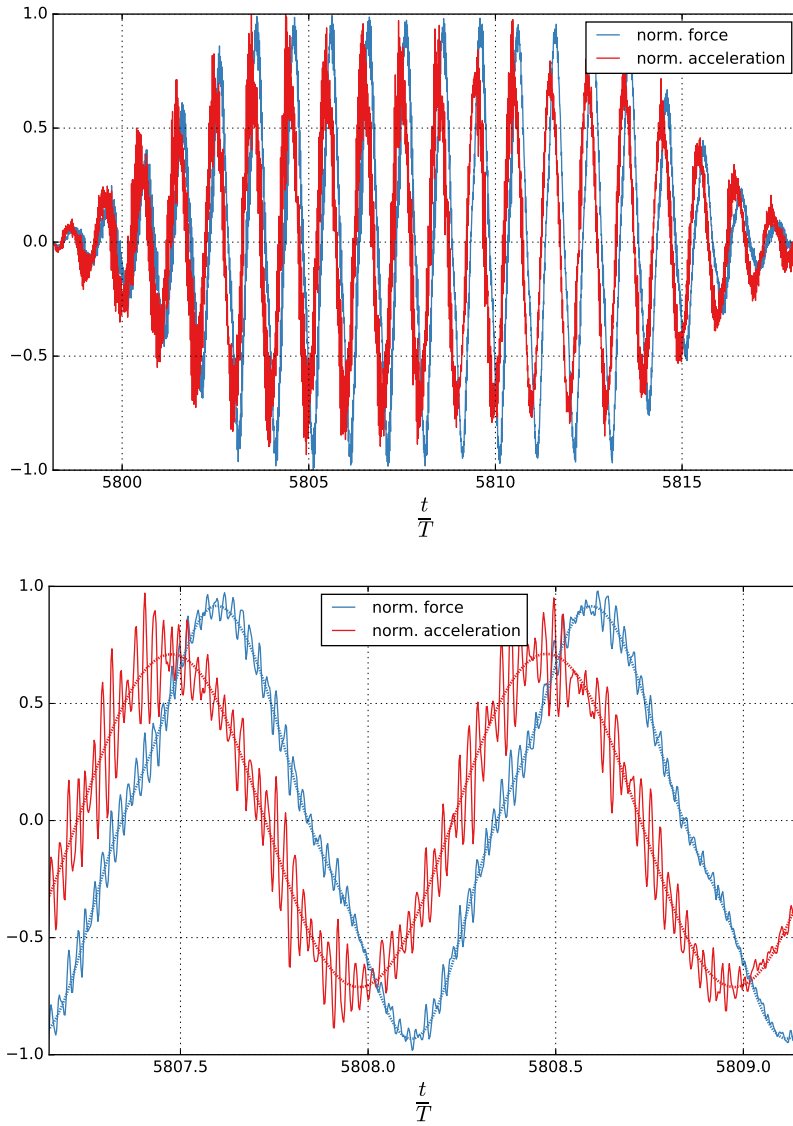


**Figure 9.2:** Example of force and acceleration measurements from experiments of 2P28\_120+5C. The figures show the measured force and acceleration normalized with their maximum during a full experimental test set (top) and the two full oscillation cycles in the middle of the set (bottom).

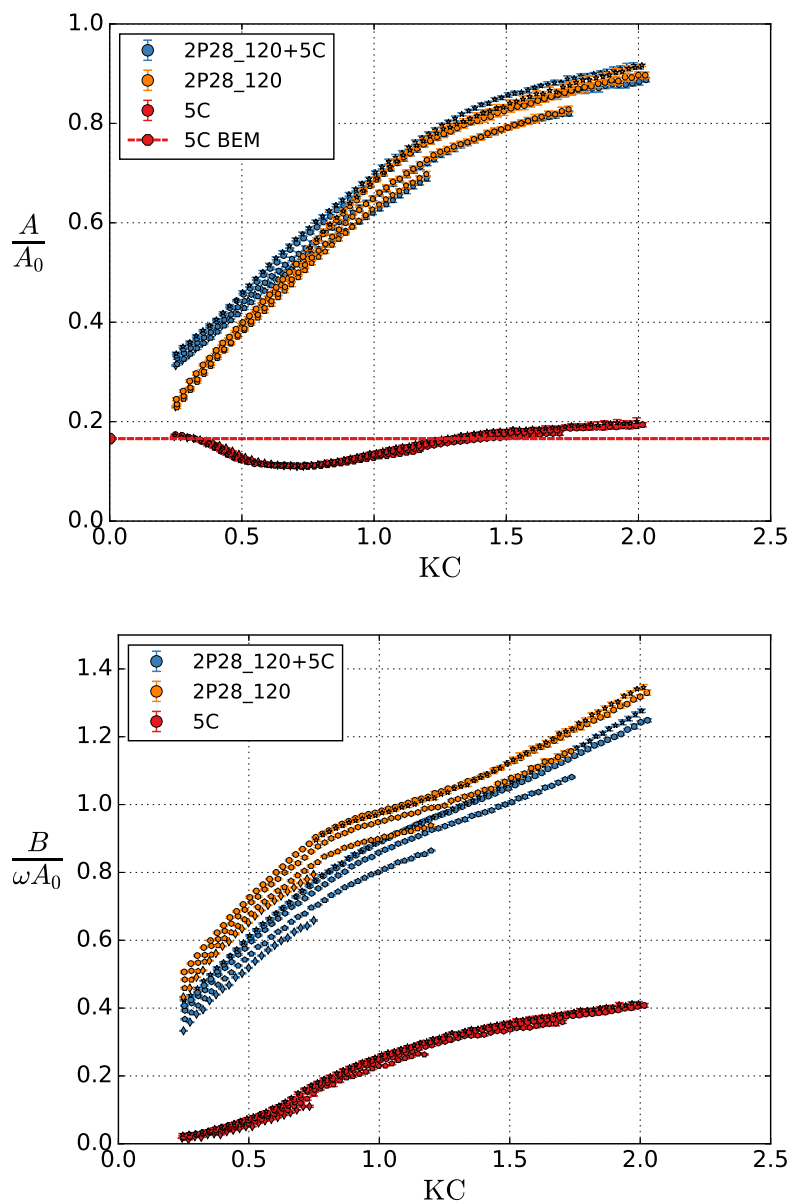


**Figure 9.3:** Added mass and damping coefficients from experimental investigations of 2P28\_120+5C, 2P28\_120 and 5C.

ing Fig. 9.4, in which the normalized force amplitude is presented. Obviously, due to the potential flow added mass of solid cylinders—and the negligible potential flow added mass of ideal perforated plates—for very small KC numbers, the hydrodynamic force amplitude of 2P28\_120+5C must be larger than of 2P28\_120. Nevertheless, for all tested KC numbers, the normalized force amplitude is larger on 2P28\_120 than on 2P28\_120+5C.

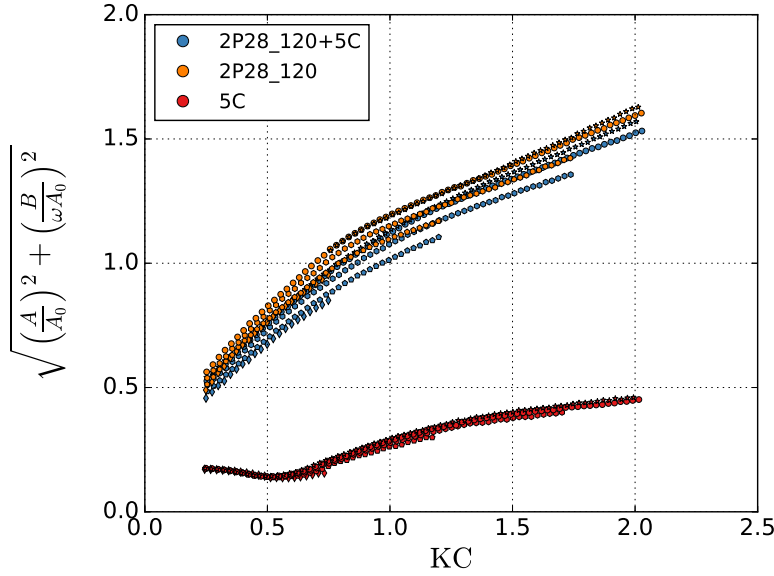


**Figure 9.4:** Normalized hydrodynamic force amplitude from experimental investigations of 2P28\_120+5C, 2P28\_120 and 5C.

In addition to the experimental results, I have included the added mass coefficient of 5C calculated with the potential flow solver. Note that the reference added mass,  $A_0$ , is for a cylinder/plate of characteristic width  $D = 420$  mm, which gives  $\frac{A}{A_0} = 0.1658$  for 5C. This is 8.12 times that of a single circular cylinder with radius  $R = 30$  mm. Consequently, there is an increase in added mass of  $\frac{8.12-5}{5} = 62\%$  due to potential flow interaction between the five cylinders. If using superposition of five individual cylinders to estimate the added mass coefficient of 5C, the added mass is considerably underestimated.

Some features of 5C are highlighted, in particular that there exists a critical minimum value of the added mass coefficient, and that the hydrodynamic force ratio is dominated by added mass for all  $KC < 0.7$ . This deviates from the perforated plates presented so far, including the model consisting of circular cylinders (C19), cf. Section 6.2.



Unlike the various perforated plate models, the added mass coefficient of 5C does not increase rapidly when increasing  $KC$  from the smallest  $KC$  numbers tested. Instead, the added mass coefficient decreases to a critical minimum value, following an increase for higher  $KC$  numbers. This behavior is similar to previous results for one cylinder. Keulegan and Carpenter [38] found the critical  $KC$  number for a single cylinder to be  $KC \approx 15$ . The results by Sarpkaya [39, 65] show a similar behavior at  $KC \approx 13$ . In the present study, the smallest added mass coefficient for the five cylinder configuration is found when the amplitude of motion is  $\eta_a = 48$  mm,  $\eta_a = 50$  mm,  $\eta_a = 49$  mm,  $\eta_a = 49$  mm, and  $\eta_a = 48$  mm, for  $T = 1.00$  s to  $T = 2.00$  s, respectively. This corresponds to a mean  $KC = 5.1$ , when normalizing with the diameter of one cylinder ( $D = 60$  mm). The speed up due to the flow restriction, caused by the row of cylinders, is not reflected in this  $KC$  number. If a simple control volume analysis is applied, where the distance between the center of the two outermost cylinders is used as the total change in area compared with a one cylinder configuration, there is  $4R$  unrestricted flow distance over a distance of  $12R$ . Consequently, the critical  $KC$  number could be expected to be of order  $4R/12R = 1/3$  of the critical  $KC$  number for one cylinder, which is in reasonable agreement with the results for one cylinder ( $KC \approx 13$ -15).

The drop in the added mass coefficient at the critical  $KC$  number is significant, but unlike the results by Sarpkaya [39] for one cylinder at similar  $\beta$  values, the added mass coefficient does not become negative in the present study. Here, the five forcing periods of oscillations correspond to  $1750 \leq \beta \leq 3500$ , and the critical added mass is approximately 65 % of the potential flow solver result, independent on the period of oscillation. On the other hand, the results for one cylinder by Sarpkaya [39] yield critical added mass coefficients of  $-0.2$ ,  $0.3$ , and  $0.6$  for  $\beta = 1985$ ,  $\beta = 3123$ , and  $\beta = 4480$ , when normalizing with the area of one cylinder. As has been pointed out by Singh [60], other studies have shown negligible  $\beta$  dependence or opposite trends to that found by Sarpkaya, with decreasing added mass coefficient when increasing  $\beta$ .

## 9.2 Parallel ideal perforated plates

Due to the importance of the perforated plates in the simplified subsea structure of Section 9.1, parallel perforated plates are studied in more detail. Both experimental and numerical studies are conducted. The studies are based on the ideal perforated plates with perforation ratio  $\tau = 0.28$ .

Two 2P28 configurations are experimentally investigated. In the first, 2P28\_60, the vertical gap distance between the two plates is 60 mm. In the second, 2P28\_120, the vertical gap distance between the two plates is 120 mm. A photo of 2P28\_120 placed in the experimental rig is presented in Fig. 9.5.

Numerical counterparts of 2P28\_60 and 2P28\_120 are simulated with the viscous flow solver. Additionally, a numerical model with gap distance 90 mm, 2P28\_90, is simulated. All models are  $D = 420$  mm wide, hence the ratios of the vertical gap distance between the two plates compared to the width of the plates

are 0.143 (2P28\_60), 0.214 (2P28\_90) and 0.286 (2P28\_120).

The numerical implementations of the parallel perforated plate configurations are similar to that of the numerical model of the single P28 plate, cf. Section 6.1.2. However, the fine regions of the grids are vertically extended to cover both perforated plates. This increases the number of grid cells and corresponding calculation times. The total number of grid cells are 80 216 (2P28\_60), 87 812 (2P28\_90) and 96 252 (2P28\_120).

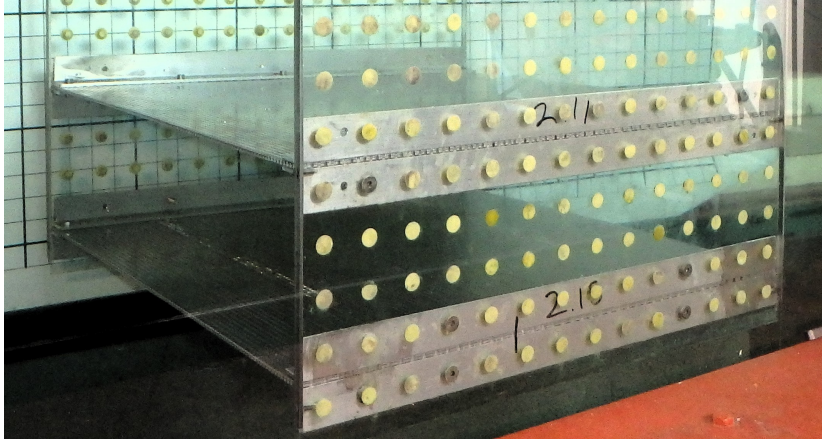


**Figure 9.5:** Photo of 2P28\_120, two ideal parallel perforated plates ( $\tau = 0.28$ ) with width  $D = 420$  mm and a gap distance of 120 mm.

### 9.2.1 Parallel versus single perforated plates

Normalized force plots for 2P28\_60 are presented in Fig. 9.6 for  $KC = 0.05$  (top subplot) and  $KC = 2.0$  (bottom subplot). The plots illustrate the total force as well as the individual forces on the upper and lower plates. Comparisons are made with the force on a corresponding single plate, P28. There is almost no difference between the force on the upstream plate and the force on the downstream plate of 2P28\_60 for  $KC = 0.05$ . Each plate has a force that resembles the force on the single P28 plate. Nevertheless, close inspection reveals that there are minor differences, suggesting minor interaction effects even at this small  $KC$  number. The amplitude of the force on the parallel configuration is slightly smaller. In addition, the phase is shifted a little to the left, indicating that the force in the parallel configuration is shifted away from the prescribed velocity ( $\propto \sin \omega t$ ) and towards the prescribed acceleration ( $\propto \cos \omega t$ ). Consequently, the relative importance of the damping force to the added mass force is reduced for the parallel plates compared to the single plate. For  $KC = 2.0$ , large differences are found between the forces on each plate, in particular, there is a strong wake effect which reduces the force amplitude on the downstream plate. Compared to the corresponding

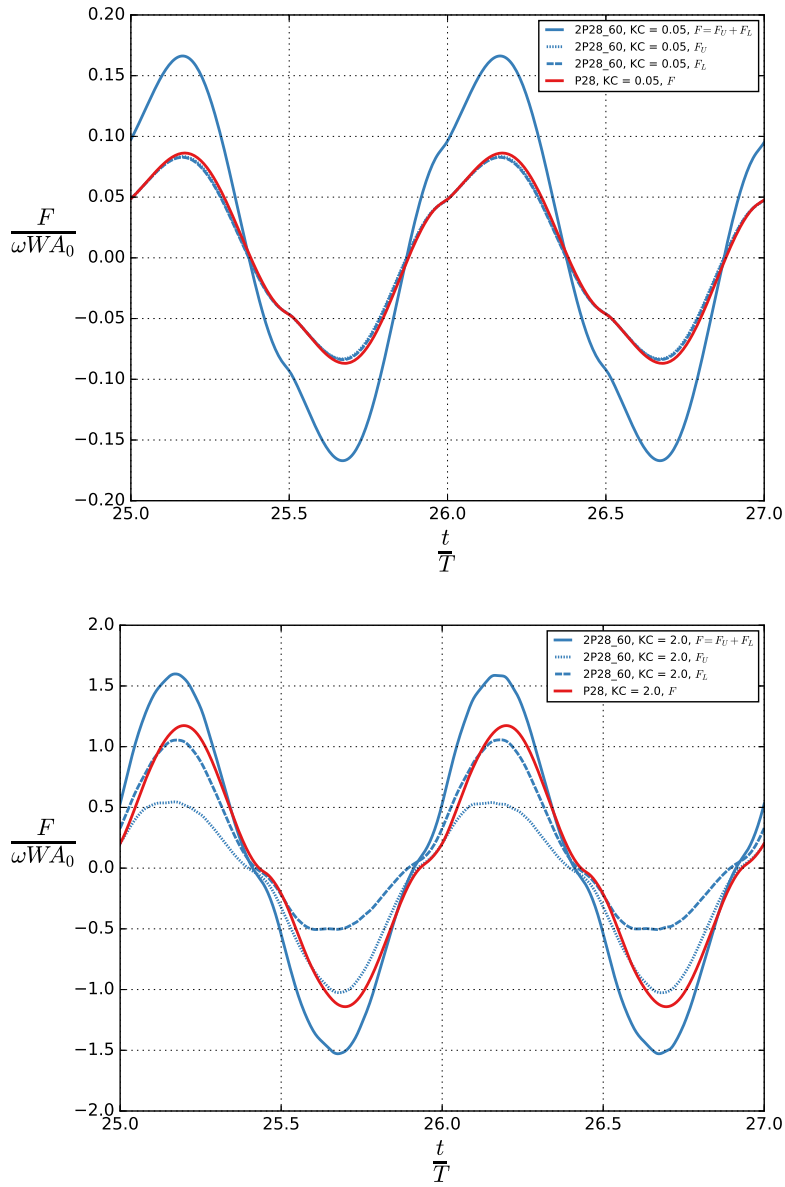


**Figure 9.6:** The normalized force on 2P28\_60 during two oscillation cycles of the numerical simulations at  $KC = 0.05$  (top) and  $KC = 2.0$  (bottom). Comparison with the force on the corresponding single plate, P28.

single plate, P28, the individual forces on both plates are reduced considerably. Further, a shift in phase towards the acceleration is noted, i.e., reduced damping force to added mass force ratio in the parallel case compared to the single plate.

The added mass and damping coefficients from the experimental investigations and numerical simulations of parallel configurations are presented in Fig. 9.7. The agreement between experimental and numerical results is in general good. In general, the coefficients depend on both KC and the vertical gap between the plates. Nonetheless, despite some differences between the three gap distances, overall the hydrodynamic coefficients are quite similar. Note that the range of tested ratios of the vertical gap distance to the width of the plates is limited; the ratios are 0.143 (2P28\_60), 0.214 (2P28\_90) and 0.286 (2P28\_120). The calculated potential flow added mass coefficients are very similar between the three configurations,  $\frac{A}{A_0} = 0.0647$  (2P28\_60),  $\frac{A}{A_0} = 0.0652$  (2P28\_90) and  $\frac{A}{A_0} = 0.0650$  (2P28\_120). Thus, only the last plotted marker and line (2P28\_120) are visible in the figure.

Included in Fig. 9.7 are the experimentally obtained coefficients for a single perforated plate multiplied by two, that is, superposition of a corresponding single plate. The plots suggest that interaction effects of parallel perforated plates are not very important for the added mass coefficients, meaning that simple superposition of the added mass of two single perforated plates could be a sufficient approach. This is especially true for  $KC < 0.8$ . For  $KC > 0.8$ , there are somewhat larger differences. Nevertheless, for all tested KC numbers and gap distances, the presently investigated parallel perforated plate configurations yield added mass coefficients that are similar (typically within 15%) to that of two corresponding single plates. Notably, this is not the case for solid plates [26, 66, 67]. In their study of multiple heave plates, Zhang and Ishihara [66] found that if the gap distance between two octagonal disks attached to a cylindrical column is relatively small, the added mass is similar to that of one single disk, whereas if the gap distance is relatively large, the added mass is similar to that of two single disks. For a range of gap distances between the two extremes, the added mass is between that of one and that of two solid disks [66]. Corresponding findings are presented by Tao et al. [67] for two circular disks attached to a cylinder, in which the KC number dependence is highlighted, i.e., the interaction between the plates, and the influence on the coefficients, depend on the gap distance and the KC number. Note that for the presently investigated parallel plate configurations, within the range of tested KC numbers, the added mass coefficient is always smaller than one (the potential flow added mass for a solid flat plate). The perforation ratio of the plates is  $\tau = 0.28$ ; larger added mass coefficients should be expected for smaller perforation ratios since more water must circumvent the plates.

Interestingly, for a given KC larger than 0.8, the added mass is in general smaller for 2P28\_60 than for two times the single plate, while it is larger for 2P28\_120 than for two times the single plate. Tian et al. [26] found a somewhat similar result for solid plates. They found that the added mass coefficients for parallel solid plates could become smaller than that of a single plate if the KC number

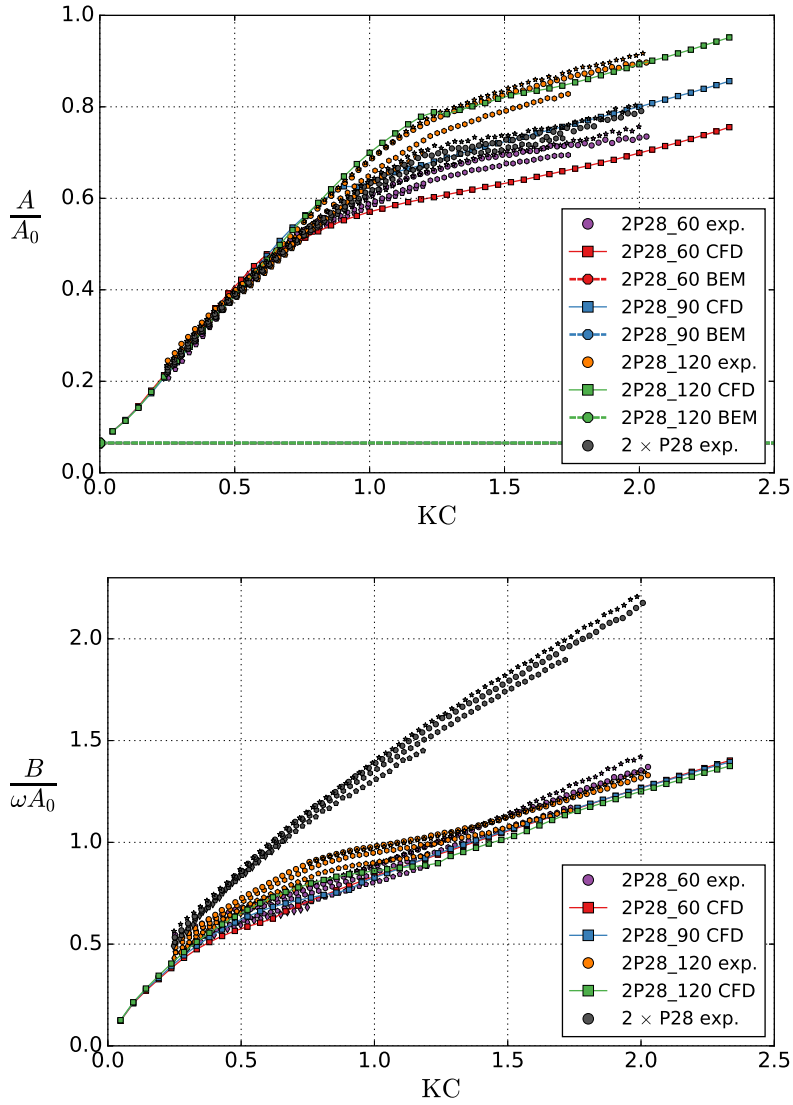


**Figure 9.7:** Added mass and damping coefficients from experimental investigations and numerical simulations of 2P28\_60, 2P28\_90 and 2P28\_120. The ratios of the gap distance to the width of the plates are 0.143 (2P28\_60), 0.214 (2P28\_90) and 0.286 (2P28\_120). Comparisons with two times the experimentally obtained coefficients of a single perforated plate, P28.

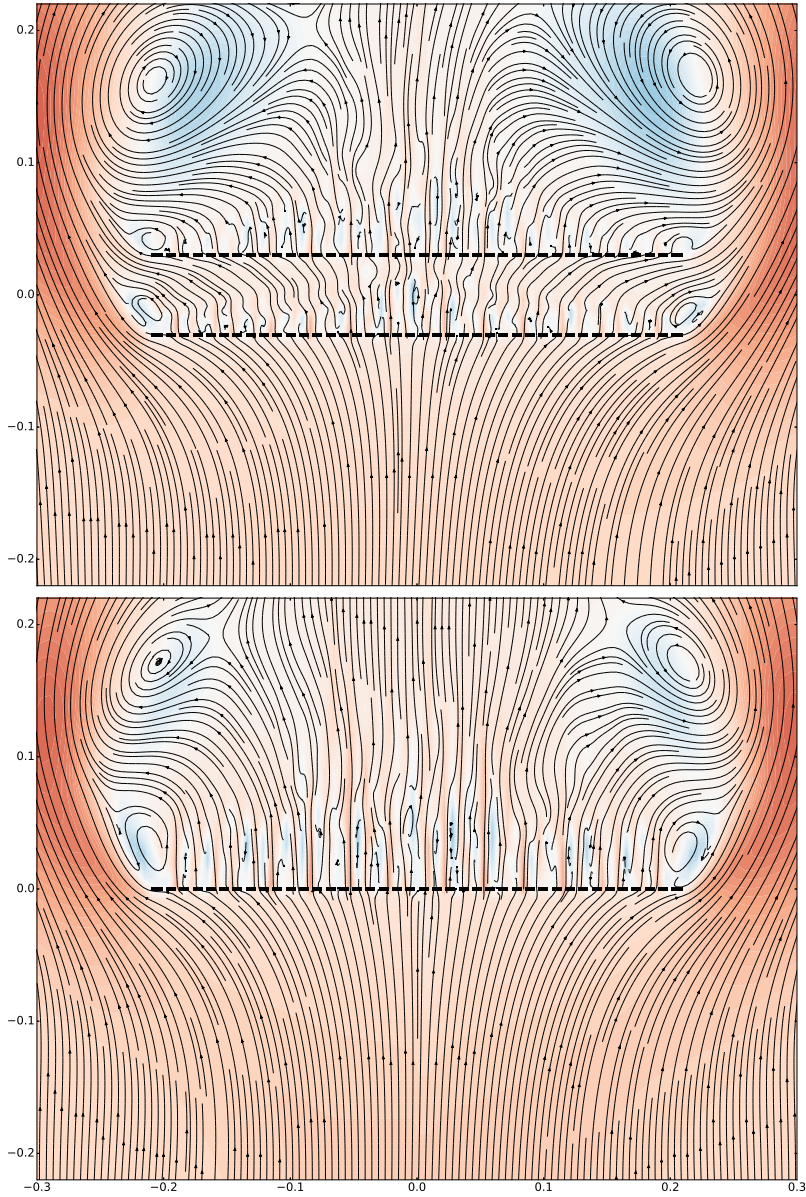


**Figure 9.8:** Flow visualizations of 2P28\_60 (top) and a corresponding single plate (bottom) with oscillating flow conditions for  $KC = 1.95$ . The time-instant is  $0.32T$  into an oscillation period ( $u = 0$ ,  $w = \frac{D}{\tau}KC \sin \omega t$ ). Color contours applied to the vertical velocity (red: positive, blue: negative).



was large and the gap distance was very small, cf. Section 1.4.5. However, unlike their results, all the presently investigated parallel perforated plate configurations have larger added mass coefficients than that of one corresponding single plate.

Contrary to the added mass coefficients, the superposition approach overestimates the damping coefficients considerably. For large KC numbers, the damping coefficients of two single plates are 40-60 % larger than those of the parallel configurations, but even for the smallest tested KC numbers, there is an interaction effect which reduces the damping coefficient of the parallel configurations compared to two single plates.

Differences between single and parallel perforated plates are illustrated with flow visualizations plots in Fig. 9.8. Streamlines are presented for 2P28\_60 and the corresponding single plate for  $KC = 1.95$  at a time-step that is  $0.32T$  into an oscillation period ( $u = 0$ ,  $w = \frac{D}{T}KC \sin \omega t$ ). The red-blue colormap presented in Fig. 6.13 is used to indicate the vertical velocity. Normalization of the colormap is made against two times the prescribed amplitude of the velocity at the boundaries, that is, the darkest blue ( $-1.0$  in Fig. 6.13) corresponds to  $w = -2\frac{D}{T}KC$  and the darkest red ( $1.0$  in Fig. 6.13) corresponds to  $w = 2\frac{D}{T}KC$ . Clearly, the extent of the global plate-end vortices is much larger than the distance between the two plates. Consequently, two combined (not four separated) plate-end vortices are generated downstream of the parallel plate configuration. These vortices are larger than what is found for the corresponding single perforated plate. However, the combined wake and pressure drop should not be expected to be twice that of a single plate.

### 9.2.2 Wave-radiation damping

A reason for deviations between the numerical viscous flow solver results and the experimental results is free-surface effects, not included in the infinite fluid simulations. The harmonic oscillations of the models generate waves in the experiments. The corresponding wave-radiation damping is calculated from energy relations [6, p. 47],

$$B_w = \frac{\rho g^2 \zeta_a^2 L}{\eta_a^2 \omega^3}. \quad (9.1)$$

In Eq. (9.1),  $\zeta_a$  is the amplitude of the radiated waves. Further,  $\rho$  is the water density,  $g$  is the gravity of Earth,  $L = 0.6$  m is the lateral dimension of the wave flume,  $\eta_a$  is the oscillation amplitude and  $\omega$  is the oscillation frequency.

The wave-radiation damping coefficients,  $\frac{B_w}{\omega A_0}$ , are presented in Fig. 9.9. The wave-radiation damping coefficients increase, in general, with increasing KC number, and depend on the period of oscillation. The largest experimentally tested configuration (2P28\_120) yields, in general, somewhat larger wave-radiation damping coefficients than the smallest configuration (2P28\_60).  $\frac{B_w}{\omega A_0}$  is in general below 0.12 and therefore rather small compared to  $\frac{B}{\omega A_0}$ , although not negligible.

In Fig. 9.10, the ratio between the wave-radiation damping and the total damping is presented. A summary is given in Table 9.1; the mean ratio for all

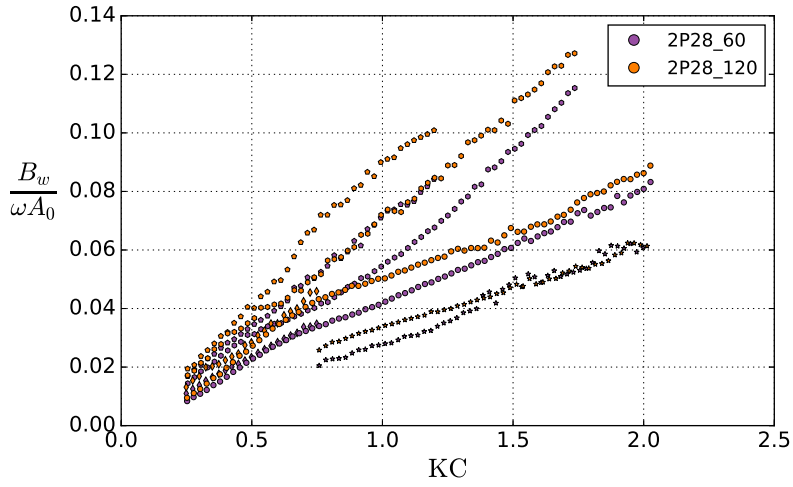


**Figure 9.9:** Wave-radiation damping,  $B_w$ , due to radiated waves in the forced oscillation experiments of P28\_60 and P28\_120. The markers for the five oscillation periods are presented in Fig. 6.5.

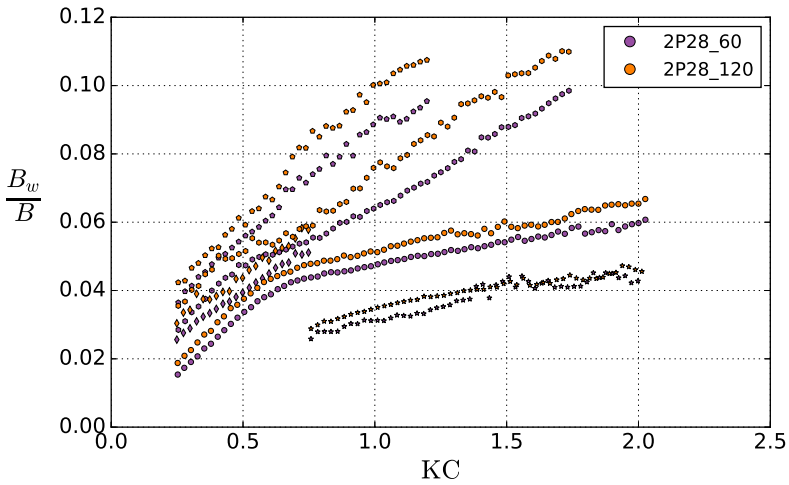


**Figure 9.10:** Ratio between wave-radiation damping and the total damping in the forced oscillation experiments of P28\_60 and P28\_120. The markers for the five oscillation periods are presented in Fig. 6.5.



tested KC numbers, as well as the maximum and minimum ratios are given. Typically, the wave-radiation damping coefficients are within 8 % of the total damping. For oscillation periods  $T = 1.25$  s and  $T = 1.50$  s, the largest tested KC numbers yield wave-radiation damping that exceeds 8 % of the total damping. The largest relative wave-radiation damping is obtained for 2P28\_120 with  $T = 1.50$  s and  $KC = 1.7$ , where the wave-radiation damping is 11 % of the total damping. The slight underestimation of the damping coefficients predicted with the numerical viscous flow solver, cf. Fig. 9.7, is of same order as the wave-radiation damping contributions in the experiments.

**Table 9.1:** Ratio between wave radiation damping and total damping,  $\frac{B_w}{B}$ , of 2P28\_60 and 2P28\_120. Note that some of the differences between the periods are due to different KC ranges, cf. Fig. 9.10.

	$T$	Mean	Max	Min
2P28_60	1.00 s	4.0 %	5.1 %	2.6 %
	1.25 s	7.0 %	9.5 %	3.6 %
	1.50 s	6.5 %	9.8 %	2.8 %
	1.75 s	4.7 %	6.1 %	1.5 %
	2.00 s	3.7 %	4.5 %	2.6 %
2P28_120	1.00 s	4.5 %	5.8 %	3.0 %
	1.25 s	7.8 %	10.7 %	4.2 %
	1.50 s	7.4 %	11.0 %	3.6 %
	1.75 s	5.1 %	6.7 %	1.9 %
	2.00 s	3.9 %	4.7 %	2.9 %

### 9.2.3 Parallel plates in orbital versus oscillating flows

In addition to the experiments and numerical simulations of oscillating flow conditions, the parallel configurations are simulated in orbital flow conditions. The resulting coefficients are presented in Fig. 9.11. Comparisons are made with the numerical simulations of oscillating flow conditions.

In general, the coefficients are similar for small KC numbers, and deviate between different configurations and flow conditions for higher KC numbers. All configurations and flow conditions have similar added mass coefficients for  $KC < 0.7$ . For higher KC numbers, the added mass coefficients are, in general, reduced in orbital flow compared to oscillating flow conditions. An exception is 2P28\_60 for  $0.9 < KC < 2.0$ . The damping coefficients deviate in general more than the added mass coefficients for the two flow conditions. Orbital flow conditions, compared to oscillating flow, reduce the damping coefficients for all configurations. Similar tendencies are found for single perforated plates; the normalized hydrodynamic force amplitude and coefficients are similar for small KC numbers and reduced in orbital compared to oscillating flow for high KC numbers, cf. Section 7.3.

The normalized hydrodynamic force amplitude is presented in Fig. 9.12. The

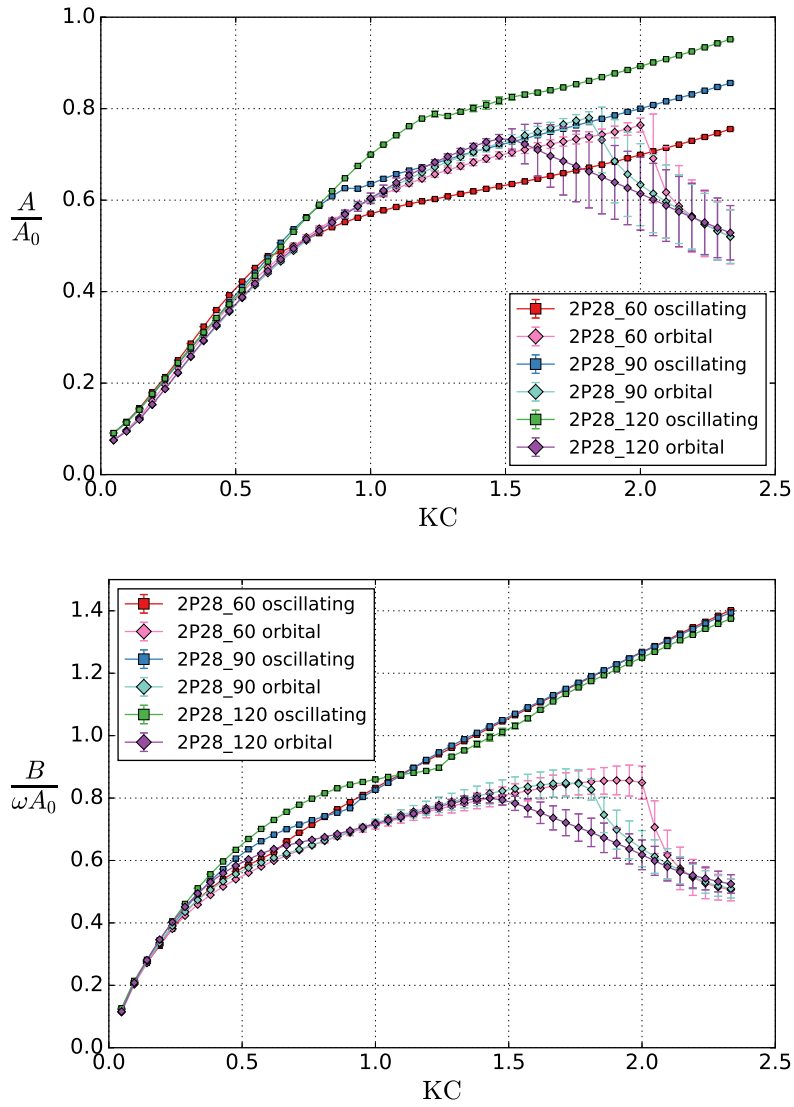


**Figure 9.11:** Added mass and damping coefficients from numerical simulations of 2P28 in oscillating flow and orbital flow conditions.

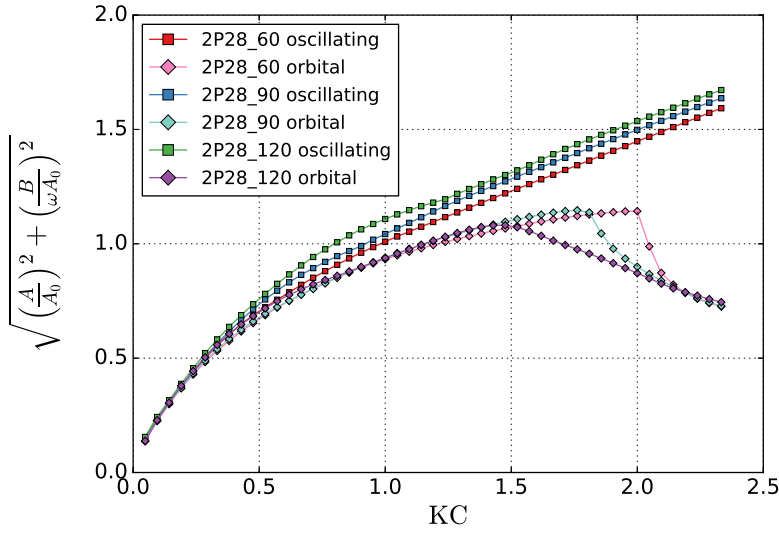


**Figure 9.12:** The normalized force amplitude from numerical simulations of 2P28 in oscillating flow and orbital flow conditions.

force reduction in orbital compared to oscillating flow conditions is found to depend on the gap between the two perforated plates in parallel. The maximum normalized force amplitude in orbital flow is at  $KC = 2.00$  (2P28\_60),  $KC = 1.76$  (2P28\_90) and  $KC = 1.48$  (2P28\_120). To investigate the effect on the total force of the configuration, caused by interaction between the two plates in orbital motion, flow visualization plots of 2P28\_60 are studied at  $KC = 1.95$  and  $KC = 2.05$ , that is, slightly below and above  $KC = 2.0$  which yields the largest normalized force amplitude. The flow visualizations are presented in Figs. 9.13–9.17. The colormap for the contours, cf. Fig. 6.13, represents the vertical velocity. Normalization of the colormap is made against two times the prescribed amplitude of the velocity at the boundaries corresponding to  $KC = 2$ , that is, the darkest blue ( $-1.0$  in Fig. 6.13) corresponds to  $w = -4\frac{D}{T}$  and the darkest red ( $1.0$  in Fig. 6.13) corresponds to  $w = 4\frac{D}{T}$ .

In Figs. 9.13 and 9.14, streamline plots covering the full model and surrounding flow patterns of 2P28\_60 in orbital flow conditions for  $KC = 1.95$  and  $KC = 2.05$  are presented. The plots are obtained at two time-steps early in the oscillation cycle. The arrow indicates the ambient prescribed flow direction. The red-blue color scale represents the vertical velocity (red positive upwards, blue positive downwards). Despite the small difference in the prescribed velocity, relatively large differences in the flow fields are demonstrated. In particular, the large vortex upstream of the right part of the lower plate, generated during an earlier phase

when the vertical velocity was negative, is considerably larger for  $KC = 2.05$  compared to  $KC = 1.95$ .

Figures 9.13 and 9.14 illustrate that the vortex ceases to exist at an earlier time instant for  $KC = 1.95$  than for  $KC = 2.05$ . In order to investigate the reason for this, flow visualizations of a zoomed-in section of the right part of the plates are presented in Figs. 9.15–9.17, for time-instants about one half-cycle prior to those in Figs. 9.13 and 9.14. Both the prescribed vertical and horizontal velocity components are negative at these time-instants, that is, the ambient flow is from upper right to lower left. These time-instants are selected as they illustrate the development of the large vortex below the right part of the lower plate in Figs. 9.13 and 9.14. Flow separation from the right plate-end of the upper plate, and global deflection of the flow, is observed at the first of these time-instants, cf. Fig. 9.15. As time increases, cf. Fig. 9.16, and the ambient horizontal velocity increases in magnitude from right to left, the plate-end vortex generated from the upper plate loses its strength in the case of  $KC = 1.95$ . Further in time, cf. Fig. 9.17, flow enters between the two plates from right to left. Contrary, for  $KC = 2.05$ , the vortex in between the plates remains for a longer time, and the flow continues to deflect globally around the whole configuration. The flow visualizations illustrate how slight differences in the flow separation from the right plate-end of the top plate plays a role in global flow behavior; the vortex blocks the flow into the gap. This results in a higher incident velocity on the lower plate, with resulting stronger vortex shedding (as was clearly shown in Fig. 9.13).

Note that the asymmetric flow patterns of orbital flow is not found in oscillating flow. Contrary, the flow field is very symmetric in oscillating flow conditions. An illustration is presented in the top subplot of Fig. 9.8 which represents the exact same configuration and  $KC$  number as presented for orbital flow in the upper subplot of Figs. 9.13–9.17, that is, 2P28\_60 at  $KC = 1.95$ . The global plate-end vortices in Fig. 9.8 continue to grow for increasing time-steps before the direction of the prescribed velocity turns at  $t = 0.5T$ . Furthermore, no inflow between the parallel plates is observed in oscillating flow.

Large standard deviations, indicating variations in the force between each oscillation cycle, were demonstrated in Fig. 9.11 in the hydrodynamic coefficients from orbital flow simulations for large  $KC$  numbers, in particular for the added mass coefficient for  $KC > 2$  (2P28\_60),  $KC > 1.8$  (2P28\_90) and  $KC > 1.5$  (2P28\_120). Taking into account the findings from inspection of streamlines in Figs. 9.13–9.17, it is likely that the plate-end flow separation, vortex generation and blocking of the flow into the gap between the plates, which is important for the force on the plates, is sensitive to small differences in the flow around these  $KC$  numbers, and that this causes the variations in the force. An illustration of this is given in Fig. 9.18 where time-series of the force on 2P28\_60 in orbital flow conditions at  $KC = 1.95$ , 2.05 and 2.14, for the whole length of the simulation, is presented. For  $KC = 1.95$ , the force increases from the ramp and reaches what seems to be near steady-state after the 10-12 first periods of oscillation. Contrary, for  $KC = 2.05$  and  $KC = 2.14$  the force decreases after an initial increase, and

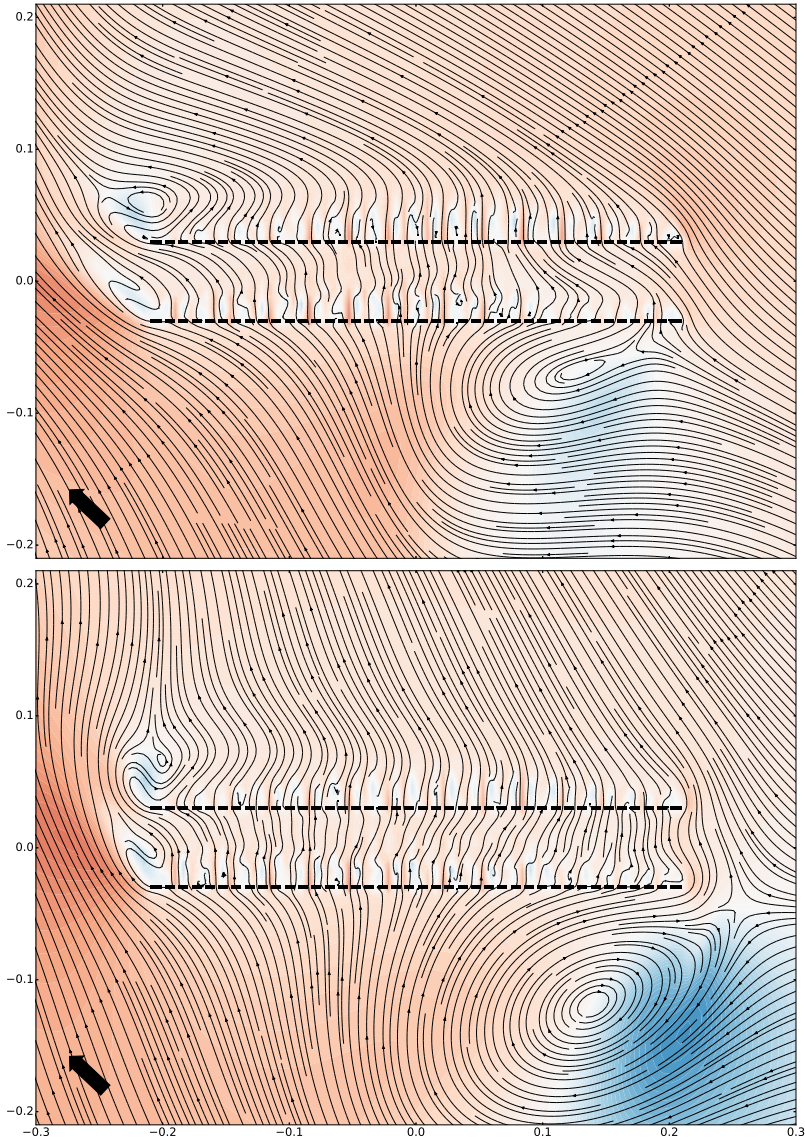


**Figure 9.13:** Flow visualizations of 2P28\_60 with orbital flow conditions for  $KC = 1.95$  (top) and  $KC = 2.05$  (bottom). The time-instant is  $0.12T$  into an oscillation period ( $u = -\frac{D}{T}KC \cos \omega t$ ,  $w = \frac{D}{T}KC \sin \omega t$ ). The colormap for the contours represent the vertical velocity (red for positive, blue for negative).

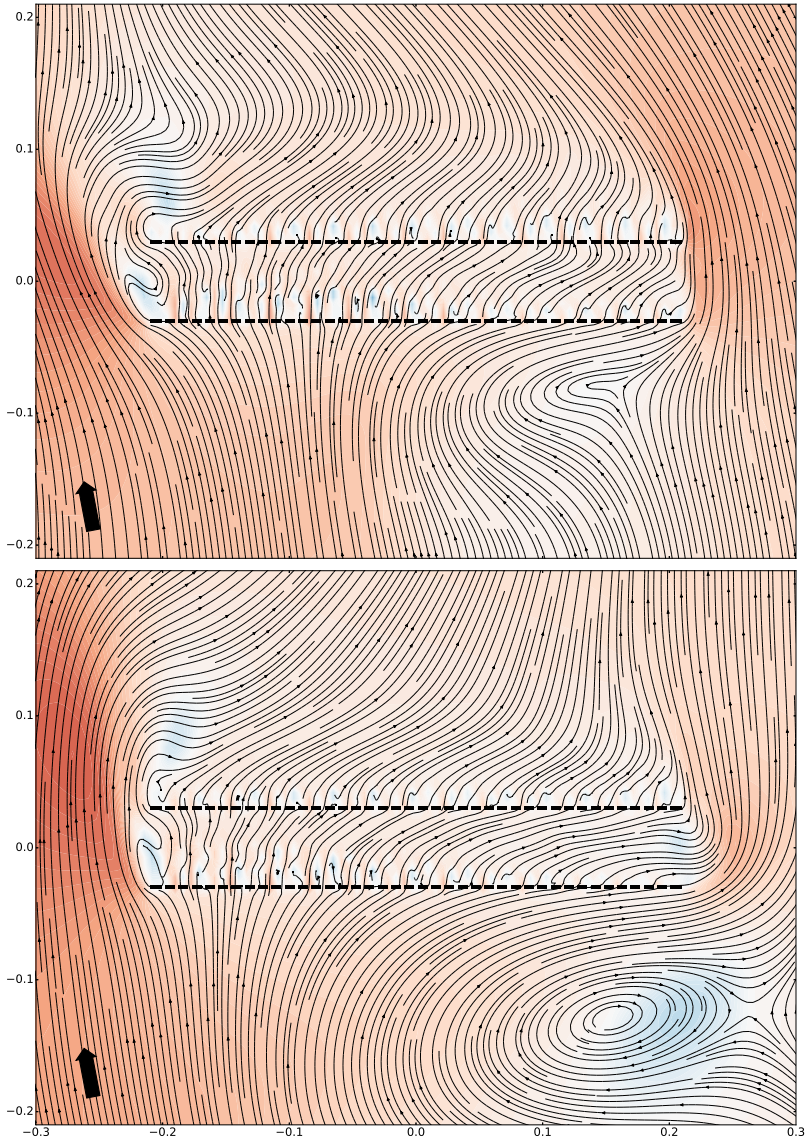


**Figure 9.14:** Flow visualizations of 2P28\_60 with orbital flow conditions for  $KC = 1.95$  (top) and  $KC = 2.05$  (bottom). The time-instant is  $0.22T$  into an oscillation period ( $u = -\frac{D}{T}KC \cos \omega t$ ,  $w = \frac{D}{T}KC \sin \omega t$ ). The colormap for the contours represent the vertical velocity (red for positive, blue for negative).



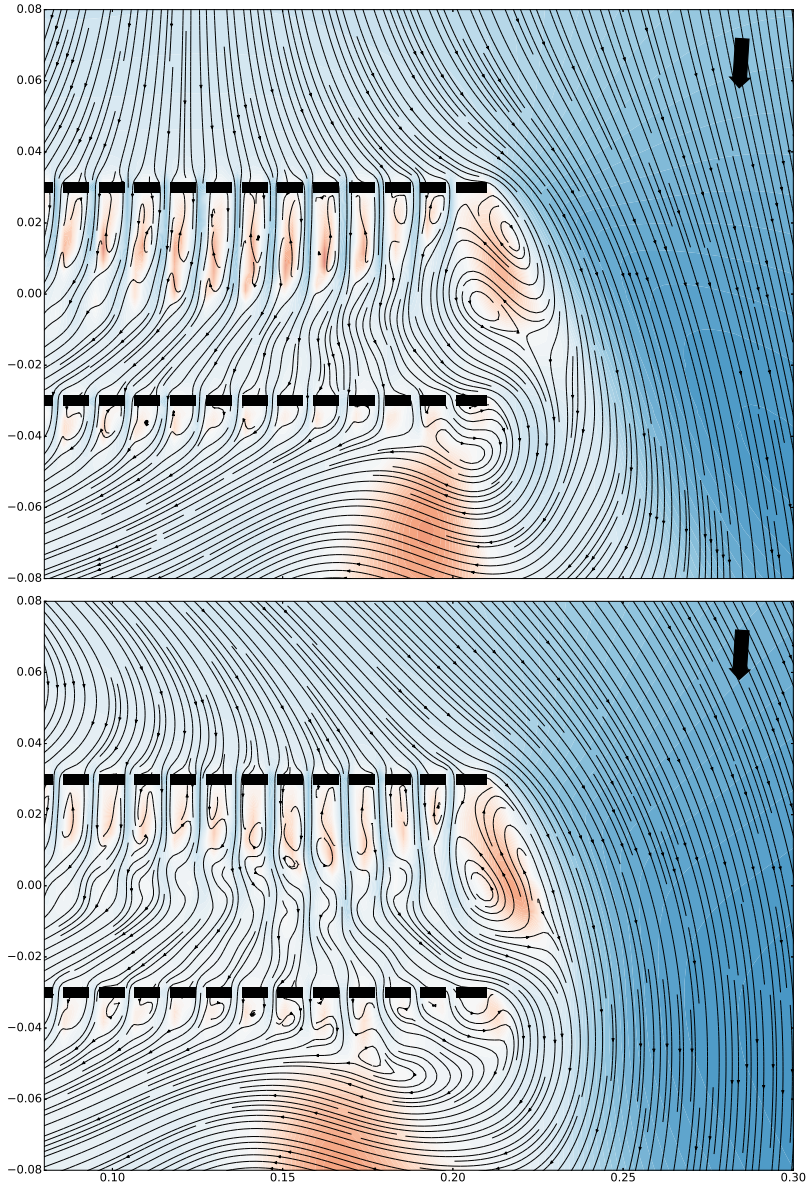


**Figure 9.15:** Flow visualizations zoomed in on the right part of 2P28\_60 with orbital flow conditions for  $KC = 1.95$  (top) and  $KC = 2.05$  (bottom). The time-instant is  $0.76T$  into an oscillation period ( $u = -\frac{D}{T}KC \cos \omega t$ ,  $w = \frac{D}{T}KC \sin \omega t$ ).

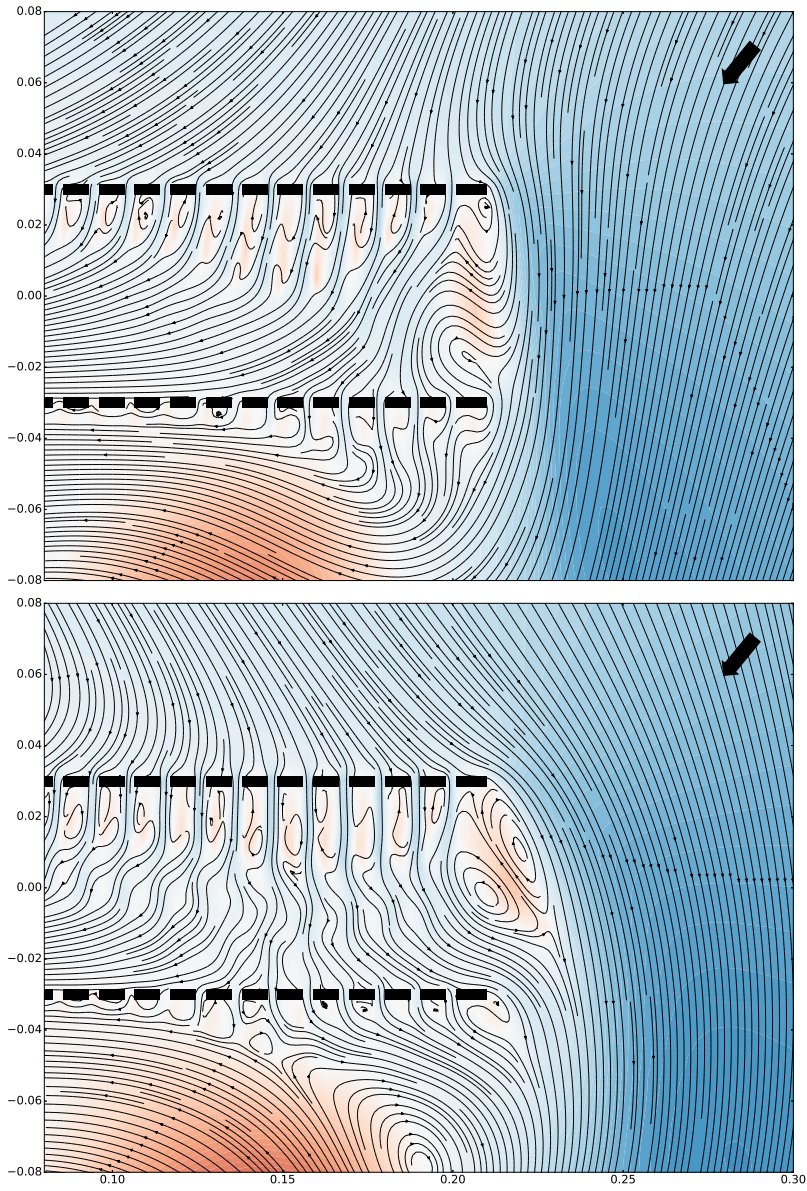


**Figure 9.16:** Flow visualizations zoomed in on the right part of 2P28\_60 with orbital flow conditions for  $KC = 1.95$  (top) and  $KC = 2.05$  (bottom). The time-instant is  $0.86T$  into an oscillation period ( $u = -\frac{D}{T}KC \cos \omega t$ ,  $w = \frac{D}{T}KC \sin \omega t$ ).



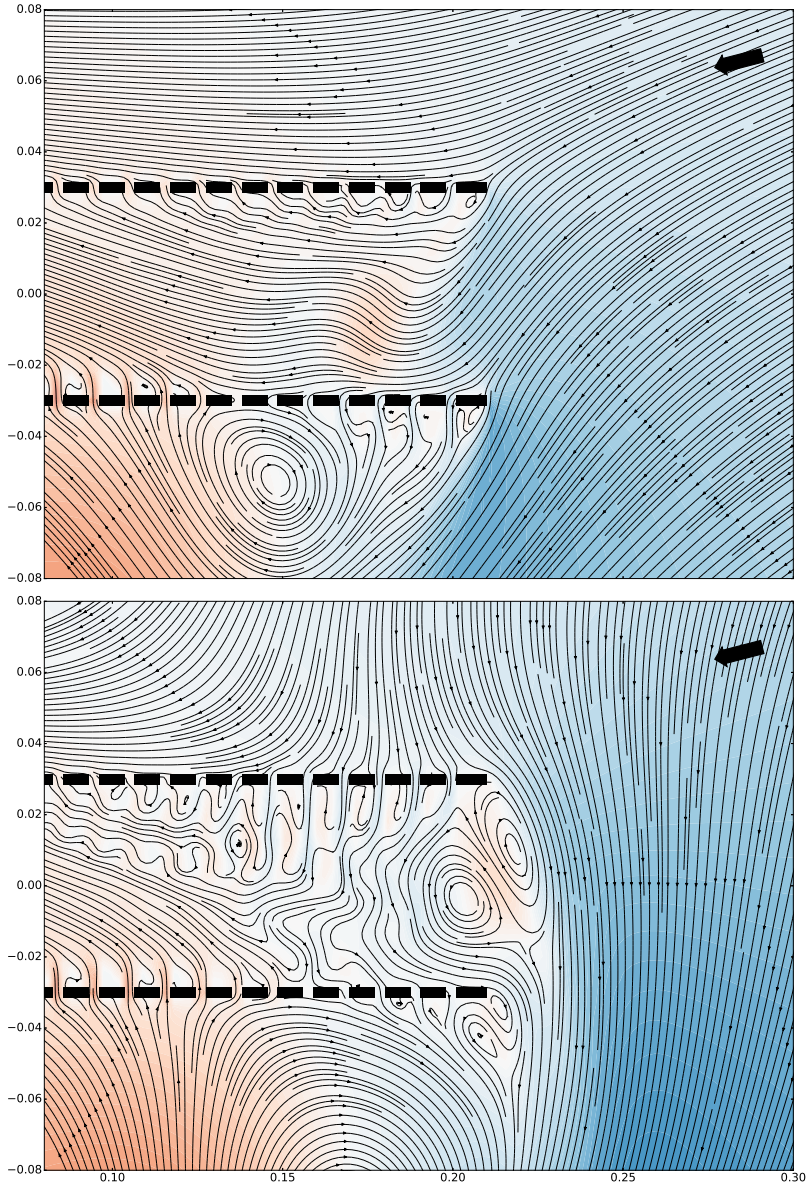


**Figure 9.17:** Flow visualizations zoomed in on the right part of 2P28\_60 with orbital flow conditions for  $KC = 1.95$  (top) and  $KC = 2.05$  (bottom). The time-instant is  $0.96T$  into an oscillation period ( $u = -\frac{D}{T}KC \cos \omega t$ ,  $w = \frac{D}{T}KC \sin \omega t$ ).

then oscillates with a smaller amplitude of motion during the rest of the simulation. These variations in force amplitude yield large standard deviations in the coefficient plots since a time-window extending from  $t = 5T$  to the end of the simulation,  $t = 30T$ , is used. There is always a questions regarding what time-interval to use. Choosing a shorter time-interval towards the end of the time-series where one seemingly has reached, at least partly to some degree, a steady state, would further decrease the mean values of the added mass and damping coefficients, while considerably reducing the standard deviation.

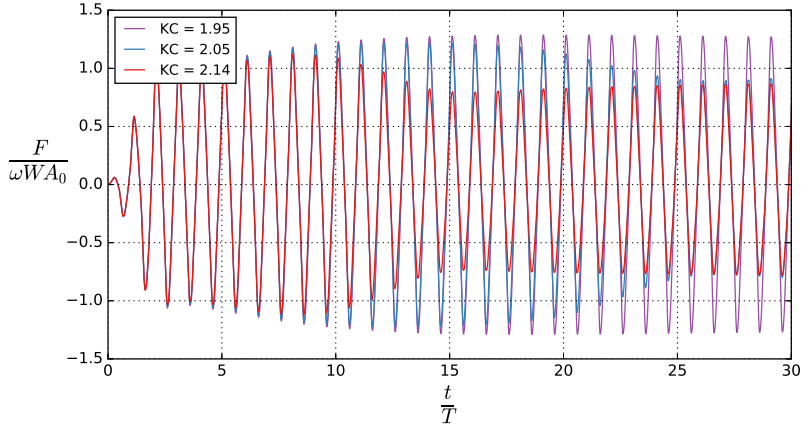


**Figure 9.18:** Time-series of the nondimensional force on 2P28\_60 in orbital flow at  $KC = 1.95$ ,  $KC = 2.05$  and  $KC = 2.14$ .

The large variations in force and coefficients occur for large KC numbers, but for smaller structures these KC numbers can be relevant. However, real sea states are irregular. Steady state does not exist. As (almost poetically) stated by Bezunartea-Barrio et al. [37], during movement in irregular seas, a structure is constantly transitioning through different KC numbers. A practical question then becomes what KC number to choose in a typical industrial study, and how to estimate the force that the structures will be exposed to during a lifting operation. The present results for parallel perforated plates suggest that for a given KC number, coefficients from oscillating flow conditions yield similar or somewhat larger hydrodynamic force amplitude than if estimated based on orbital flow conditions. Corresponding results were obtained for a single perforated plate, cf. Section 7.3. Hence, oscillating flow studies are relevant for estimating the hydrodynamic force on perforated platelike structures in waves.

### 9.3 Hydrodynamic interaction of perforated plates and channel walls

In an attempt to investigate the forces on ideal perforated plates without allowing the massive flow separation at the plate-ends, experiments and numerical simulations were set up using channel walls on both sides of the experimental rig. This allows for testing of oscillating flow conditions inside a channel. The ideal perforated plates P19 and P28 were tested in this channel configuration. The channel walls were placed approximately 2 cm from the ends of the perforated plates in both the experiments and the numerical simulations. Results from the channel flow investigations are denoted with a C appended to the model name, that is, P19C and P28C for, respectively, the ideal perforated plates with perforation ratios  $\tau = 0.19$  and  $\tau = 0.28$ .

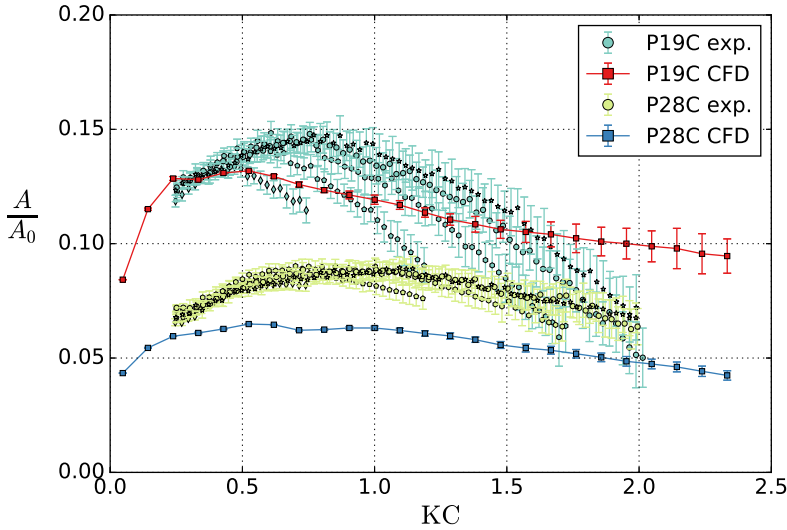


**Figure 9.19:** Added mass coefficients from experimental investigations and numerical simulations of P19C and P28C.

The added mass and damping coefficients of P19C and P28C are presented in Figs. 9.19 and 9.20. When the plates are forced to oscillate inside the channel, vortex shedding from flow separation at the plate-ends will be limited. The possibility for the fluid to flow around the plate is also limited, since the water is forced to pass the plate either through the perforated openings or through the small gaps between the plate-end and the channel walls. As a result, the force that acts on the plate will be in almost exact phase with the velocity of the ambient flow or plate, and therefore completely dominated by a large damping force (and

correspondingly large damping coefficient), and only yields a minor added mass coefficient. Note the difference in y-axis in the plots; the damping coefficients are dominating completely. Both the experimental and numerical results indicate a nearly perfect linear relation between the damping coefficient and KC, meaning that a quadratic pressure-loss model is very good for this setup. Consequently, if a quadratic damping model is applied, the quadratic damping coefficient ( $C_D$ ) is almost constant with KC.

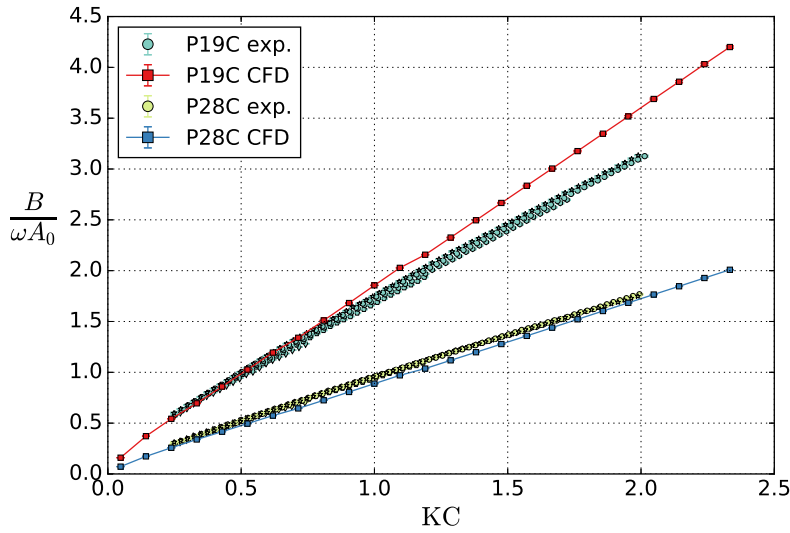


**Figure 9.20:** Damping coefficients from experimental investigations and numerical simulations of P19C and P28C.

The numerical and experimental channel flow added mass coefficients agree reasonable well. One reason for differences between the numerical and experimental results is uncertainty related to the distance from the plate-ends to the channel walls; neither the channel walls nor the experimental rig are perfectly straight. Consequently, the distance from the plate-ends to the channel walls vary slightly during an oscillation period. Further, some period dependence in the experiments are noted, in particular for P19C where the drop in added mass occurs at different KC numbers for different periods of oscillation. This can be related to free-surface effects, not captured in the CFD simulations.

The total hydrodynamic force on the perforated plates is larger in channel flow conditions compared to open conditions. A presentation of the normalized force amplitude, i.e., the square root of the sum of the normalized added mass and damping coefficients squared, is given in Fig. 9.21. For the smallest KC numbers tested, the normalized force amplitude on the plates are similar in open condi-

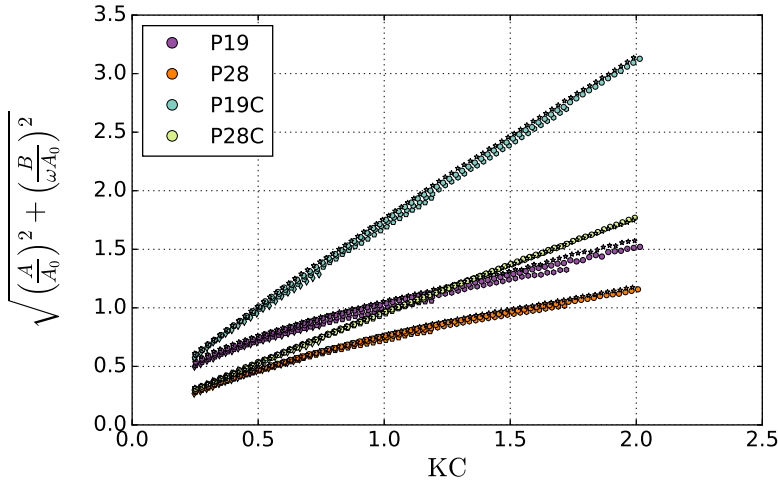


**Figure 9.21:** The normalized force amplitude on P19, P28, P19C and P28C.

tions and in the channel. Contrary, for moderate and large KC numbers, there is a considerable larger force in the channel. The effect is dependent on the perforation ratio; increasingly so as the perforation ratio is decreased. The fact that the hydrodynamic force on the plates increases considerably in channel flow conditions, and that the damping force is dominating completely, can have relevance for operations performed in an environment restricted by walls or boundaries. Moonpool operations, where objects are lowered through an opening in the hull of the ship, is a relevant example.

Differences between open and channel flow conditions are illustrated in Fig. 9.22. Here, flow visualizations from the numerical simulations of the perforated plate with  $\tau = 0.19$ , are presented for  $KC = 1.0$ . The plots are obtained at a time-step 28 % into an oscillation period, that is, the vertical velocity is  $w = \frac{D}{T} \sin(0.6\pi)$  at the boundaries. The colormap for the contours, cf. Fig. 6.13, represents the vertical velocity. Normalization of the colormap is made against three times the prescribed amplitude of the velocity at the boundaries, that is, the darkest blue ( $-1.0$  in Fig. 6.13) corresponds to  $w = -3\frac{D}{T}KC$  and the darkest red ( $1.0$  in Fig. 6.13) corresponds to  $w = 3\frac{D}{T}KC$ . In both channel and open conditions, the fluid flow is forced through the perforations of the plates. Further, in open conditions, large vortices are developed from the plate-ends. For channel flow conditions, a similar vortex is not seen. Instead, the fluid between the plate and the channel wall is accelerated in the vertical direction, similar to the acceleration of fluid through the openings, but to a greater extent.

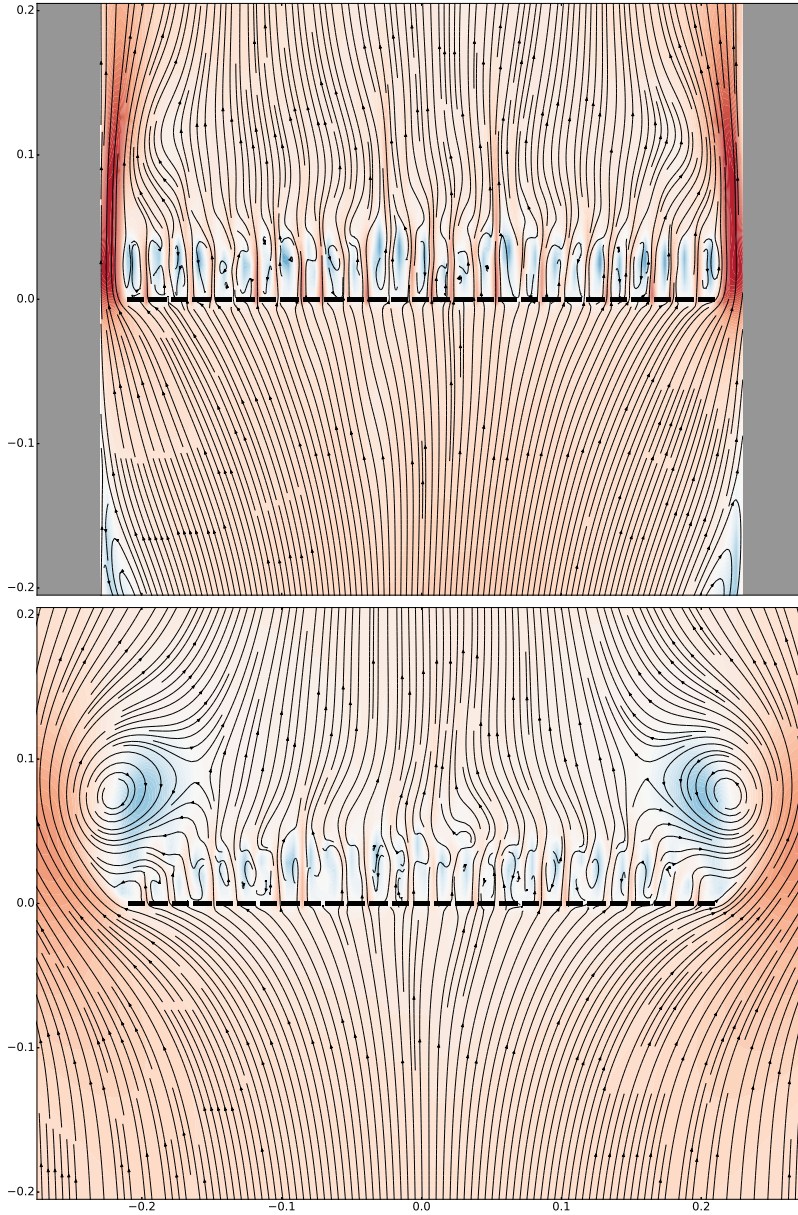


**Figure 9.22:** Streamline plots of a perforated plate in channel, P19C (top), and a perforated plate in infinite fluid, P19 (bottom), at  $KC = 1.0$ . The colormap for the contours represent the vertical velocity (red for positive, blue for negative).



## 9.4 Simplified mudmats

A mudmat is a relatively flat protection structure used on various subsea modules. Typically, a mudmat consists of plate elements with openings between them. The plate elements can have small holes, but the perforation ratio of these plate elements is usually very small.

In addition to single solid plates, our collaboration study—presented at OMAE in 2019 [62]—included simplified mudmats. The simplified mudmats consist of multiple solid plate elements placed next to each other with varying gaps between them. Each plate element is 60 mm wide and 4 mm thick. A photo of the plate elements, illustrating both the width and the thickness, is presented in Fig. 8.2.

When there are gaps between the plate elements, the open-area ratio of a simplified mudmat is

$$1 - \frac{n_p d}{D}, \quad (9.2)$$

with  $n_p$  being the number of plates,  $d = 60$  mm is the width of each plate element, and  $D$  is the total width of the configuration. Consequently, a simplified mudmat can be thought of as a perforated plate with perforation ratio equal to the open area ratio. In the hole size sensitivity study, cf. Section 5.5.2, small differences are in general found in the force coefficients when varying the number of plate elements used to model a perforated plate beyond a certain threshold value of  $n_p \simeq 7$ . Similar results have been observed in experimental studies [25, 26]. However, when the width of each plate element is relatively large and the number of openings is very small, as is relevant for mudmats, the perforated plate approximation is questionable. An example is for very small KC numbers in which the number of openings is the important parameter, not the perforation ratio, cf. Section 4.1.2.

The study of simplified mudmats includes configurations with one, two and three openings. An extended analysis of the two-plate configurations with a single opening between them is presented in the following. For results obtained for configurations consisting of more than one hole, I refer to the cited conference paper [62].

**Table 9.2:** Parameters of two-plate configurations. Illustrations in Fig. 9.23.  $d_g$  is the distance of the gap.

Configuration	Plates	Gap: $d_g$	$D$	$1 - \frac{n_p d}{D}$
$d_g = 0.5d$	$2 \times 60$ mm	30 mm	150 mm	0.2
$d_g = 1.0d$	$2 \times 60$ mm	60 mm	180 mm	0.33
$d_g = 1.5d$	$2 \times 60$ mm	90 mm	210 mm	0.43
$d_g = 2.0d$	$2 \times 60$ mm	120 mm	240 mm	0.5

Four configurations consisting of two plate elements with a single opening between them, are tested. The configurations are all similar except for the distance

of the gap,  $d_g$ , between the two plate elements. Tested gap distances between the two plates are  $d_g = 0.5d$ ,  $d_g = 1.0d$ ,  $d_g = 1.5d$  and  $d_g = 2.0d$ , with  $d$  being the width of a single plate element. Consequently,  $D$  in Eq. (9.2), and thus,  $KC \propto D^{-1}$  and  $A_0 \propto D^2$  vary between the configurations. In Table 9.2, the relevant parameters is presented; illustrations are provided in Fig. 9.23.

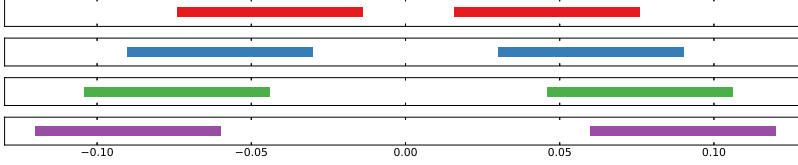


**Figure 9.23:** Illustrations of the four two-plate configurations, cf. Table 9.2.

The experimentally obtained hydrodynamic coefficients are presented in Figs. 9.24 and 9.25. The results are obtained for a period of oscillation equal to  $T = 2.00$  s. The coefficients are here normalized against two times the added mass of one single plate of width  $d$ , here denoted  $A_0^*$ ,

$$A_0^* = 2\rho\pi\frac{d^2}{4}L. \quad (9.3)$$

$L$  is the lateral distance of the physical model ( $L = 1$  in two-dimensional simulations). The amplitude of motion is normalized against two times the width of a single plate,

$$KC^* = 2\pi\frac{\eta_a}{2d}. \quad (9.4)$$

By utilizing this normalization, nondimensional coefficients are presented in terms of nondimensional amplitudes, but various gap distances can be compared directly. Included in the plots are the corresponding results from experiments of one plate element multiplied by two, which is the limiting case of having the two plates infinitely far apart. The corresponding analytical expressions by Graham [22], cf. Section 8.1, are also included.

Large differences are found in the added mass coefficients, in particular for large amplitudes of motion. The added mass is, in general, largest for the configuration with the smallest distance between the two plate elements. For  $KC^* < 4$ , the added mass of this configuration is similar to two times the added mass of the single plate. The configurations with larger gap distances have, in general, smaller added mass than two times the solid plate for  $KC^* < 4$ . For large amplitudes of motion, there is a large scatter in the added mass coefficients. The overall trend is that increasing the distance between the two plates reduces the added mass coefficient.

The added mass of the various configurations are calculated with the potential flow solver using 100 sources per plate element. The potential flow added mass of the two-plate configurations are larger than that of a single plate times two.



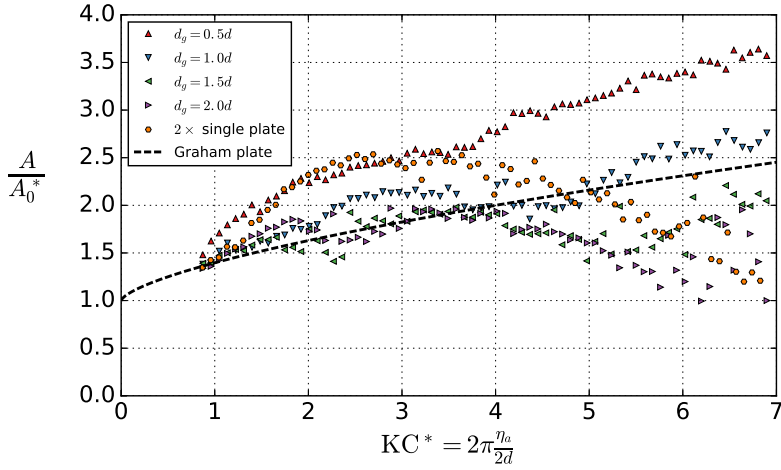


**Figure 9.24:** Added mass of two-plate configurations of varying gap distances. Normalization against the added mass of two times a solid plate of width  $d$ . Comparison with Graham's method for solid plates, cf. Section 8.1.

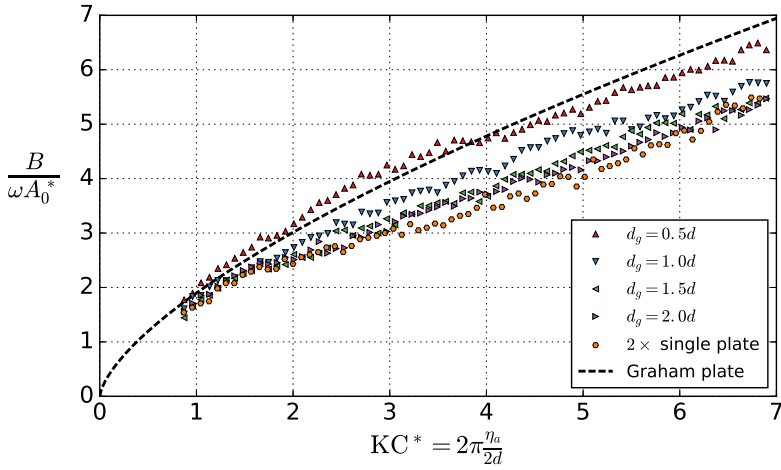


**Figure 9.25:** Damping of two-plate configurations of varying gap distances. Normalization against the added mass of two times a solid plate of width  $d$ . Comparison with Graham's analytical method for solid plates, cf. Section 8.1.

Compared to the potential flow added mass of a single plate times two ( $\frac{A}{A_0^*} = 1.107$ ), the two-plate configurations yield the following increases: 9.8 % ( $d_g = 0.5d$ ), 4.9 % ( $d_g = 1.0d$ ), 2.9 % ( $d_g = 1.5d$ ), and 1.9 % ( $d_g = 2.0d$ ).

The relative differences in damping are smaller between the various configurations. All two-plate configurations have, in general, larger damping than two times the solid plate. In general, the damping reduces when the distance between the plates is increased. A likely reason is that the flow is accelerated in the gap opening, increasing the strength of the flow separation which increases the damping. Note that all configurations are damping dominant, cf. the y-axes of Figs. 9.24 and 9.25. Consequently, the normalized force amplitude is dominated by damping. The damping dominance increases, in general, with increasing  $KC^*$ . A consequence of this is that the large scatter in added mass for  $KC^* > 4$  is of little importance for the force on the models.

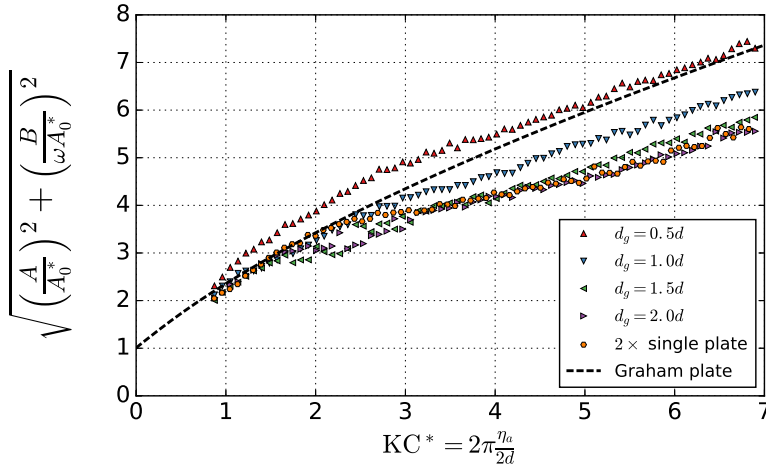


**Figure 9.26:** Normalized force amplitude of two-plate configurations of varying gap distances. Comparison with Graham's method for solid plates, cf. Section 8.1.

In Fig. 9.26, the normalized force amplitude is presented. The normalized force amplitude is here expressed as

$$\frac{F_a^*}{\omega^2 \eta_a A_0^*} = \sqrt{\left(\frac{A}{A_0^*}\right)^2 + \left(\frac{B}{\omega A_0^*}\right)^2}. \quad (9.5)$$

Due to the damping dominance, the results are similar to the damping coefficients alone, cf. Fig. 9.25.

In Fig. 9.27, the normalized force amplitude is expressed relative to the normalized force amplitude of a single plate multiplied by two. This comparison ex-

presses the additional force due to interaction effects between the two plate elements. Note the added uncertainty of such a presentation since experimental results are divided by experimental results.

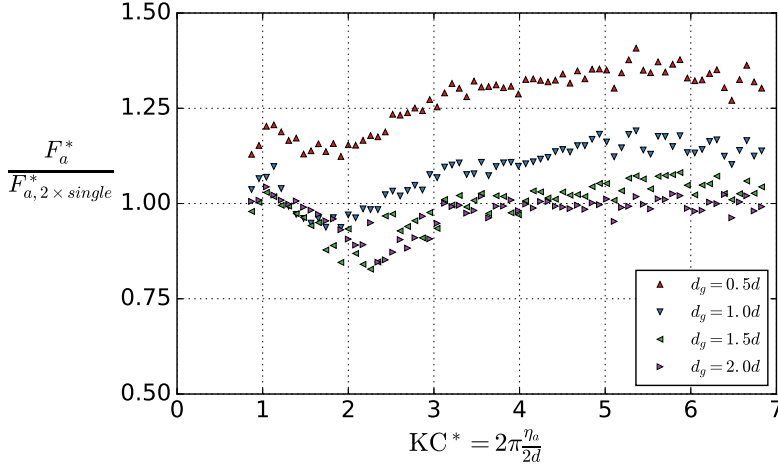


**Figure 9.27:** The normalized force amplitude of the two-plate configurations compared to the normalized force amplitude of a single plate times two.

The results of Fig. 9.27 clearly illustrate that two plate elements placed close to each other can increase the force considerably compared to superposition of two single plates. On average (the mean for all considered  $KC^*$ ), the normalized force amplitude is 28 % and 8.6 % larger when the gap is, respectively,  $d_g = 0.5d$  and  $d_g = 1.0d$ . These increases are significant (probability values:  $p = 1e-8$  and  $p = 0.025$ ). Contrary, when the gap is  $d_g = 1.5d$  or  $d_g = 2.0d$ , no increase in force is found. Interestingly, the increase in force is only somewhat sensitive to the flow velocity, e.g. for  $6 < KC^* < 7$  the mean increase in force is similar to that found for  $3 < KC^* < 4$ , independent of the configuration considered.

Numerical simulations of the four two-plate configurations are performed. Additionally, a corresponding solid plate ( $D = 60$  mm,  $t = 4$  mm) is simulated. Illustrations of the fine region grids of the two-plate configurations are presented in Fig. 9.28.

The normalized force amplitude from the numerical simulations is presented in Fig. 9.29. There is in general acceptable agreement between the numerical and experimental results, cf. Fig. 9.26. However, the force on the single plate multiplied by two is, in general, smaller than the force on the configuration with  $d_g = 0.5d$  and larger than the force on the configurations with  $d_g = 1.0d$ ,  $d_g = 1.5d$  and  $d_g = 2.0d$ . This is not intuitive. As discussed for the simulations of a single plate with regards to the applicability of Graham's method, cf. Section

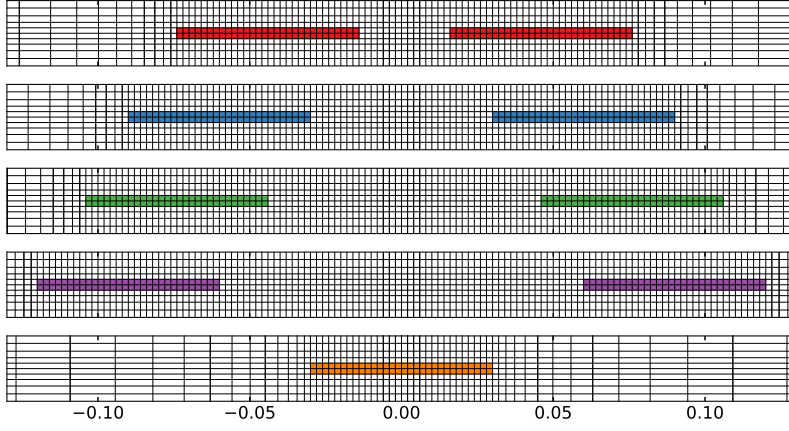


**Figure 9.28:** The fine region grids of the four two-plate configurations and the corresponding single plate configuration.

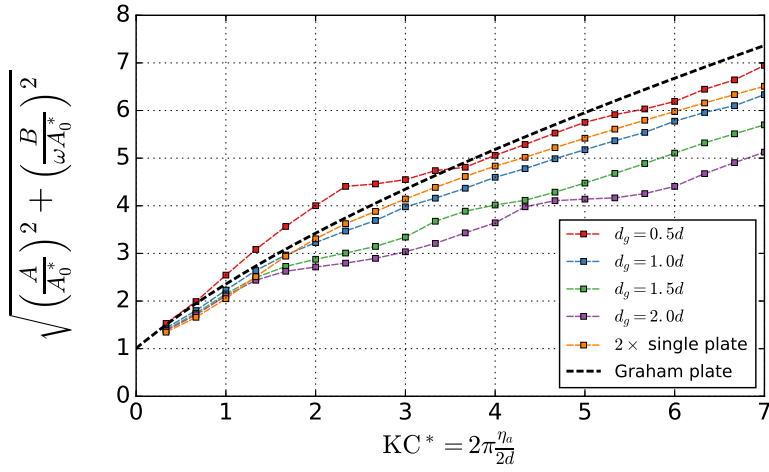


**Figure 9.29:** The normalized force amplitude of the two-plate configurations compared to the normalized force amplitude of a single plate times two. Analytical single plate results by Graham included [22].

8.1, the validity of the viscous flow solver is questionable for high KC numbers when simulating a solid plate; for  $KC > 5$  ( $KC^* > 2.5$ ), the force on a very flat plate ( $\frac{D}{\ell} = 100$ ) is overpredicted compared to the experiments of  $\frac{D}{\ell} = 15$  and  $\frac{D}{\ell} = 30$ , cf. Fig. 8.4. For smaller KC numbers, the normalized force amplitude of the numerical simulations of the single plate is similar to the experimental results. Interestingly, the anomaly is not found for the two-plate configurations; the numerical and experimental results agree, in general, well for the whole range of simulated  $KC^*$  numbers. Why the viscous flow solver is (seemingly) better at simulating two plates than one plate remains unknown.

Both experimental and numerical results indicate a considerable increase in force when the gap between two plates is reduced. In order to study these effects in more detail, flow visualization plots of the two-plate configurations are presented. The flow visualization plots are presented in Figs. 9.30–9.33. The colormap for the contours, cf. Fig. 6.13, represents the vertical velocity. Equal normalization of the colormap is applied in all these figures, with the darkest blue ( $-1.0$  in Fig. 6.13) corresponding to  $w = -2.4\frac{d}{T}$  and the darkest red ( $1.0$  in Fig. 6.13) corresponding to  $w = 2.4\frac{d}{T}$ .

In Fig. 9.30, streamlines obtained for  $KC^* = 1$  are presented. The plots are obtained when  $t = 29.3T$ , hence the ambient vertical velocity component is positive upwards,  $w = 0.12 \sin 0.6\pi$ . The plot color indicate the vertical velocity, red for positive, blue for negative. In terms of KC normalized by the width of a single plate,  $KC = 2KC^* = 2$ . For  $KC = 2$ , a single plate is in the symmetric region according to Singh [60], cf. Section 8.1. In the symmetric region, the plate-end vortices have similar size. Accordingly, the plate-end vortices of all two-plate configurations are similarly sized. However, reducing the gap distance reduces the symmetry due to increased flow through the opening.

A difference between the two-plate configurations is upstream of the gap between the two plates. Upstream of the plate centers, stagnation points are observed near the center-plane of the configuration. The flow is accelerated towards the plate-ends. For  $d_g = 0.5d$  and  $d_g = 1.0d$ , the acceleration of the flow creates a region of reversed flow upstream of the gap. This is not observed for  $d_g = 1.5d$  and  $d_g = 2.0d$  when  $t = 29.3T$ . However, similar patterns are found for  $d_g = 1.5d$  and  $d_g = 2.0d$  as well, as time goes by and the ambient prescribed velocity is reduced. An example is presented in Fig. 9.31, in which the time-step is  $t = 29.42T$  ( $w = 0.12 \sin 0.84\pi$ ). For  $d_g = 2.0d$ , in terms of the total width ( $D$ ) of the configuration, the KC number is only  $KC = 0.5$ . Nevertheless, the streamline plots reveal considerable interaction effects.

Similar plots for  $KC^* = 2$  are presented in Figs. 9.32 and 9.33. According to Singh [60], a single plate would be in the lower end of the asymmetric region when  $KC = 2KC^* = 4$ . Clearly, the plate-end vortices are larger and more asymmetric than those found for  $KC^* = 1$ . The plots are obtained for equal time-steps as in Figs. 9.30 and 9.31, that is,  $t = 29.3T$  and  $t = 29.4T$ ; the vertical velocity component is positive upwards,  $w = 0.24 \sin 0.6\pi$  and  $w = 0.24 \sin 0.8\pi$ . Reversal of flow upstream of the gap is now visible at  $t = 29.3T$  for  $d_g = 1.5$  in addition to

$d_g = 0.5d$  and  $d_g = 1.0$ . Only the configurations with smallest and largest gaps,  $d_g = 0.5d$  and  $d_g = 2.0d$ , are presented in Fig. 9.33. This allows extending the plots vertically such that more of the flow patterns are visible. At this time-step, the reversal of flow upstream of the gap is asymmetric for  $d_g = 0.5d$  and symmetric for  $d_g = 2.0d$ . The streamline plot indicates that decreasing the gap distance increases the size and strength of the plate-end vortices.

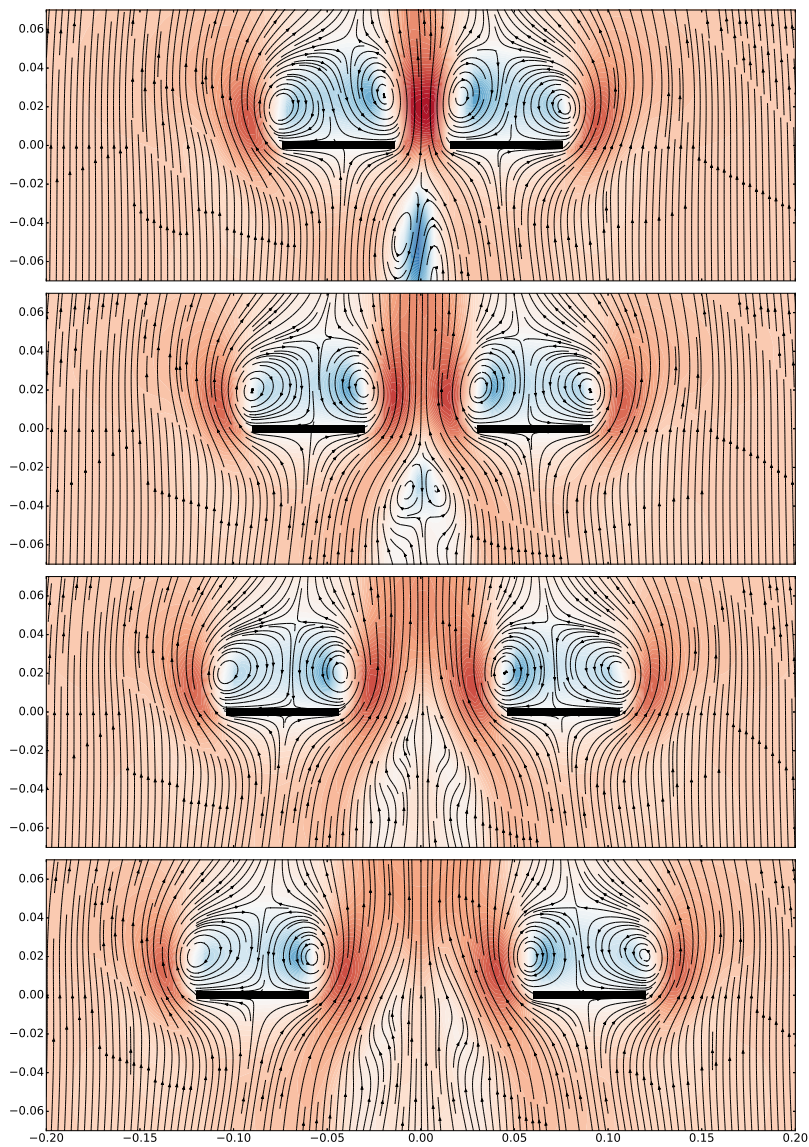


**Figure 9.30:** Streamline plots of the two-plate configurations at  $KC^* = 1$ ,  $t = 29.3T$ . The colormap for the contours represent the vertical velocity (red for positive, blue for negative).



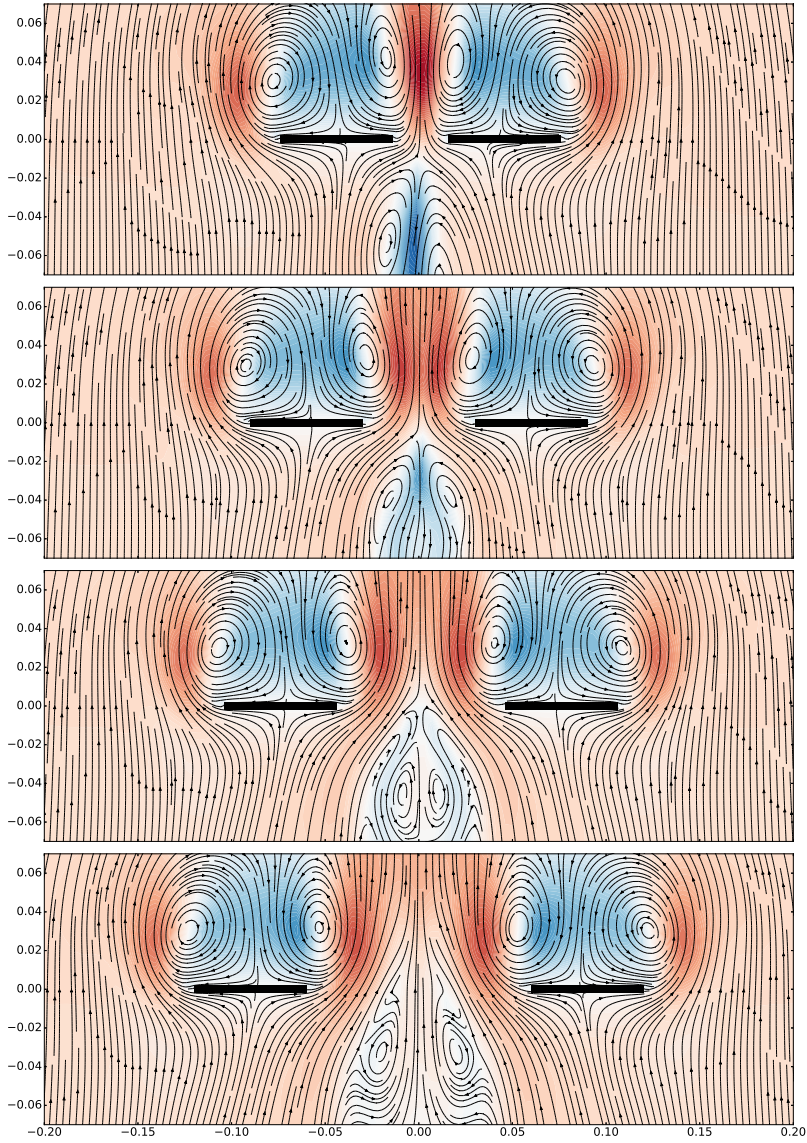


**Figure 9.31:** Streamline plots of the two-plate configurations at  $KC^* = 1$ ,  $t = 29.42T$ . The colormap for the contours represent the vertical velocity (red for positive, blue for negative).



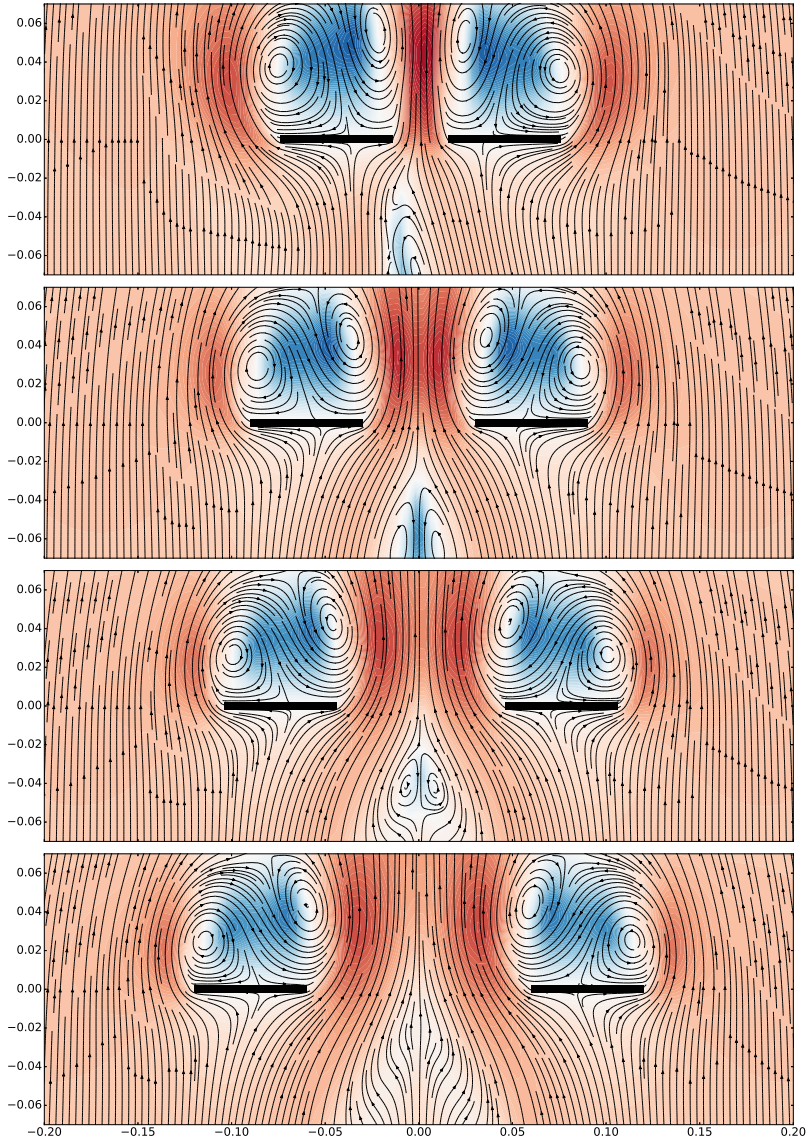


**Figure 9.32:** Streamline plots of the two-plate configurations at  $KC^* = 2$ ,  $t = 29.3T$ . The colormap for the contours represent the vertical velocity (red for positive, blue for negative).

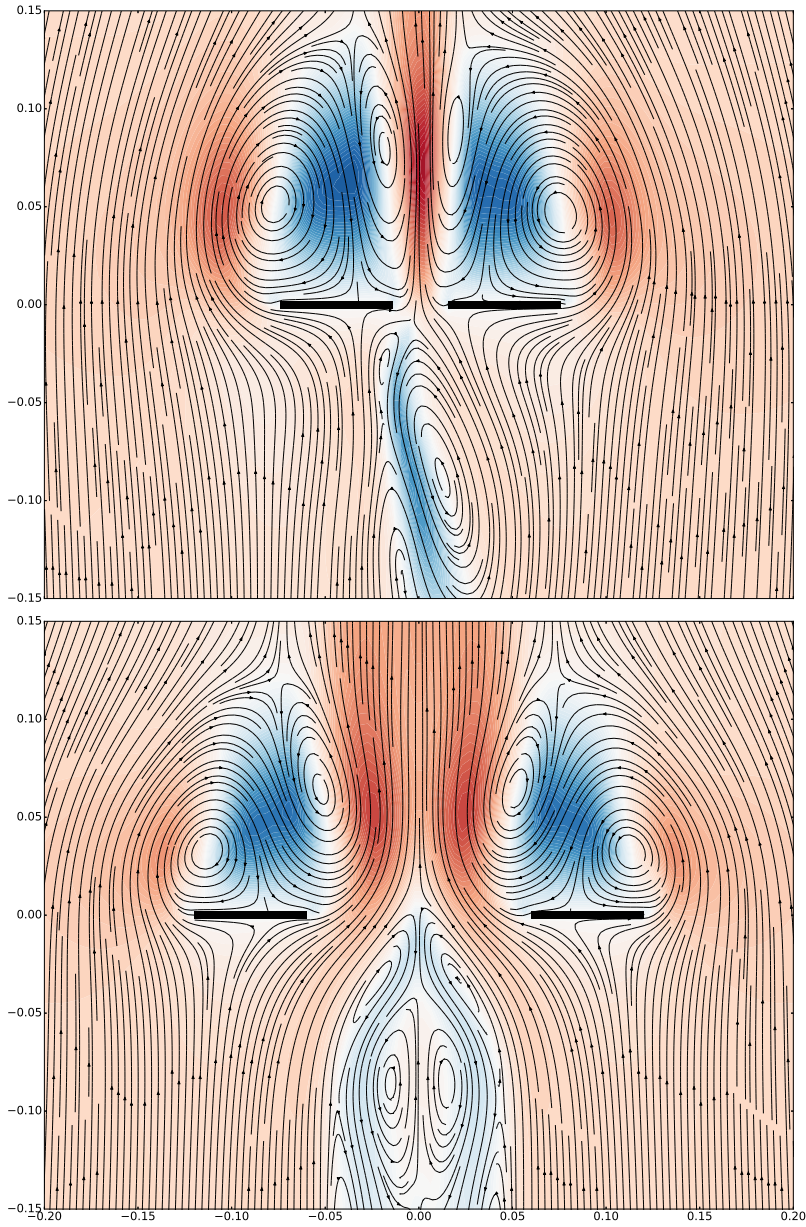


**Figure 9.33:** Streamline plots of  $d_g = 0.5d$  and  $d_g = 2.0d$  at  $KC^* = 2$ ,  $t = 29.42T$ . The colormap for the contours represent the vertical velocity (red for positive, blue for negative).



# Conclusion

The hydrodynamic loads on simplified structures relevant for deployment of sub-sea modules were studied in a two-dimensional setting. Experimental investigations and numerical simulations were performed. In the experiments, models were fixed in incident waves or forced to oscillate. Numerical simulations were conducted for models fixed in incident waves, oscillating flow and orbital flow.

The main focus was on perforated platelike structures. The importance of the damping force was discussed; the hydrodynamic force of ideal perforated plates was dominated by damping for  $\tau \geq 0.1$ . In general, the added mass and damping coefficients increased with increasing KC number and decreasing perforation ratio. An exception was for small perforation ratios and limited KC numbers, in which case the damping of dense perforated plates was larger than that of a corresponding solid plate. The coefficients depended on the structural details of the plate, but were relatively insensitive to the number of perforations or holes.

The importance of plate-end flow separation of perforated plates was highlighted and quantified for two perforated plates of  $\tau = 0.19$  and  $\tau = 0.28$ . In general, the importance increased with increasing KC and decreasing  $\tau$ . Nevertheless, even for small KC numbers, the plate-end flow separation had an effect. When omitting the plate-end flow separation, considerable changes in the force coefficients were found for  $KC > 0.2$  ( $\tau = 0.19$ ) and  $KC > 0.3$  ( $\tau = 0.28$ ).

The normalized force amplitude of perforated plates fully submerged in incident waves increased, in general, with increasing KC number, increasing wavelength and increasing distance to the mean free-surface. The force was similar to the force on models in oscillating flow for small KC numbers, but considerably smaller for large KC numbers. Moreover, the hydrodynamic loads of single and parallel perforated plates in orbital flow was similar to that of oscillating flow for small KC numbers, and smaller than in oscillating flow for large KC numbers. Contrary to the near symmetric plate-end vortices that was found in oscillating flow, the plate-end flow separation was asymmetric in orbital flow. This reduced the force in orbital compared to oscillating flow, and is a likely reason why the force was smaller on fully submerged perforated plates in incident waves than in oscillating flow.

Some aspects of interaction effects were investigated. In oscillating flow, the hydrodynamic loads on a structure consisting of two perforated plates with five relatively large bodies in between, was completely dominated by the loads on the

perforated plates. For two parallel perforated plates in oscillating flow, interaction effects considerably reduced the total force on the configuration compared to superposition of two single plates. The force was reduced on both plates, in particular the instantaneously downstream plate. The added mass of parallel perforated plates was similar to superposition of two corresponding single plates, however, the damping was considerably reduced.

Based on the present results, simple expressions for the force on perforated plates—inspired by the method by Graham for solid plates—were presented. The expressions yield the added mass and damping coefficients of ideal perforated plates in oscillating flow as functions of the perforation ratio and the KC number.

In general, good agreement between the experimental and numerical results was found in the present study. This was somewhat surprising given that relatively simple numerical tools were used, in particular the implemented CFD code was intended to be a two-dimensional DNS solver, without any turbulence model.

# Bibliography

- [1] Rystad Energy, *Rystad forecasts a boom in xmas trees*, <https://www.rystadenergy.com/newsevents/news/press-releases/Rystad-forecasts-a-boom-in-Xmas-trees/>, [Accessed 2019-08-01].
- [2] Equinor, *Åsgard subsea gas compression*, <https://www.equinor.com/en/where-we-are/norway/asgard-subsea-gas-compression.html>, [Accessed 2019-08-01].
- [3] NTNU, *Marine operations — MOVE*, <https://www.ntnu.edu/move>, [Accessed 2019-09-04].
- [4] DNV GL AS, *Modelling and analysis of marine operations. DNVGL-RP-N103. Edition July 2017*, [Obtained 2017-09-14].
- [5] A. Sarkar and O. T. Gudmestad, “Splash zone lifting analysis of subsea structures, OMAE2010-20489,” in *Proceedings of the International Conference on Offshore Mechanics and Arctic Engineering*, 2010, pp. 303–312.
- [6] O. M. Faltinsen, *Sea Loads on ships and offshore structures*. Cambridge University Press, 1993.
- [7] DNV GL AS, *Environmental conditions and environmental loads. DNVGL-RP-C205. Edition August 2017*, [Obtained 2019-06-04].
- [8] C. A. Garrido-Mendoza, K. P. Thiagarajan, A. Souto-Iglesias, A. Colagrossi, and B. Bouscasse, “Computation of flow features and hydrodynamic coefficients around heave plates oscillating near a seabed,” *Journal of Fluids and Structures*, vol. 59, pp. 406–431, 2015.
- [9] P. C. Sandvik, F. Solaas, and F. G. Nielsen, “Hydrodynamic forces on ventilated structures,” in *Proceedings of the International Offshore and Polar Engineering Conference*, 2006, pp. 54–58.
- [10] F. Solaas and P. C. Sandvik, “Hydrodynamic coefficients for suction anchors during installation operations, OMAE2017-62447,” in *Proceedings of the International Conference on Offshore Mechanics and Arctic Engineering*, 2017.
- [11] O. Øritsland, E. Lehn, and O. E. Reitan, *Hydrodynamic forces on sub-sea modules. Model test results*. Marintek report PR 53 532013 03 86, August 1986.

- [12] O. Øritsland, *Wave forces on sub-sea modules during lifting in the splash zone*. Marintek report PR 53 532013 08 86, December 1986.
- [13] O. Øritsland, *Hydrodynamic forces on subsea modules during lifting operations*. Marintek report MT51 87-0194 511003.02, August 1987.
- [14] O. Øritsland, *A summary of subsea module hydrodynamic data*. Marintek report MT51 89-0045 511110.05, February 1989.
- [15] B. Molin, "On the added mass and damping of porous or slotted cylinders," in *Proc. 4th int. workshop water waves & floating bodies*, 1989.
- [16] B. Molin, "On the added mass and damping of periodic arrays of fully or partially porous disks," *Journal of Fluids and Structures*, vol. 15, no. 2, pp. 275–290, 2001.
- [17] B. Molin and F. G. Nielsen, "Heave added mass and damping of a perforated disk below the free surface," in *Proceedings of the 19th International Workshop on Water Waves and Floating Bodies, Cortona, Italy*, 2004.
- [18] B. Molin, F. Remy, and T. Rippol, "Experimental study of the heave added mass and damping of solid and perforated disks close to the free surface," in *Maritime Industry, Ocean Engineering and Coastal Resources — Proceedings of the 12th International Congress of the International Maritime Association of the Mediterranean, IMAM 2007*, vol. 2, 2007, pp. 879–887.
- [19] B. Molin, "Hydrodynamic modeling of perforated structures," *Applied Ocean Research*, vol. 33, no. 1, pp. 1–11, 2011.
- [20] S. An and O. M. Faltinsen, "An experimental and numerical study of heave added mass and damping of horizontally submerged and perforated rectangular plates," *Journal of Fluids and Structures*, vol. 39, pp. 87–101, 2013.
- [21] R. D. Blevins, *Applied fluid dynamics handbook*. Krieger Pub., 2003.
- [22] J. M. R. Graham, "The forces on sharp-edged cylinders in oscillatory flow at low Keulegan–Carpenter numbers," *Journal of Fluid Mechanics*, vol. 97, no. 2, pp. 331–346, 1980.
- [23] L. Tao and D. Dray, "Hydrodynamic performance of solid and porous heave plates," *Ocean Engineering*, vol. 35, no. 10, pp. 1006–1014, 2008.
- [24] S. An and O. M. Faltinsen, "Linear free-surface effects on a horizontally submerged and perforated 2D thin plate in finite and infinite water depths," *Applied Ocean Research*, vol. 37, pp. 220–234, 2012.
- [25] J. Li, S. Liu, M. Zhao, and B. Teng, "Experimental investigation of the hydrodynamic characteristics of heave plates using forced oscillation," *Ocean Engineering*, vol. 66, pp. 82–91, 2013.
- [26] X. Tian, L. Tao, X. Li, and J. Yang, "Hydrodynamic coefficients of oscillating flat plates at 0.15 KC 3.15," *Journal of Marine Science and Technology*, vol. 22, pp. 101–113, 2017.

- [27] I. S. Ertesvåg, *Turbulent strøyming og forbrenning: Frå turbulenteori til ingeniørverkty*. Tapir akademisk forlag, 2000.
- [28] W. L. Hosch, *Navier–Stokes equation*, <https://www.britannica.com/science/Navier-Stokes-equation>, [Accessed 2019-08-01].
- [29] F. M. White, *Viscous fluid flow*. McGraw-Hill, 2006.
- [30] N. Aeronautics and S. A. (NASA), *Navier–Stokes equations*, <https://www.grc.nasa.gov/www/k-12/airplane/nseqs.html>, [Accessed 2019-10-30].
- [31] H. Schlichting, *Boundary-layer theory*, 7th ed. McGraw-Hill, 1979.
- [32] J. N. Newman, *Marine hydrodynamics*. MIT Press, 1977.
- [33] H. K. Versteeg and W. Malalasekera, *An introduction to computational fluid dynamics: The finite volume method*, 2nd ed. Pearson Education Limited, 2007.
- [34] J. R. Morison, M. P. O'Brien, J. W. Johnson, and S. A. Schaaf, "The force exerted by surface waves on piles," *Journal of Petroleum Technology*, vol. 2, no. 5, pp. 149–154, 1950.
- [35] K. P. Thiagarajan and A. W. Troesch, "Effects of appendages and small currents on the hydrodynamic heave damping of TLP columns," *Journal of Offshore Mechanics and Arctic Engineering*, vol. 120, no. 1, pp. 37–42, 1998.
- [36] S. K. Chakrabarti, *Hydrodynamics of offshore structures*. Computational Mechanics Publications, 1987.
- [37] A. Bezunartea-Barrio, S. Fernandez-Ruano, A. Maron-Loureiro, E. Molinelli-Fernandez, F. Moreno-Buron, J. Oria-Escudero, J. Rios-Tubio, C. Soriano-Gomez, A. Valea-Peces, C. Lopez-Pavon, and A. Souto-Iglesias, "Scale effects on heave plates for semi-submersible floating offshore wind turbines: Case study with a solid plain plate," *Journal of Offshore Mechanics and Arctic Engineering*, vol. 142, no. 3, 2019.
- [38] G. H. Keulegan and L. H. Carpenter, "Forces on cylinders and plates in an oscillating fluid," *Journal of Research of the National Bureau of Standards Research Paper*, vol. 60, pp. 423–440, 1958.
- [39] T. Sarpkaya, "Vortex shedding and resistance in harmonic flow about smooth and rough circular cylinders at high Reynolds numbers," Monterey, California. Naval Postgraduate School, Tech. Rep., 1976.
- [40] P. F. Lader, "Geometry and kinematics of breaking waves," PhD thesis, NTNU, 2002.
- [41] Anton Paar Wiki: Viscopedia, *Viscosity of water; reference IAPWS 2008*, <https://wiki.anton-paar.com/en/water/>, [Accessed 2019-08-14].
- [42] HBM, *Catman DAQ software: Visualize - save - automate - analyze*, <https://www.hbm.com/en/2290/catman-data-acquisition-software/>, [Accessed 2019-11-13].



- [43] M. Greenhow and S. I. Ahn, "Added mass and damping of horizontal circular cylinder sections," *Ocean Engineering*, vol. 15, no. 5, pp. 495–504, 1988.
- [44] J. Katz, *Low-speed aerodynamics*, 2nd ed. Cambridge University Press, 2001.
- [45] T. von Kármán, "The impact on seaplane floats during landing," 1929.
- [46] A. J. Chorin, "Numerical solution of the Navier–Stokes equations," *Mathematics of Computation*, vol. 22, no. 104, pp. 745–762, 1968.
- [47] T. Kristiansen and O. M. Faltinsen, "Gap resonance analyzed by a new domain-decomposition method combining potential and viscous flow draft," *Applied Ocean Research*, vol. 34, pp. 198–208, 2012.
- [48] S. V. Patankar, *Numerical heat transfer and fluid flow*. Hemisphere Publishing Corporation (CRC Press, Taylor & Francis Group), 1980.
- [49] S. P. Vanka, "Block-implicit multigrid solution of Navier–Stokes equations in primitive variables," *Journal of Computational Physics*, vol. 65, no. 1, pp. 138–158, 1986.
- [50] R. Schreiber and H. B. Keller, "Driven cavity flows by efficient numerical techniques," *Journal of Computational Physics*, vol. 49, no. 2, pp. 310–333, 1983.
- [51] P. W. Bearman, M. J. Downie, J. M. R. Graham, and E. D. Obasaju, "Forces on cylinders in viscous oscillatory flow at low Keulegan–Carpenter numbers," *Journal of Fluid Mechanics*, vol. 154, pp. 337–356, 1985.
- [52] K. Herfjord, "A study of two-dimensional separated flow by a combination of the finite element method and Navier–Stokes equations," PhD thesis, NTH, 1996.
- [53] Y.-M. Scolan and O. M. Faltinsen, "Numerical studies of separated flow from bodies with sharp corners by the vortex in cell method," *Journal of Fluids and Structures*, vol. 8, no. 2, pp. 201–230, 1994.
- [54] P. M. C. Morse and K. U. Ingard, *Theoretical acoustics*. McGraw-Hill, 1968.
- [55] Matplotlib 3.1.2 documentation, *Choosing colormaps in matplotlib*, <https://matplotlib.org/3.1.1/tutorials/colors/colormaps.html>, [Accessed 2020-03-30].
- [56] R. Firoozkoobi, "Experimental, numerical and analytical investigation of the effect of screens on sloshing," PhD thesis, NTNU, 2013.
- [57] Fish Tech AS, *Perforert plate aluminium ø-2 mm, 2000x1000x1,5 mm, 5754*, <https://www.fishtech.no/produkter/detaljer/perforert-plate-aluminium-oe-2-mm-2000x1000x15-mm-5754/1518/6>, [Accessed 2019-09-04].
- [58] Fish Tech AS, *Perforert plate aluminium ø-3 mm, 2000x1000x1,5 mm, 5754*, <https://www.fishtech.no/produkter/detaljer/perforert-plate-aluminium-oe-3-mm-2000x1000x15-mm/1041/6>, [Accessed 2019-09-04].

- [59] Maxbo, *Profil aluminium firkantrør 1000/10x10x1mm*, <https://www.maxbo.no/profil-aluminium-firkantror-1000-10x10x1mm-p863897>, [Accessed 2019-10-25].
- [60] S. Singh, "Forces on bodies in an oscillatory flow," PhD thesis, Department of Aeronautics, Imperial College, University of London, 1979.
- [61] X. Tian, J. Yang, X. Li, and Y. Shen, "Effects of reynolds number on the hydrodynamic characteristics of heave damping plate," *Chuan Bo Li Xue/Journal of Ship Mechanics*, vol. 17, no. 12, 2013.
- [62] F. Solaas, F. Mentzoni, M. Abrahamsen-Prsic, and T. Kristiansen, "An experimental and numerical study of added mass and damping for side by side plates in oscillating flow, OMAE2019-96008," in *Proceedings of the International Conference on Offshore Mechanics and Arctic Engineering*, 2019.
- [63] F. Irgens, *Formelsamling mekanikk. Tapir akademiske forlag, Trondheim*, 2005.
- [64] W. K. Meyerhoff, "Added masses of thin rectangular plates calculated from potential theory," *Journal of Ship Research*, vol. 14, no. 2, pp. 100–111, 1970.
- [65] T. Sarpkaya, "Force on a circular cylinder in viscous oscillatory flow at low Keulegan–Carpenter numbers," *Journal of Fluid Mechanics*, vol. 165, pp. 61–71, 1986.
- [66] S. Zhang and T. Ishihara, "Numerical study of hydrodynamic coefficients of multiple heave plates by large eddy simulations with volume of fluid method," *Ocean Engineering*, vol. 163, pp. 583–598, 2018.
- [67] L. Tao, B. Molin, Y.-M. Scolan, and K. P. Thiagarajan, "Spacing effects on hydrodynamics of heave plates on offshore structures," *Journal of Fluids and Structures*, vol. 23, no. 8, pp. 1119–1136, 2007.



## **Appendix A**

# **Experimental time-series and spectra**

Some examples of time-series and spectra from the experimental investigations are presented in the following. The plots are obtained for the C19 model forced to oscillate at either small or large amplitudes of oscillation, and small or large periods of oscillation. The measured and band-pass filtered force and acceleration are presented.

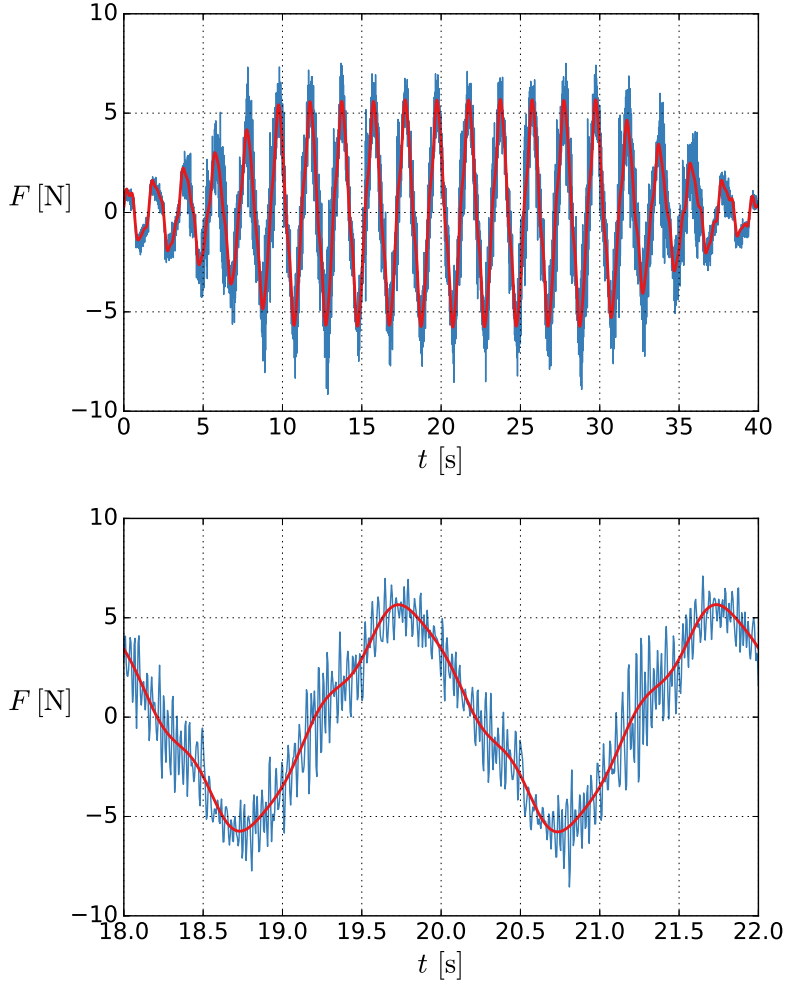


**Figure A.1:** Forced oscillation experiments of C19.  $\eta_a = 1.7$  cm ( $KC = 0.35$ ),  $T = 2.0$  s. Time-series of measured (blue) and filtered (red) force. The sampling rate is 200 Hz. Top subplot: The full set with five oscillation cycles of ramp-in, 10 oscillation cycles with the prescribed amplitude of motion and five oscillation cycles of ramp-out. Bottom subplot: The two oscillation cycles in the middle of the set. Spectrum in Fig. A.3.

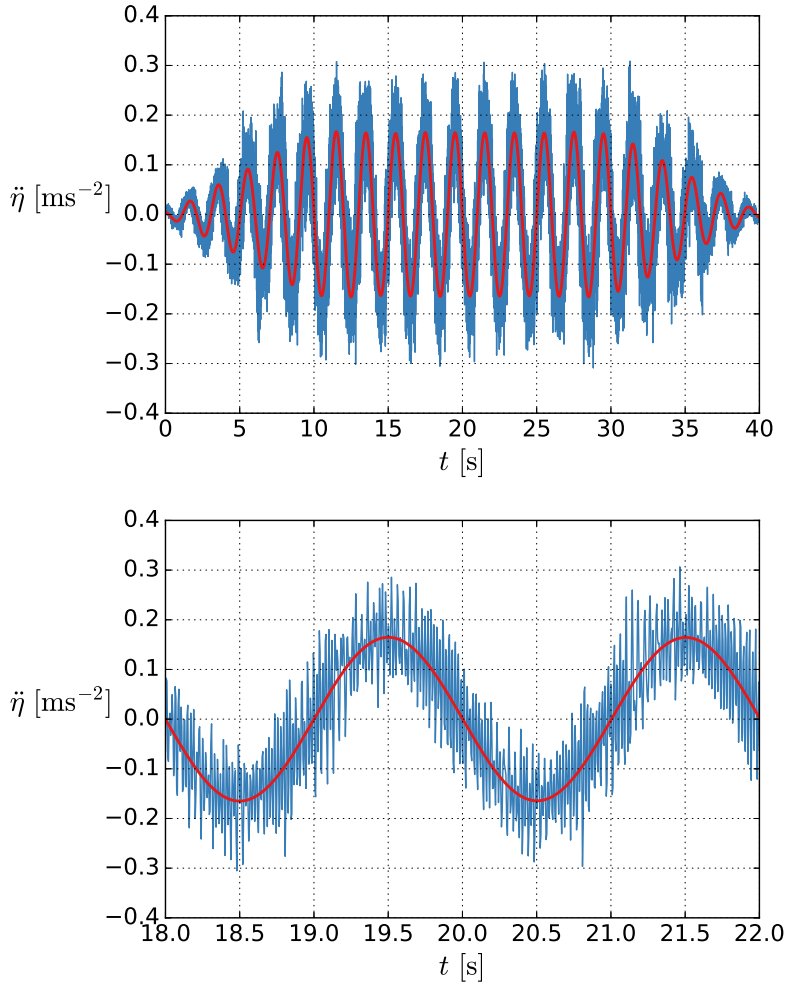


**Figure A.2:** Forced oscillation experiments of C19.  $\eta_a = 1.7 \text{ cm}$  ( $KC = 0.35$ ),  $T = 2.0 \text{ s}$ . Time-series of measured (blue) and filtered (red) acceleration. The sampling rate is 200 Hz. Top subplot: The full set with five oscillation cycles of ramp-in, 10 oscillation cycles with the prescribed amplitude of motion and five oscillation cycles of ramp-out. Bottom subplot: The two oscillation cycles in the middle of the set. Spectrum in Fig. A.4.

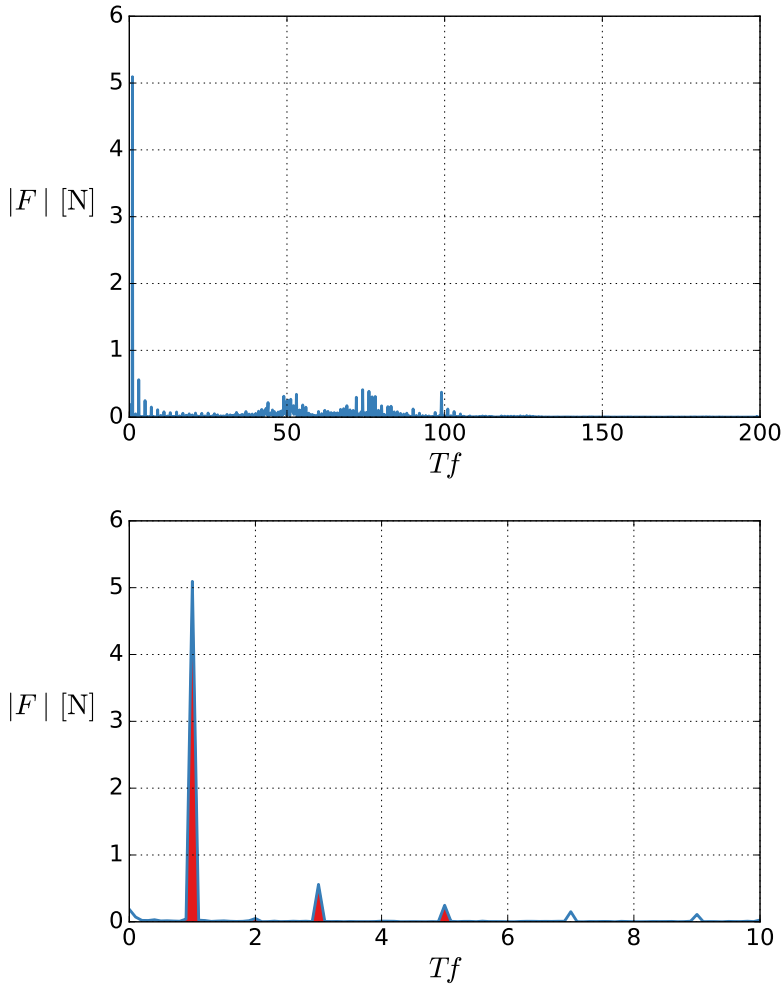


**Figure A.3:** Forced oscillation experiments of C19.  $\eta_a = 1.7$  cm ( $KC = 0.35$ ),  $T = 2.0$  s. Magnitude spectrum of measured force during the ten oscillation cycles with the prescribed amplitude of motion. The band-pass filter is indicated with red fill color.  $f$  is the frequency. The sampling rate is 200 Hz. Top subplot: Full spectrum. Bottom subplot: The first 10 harmonics.

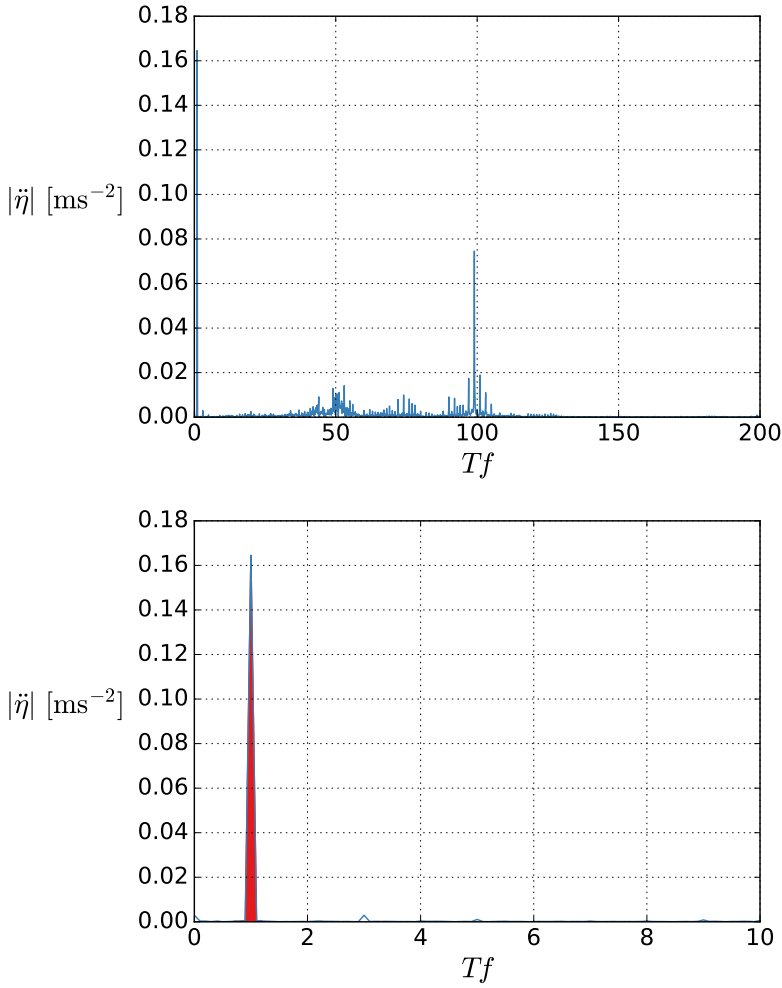


**Figure A.4:** Forced oscillation experiments of C19.  $\eta_a = 1.7$  cm ( $KC = 0.35$ ),  $T = 2.0$  s. Magnitude spectrum of measured acceleration during the ten oscillation cycles with the prescribed amplitude of motion. The band-pass filter is indicated with red fill color.  $f$  is the frequency. The sampling rate is 200 Hz. Top subplot: Full spectrum. Bottom subplot: The first 10 harmonics.



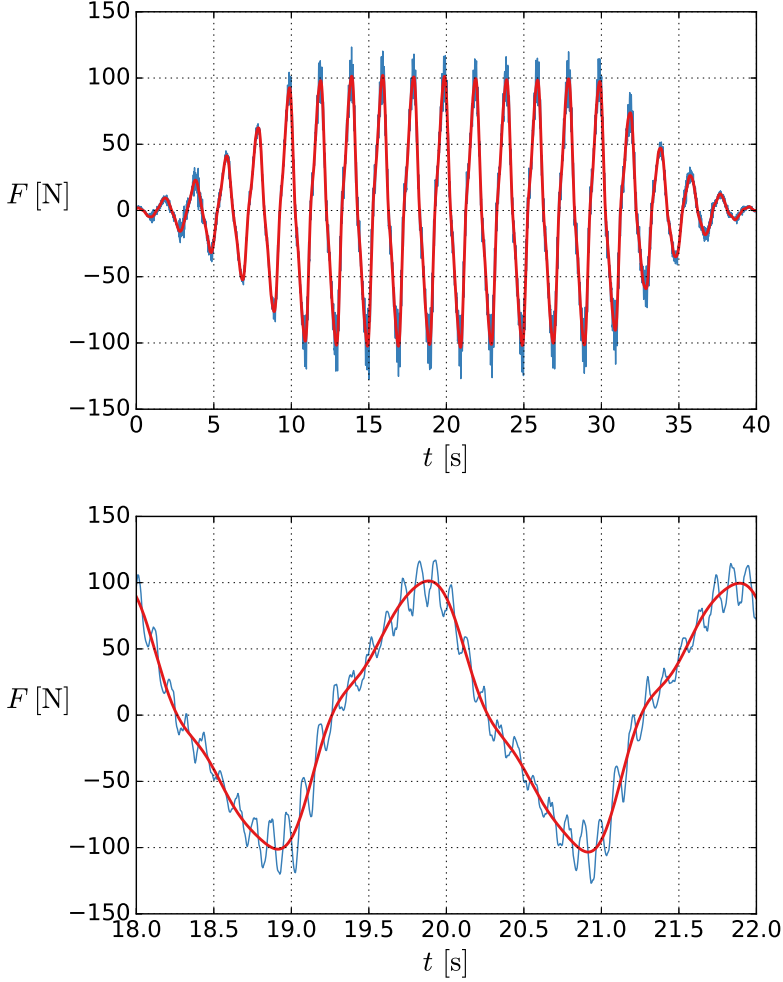


**Figure A.5:** Forced oscillation experiments of C19.  $\eta_a = 13$  cm ( $KC = 2.82$ ),  $T = 2.0$  s. Time-series of measured (blue) and filtered (red) force. The sampling rate is 200 Hz. Top subplot: The full set with five oscillation cycles of ramp-in, 10 oscillation cycles with the prescribed amplitude of motion and five oscillation cycles of ramp-out. Bottom subplot: The two oscillation cycles in the middle of the set. Spectrum in Fig. A.7.

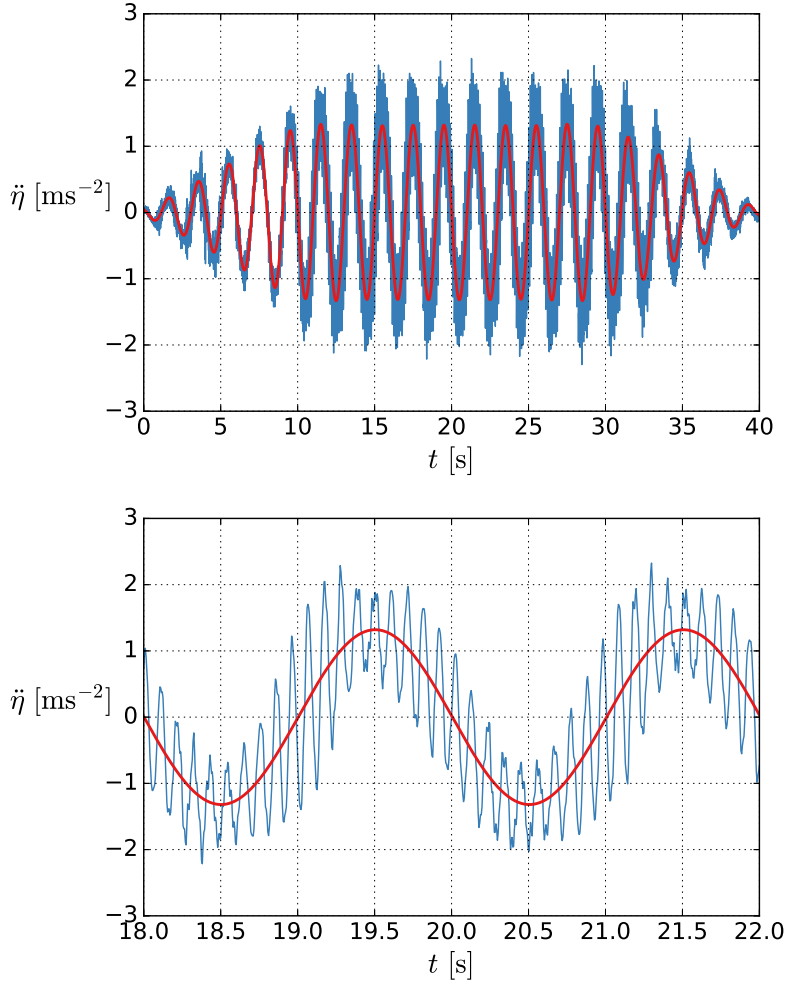


**Figure A.6:** Forced oscillation experiments of C19.  $\eta_a = 13 \text{ cm}$  ( $KC = 2.82$ ),  $T = 2.0 \text{ s}$ . Time-series of measured (blue) and filtered (red) acceleration. The sampling rate is 200 Hz. Top subplot: The full set with five oscillation cycles of ramp-in, 10 oscillation cycles with the prescribed amplitude of motion and five oscillation cycles of ramp-out. Bottom subplot: The two oscillation cycles in the middle of the set. Spectrum in Fig. A.8.

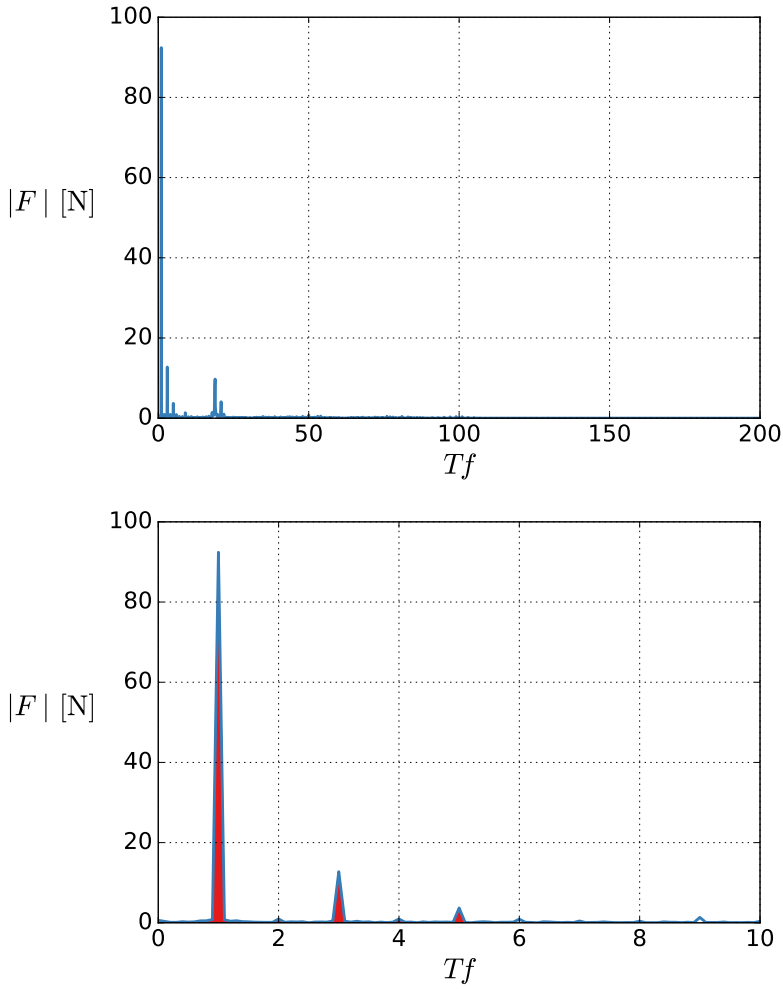


**Figure A.7:** Forced oscillation experiments of C19.  $\eta_a = 13$  cm ( $KC = 2.82$ ),  $T = 2.0$  s. Magnitude spectrum of measured force during the ten oscillation cycles with the prescribed amplitude of motion. The band-pass filter is indicated with red fill color.  $f$  is the frequency. The sampling rate is 200 Hz. Top subplot: Full spectrum. Bottom subplot: The first 10 harmonics.

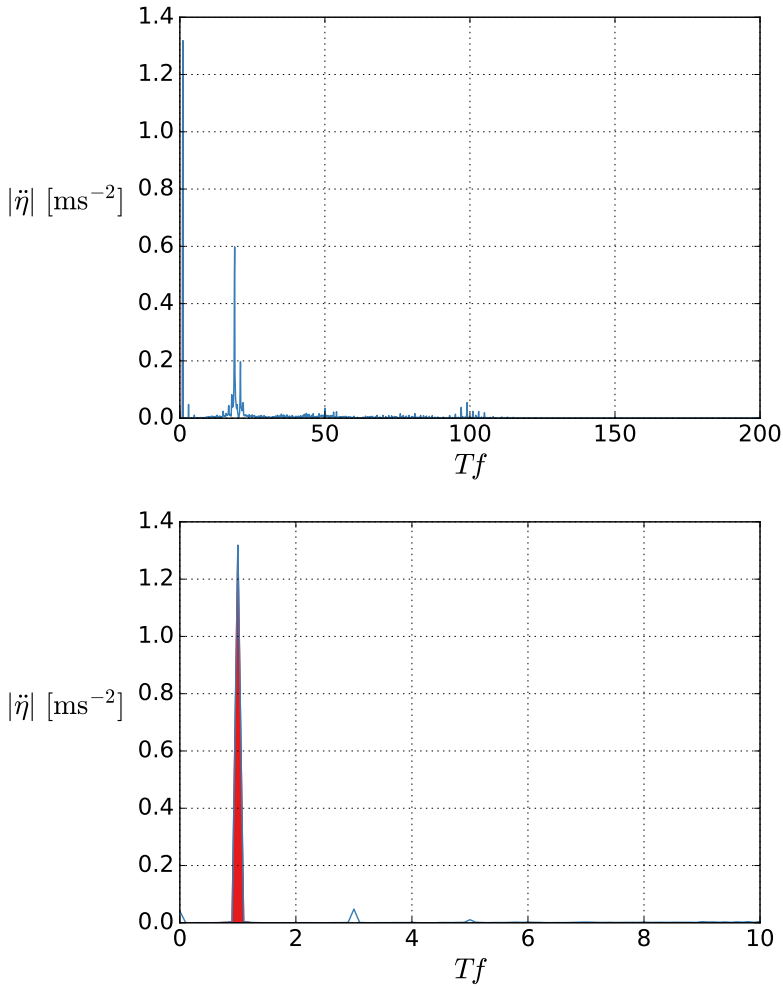


**Figure A.8:** Forced oscillation experiments of C19.  $\eta_a = 13$  cm ( $KC = 2.82$ ),  $T = 2.0$  s. Magnitude spectrum of measured acceleration during the ten oscillation cycles with the prescribed amplitude of motion. The band-pass filter is indicated with red fill color.  $f$  is the frequency. The sampling rate is 200 Hz. Top subplot: Full spectrum. Bottom subplot: The first 10 harmonics.

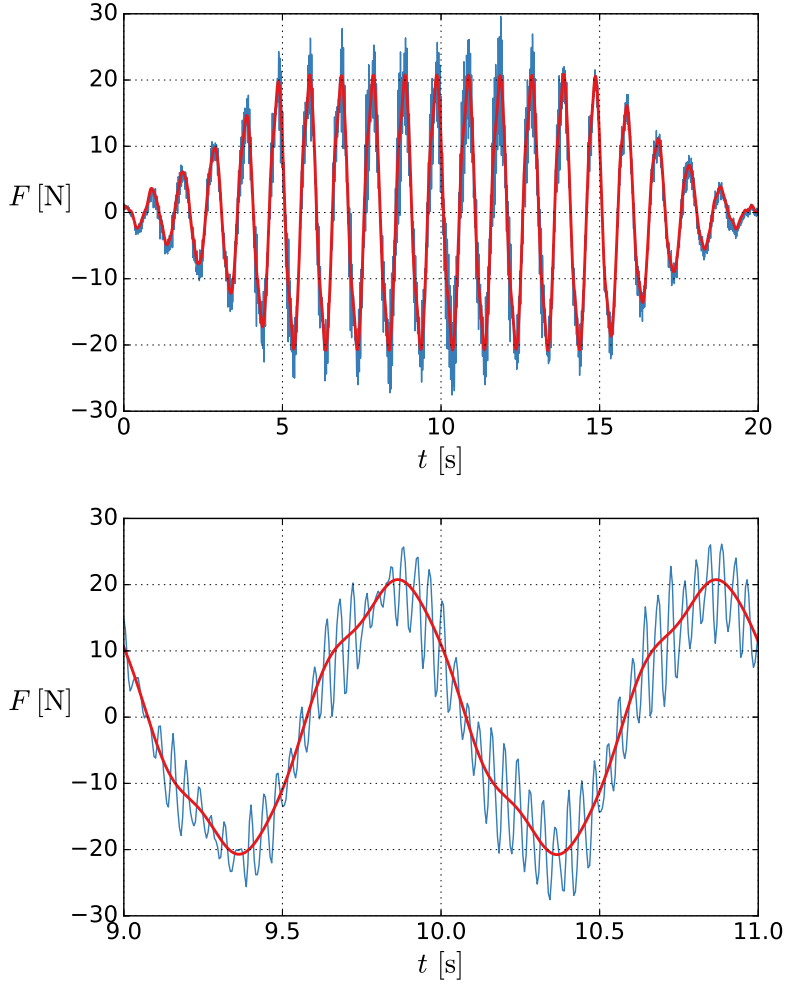


**Figure A.9:** Forced oscillation experiments of C19.  $\eta_a = 1.7$  cm ( $KC = 0.35$ ),  $T = 1.0$  s. Time-series of measured (blue) and filtered (red) force. The sampling rate is 200 Hz. Top subplot: The full set with five oscillation cycles of ramp-in, 10 oscillation cycles with the prescribed amplitude of motion and five oscillation cycles of ramp-out. Bottom subplot: The two oscillation cycles in the middle of the set. Spectrum in Fig. A.11.

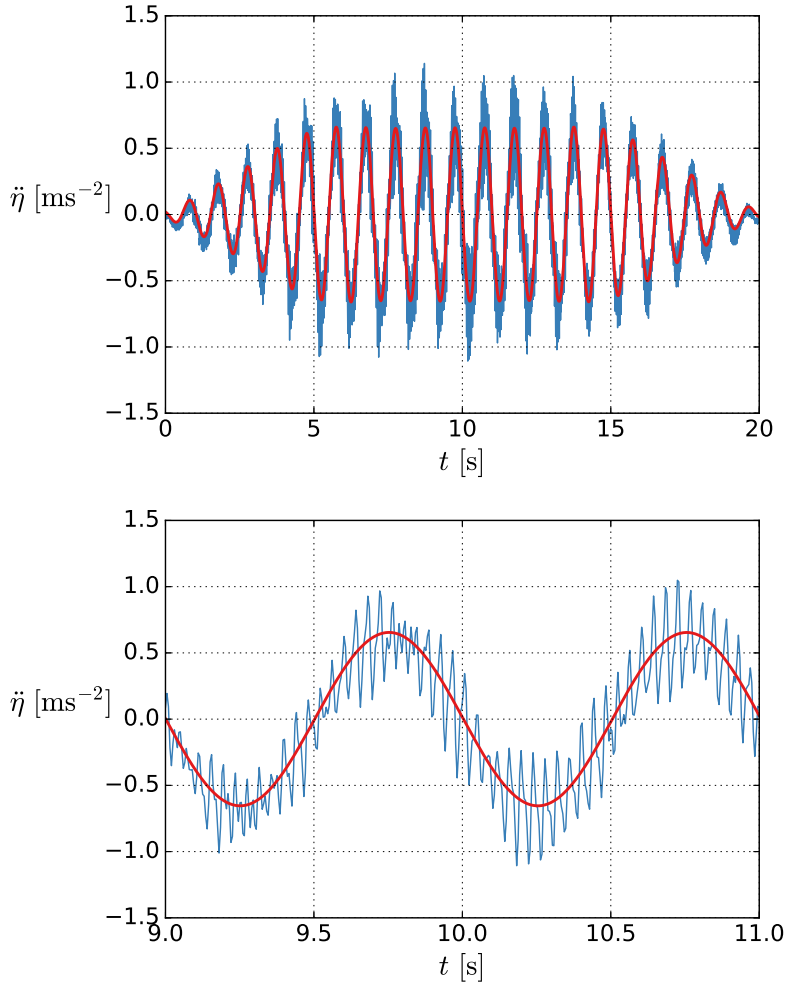


**Figure A.10:** Forced oscillation experiments of C19.  $\eta_a = 1.7 \text{ cm}$  ( $KC = 0.35$ ),  $T = 1.0 \text{ s}$ . Time-series of measured (blue) and filtered (red) acceleration. The sampling rate is 200 Hz. Top subplot: The full set with five oscillation cycles of ramp-in, 10 oscillation cycles with the prescribed amplitude of motion and five oscillation cycles of ramp-out. Bottom subplot: The two oscillation cycles in the middle of the set. Spectrum in Fig. A.12.

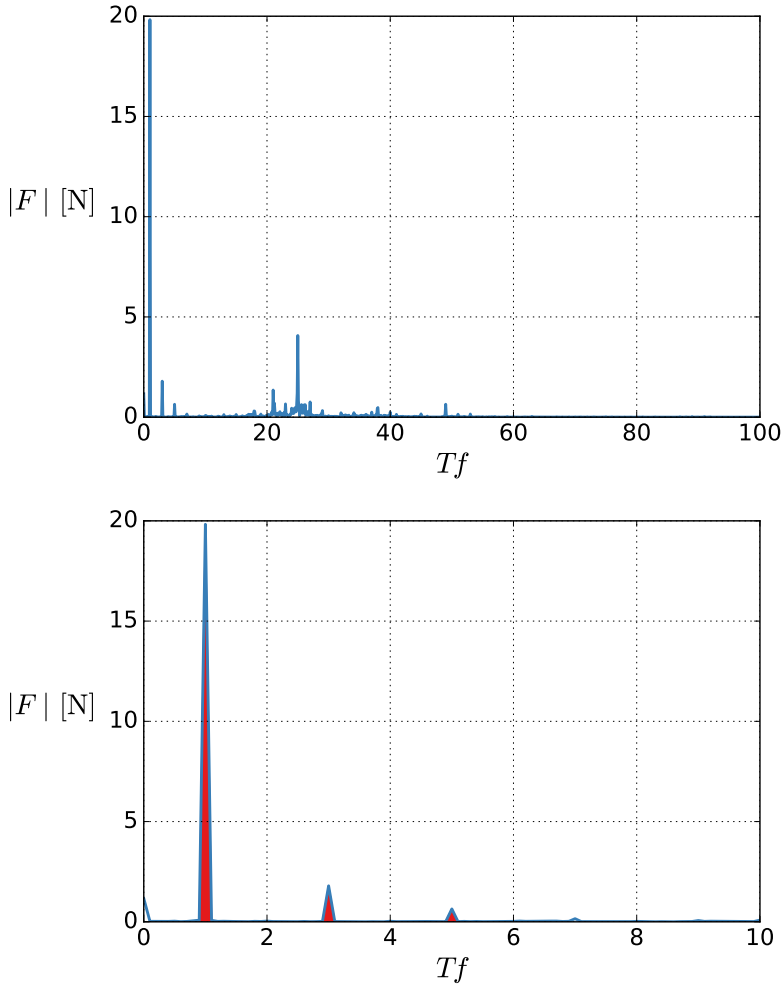


**Figure A.11:** Forced oscillation experiments of C19.  $\eta_a = 1.7$  cm ( $KC = 0.35$ ),  $T = 1.0$  s. Magnitude spectrum of measured force during the ten oscillation cycles with the prescribed amplitude of motion. The band-pass filter is indicated with red fill color.  $f$  is the frequency. The sampling rate is 200 Hz. Top subplot: Full spectrum. Bottom subplot: The first 10 harmonics.

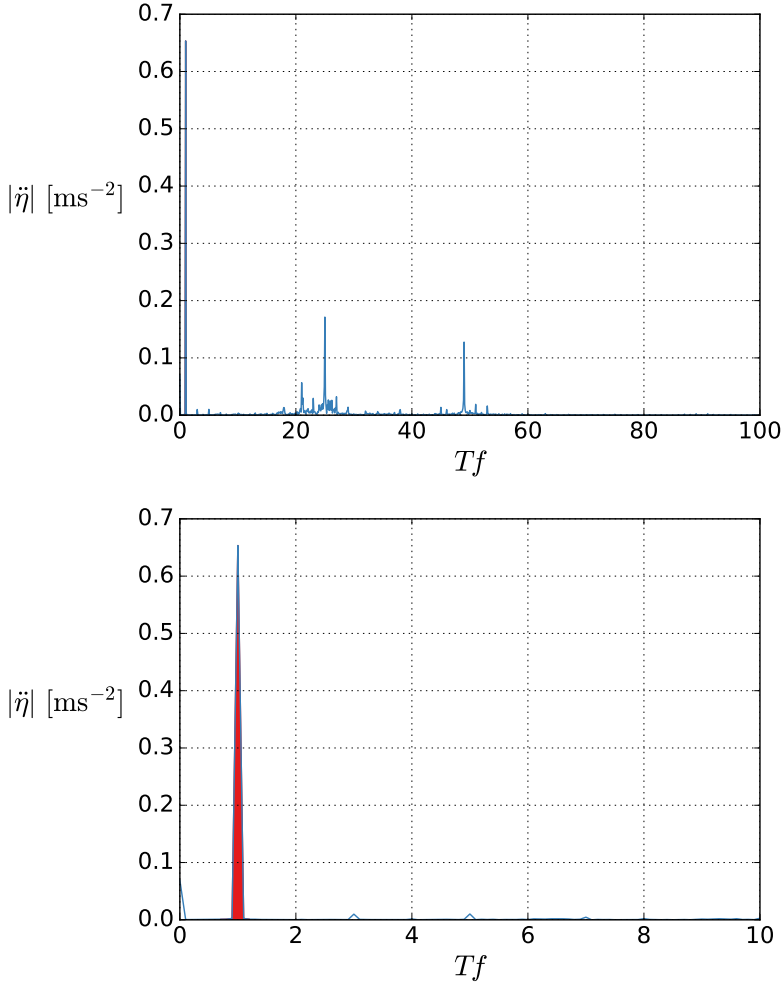


**Figure A.12:** Forced oscillation experiments of C19.  $\eta_a = 1.7 \text{ cm}$  ( $KC = 0.35$ ),  $T = 1.0 \text{ s}$ . Magnitude spectrum of measured acceleration during the ten oscillation cycles with the prescribed amplitude of motion. The band-pass filter is indicated with red fill color.  $f$  is the frequency. The sampling rate is 200 Hz. Top subplot: Full spectrum. Bottom subplot: The first 10 harmonics.



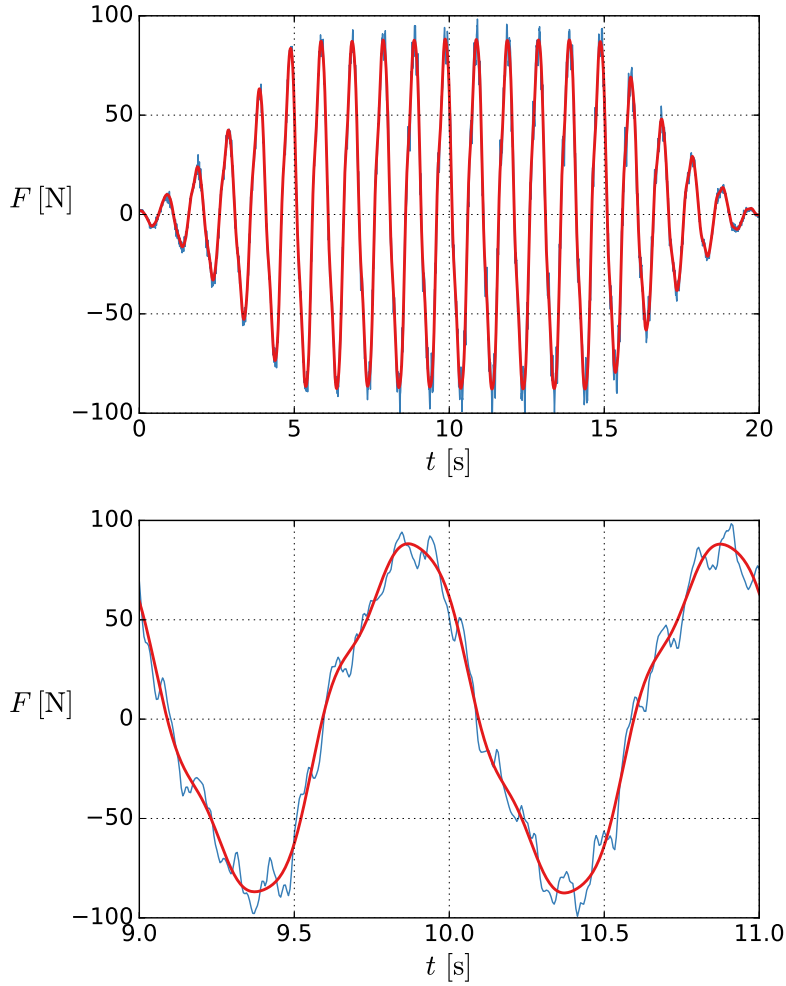


**Figure A.13:** Forced oscillation experiments of C19.  $\eta_a = 5.0$  cm ( $KC = 1.05$ ),  $T = 1.0$  s. Time-series of measured (blue) and filtered (red) force. The sampling rate is 200 Hz. Top subplot: The full set with five oscillation cycles of ramp-in, 10 oscillation cycles with the prescribed amplitude of motion and five oscillation cycles of ramp-out. Bottom subplot: The two oscillation cycles in the middle of the set. Spectrum in Fig. A.15.

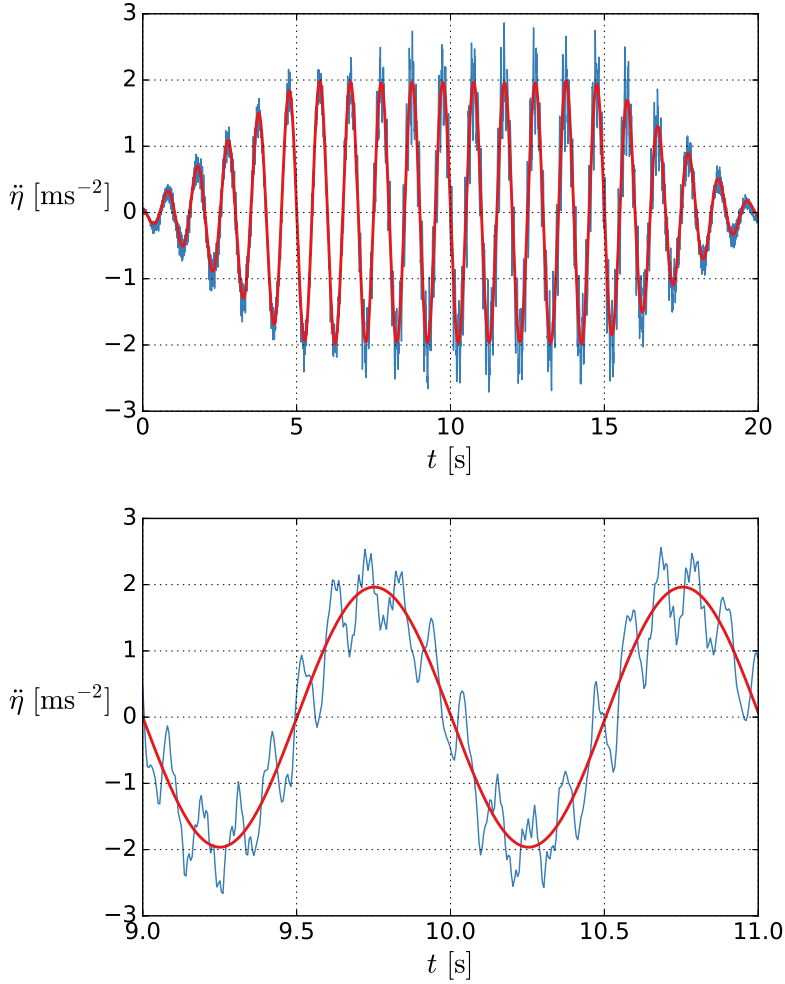


**Figure A.14:** Forced oscillation experiments of C19.  $\eta_a = 5.0 \text{ cm}$  ( $KC = 1.05$ ),  $T = 1.0 \text{ s}$ . Time-series of measured (blue) and filtered (red) acceleration. The sampling rate is 200 Hz. Top subplot: The full set with five oscillation cycles of ramp-in, 10 oscillation cycles with the prescribed amplitude of motion and five oscillation cycles of ramp-out. Bottom subplot: The two oscillation cycles in the middle of the set. Spectrum in Fig. A.16.

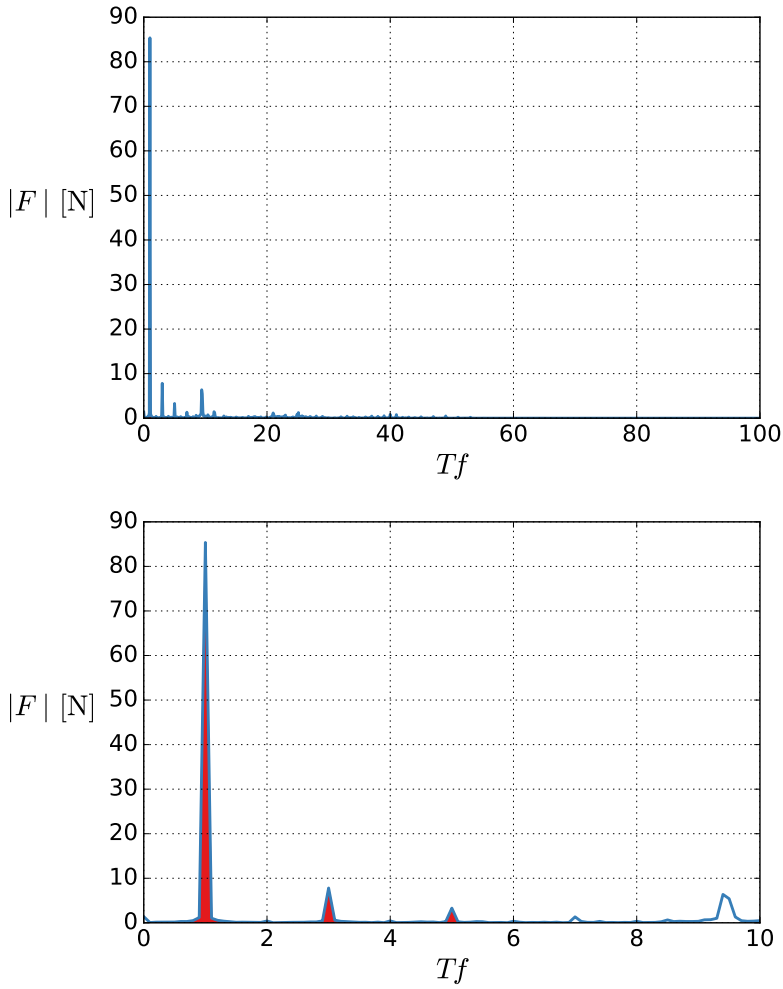


**Figure A.15:** Forced oscillation experiments of C19.  $\eta_a = 5.0 \text{ cm}$  ( $KC = 1.05$ ),  $T = 1.0 \text{ s}$ . Magnitude spectrum of measured force during the ten oscillation cycles with the prescribed amplitude of motion. The band-pass filter is indicated with red fill color.  $f$  is the frequency. The sampling rate is 200 Hz. Top subplot: Full spectrum. Bottom subplot: The first 10 harmonics.

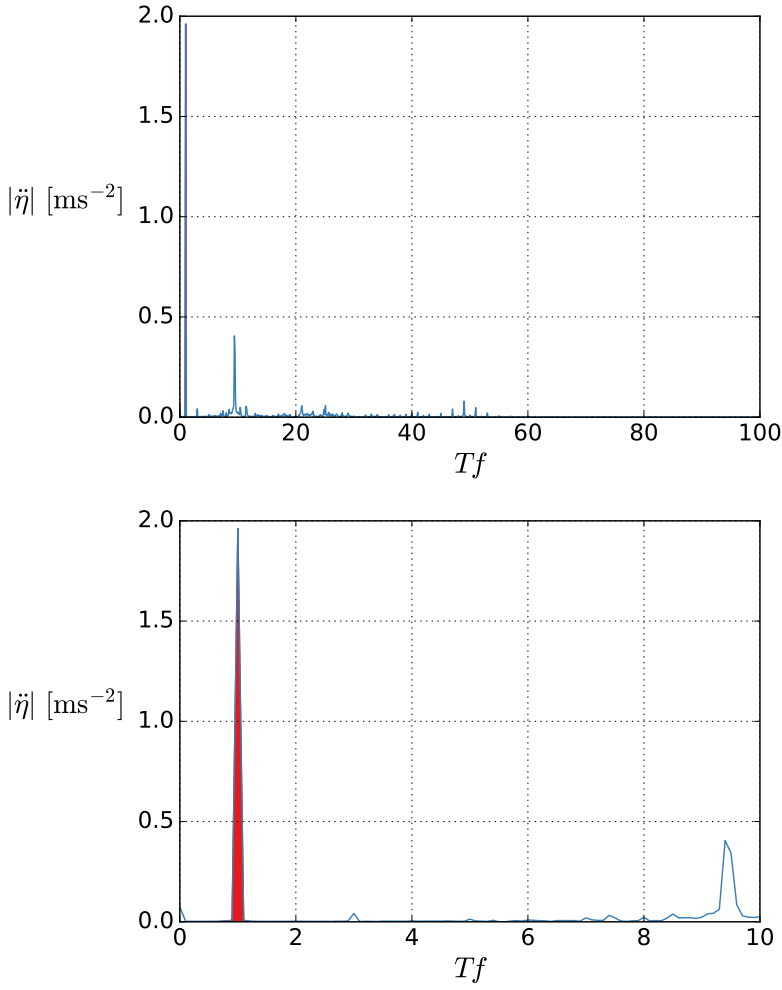


**Figure A.16:** Forced oscillation experiments of C19.  $\eta_a = 5.0 \text{ cm}$  ( $KC = 1.05$ ),  $T = 1.0 \text{ s}$ . Magnitude spectrum of measured acceleration during the ten oscillation cycles with the prescribed amplitude of motion. The band-pass filter is indicated with red fill color.  $f$  is the frequency. The sampling rate is 200 Hz. Top subplot: Full spectrum. Bottom subplot: The first 10 harmonics.







**Previous PhD theses published at the Department of Marine Technology  
(earlier: Faculty of Marine Technology)  
NORWEGIAN UNIVERSITY OF SCIENCE AND TECHNOLOGY**

<b>Report No.</b>	<b>Author</b>	<b>Title</b>
	Kavlie, Dag	Optimization of Plane Elastic Grillages, 1967
	Hansen, Hans R.	Man-Machine Communication and Data-Storage Methods in Ship Structural Design, 1971
	Gisvold, Kaare M.	A Method for non-linear mixed -integer programming and its Application to Design Problems, 1971
	Lund, Sverre	Tanker Frame Optimalization by means of SUMT-Transformation and Behaviour Models, 1971
	Vinje, Tor	On Vibration of Spherical Shells Interacting with Fluid, 1972
	Lorentz, Jan D.	Tank Arrangement for Crude Oil Carriers in Accordance with the new Anti-Pollution Regulations, 1975
	Carlsen, Carl A.	Computer-Aided Design of Tanker Structures, 1975
	Larsen, Carl M.	Static and Dynamic Analysis of Offshore Pipelines during Installation, 1976
UR-79-01	Brigt Hatlestad, MK	The finite element method used in a fatigue evaluation of fixed offshore platforms. (Dr.Ing. Thesis)
UR-79-02	Erik Pettersen, MK	Analysis and design of cellular structures. (Dr.Ing. Thesis)
UR-79-03	Sverre Valsgård, MK	Finite difference and finite element methods applied to nonlinear analysis of plated structures. (Dr.Ing. Thesis)
UR-79-04	Nils T. Nordsve, MK	Finite element collapse analysis of structural members considering imperfections and stresses due to fabrication. (Dr.Ing. Thesis)
UR-79-05	Ivar J. Fylling, MK	Analysis of towline forces in ocean towing systems. (Dr.Ing. Thesis)
UR-80-06	Nils Sandsmark, MM	Analysis of Stationary and Transient Heat Conduction by the Use of the Finite Element Method. (Dr.Ing. Thesis)
UR-80-09	Sverre Haver, MK	Analysis of uncertainties related to the stochastic modeling of ocean waves. (Dr.Ing. Thesis)
UR-81-15	Odland, Jonas	On the Strength of welded Ring stiffened cylindrical Shells primarily subjected to axial Compression
UR-82-17	Engesvik, Knut	Analysis of Uncertainties in the fatigue Capacity of



## Welded Joints

UR-82-18	Rye, Henrik	Ocean wave groups
UR-83-30	Eide, Oddvar Inge	On Cumulative Fatigue Damage in Steel Welded Joints
UR-83-33	Mo, Olav	Stochastic Time Domain Analysis of Slender Offshore Structures
UR-83-34	Amdahl, Jørgen	Energy absorption in Ship-platform impacts
UR-84-37	Mørch, Morten	Motions and mooring forces of semi submersibles as determined by full-scale measurements and theoretical analysis
UR-84-38	Soares, C. Guedes	Probabilistic models for load effects in ship structures
UR-84-39	Aarsnes, Jan V.	Current forces on ships
UR-84-40	Czujko, Jerzy	Collapse Analysis of Plates subjected to Biaxial Compression and Lateral Load
UR-85-46	Alf G. Engseth, MK	Finite element collapse analysis of tubular steel offshore structures. (Dr.Ing. Thesis)
UR-86-47	Dengody Sheshappa, MP	A Computer Design Model for Optimizing Fishing Vessel Designs Based on Techno-Economic Analysis. (Dr.Ing. Thesis)
UR-86-48	Vidar Aanesland, MH	A Theoretical and Numerical Study of Ship Wave Resistance. (Dr.Ing. Thesis)
UR-86-49	Heinz-Joachim Wessel, MK	Fracture Mechanics Analysis of Crack Growth in Plate Girders. (Dr.Ing. Thesis)
UR-86-50	Jon Taby, MK	Ultimate and Post-ultimate Strength of Dented Tubular Members. (Dr.Ing. Thesis)
UR-86-51	Walter Lian, MH	A Numerical Study of Two-Dimensional Separated Flow Past Bluff Bodies at Moderate KC-Numbers. (Dr.Ing. Thesis)
UR-86-52	Bjørn Sortland, MH	Force Measurements in Oscillating Flow on Ship Sections and Circular Cylinders in a U-Tube Water Tank. (Dr.Ing. Thesis)
UR-86-53	Kurt Strand, MM	A System Dynamic Approach to One-dimensional Fluid Flow. (Dr.Ing. Thesis)
UR-86-54	Arne Edvin Løken, MH	Three Dimensional Second Order Hydrodynamic Effects on Ocean Structures in Waves. (Dr.Ing. Thesis)
UR-86-55	Sigurd Falch, MH	A Numerical Study of Slamming of Two-Dimensional Bodies. (Dr.Ing. Thesis)
UR-87-56	Arne Braathen, MH	Application of a Vortex Tracking Method to the Prediction of Roll Damping of a Two-Dimension Floating Body. (Dr.Ing. Thesis)

UR-87-57	Bernt Leira, MK	Gaussian Vector Processes for Reliability Analysis involving Wave-Induced Load Effects. (Dr.Ing. Thesis)
UR-87-58	Magnus Småvik, MM	Thermal Load and Process Characteristics in a Two-Stroke Diesel Engine with Thermal Barriers (in Norwegian). (Dr.Ing. Thesis)
MTA-88-59	Bernt Arild Bremdal, MP	An Investigation of Marine Installation Processes – A Knowledge - Based Planning Approach. (Dr.Ing. Thesis)
MTA-88-60	Xu Jun, MK	Non-linear Dynamic Analysis of Space-framed Offshore Structures. (Dr.Ing. Thesis)
MTA-89-61	Gang Miao, MH	Hydrodynamic Forces and Dynamic Responses of Circular Cylinders in Wave Zones. (Dr.Ing. Thesis)
MTA-89-62	Martin Greenhow, MH	Linear and Non-Linear Studies of Waves and Floating Bodies. Part I and Part II. (Dr.Techn. Thesis)
MTA-89-63	Chang Li, MH	Force Coefficients of Spheres and Cubes in Oscillatory Flow with and without Current. (Dr.Ing. Thesis)
MTA-89-64	Hu Ying, MP	A Study of Marketing and Design in Development of Marine Transport Systems. (Dr.Ing. Thesis)
MTA-89-65	Arild Jæger, MH	Seakeeping, Dynamic Stability and Performance of a Wedge Shaped Planing Hull. (Dr.Ing. Thesis)
MTA-89-66	Chan Siu Hung, MM	The dynamic characteristics of tilting-pad bearings
MTA-89-67	Kim Wikstrøm, MP	Analysis av projekteringen for ett offshore projekt. (Licenciat-avhandling)
MTA-89-68	Jiao Guoyang, MK	Reliability Analysis of Crack Growth under Random Loading, considering Model Updating. (Dr.Ing. Thesis)
MTA-89-69	Arnt Olufsen, MK	Uncertainty and Reliability Analysis of Fixed Offshore Structures. (Dr.Ing. Thesis)
MTA-89-70	Wu Yu-Lin, MR	System Reliability Analyses of Offshore Structures using improved Truss and Beam Models. (Dr.Ing. Thesis)
MTA-90-71	Jan Roger Hoff, MH	Three-dimensional Green function of a vessel with forward speed in waves. (Dr.Ing. Thesis)
MTA-90-72	Rong Zhao, MH	Slow-Drift Motions of a Moored Two-Dimensional Body in Irregular Waves. (Dr.Ing. Thesis)
MTA-90-73	Atle Minsaas, MP	Economical Risk Analysis. (Dr.Ing. Thesis)
MTA-90-74	Knut-Aril Farnes, MK	Long-term Statistics of Response in Non-linear Marine Structures. (Dr.Ing. Thesis)
MTA-90-75	Torbjørn Sotberg, MK	Application of Reliability Methods for Safety Assessment of Submarine Pipelines. (Dr.Ing. Thesis)

		Thesis)
MTA-90-76	Zeuthen, Steffen, MP	SEAMAID. A computational model of the design process in a constraint-based logic programming environment. An example from the offshore domain. (Dr.Ing. Thesis)
MTA-91-77	Haagensen, Sven, MM	Fuel Dependant Cyclic Variability in a Spark Ignition Engine - An Optical Approach. (Dr.Ing. Thesis)
MTA-91-78	Løland, Geir, MH	Current forces on and flow through fish farms. (Dr.Ing. Thesis)
MTA-91-79	Hoen, Christopher, MK	System Identification of Structures Excited by Stochastic Load Processes. (Dr.Ing. Thesis)
MTA-91-80	Haugen, Stein, MK	Probabilistic Evaluation of Frequency of Collision between Ships and Offshore Platforms. (Dr.Ing. Thesis)
MTA-91-81	Sødahl, Nils, MK	Methods for Design and Analysis of Flexible Risers. (Dr.Ing. Thesis)
MTA-91-82	Ormberg, Harald, MK	Non-linear Response Analysis of Floating Fish Farm Systems. (Dr.Ing. Thesis)
MTA-91-83	Marley, Mark J., MK	Time Variant Reliability under Fatigue Degradation. (Dr.Ing. Thesis)
MTA-91-84	Krokstad, Jørgen R., MH	Second-order Loads in Multidirectional Seas. (Dr.Ing. Thesis)
MTA-91-85	Molteberg, Gunnar A., MM	The Application of System Identification Techniques to Performance Monitoring of Four Stroke Turbocharged Diesel Engines. (Dr.Ing. Thesis)
MTA-92-86	Mørch, Hans Jørgen Bjelke, MH	Aspects of Hydrofoil Design: with Emphasis on Hydrofoil Interaction in Calm Water. (Dr.Ing. Thesis)
MTA-92-87	Chan Siu Hung, MM	Nonlinear Analysis of Rotordynamic Instabilities in Highspeed Turbomachinery. (Dr.Ing. Thesis)
MTA-92-88	Bessason, Bjarni, MK	Assessment of Earthquake Loading and Response of Seismically Isolated Bridges. (Dr.Ing. Thesis)
MTA-92-89	Langli, Geir, MP	Improving Operational Safety through exploitation of Design Knowledge - an investigation of offshore platform safety. (Dr.Ing. Thesis)
MTA-92-90	Sævik, Svein, MK	On Stresses and Fatigue in Flexible Pipes. (Dr.Ing. Thesis)
MTA-92-91	Ask, Tor Ø., MM	Ignition and Flame Growth in Lean Gas-Air Mixtures. An Experimental Study with a Schlieren System. (Dr.Ing. Thesis)
MTA-86-92	Hessen, Gunnar, MK	Fracture Mechanics Analysis of Stiffened Tubular Members. (Dr.Ing. Thesis)

MTA-93-93	Steinebach, Christian, MM	Knowledge Based Systems for Diagnosis of Rotating Machinery. (Dr.Ing. Thesis)
MTA-93-94	Dalane, Jan Inge, MK	System Reliability in Design and Maintenance of Fixed Offshore Structures. (Dr.Ing. Thesis)
MTA-93-95	Steen, Sverre, MH	Cobblestone Effect on SES. (Dr.Ing. Thesis)
MTA-93-96	Karunakaran, Daniel, MK	Nonlinear Dynamic Response and Reliability Analysis of Drag-dominated Offshore Platforms. (Dr.Ing. Thesis)
MTA-93-97	Hagen, Arnulf, MP	The Framework of a Design Process Language. (Dr.Ing. Thesis)
MTA-93-98	Nordrik, Rune, MM	Investigation of Spark Ignition and Autoignition in Methane and Air Using Computational Fluid Dynamics and Chemical Reaction Kinetics. A Numerical Study of Ignition Processes in Internal Combustion Engines. (Dr.Ing. Thesis)
MTA-94-99	Passano, Elizabeth, MK	Efficient Analysis of Nonlinear Slender Marine Structures. (Dr.Ing. Thesis)
MTA-94-100	Kvålsvold, Jan, MH	Hydroelastic Modelling of Wetdeck Slamming on Multihull Vessels. (Dr.Ing. Thesis)
MTA-94-102	Bech, Sidsel M., MK	Experimental and Numerical Determination of Stiffness and Strength of GRP/PVC Sandwich Structures. (Dr.Ing. Thesis)
MTA-95-103	Paulsen, Hallvard, MM	A Study of Transient Jet and Spray using a Schlieren Method and Digital Image Processing. (Dr.Ing. Thesis)
MTA-95-104	Hovde, Geir Olav, MK	Fatigue and Overload Reliability of Offshore Structural Systems, Considering the Effect of Inspection and Repair. (Dr.Ing. Thesis)
MTA-95-105	Wang, Xiaozhi, MK	Reliability Analysis of Production Ships with Emphasis on Load Combination and Ultimate Strength. (Dr.Ing. Thesis)
MTA-95-106	Ulstein, Tore, MH	Nonlinear Effects of a Flexible Stern Seal Bag on Cobblestone Oscillations of an SES. (Dr.Ing. Thesis)
MTA-95-107	Solaas, Frøydis, MH	Analytical and Numerical Studies of Sloshing in Tanks. (Dr.Ing. Thesis)
MTA-95-108	Hellan, Øyvind, MK	Nonlinear Pushover and Cyclic Analyses in Ultimate Limit State Design and Reassessment of Tubular Steel Offshore Structures. (Dr.Ing. Thesis)
MTA-95-109	Hermundstad, Ole A., MK	Theoretical and Experimental Hydroelastic Analysis of High Speed Vessels. (Dr.Ing. Thesis)
MTA-96-110	Bratland, Anne K., MH	Wave-Current Interaction Effects on Large-Volume Bodies in Water of Finite Depth. (Dr.Ing. Thesis)
MTA-96-111	Herfjord, Kjell, MH	A Study of Two-dimensional Separated Flow by a Combination of the Finite Element Method and

		Navier-Stokes Equations. (Dr.Ing. Thesis)
MTA-96-112	Æsøy, Vilmar, MM	Hot Surface Assisted Compression Ignition in a Direct Injection Natural Gas Engine. (Dr.Ing. Thesis)
MTA-96-113	Eknes, Monika L., MK	Escalation Scenarios Initiated by Gas Explosions on Offshore Installations. (Dr.Ing. Thesis)
MTA-96-114	Erikstad, Stein O., MP	A Decision Support Model for Preliminary Ship Design. (Dr.Ing. Thesis)
MTA-96-115	Pedersen, Egil, MH	A Nautical Study of Towed Marine Seismic Streamer Cable Configurations. (Dr.Ing. Thesis)
MTA-97-116	Moksnes, Paul O., MM	Modelling Two-Phase Thermo-Fluid Systems Using Bond Graphs. (Dr.Ing. Thesis)
MTA-97-117	Halse, Karl H., MK	On Vortex Shedding and Prediction of Vortex-Induced Vibrations of Circular Cylinders. (Dr.Ing. Thesis)
MTA-97-118	Igland, Ragnar T., MK	Reliability Analysis of Pipelines during Laying, considering Ultimate Strength under Combined Loads. (Dr.Ing. Thesis)
MTA-97-119	Pedersen, Hans-P., MP	Levendefiskteknologi for fiskefartøy. (Dr.Ing. Thesis)
MTA-98-120	Vikestad, Kyrre, MK	Multi-Frequency Response of a Cylinder Subjected to Vortex Shedding and Support Motions. (Dr.Ing. Thesis)
MTA-98-121	Azadi, Mohammad R. E., MK	Analysis of Static and Dynamic Pile-Soil-Jacket Behaviour. (Dr.Ing. Thesis)
MTA-98-122	Ulltang, Terje, MP	A Communication Model for Product Information. (Dr.Ing. Thesis)
MTA-98-123	Torbergsen, Erik, MM	Impeller/Diffuser Interaction Forces in Centrifugal Pumps. (Dr.Ing. Thesis)
MTA-98-124	Hansen, Edmond, MH	A Discrete Element Model to Study Marginal Ice Zone Dynamics and the Behaviour of Vessels Moored in Broken Ice. (Dr.Ing. Thesis)
MTA-98-125	Videiro, Paulo M., MK	Reliability Based Design of Marine Structures. (Dr.Ing. Thesis)
MTA-99-126	Mainçon, Philippe, MK	Fatigue Reliability of Long Welds Application to Titanium Risers. (Dr.Ing. Thesis)
MTA-99-127	Haugen, Elin M., MH	Hydroelastic Analysis of Slamming on Stiffened Plates with Application to Catamaran Wetdecks. (Dr.Ing. Thesis)
MTA-99-128	Langhelle, Nina K., MK	Experimental Validation and Calibration of Nonlinear Finite Element Models for Use in Design of Aluminium Structures Exposed to Fire. (Dr.Ing. Thesis)
MTA-99-	Berstad, Are J., MK	Calculation of Fatigue Damage in Ship Structures.

129		(Dr.Ing. Thesis)
MTA-99-130	Andersen, Trond M., MM	Short Term Maintenance Planning. (Dr.Ing. Thesis)
MTA-99-131	Tveiten, Bård Wathne, MK	Fatigue Assessment of Welded Aluminium Ship Details. (Dr.Ing. Thesis)
MTA-99-132	Søreide, Fredrik, MP	Applications of underwater technology in deep water archaeology. Principles and practice. (Dr.Ing. Thesis)
MTA-99-133	Tønnessen, Rune, MH	A Finite Element Method Applied to Unsteady Viscous Flow Around 2D Blunt Bodies With Sharp Corners. (Dr.Ing. Thesis)
MTA-99-134	Elvekrok, Dag R., MP	Engineering Integration in Field Development Projects in the Norwegian Oil and Gas Industry. The Supplier Management of Norne. (Dr.Ing. Thesis)
MTA-99-135	Fagerholt, Kjetil, MP	Optimeringsbaserte Metoder for Ruteplanlegging innen skipsfart. (Dr.Ing. Thesis)
MTA-99-136	Bysveen, Marie, MM	Visualization in Two Directions on a Dynamic Combustion Rig for Studies of Fuel Quality. (Dr.Ing. Thesis)
MTA-2000-137	Storteig, Eskild, MM	Dynamic characteristics and leakage performance of liquid annular seals in centrifugal pumps. (Dr.Ing. Thesis)
MTA-2000-138	Sagli, Gro, MK	Model uncertainty and simplified estimates of long term extremes of hull girder loads in ships. (Dr.Ing. Thesis)
MTA-2000-139	Tronstad, Harald, MK	Nonlinear analysis and design of cable net structures like fishing gear based on the finite element method. (Dr.Ing. Thesis)
MTA-2000-140	Kroneberg, André, MP	Innovation in shipping by using scenarios. (Dr.Ing. Thesis)
MTA-2000-141	Haslum, Herbjørn Alf, MH	Simplified methods applied to nonlinear motion of spar platforms. (Dr.Ing. Thesis)
MTA-2001-142	Samdal, Ole Johan, MM	Modelling of Degradation Mechanisms and Stressor Interaction on Static Mechanical Equipment Residual Lifetime. (Dr.Ing. Thesis)
MTA-2001-143	Baarholm, Rolf Jarle, MH	Theoretical and experimental studies of wave impact underneath decks of offshore platforms. (Dr.Ing. Thesis)
MTA-2001-144	Wang, Lihua, MK	Probabilistic Analysis of Nonlinear Wave-induced Loads on Ships. (Dr.Ing. Thesis)
MTA-2001-145	Kristensen, Odd H. Holt, MK	Ultimate Capacity of Aluminium Plates under Multiple Loads, Considering HAZ Properties. (Dr.Ing. Thesis)
MTA-2001-146	Greco, Marilena, MH	A Two-Dimensional Study of Green-Water

		Loading. (Dr.Ing. Thesis)
MTA-2001-147	Heggelund, Svein E., MK	Calculation of Global Design Loads and Load Effects in Large High Speed Catamarans. (Dr.Ing. Thesis)
MTA-2001-148	Babalola, Olusegun T., MK	Fatigue Strength of Titanium Risers – Defect Sensitivity. (Dr.Ing. Thesis)
MTA-2001-149	Mohammed, Abuu K., MK	Nonlinear Shell Finite Elements for Ultimate Strength and Collapse Analysis of Ship Structures. (Dr.Ing. Thesis)
MTA-2002-150	Holmedal, Lars E., MH	Wave-current interactions in the vicinity of the sea bed. (Dr.Ing. Thesis)
MTA-2002-151	Rognebakke, Olav F., MH	Sloshing in rectangular tanks and interaction with ship motions. (Dr.Ing. Thesis)
MTA-2002-152	Lader, Pål Furset, MH	Geometry and Kinematics of Breaking Waves. (Dr.Ing. Thesis)
MTA-2002-153	Yang, Qinzheng, MH	Wash and wave resistance of ships in finite water depth. (Dr.Ing. Thesis)
MTA-2002-154	Melhus, Øyvind, MM	Utilization of VOC in Diesel Engines. Ignition and combustion of VOC released by crude oil tankers. (Dr.Ing. Thesis)
MTA-2002-155	Ronæss, Marit, MH	Wave Induced Motions of Two Ships Advancing on Parallel Course. (Dr.Ing. Thesis)
MTA-2002-156	Økland, Ole D., MK	Numerical and experimental investigation of whipping in twin hull vessels exposed to severe wet deck slamming. (Dr.Ing. Thesis)
MTA-2002-157	Ge, Chunhua, MK	Global Hydroelastic Response of Catamarans due to Wet Deck Slamming. (Dr.Ing. Thesis)
MTA-2002-158	Byklum, Eirik, MK	Nonlinear Shell Finite Elements for Ultimate Strength and Collapse Analysis of Ship Structures. (Dr.Ing. Thesis)
IMT-2003-1	Chen, Haibo, MK	Probabilistic Evaluation of FPSO-Tanker Collision in Tandem Offloading Operation. (Dr.Ing. Thesis)
IMT-2003-2	Skaugset, Kjetil Bjørn, MK	On the Suppression of Vortex Induced Vibrations of Circular Cylinders by Radial Water Jets. (Dr.Ing. Thesis)
IMT-2003-3	Chezian, Muthu	Three-Dimensional Analysis of Slamming. (Dr.Ing. Thesis)
IMT-2003-4	Buhaug, Øyvind	Deposit Formation on Cylinder Liner Surfaces in Medium Speed Engines. (Dr.Ing. Thesis)
IMT-2003-5	Tregde, Vidar	Aspects of Ship Design: Optimization of Aft Hull with Inverse Geometry Design. (Dr.Ing. Thesis)
IMT-	Wist, Hanne Therese	Statistical Properties of Successive Ocean Wave

2003-6		Parameters. (Dr.Ing. Thesis)
IMT-2004-7	Ransau, Samuel	Numerical Methods for Flows with Evolving Interfaces. (Dr.Ing. Thesis)
IMT-2004-8	Soma, Torkel	Blue-Chip or Sub-Standard. A data interrogation approach of identity safety characteristics of shipping organization. (Dr.Ing. Thesis)
IMT-2004-9	Ersdal, Svein	An experimental study of hydrodynamic forces on cylinders and cables in near axial flow. (Dr.Ing. Thesis)
IMT-2005-10	Brodtkorb, Per Andreas	The Probability of Occurrence of Dangerous Wave Situations at Sea. (Dr.Ing. Thesis)
IMT-2005-11	Yttervik, Rune	Ocean current variability in relation to offshore engineering. (Dr.Ing. Thesis)
IMT-2005-12	Fredheim, Arne	Current Forces on Net-Structures. (Dr.Ing. Thesis)
IMT-2005-13	Heggernes, Kjetil	Flow around marine structures. (Dr.Ing. Thesis)
IMT-2005-14	Fouques, Sebastien	Lagrangian Modelling of Ocean Surface Waves and Synthetic Aperture Radar Wave Measurements. (Dr.Ing. Thesis)
IMT-2006-15	Holm, Håvard	Numerical calculation of viscous free surface flow around marine structures. (Dr.Ing. Thesis)
IMT-2006-16	Bjørheim, Lars G.	Failure Assessment of Long Through Thickness Fatigue Cracks in Ship Hulls. (Dr.Ing. Thesis)
IMT-2006-17	Hansson, Lisbeth	Safety Management for Prevention of Occupational Accidents. (Dr.Ing. Thesis)
IMT-2006-18	Zhu, Xinying	Application of the CIP Method to Strongly Nonlinear Wave-Body Interaction Problems. (Dr.Ing. Thesis)
IMT-2006-19	Reite, Karl Johan	Modelling and Control of Trawl Systems. (Dr.Ing. Thesis)
IMT-2006-20	Smogeli, Øyvind Notland	Control of Marine Propellers. From Normal to Extreme Conditions. (Dr.Ing. Thesis)
IMT-2007-21	Storhaug, Gaute	Experimental Investigation of Wave Induced Vibrations and Their Effect on the Fatigue Loading of Ships. (Dr.Ing. Thesis)
IMT-2007-22	Sun, Hui	A Boundary Element Method Applied to Strongly Nonlinear Wave-Body Interaction Problems. (PhD Thesis, CeSOS)
IMT-2007-23	Rustad, Anne Marthine	Modelling and Control of Top Tensioned Risers. (PhD Thesis, CeSOS)
IMT-2007-24	Johansen, Vegar	Modelling flexible slender system for real-time simulations and control applications
IMT-2007-25	Wroldsen, Anders Sunde	Modelling and control of tensegrity structures.



(PhD Thesis, CeSOS)

IMT-2007-26	Aronsen, Kristoffer Høye	An experimental investigation of in-line and combined inline and cross flow vortex induced vibrations. (Dr. avhandling, IMT)
IMT-2007-27	Gao, Zhen	Stochastic Response Analysis of Mooring Systems with Emphasis on Frequency-domain Analysis of Fatigue due to Wide-band Response Processes (PhD Thesis, CeSOS)
IMT-2007-28	Thorstensen, Tom Anders	Lifetime Profit Modelling of Ageing Systems Utilizing Information about Technical Condition. (Dr.ing. thesis, IMT)
IMT-2008-29	Refsnes, Jon Erling Gorset	Nonlinear Model-Based Control of Slender Body AUVs (PhD Thesis, IMT)
IMT-2008-30	Berntsen, Per Ivar B.	Structural Reliability Based Position Mooring. (PhD-Thesis, IMT)
IMT-2008-31	Ye, Naiquan	Fatigue Assessment of Aluminium Welded Box-stiffener Joints in Ships (Dr.ing. thesis, IMT)
IMT-2008-32	Radan, Damir	Integrated Control of Marine Electrical Power Systems. (PhD-Thesis, IMT)
IMT-2008-33	Thomassen, Paul	Methods for Dynamic Response Analysis and Fatigue Life Estimation of Floating Fish Cages. (Dr.ing. thesis, IMT)
IMT-2008-34	Pákozdi, Csaba	A Smoothed Particle Hydrodynamics Study of Two-dimensional Nonlinear Sloshing in Rectangular Tanks. (Dr.ing.thesis, IMT/ CeSOS)
IMT-2007-35	Grytøyr, Guttorm	A Higher-Order Boundary Element Method and Applications to Marine Hydrodynamics. (Dr.ing.thesis, IMT)
IMT-2008-36	Drummen, Ingo	Experimental and Numerical Investigation of Nonlinear Wave-Induced Load Effects in Containerships considering Hydroelasticity. (PhD thesis, CeSOS)
IMT-2008-37	Skejic, Renato	Maneuvering and Seakeeping of a Singel Ship and of Two Ships in Interaction. (PhD-Thesis, CeSOS)
IMT-2008-38	Harlem, Alf	An Age-Based Replacement Model for Repairable Systems with Attention to High-Speed Marine Diesel Engines. (PhD-Thesis, IMT)
IMT-2008-39	Alsos, Hagbart S.	Ship Grounding. Analysis of Ductile Fracture, Bottom Damage and Hull Girder Response. (PhD-thesis, IMT)
IMT-2008-40	Graczyk, Mateusz	Experimental Investigation of Sloshing Loading and Load Effects in Membrane LNG Tanks Subjected to Random Excitation. (PhD-thesis, CeSOS)
IMT-2008-41	Taghipour, Reza	Efficient Prediction of Dynamic Response for Flexible amd Multi-body Marine Structures. (PhD-

thesis, CeSOS)

IMT- 2008-42	Ruth, Eivind	Propulsion control and thrust allocation on marine vessels. (PhD thesis, CeSOS)
IMT- 2008-43	Nystad, Bent Helge	Technical Condition Indexes and Remaining Useful Life of Aggregated Systems. PhD thesis, IMT
IMT- 2008-44	Soni, Prashant Kumar	Hydrodynamic Coefficients for Vortex Induced Vibrations of Flexible Beams, PhD thesis, CeSOS
IMT- 2009-45	Amlashi, Hadi K.K.	Ultimate Strength and Reliability-based Design of Ship Hulls with Emphasis on Combined Global and Local Loads. PhD Thesis, IMT
IMT- 2009-46	Pedersen, Tom Arne	Bond Graph Modelling of Marine Power Systems. PhD Thesis, IMT
IMT- 2009-47	Kristiansen, Trygve	Two-Dimensional Numerical and Experimental Studies of Piston-Mode Resonance. PhD-Thesis, CeSOS
IMT- 2009-48	Ong, Muk Chen	Applications of a Standard High Reynolds Number Model and a Stochastic Scour Prediction Model for Marine Structures. PhD-thesis, IMT
IMT- 2009-49	Hong, Lin	Simplified Analysis and Design of Ships subjected to Collision and Grounding. PhD-thesis, IMT
IMT- 2009-50	Koushan, Kamran	Vortex Induced Vibrations of Free Span Pipelines, PhD thesis, IMT
IMT- 2009-51	Korsvik, Jarl Eirik	Heuristic Methods for Ship Routing and Scheduling. PhD-thesis, IMT
IMT- 2009-52	Lee, Jihoon	Experimental Investigation and Numerical in Analyzing the Ocean Current Displacement of Longlines. Ph.d.-Thesis, IMT.
IMT- 2009-53	Vestbøstad, Tone Gran	A Numerical Study of Wave-in-Deck Impact using a Two-Dimensional Constrained Interpolation Profile Method, Ph.d.thesis, CeSOS.
IMT- 2009-54	Bruun, Kristine	Bond Graph Modelling of Fuel Cells for Marine Power Plants. Ph.d.-thesis, IMT
IMT 2009-55	Holstad, Anders	Numerical Investigation of Turbulence in a Sekwed Three-Dimensional Channel Flow, Ph.d.-thesis, IMT.
IMT 2009-56	Ayala-Uraga, Efen	Reliability-Based Assessment of Deteriorating Ship-shaped Offshore Structures, Ph.d.-thesis, IMT
IMT 2009-57	Kong, Xiangjun	A Numerical Study of a Damaged Ship in Beam Sea Waves. Ph.d.-thesis, IMT/CeSOS.
IMT 2010-58	Kristiansen, David	Wave Induced Effects on Floaters of Aquaculture Plants, Ph.d.-thesis, CeSOS.

IMT 2010-59	Ludvigsen, Martin	An ROV-Toolbox for Optical and Acoustic Scientific Seabed Investigation. Ph.d.-thesis IMT.
IMT 2010-60	Hals, Jørgen	Modelling and Phase Control of Wave-Energy Converters. Ph.d.thesis, CeSOS.
IMT 2010- 61	Shu, Zhi	Uncertainty Assessment of Wave Loads and Ultimate Strength of Tankers and Bulk Carriers in a Reliability Framework. Ph.d. Thesis, IMT/ CeSOS
IMT 2010-62	Shao, Yanlin	Numerical Potential-Flow Studies on Weakly-Nonlinear Wave-Body Interactions with/without Small Forward Speed, Ph.d.thesis,CeSOS.
IMT 2010-63	Califano, Andrea	Dynamic Loads on Marine Propellers due to Intermittent Ventilation. Ph.d.thesis, IMT.
IMT 2010-64	El Khoury, George	Numerical Simulations of Massively Separated Turbulent Flows, Ph.d.-thesis, IMT
IMT 2010-65	Seim, Knut Sponheim	Mixing Process in Dense Overflows with Emphasis on the Faroe Bank Channel Overflow. Ph.d.thesis, IMT
IMT 2010-66	Jia, Huirong	Structural Analysis of Intact and Damaged Ships in a Collision Risk Analysis Perspective. Ph.d.thesis CeSoS.
IMT 2010-67	Jiao, Linlin	Wave-Induced Effects on a Pontoon-type Very Large Floating Structures (VLFS). Ph.D.-thesis, CeSOS.
IMT 2010-68	Abrahamsen, Bjørn Christian	Sloshing Induced Tank Roof with Entrapped Air Pocket. Ph.d.thesis, CeSOS.
IMT 2011-69	Karimirad, Madjid	Stochastic Dynamic Response Analysis of Spar-Type Wind Turbines with Catenary or Taut Mooring Systems. Ph.d.-thesis, CeSOS.
IMT - 2011-70	Erlend Meland	Condition Monitoring of Safety Critical Valves. Ph.d.-thesis, IMT.
IMT – 2011-71	Yang, Limin	Stochastic Dynamic System Analysis of Wave Energy Converter with Hydraulic Power Take-Off, with Particular Reference to Wear Damage Analysis, Ph.d. Thesis, CeSOS.
IMT – 2011-72	Visscher, Jan	Application of Particle Image Velocimetry on Turbulent Marine Flows, Ph.d.Thesis, IMT.
IMT – 2011-73	Su, Biao	Numerical Predictions of Global and Local Ice Loads on Ships. Ph.d.Thesis, CeSOS.
IMT – 2011-74	Liu, Zhenhui	Analytical and Numerical Analysis of Iceberg Collision with Ship Structures. Ph.d.Thesis, IMT.
IMT – 2011-75	Aarsæther, Karl Gunnar	Modeling and Analysis of Ship Traffic by Observation and Numerical Simulation. Ph.d.Thesis, IMT.

Imt – 2011-76	Wu, Jie	Hydrodynamic Force Identification from Stochastic Vortex Induced Vibration Experiments with Slender Beams. Ph.d.Thesis, IMT.
Imt – 2011-77	Amini, Hamid	Azimuth Propulsors in Off-design Conditions. Ph.d.Thesis, IMT.
IMT – 2011-78	Nguyen, Tan-Hoi	Toward a System of Real-Time Prediction and Monitoring of Bottom Damage Conditions During Ship Grounding. Ph.d.thesis, IMT.
IMT- 2011-79	Tavakoli, Mohammad T.	Assessment of Oil Spill in Ship Collision and Grounding. Ph.d.thesis, IMT.
IMT- 2011-80	Guo, Bingjie	Numerical and Experimental Investigation of Added Resistance in Waves. Ph.d.Thesis, IMT.
IMT- 2011-81	Chen, Qiaofeng	Ultimate Strength of Aluminium Panels, considering HAZ Effects, IMT
IMT- 2012-82	Kota, Ravikiran S.	Wave Loads on Decks of Offshore Structures in Random Seas, CeSOS.
IMT- 2012-83	Sten, Ronny	Dynamic Simulation of Deep Water Drilling Risers with Heave Compensating System, IMT.
IMT- 2012-84	Berle, Øyvind	Risk and resilience in global maritime supply chains, IMT.
IMT- 2012-85	Fang, Shaoji	Fault Tolerant Position Mooring Control Based on Structural Reliability, CeSOS.
IMT- 2012-86	You, Jikun	Numerical studies on wave forces and moored ship motions in intermediate and shallow water, CeSOS.
IMT- 2012-87	Xiang ,Xu	Maneuvering of two interacting ships in waves, CeSOS
IMT- 2012-88	Dong, Wenbin	Time-domain fatigue response and reliability analysis of offshore wind turbines with emphasis on welded tubular joints and gear components, CeSOS
IMT- 2012-89	Zhu, Suji	Investigation of Wave-Induced Nonlinear Load Effects in Open Ships considering Hull Girder Vibrations in Bending and Torsion, CeSOS
IMT- 2012-90	Zhou, Li	Numerical and Experimental Investigation of Station-keeping in Level Ice, CeSOS
IMT- 2012-91	Ushakov, Sergey	Particulate matter emission characteristics from diesel engines operating on conventional and alternative marine fuels, IMT
IMT- 2013-1	Yin, Decao	Experimental and Numerical Analysis of Combined In-line and Cross-flow Vortex Induced Vibrations, CeSOS

IMT-2013-2	Kurniawan, Adi	Modelling and geometry optimisation of wave energy converters, CeSOS
IMT-2013-3	Al Ryati, Nabil	Technical condition indexes doe auxiliary marine diesel engines, IMT
IMT-2013-4	Firoozkoohi, Reza	Experimental, numerical and analytical investigation of the effect of screens on sloshing, CeSOS
IMT-2013-5	Ommani, Babak	Potential-Flow Predictions of a Semi-Displacement Vessel Including Applications to Calm Water Broaching, CeSOS
IMT-2013-6	Xing, Yihan	Modelling and analysis of the gearbox in a floating spar-type wind turbine, CeSOS
IMT-7-2013	Balland, Océane	Optimization models for reducing air emissions from ships, IMT
IMT-8-2013	Yang, Dan	Transitional wake flow behind an inclined flat plate-----Computation and analysis, IMT
IMT-9-2013	Abdillah, Suyuthi	Prediction of Extreme Loads and Fatigue Damage for a Ship Hull due to Ice Action, IMT
IMT-10-2013	Ramirez, Pedro Agustin Pérez	Ageing management and life extension of technical systems- Concepts and methods applied to oil and gas facilities, IMT
IMT-11-2013	Chuang, Zhenju	Experimental and Numerical Investigation of Speed Loss due to Seakeeping and Maneuvering. IMT
IMT-12-2013	Etemaddar, Mahmoud	Load and Response Analysis of Wind Turbines under Atmospheric Icing and Controller System Faults with Emphasis on Spar Type Floating Wind Turbines, IMT
IMT-13-2013	Lindstad, Haakon	Strategies and measures for reducing maritime CO2 emissons, IMT
IMT-14-2013	Haris, Sabril	Damage interaction analysis of ship collisions, IMT
IMT-15-2013	Shainee, Mohamed	Conceptual Design, Numerical and Experimental Investigation of a SPM Cage Concept for Offshore Mariculture, IMT
IMT-16-2013	Gansel, Lars	Flow past porous cylinders and effects of biofouling and fish behavior on the flow in and around Atlantic salmon net cages, IMT
IMT-17-2013	Gaspar, Henrique	Handling Aspects of Complexity in Conceptual Ship Design, IMT
IMT-18-2013	Thys, Maxime	Theoretical and Experimental Investigation of a Free Running Fishing Vessel at Small Frequency of Encounter, CeSOS
IMT-19-2013	Aglen, Ida	VIV in Free Spanning Pipelines, CeSOS

IMT-1-2014	Song, An	Theoretical and experimental studies of wave diffraction and radiation loads on a horizontally submerged perforated plate, CeSOS
IMT-2-2014	Rogne, Øyvind Ygre	Numerical and Experimental Investigation of a Hinged 5-body Wave Energy Converter, CeSOS
IMT-3-2014	Dai, Lijuan	Safe and efficient operation and maintenance of offshore wind farms ,IMT
IMT-4-2014	Bachynski, Erin Elizabeth	Design and Dynamic Analysis of Tension Leg Platform Wind Turbines, CeSOS
IMT-5-2014	Wang, Jingbo	Water Entry of Freefall Wedged – Wedge motions and Cavity Dynamics, CeSOS
IMT-6-2014	Kim, Ekaterina	Experimental and numerical studies related to the coupled behavior of ice mass and steel structures during accidental collisions, IMT
IMT-7-2014	Tan, Xiang	Numerical investigation of ship's continuous- mode icebreaking in level ice, CeSOS
IMT-8-2014	Muliawan, Made Jaya	Design and Analysis of Combined Floating Wave and Wind Power Facilities, with Emphasis on Extreme Load Effects of the Mooring System, CeSOS
IMT-9-2014	Jiang, Zhiyu	Long-term response analysis of wind turbines with an emphasis on fault and shutdown conditions, IMT
IMT-10-2014	Dukan, Fredrik	ROV Motion Control Systems, IMT
IMT-11-2014	Grimsmo, Nils I.	Dynamic simulations of hydraulic cylinder for heave compensation of deep water drilling risers, IMT
IMT-12-2014	Kvittem, Marit I.	Modelling and response analysis for fatigue design of a semisubmersible wind turbine, CeSOS
IMT-13-2014	Akhtar, Juned	The Effects of Human Fatigue on Risk at Sea, IMT
IMT-14-2014	Syahroni, Nur	Fatigue Assessment of Welded Joints Taking into Account Effects of Residual Stress, IMT
IMT-1-2015	Bøckmann, Eirik	Wave Propulsion of ships, IMT
IMT-2-2015	Wang, Kai	Modelling and dynamic analysis of a semi-submersible floating vertical axis wind turbine, CeSOS
IMT-3-2015	Fredriksen, Arnt Gunvald	A numerical and experimental study of a two-dimensional body with moonpool in waves and current, CeSOS
IMT-4-2015	Jose Patricio Gallardo Canabes	Numerical studies of viscous flow around bluff bodies, IMT

IMT-5-2015	Vegard Longva	Formulation and application of finite element techniques for slender marine structures subjected to contact interactions, IMT
IMT-6-2015	Jacobus De Vaal	Aerodynamic modelling of floating wind turbines, CeSOS
IMT-7-2015	Fachri Nasution	Fatigue Performance of Copper Power Conductors, IMT
IMT-8-2015	Oleh I Karpa	Development of bivariate extreme value distributions for applications in marine technology, CeSOS
IMT-9-2015	Daniel de Almeida Fernandes	An output feedback motion control system for ROVs, AMOS
IMT-10-2015	Bo Zhao	Particle Filter for Fault Diagnosis: Application to Dynamic Positioning Vessel and Underwater Robotics, CeSOS
IMT-11-2015	Wenting Zhu	Impact of emission allocation in maritime transportation, IMT
IMT-12-2015	Amir Rasekhi Nejad	Dynamic Analysis and Design of Gearboxes in Offshore Wind Turbines in a Structural Reliability Perspective, CeSOS
IMT-13-2015	Arturo Jesús Ortega Malca	Dynamic Response of Flexibles Risers due to Unsteady Slug Flow, CeSOS
IMT-14-2015	Dagfinn Husjord	Guidance and decision-support system for safe navigation of ships operating in close proximity, IMT
IMT-15-2015	Anirban Bhattacharyya	Ducted Propellers: Behaviour in Waves and Scale Effects, IMT
IMT-16-2015	Qin Zhang	Image Processing for Ice Parameter Identification in Ice Management, IMT
IMT-1-2016	Vincentius Rumawas	Human Factors in Ship Design and Operation: An Experiential Learning, IMT
IMT-2-2016	Martin Storheim	Structural response in ship-platform and ship-ice collisions, IMT
IMT-3-2016	Mia Abrahamsen Prsic	Numerical Simulations of the Flow around single and Tandem Circular Cylinders Close to a Plane Wall, IMT
IMT-4-2016	Tufan Arslan	Large-eddy simulations of cross-flow around ship sections, IMT

IMT-5-2016	Pierre Yves-Henry	Parametrisation of aquatic vegetation in hydraulic and coastal research,IMT
IMT-6-2016	Lin Li	Dynamic Analysis of the Instalation of Monopiles for Offshore Wind Turbines, CeSOS
IMT-7-2016	Øivind Kåre Kjerstad	Dynamic Positioning of Marine Vessels in Ice, IMT
IMT-8-2016	Xiaopeng Wu	Numerical Analysis of Anchor Handling and Fish Trawling Operations in a Safety Perspective, CeSOS
IMT-9-2016	Zhengshun Cheng	Integrated Dynamic Analysis of Floating Vertical Axis Wind Turbines, CeSOS
IMT-10-2016	Ling Wan	Experimental and Numerical Study of a Combined Offshore Wind and Wave Energy Converter Concept
IMT-11-2016	Wei Chai	Stochastic dynamic analysis and reliability evaluation of the roll motion for ships in random seas, CeSOS
IMT-12-2016	Øyvind Selnes Patricksson	Decision support for conceptual ship design with focus on a changing life cycle and future uncertainty, IMT
IMT-13-2016	Mats Jørgen Thorsen	Time domain analysis of vortex-induced vibrations, IMT
IMT-14-2016	Edgar McGuinness	Safety in the Norwegian Fishing Fleet – Analysis and measures for improvement, IMT
IMT-15-2016	Sepideh Jafarzadeh	Energy efficiency and emission abatement in the fishing fleet, IMT
IMT-16-2016	Wilson Ivan Guachamin Acero	Assessment of marine operations for offshore wind turbine installation with emphasis on response-based operational limits, IMT
IMT-17-2016	Mauro Caneloro	Tools and Methods for Autonomous Operations on Seabed and Water Coumn using Underwater Vehicles, IMT
IMT-18-2016	Valentin Chabaud	Real-Time Hybrid Model Testing of Floating Wind Tubines, IMT
IMT-1-2017	Mohammad Saud Afzal	Three-dimensional streaming in a sea bed boundary layer
IMT-2-2017	Peng Li	A Theoretical and Experimental Study of Wave-induced Hydroelastic Response of a Circular Floating Collar
IMT-3-2017	Martin Bergström	A simulation-based design method for arctic maritime transport systems



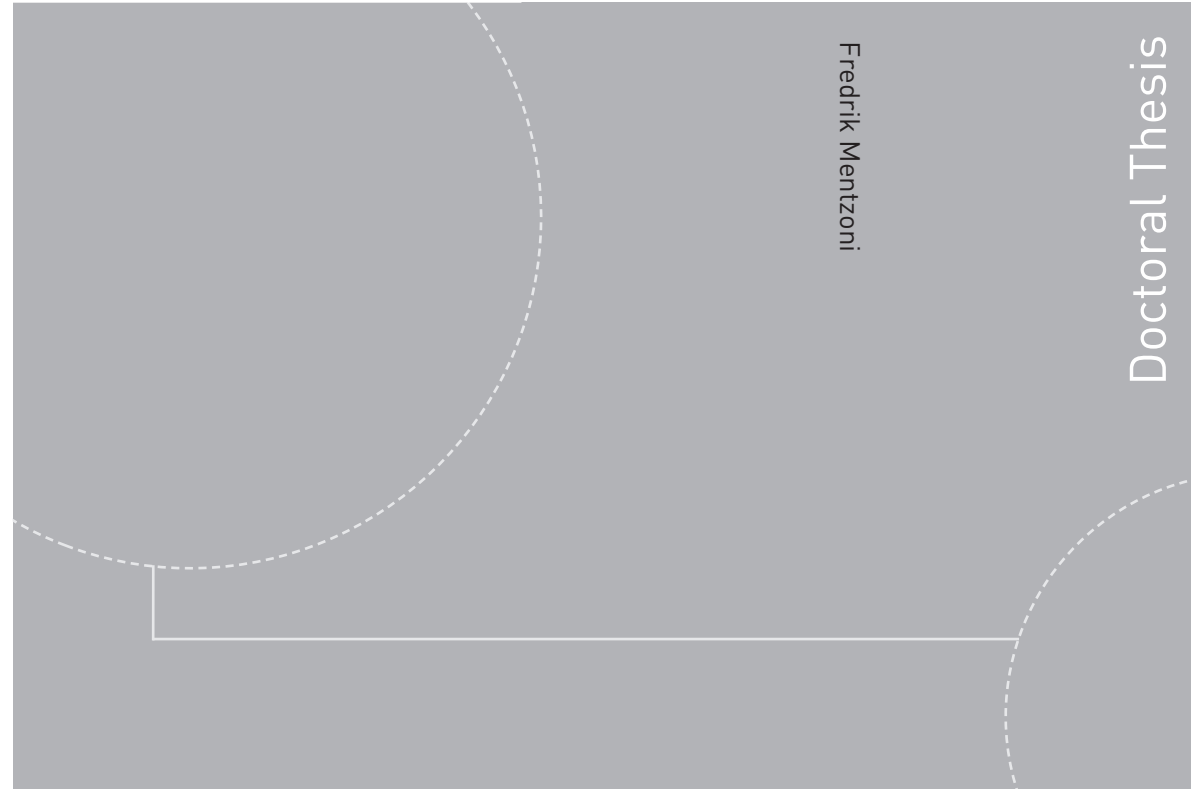
IMT-4-2017	Bhushan Taskar	The effect of waves on marine propellers and propulsion
IMT-5-2017	Mohsen Bardestani	A two-dimensional numerical and experimental study of a floater with net and sinker tube in waves and current
IMT-6-2017	Fatemeh Hoseini Dadmarzi	Direct Numerical Simulation of turbulent wakes behind different plate configurations
IMT-7-2017	Michel R. Miyazaki	Modeling and control of hybrid marine power plants
IMT-8-2017	Giri Rajasekhar Gunnu	Safety and efficiency enhancement of anchor handling operations with particular emphasis on the stability of anchor handling vessels
IMT-9-2017	Kevin Koosup Yum	Transient Performance and Emissions of a Turbocharged Diesel Engine for Marine Power Plants
IMT-10-2017	Zhaolong Yu	Hydrodynamic and structural aspects of ship collisions
IMT-11-2017	Martin Hassel	Risk Analysis and Modelling of Allisions between Passing Vessels and Offshore Installations
IMT-12-2017	Astrid H. Brodtkorb	Hybrid Control of Marine Vessels – Dynamic Positioning in Varying Conditions
IMT-13-2017	Kjersti Bruserud	Simultaneous stochastic model of waves and current for prediction of structural design loads
IMT-14-2017	Finn-Idar Grøtta Giske	Long-Term Extreme Response Analysis of Marine Structures Using Inverse Reliability Methods
IMT-15-2017	Stian Skjong	Modeling and Simulation of Maritime Systems and Operations for Virtual Prototyping using co-Simulations
IMT-1-2018	Yingguang Chu	Virtual Prototyping for Marine Crane Design and Operations
IMT-2-2018	Sergey Gavrilin	Validation of ship manoeuvring simulation models
IMT-3-2018	Jeevith Hegde	Tools and methods to manage risk in autonomous subsea inspection, maintenance and repair operations
IMT-4-2018	Ida M. Strand	Sea Loads on Closed Flexible Fish Cages
IMT-5-2018	Erlend Kvinge Jørgensen	Navigation and Control of Underwater Robotic Vehicles

IMT-6-2018	Bård Stovner	Aided Intertial Navigation of Underwater Vehicles
IMT-7-2018	Erlend Liavåg Grotle	Thermodynamic Response Enhanced by Sloshing in Marine LNG Fuel Tanks
IMT-8-2018	Børge Rokseth	Safety and Verification of Advanced Maritime Vessels
IMT-9-2018	Jan Vidar Ulveseter	Advances in Semi-Empirical Time Domain Modelling of Vortex-Induced Vibrations
IMT-10-2018	Chenyu Luan	Design and analysis for a steel braceless semi-submersible hull for supporting a 5-MW horizontal axis wind turbine
IMT-11-2018	Carl Fredrik Rehn	Ship Design under Uncertainty
IMT-12-2018	Øyvind Ødegård	Towards Autonomous Operations and Systems in Marine Archaeology
IMT-13-2018	Stein Melvær Nornes	Guidance and Control of Marine Robotics for Ocean Mapping and Monitoring
IMT-14-2018	Petter Norgren	Autonomous Underwater Vehicles in Arctic Marine Operations: Arctic marine research and ice monitoring
IMT-15-2018	Minjoo Choi	Modular Adaptable Ship Design for Handling Uncertainty in the Future Operating Context
MT-16-2018	Ole Alexander Eidsvik	Dynamics of Remotely Operated Underwater Vehicle Systems
IMT-17-2018	Mahdi Ghane	Fault Diagnosis of Floating Wind Turbine Drivetrain- Methodologies and Applications
IMT-18-2018	Christoph Alexander Thieme	Risk Analysis and Modelling of Autonomous Marine Systems
IMT-19-2018	Yugao Shen	Operational limits for floating-collar fish farms in waves and current, without and with well-boat presence
IMT-20-2018	Tianjiao Dai	Investigations of Shear Interaction and Stresses in Flexible Pipes and Umbilicals
IMT-21-2018	Sigurd Solheim Pettersen	Resilience by Latent Capabilities in Marine Systems
IMT-22-2018	Thomas Sauder	Fidelity of Cyber-physical Empirical Methods. Application to the Active Truncation of Slender Marine Structures
IMT-23-2018	Jan-Tore Horn	Statistical and Modelling Uncertainties in the Design of Offshore Wind Turbines

IMT-24-2018	Anna Swider	Data Mining Methods for the Analysis of Power Systems of Vessels
IMT-1-2019	Zhao He	Hydrodynamic study of a moored fish farming cage with fish influence
IMT-2-2019	Isar Ghamari	Numerical and Experimental Study on the Ship Parametric Roll Resonance and the Effect of Anti-Roll Tank
IMT-3-2019	Håkon Strandenes	Turbulent Flow Simulations at Higher Reynolds Numbers
IMT-4-2019	Siri Mariane Holen	Safety in Norwegian Fish Farming – Concepts and Methods for Improvement
IMT-5-2019	Ping Fu	Reliability Analysis of Wake-Induced Riser Collision
IMT-6-2019	Vladimir Krivopolianskii	Experimental Investigation of Injection and Combustion Processes in Marine Gas Engines using Constant Volume Rig
IMT-7-2019	Anna Maria Kozłowska	Hydrodynamic Loads on Marine Propellers Subject to Ventilation and out of Water Condition.
IMT-8-2019	Hans-Martin Heyn	Motion Sensing on Vessels Operating in Sea Ice: A Local Ice Monitoring System for Transit and Stationkeeping Operations under the Influence of Sea Ice
IMT-9-2019	Stefan Vilsen	Method for Real-Time Hybrid Model Testing of Ocean Structures – Case on Slender Marine Systems
IMT-10-2019	Finn-Christian W. Hanssen	Non-Linear Wave-Body Interaction in Severe Waves
IMT-11-2019	Trygve Olav Fossum	Adaptive Sampling for Marine Robotics
IMT-12-2019	Jørgen Bremnes Nielsen	Modeling and Simulation for Design Evaluation
IMT-13-2019	Yuna Zhao	Numerical modelling and dyncamic analysis of offshore wind turbine blade installation
IMT-14-2019	Daniela Myland	Experimental and Theoretical Investigations on the Ship Resistance in Level Ice
IMT-15-2019	Zhengru Ren	Advanced control algorithms to support automated offshore wind turbine installation
IMT-16-2019	Drazen Polic	Ice-propeller impact analysis using an inverse propulsion machinery simulation approach
IMT-17-2019	Endre Sandvik	Sea passage scenario simulation for ship system performance evaluation

IMT-18-2019	Loup Suja-Thauvin	Response of Monopile Wind Turbines to Higher Order Wave Loads
IMT-19-2019	Emil Smilden	Structural control of offshore wind turbines – Increasing the role of control design in offshore wind farm development
IMT-20-2019	Aleksandar-Sasa Milakovic	On equivalent ice thickness and machine learning in ship ice transit simulations
IMT-1-2020	Amrit Shankar Verma	Modelling, Analysis and Response-based Operability Assessment of Offshore Wind Turbine Blade Installation with Emphasis on Impact Damages
IMT-2-2020	Bent Oddvar Arnesen Haugaløkken	Autonomous Technology for Inspection, Maintenance and Repair Operations in the Norwegian Aquaculture
IMT-3-2020	Seongpil Cho	Model-based fault detection and diagnosis of a blade pitch system in floating wind turbines
IMT-4-2020	Jose Jorge Garcia Agis	Effectiveness in Decision-Making in Ship Design under Uncertainty
IMT-5-2020	Thomas H. Viuff	Uncertainty assessment of wave-and current-induced global response of floating bridges
IMT-6-2020	Fredrik Mentzoni	Hydrodynamic Loads on Complex Structures in the Wave Zone

ISBN 978-82-326-4666-1 (printed version)  
ISBN 978-82-326-4667-8 (electronic version)  
ISSN 1503-8181



Doctoral theses at NTNU, 2020:159

Fredrik Mentzoni

## Hydrodynamic Loads on Complex Structures in the Wave Zone

 **NTNU**  
Norwegian University of  
Science and Technology

Doctoral theses at NTNU, 2020:159

 **NTNU**

**NTNU**  
Norwegian University of  
Science and Technology  
Faculty of Engineering  
Department of Marine Technology

 **NTNU**  
Norwegian University of  
Science and Technology